

Probing volcano plumbing systems through radar and seismic interferometric observations on active volcanoes

Martins, Joana E.

DOI

10.4233/uuid:6441575d-dfb8-4519-94c9-66663a348493

Publication date

Document Version

Final published version

Citation (APA)

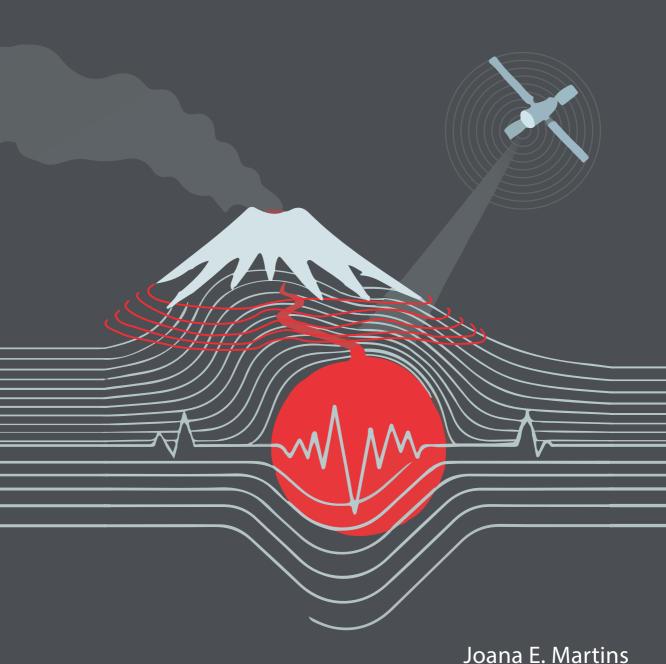
Martins, J. E. (2025). *Probing volcano plumbing systems through radar and seismic interferometric observations on active volcanoes*. [Dissertation (TU Delft), Delft University of Technology]. https://doi.org/10.4233/uuid:6441575d-dfb8-4519-94c9-66663a348493

To cite this publication, please use the final published version (if applicable). Please check the document version above.

Other than for strictly personal use, it is not permitted to download, forward or distribute the text or part of it, without the consent of the author(s) and/or copyright holder(s), unless the work is under an open content license such as Creative Commons.

Takedown policyPlease contact us and provide details if you believe this document breaches copyrights. We will remove access to the work immediately and investigate your claim.

Probing volcano plumbing systems through radar and seismic interferometric observations on active volcanoes



Probing volcano plumbing systems through radar and seismic interferometric observations on active volcanoes

Probing volcano plumbing systems through radar and seismic interferometric observations on active volcanoes

Dissertation

for the purpose of obtaining the degree of doctor at Delft University of Technology, by the authority of the Rector Magnificus Prof.dr.ir. T.H.J.J. van der Hagen, chair of the Board for Doctorates, to be defended publicly on Wednesday 8 October, 2025 at 15:00 o'clock

by

Joana Carolina ESTEVES MARTINS

Master of Science in Geophysics, Universidade de Lisboa Born in Porto, Portugal This dissertation has been approved by the promotors.

Composition of the doctoral committee:

Rector Magnificus, chairman

Prof. dr. ir. R.F. Hanssen, Delft University of Technology, promotor Prof. dr. A.J. Hooper, University of Leeds, United Kingdom, promotor

Independent committee members:

Prof. dr. F. Sigmundsson University of Iceland

Dr. M.J. van der Meulen TNO – Geological Survey of the Netherlands
Dr. E. de Zeeuw-van Dalfsen Royal Netherlands Meteorological Institute /

Delft University of Technology

Prof. dr. ir. E.C. Slob Delft University of Technology Prof. dr. H. Hajibeygi Delft University of Technology

ESTEVES MARTINS, Joana Carolina

Probing volcano plumbing systems through radar and seismic interferometric observations on active volcanoes

Delft University of Technology







Keywords: Volcano, Magmatic Plumbing System (MPS), Seismic, Radar, In-

terferometry, Remote Sensing, Ambient Noise, InSAR, Time series, Geophysical Modelling, Tomography, Satellite Geodesy, Torfajökull, Eyjafjallajökull, Reykjanes Peninsula, Iceland, Surface Deformation,

Earth Observation

Printed by: Ridderprint, The Netherlands.

Cover photo copyright © Joana Martins.

Cover design by Joana Martins and José Pedro Martins powered by Nano Banana.

ISBN: 978-94-6522-796-2

Published and distributed by J. Martins. Email: joanaemartins@protonmail.com

An electronic version of this dissertation is available at

http://repository.tudelft.nl/.

Copyright © 2025 by J. E. Martins. All rights reserved. No part of the material protected by this copyright notice may be reproduced or utilized in any form or by any means, electronic or mechanical, including photocopying, recording or by any information storage and retrieval system, without prior permission of the author.



Pı	eface	•	11
Ał	ostrac	et	ii
Sa	men	vatting	v
No	omen	aclature	ix
1	Intr	oduction	1
	1.1	Motivation	1
	1.2	Background	1
		1.2.1 Magma reservoir vs magma mush paradigm	2
		1.2.2 Understanding volcanic hazards and climate	3
		1.2.3 Harvesting geothermal potential	4
	1.3	Remote sensing for MPS imaging	5
		1.3.1 Volcano seismology	6
		1.3.2 Volcano Geodesy	8
	1.4	Problem statement	10
	1.5	Research Objectives	12
	1.6	Outline	15
2	Met	hods and data	17
	2.1	Gauss-Markov model formulation	17
	2.2	The observations	20
		2.2.1 Interferometry	20
		2.2.2 Seismic wave velocity	21
		2.2.3 Radar deformation rates	23
	2.3	The unknowns and functional model: MPS Geometry Estimation	25
		2.3.1 MPS unknowns: geometry, size and location	25
		2.3.2 Functional Model for Ambient Noise Tomography (ANT)	26
		2.3.3 Functional Model for MPS geometry from InSAR	26
	2.4	Areas of interest	28
		2.4.1 Eyjafjallajökull volcano	28
		2.4.2 Torfajökull volcano	30
		2.4.3 Reykjanes Peninsula	32
	2.5	Data	33
		2.5.1 Seismic data	33
		2.5.2 Radar data	35

3	Ima	ging Torfajökull volcano with ANSI tomography	37
	3.1	Introduction	
	3.2	Retrieval of Surface Waves from Ambient Noise	39
		3.2.1 Pre-Processing of the Ambient Noise	39
		3.2.2 Frequency Selection	39
		3.2.3 Crosscorrelation and Temporal Stacking	42
		3.2.4 Direction and Slowness of the Microseism Noise	43
	3.3	Velocity Variations at Depth from Surface Waves	47
		3.3.1 Average Dispersion Curve	
		3.3.2 Path Dispersion	
		3.3.3 Source Phase Estimation	
		3.3.4 Azimuthal Velocity Variations	
	3.4	Tomography	
		3.4.1 Tikhonov Regularization	
		3.4.2 Checkerboard Tests	
	3.5	Results	
		3.5.1 Surface-wave Tomography	
		3.5.2 3D S-wave Velocity	
	3.6	Discussion	
	0.0	3.6.1 Quality Control	
	3.7	Conclusions	
			-
4		S-wave velocity imaging of Reykjanes Peninsula with ANT	63
		Introduction	
	4.2	Data and Methodology	
		4.2.1 BSW From Cross-correlations	
		4.2.2 Surface-wave Phase Velocity Picking	
		4.2.3 Tomography	
		4.2.4 Checkerboard Resolution	
		4.2.5 Depth Velocity Estimation	
		Results	
	4.4	Discussion	
		4.4.1 Resolution	
		4.4.2 Insights on the Geothermal Fields	
		4.4.3 Future Applications	
	4.5	Conclusions	79
5	The	Eyjafjallajökull 2010 eruption: InSAR, GNSS and seismic constraints	87
J	5.1	Introduction	
	5.1	5.1.1 The 20 years of Unrest	
		5.1.2 The 2010 Eruption	
	5.2	Data and Methodology	
	5.2	5.2.1 SAR data	
		5.2.2 Interferograms	
		5.2.3 InSAR Time Series	
		5.2.4 Consistency check with GNSS	(10)

	5.3	Eruptive Deformation Cycle: InSAR and GNSS results
		5.3.2 Co-Eruptive Deformation Pause and Post-eruptive Subsidence 107
	5.4	Modelling Magma Sources: Co- and Post-Eruptive Results
		5.4.1 Geomechanical Forward Model with Seismicity Constraints 110
		5.4.2 Inverse Modelling: Post-eruptive phase
	5.5	Discussion and conclusions
6		S of Torfajökull volcano with Geodetic and Seismic Imaging 117
	6.1	Introduction
		Data and Methodology
	6.3	Modelling
		6.3.1 Seismic Imaging
	C 4	6.3.2 Geodetic Imaging
	6.4	Results 6.4.1 InSAR Time Series 123
		6.4.2 Modelling
	6.5	Conceptual Model of Torfajökull Magmatic System
		Summary and Discussion
7	Sun	nmary And Conclusions 133
7	Sun 7.1	nmary And Conclusions 133 Scientific contribution
7		
7		Scientific contribution
7	7.1	Scientific contribution
7	7.1	Scientific contribution
7	7.1	Scientific contribution
	7.1 7.2 7.3	Scientific contribution
Bi	7.1 7.2 7.3 bliog	Scientific contribution
Bi	7.1 7.2 7.3 bliog Sup	Scientific contribution
Bi	7.1 7.2 7.3 bliog Sup	Scientific contribution
Bi A	7.1 7.2 7.3 bliog Sup A.1 A.2	Scientific contribution

Preface

This thesis was carried out within the Department of Geoscience and Remote Sensing, Delft University of Technology, between 2010 and 2014, and completed during my subsequent position at TNO – Geological Survey of the Netherlands. The work was carried out in the context of international collaborations on volcanic hazard monitoring and geophysical imaging. During this period, I also conducted two months of research at the University of Leeds, one week at the University of Cambridge, and four weeks of fieldwork in Iceland, which provided valuable experience and contributed to the development of this work.

The research was funded by the Portuguese Foundation for Science and Technology (FCT, grant DFRH-SFRH/BD/61663/2009) and was conducted within the framework of the FUTUREVOLC (EU FP7 project 308377) and IMAGE (EU FP7 project 608553) projects. The seismic data for Torfajökull were provided by Cambridge University and archived at the IRIS data centre, while the Reykjanes seismic data were made available through IMAGE. ESA kindly provided ERS and ENVISAT data, and DLR supplied TerraSAR-X data under FUTUREVOLC. Earthquake and GNSS data used in the maps of Iceland were sourced from the SIL seismic catalogue and made available through the Icelandic Meteorological Office, the University of Iceland, and ISOR.

This thesis is a compilation of my work disseminated through conferences and journals, re-adapted into a coherent monograph. I declare that the work submitted is my own and that appropriate credit to others has been given throughout this manuscript by corresponding referencing. To optimise the narrative and avoid repetition, I have adapted and reorganised sections such as descriptions of the areas of interest and methodological details when they appeared in more than one publication.

Throughout this thesis, I use "I" when discussing personal decisions, ensuring transparency regarding my contributions and responsibilities, and I use "we" whenever the work involves collaboration with other individuals who contributed with insights or expertise as a collaborative result (e.g., through publications) to acknowledge the collective effort. In other cases, I use passive voices to maintain a neutral tone to highlight the results of the research process rather than to emphasize personal decision making.

Abstract

Understanding the properties of magmatic plumbing systems beneath active volcanoes is crucial to better characterise volcanic processes at both local and global scales. Locally, this helps identify crustal reservoirs, determine magma supply rates, and map migration processes throughout the eruptive cycle – information that directly informs our scientific understanding of volcanic processes, improves volcanic-hazard mapping, and supports the development and management of geothermal resources. Globally, such insights improve our understanding of how these systems interact within the solid Earth, oceans, and atmosphere.

Despite its importance, directly measuring the Earth's subsurface remains a challenge. Deformation measurements from Interferometric Synthetic Aperture Radar (InSAR) and subsequent geophysical modelling offer potential solutions, but have limitations related to resolution and uncertainties in estimating the geometry, depth, and volume change of magma sources. In addition, estimates of elastic and rheological properties are often lacking and rely on unverified assumptions.

To overcome these challenges, this study introduces an interdisciplinary approach, leveraging the integrated strengths of seismic and geodetic space-time metrics and using Icelandic volcanoes as case studies. The objectives of this study are as follows: (i) derive phase velocities from seismic ambient noise using seismic interferometry to enhance 3D shear-wave tomography of volcanic structures; (ii) estimate InSAR-derived time series to model surface deformation and provide estimates for the geometry, depth, and volume changes of magmatic plumbing systems, incorporating seismic or other geodetic constraints whenever possible; and (iii) assess the effectiveness of the above-mentioned methods using real and simulated data active volcanoes for which the techniques are individually or mutually applied.

For the first objective (i), I used ambient seismic noise seismic interferometry, to estimate empirical Green functions between seismic station pairs, enabling the derivation of phase velocities. I estimated the phase velocities using a novel two-step approach: an initial frequency-domain estimation followed by a refinement in the time domain, yielding reliable phase velocity picks. To ensure a good distribution across azimuthal quadrants, I applied a beamforming analysis, which reinforced the ambient noise quality in terms of azimuthal coverage. To deal with ill-posedness problems, I developed a tomographic inversion procedure using Tikhonov regularisation and cross-validation procedures, with sensitivity tests conducted to evaluate inversion robustness. Finally, using the surface-wave dispersion curves estimated through the tomographic inversion, I used a Monte Carlo-based neighbourhood algorithm to derive the depth-dependent S-wave velocity models.

On the geodetic side, for objective (ii), I estimate the time series from InSAR using StaMPS. After estimating the deformation rate from the derived time series, I apply inverse or forward modelling depending on the research problem inherent to each

volcano. For inverse modelling, I use the Gauss-Markov formulation to define optimal functional and stochastic models for surface deformation and Bayesian statistical methods to estimate posterior parameter probabilities. I incorporate geodetic data, such as GNSS in two ways, first to identify possible mismatches between InSAR and GNSS at the locations of the GNSS stations and then constrain the estimation of MPS size, geometry and depth during inversion.

Finally, for objective (iii), the effectiveness of the two-technique approach resulted in enhanced information on the three active volcanoes using both real and simulated data. As real data, I applied InSAR over three satellite missions; ERS and ENVISAT over the Torfajökull volcano and TerraSAR-X over the Eyjafjallajökull 2010 eruption. For seismic data, I used an historical network of 22 seismometers deployed in the summer of 2005, operating (approximately 3 months) over and around the Torfajökull caldera. For the Reykjanes Peninsula, I used 30 seismometers that operated from March 2014 to August 2015 (approximately 1,5 years). I used simulated data, or checkerboard sensitivity tests throughout the seismic tomography processing, to understand if the chosen resolutions could solve the geometric details.

The effectiveness of seismic and geodetic spacetime metrics produced the following key results in each volcano.

At Torfajökull volcano, the final 3D shear-wave velocity model shows low velocity variations between -10% and -15% located in the eastern and south-western investigation areas, outside the volcano caldera. Beneath the volcano caldera and at shallower depths (up to ~3 km depth), velocity variations down to ~-10% in small areas may also indicate hot material. Possibly the presence of small pockets of magma that may be the origin of the high-temperature geothermal field at the surface. From 3.5 km to higher depths, low-velocity anomalies reaching between -10 and -15% variations extend spatially in a NW-SE fashion within the volcano caldera. The anomalies below -10% variation from the average velocities may indicate the existence of warm material, possible molten or partial molten cavities, and channels for all depths explored. Highvelocity anomalies correlate with a ring-like structure following the shape and location of the caldera outline, while the strong high-velocity anomalies following the north and northeast quadrants correlate well with lavas erupted at the surface. The model ranges between 1.5 km to 6 km depth and has horizontal and vertical resolutions of 4 km and 500 m, respectively. The deformation modelling indicates tectonic extension, aligned with the residual displacement patterns after the fit of a spheroidal magma source at ~5 km depth, sized 4.5 x 5 km oriented NE-SW. The estimation of the source depth from InSAR coincides nicely with the low-velocity anomalies of the derived 3D S-wave velocity model.

Including GNSS data in Eyjafjallajökull led to a refined source model for the posteruptive deformation of the Eyjafjallajökull 2010 eruption. GNSS-constrained geodetic inversions are inconsistent with a two-dimensional sill beneath the summit; instead they favour a three-dimensional ellipsoidal source (long axis is 2.7-4.2 km, short axis is 0.55-0.74 km and strike of the long axis is $60-73^{\circ}$), at 6.4-7.2 km depth and equivalent to a volume reduction of $\sim 0.02-0.026$ km³. Forward models employing the previously suggested stack-of-sills do not reproduce the InSAR surface displacements, implying that seismic relocations that trace apparent sill stacks likely mark brittle failure and tran-

iv Contents

sient fluid pathways in a heterogeneous system. Together with petrological evidence, these geodetic results support a mush-dominated magma reservoir at Eyjafjallajökull, reinforcing a broader shift in volcanology from simple sill/chamber models toward dynamic, crystal-rich networks.

In the western Reykjanes Peninsula, tomography highlighted significant and well-constrained low-velocity seismic zones with the strongest (below -15%) beneath the Svartsengi and Eldvörp geothermal fields. The low-velocity anomaly at Svartsengi coincides with the uplift source associated with the 2024 Grindavík eruption series. Similar anomalies are present beneath the Geldingadalur, Fagradalsfjall, and Litli-Hrutur eruption sites, although interpretations at these edges of the model must be treated with caution because checkerboard tests indicate reduced resolution there. Taken together, the spatial coincidence between low-velocity zones and eruptive sites suggests that these anomalies mark magma regions associated with the 2024 activity, but higher-resolution imaging and additional independent datasets are required to confirm a direct causal link.

Samenvatting

Om actieve vulkanen te kunnen begrijpen is het nodig om de aan- en afvoerkanalen van magma beter te karakteriseren, zowel op lokale als mondiale schaal. Lokaal helpt dit bij het identificeren van magmatische reservoirs, het bepalen van magmatoevoersnelheden en het in kaart brengen van magma-migratieprocessen gedurende de eruptieve cyclus – informatie die direct bijdraagt aan ons wetenschappelijk begrip van vulkanische processen, de verbetering van vulkanische risicokaarten en de ontwikkeling en het beheer van geothermische hulpbronnen. Op mondiaal niveau verbeteren dergelijke inzichten ons begrip van hoe deze systemen interageren binnen de vaste aarde, de oceanen en de atmosfeer.

Desalniettemin blijft het een uitdaging om de ondergrond van de aarde direct waar te nemen. Deformatiemetingen met Interferometrische Synthetisc Apertuur Radar (InSAR) en daaropvolgende geofysische modellering bieden mogelijke oplossingen, maar hebben beperkingen in hun resolutie en onzekerheden bij het schatten van de geometrie, diepte en volumeverandering van magmabronnen. Daarnaast ontbreken vaak schattingen van elastische en reologische eigenschappen en zijn ze gebaseerd op niet-geverifieerde aannames.

De onderliggende studie beoogt deze uitdagingen te overwinnen, middels een interdisciplinaire benadering die de sterke punten van seismische en geodetische methodes combineert, met IJslandse vulkanen als casestudies. De eerste doelstelling hierbij is het afleiden van fase-snelheden uit seismische omgevingsruis met behulp van seismische interferometrie om de 3D shear-wave tomografie van vulkanische structuren te verbeteren. De tweede doelstelling is het schatten van tijdreeksen uit InSAR om oppervlaktevervorming te modelleren en schattingen te geven van de geometrie, diepte en volumeveranderingen van magmatische systemen, waarbij indien mogelijk seismische of andere geodetische beperkingen worden meegenomen. De derde en laatste doelstelling is het beoordelen van de effectiviteit van de bovengenoemde methoden met behulp van echte en gesimuleerde gegevens van actieve vulkanen, waarop de technieken afzonderlijk of in combinatie worden toegepast.

Voor de eerste doelstelling wordt seismische interferometrie met omgevingsseismische ruis gebruikt om empirische Greensfuncties tussen seismische stationparen te schatten, wat de afleiding van fase-snelheden mogelijk maakt. De fase-snelheden wordt geschat met een nieuwe tweestapsbenadering: een initiële frequentiedomeinschatting gevolgd door een verfijning in het tijdsdomein, wat resulteert in betrouwbare fase-snelheidspunten. Om een goede spreiding over de richtingen te waarborgen, wordt een beamforming-analyse toegepast, die de kwaliteit van de omgevingsruis versterkt in termen van azimutale dekking. Om de slecht-gestelde problemen aan te pakken is een tomografische inversie met behulp van Tikhonov-regularisatie en kruisvalidatieprocedures ontwikkeld, waarbij gevoeligheidstesten worden uitgevoerd om de robuustheid van de inversie te evalueren. Ten slotte worden de oppervlakte-golf dispersiecurves,

vi Contents

geschat via de tomografische inversie, gebruikt om met een op Monte Carlo gebaseerde naburigheidsalgoritme de diepte-afhankelijke S-golf snelheidsmodellen af te leiden.

Voor de tweede, geodetische, doelstelling worden tijdreeksen van InSAR geschat. Nadat de deformatiesnelheid uit de afgeleide tijdreeksen is bepaald, wordt een inverse of voorwaartse modellering toegepast, afhankelijk van het specifieke onderzoeksprobleem van een vulkaan. Voor de inverse modellering wordt een Gauss-Markov-formulering gebruikt om optimale functie- en stochastische modellen voor oppervlaktevervorming te definiëren, en Bayesiaanse statistische methoden om de posteriori kansdichtheden van de parameters te schatten. De geodetische gegevens, zoals GNSS, worden op twee manieren geïntegreerd. Ten eerste om mogelijke discrepanties tussen InSAR en GNSS te identificeren op de locaties van de GNSS-stations, en ten tweede om de schatting van de grootte, geometrie en diepte van de magmatische systemen te begrenzen tijdens de inversie.

Tot slot (de derde doelstelling) resulteert de benadering met zowel de seismische als de geodetische techniek gecombineerd in verbeterde informatie over drie specifieke actieve vulkanen, waarbij zowel meet- als gesimuleerde waarnemingen worden gebruikt. InSAR is toegepast op drie satellietmissies: ERS en ENVISAT met betrekking tot de Torfajökull-vulkaan en TerraSAR-X met betrekking tot de Eyjafjallajökull-uitbarsting van 2010. Seismische gegevens van een historisch netwerk met seismometers worden gebruikt. Deze waren in de zomer van 2005 gedurende ongeveer drie maanden actief in en rond de Torfajökull-caldera. Voor het Reykjanes-schiereiland wordt een netwerk van seismometers gebruikt dat actief was van maart 2014 tot augustus 2015. Daarnaast worden gegevens gesimuleerd, via *checkerboard*-gevoeligheidstesten. Hiermee kan tijdens de verwerking van de seismische tomografie worden beoordeeld of de gekozen resoluties de geometrische details voldoende kunnen oplossen.

Bij de Torfajökull-vulkaan toont het uiteindelijke 3D shear-wave snelheidsmodel lage snelheidsvariaties tussen -10% en -15% in de oostelijke en zuidwestelijke onderzoeksgebieden, buiten de caldera van de vulkaan. Onder de caldera en op ondiepere dieptes (tot ongeveer $3 \, \mathrm{km}$ diepte) kunnen snelheidsvariaties tot ongeveer -10% in kleine gebieden mogelijk wijzen op heet materiaal, mogelijk de aanwezigheid van kleine magmareservoirs die instrumenteeel kunnen zijn voor het hogetemperatuurgeothermische veld aan het oppervlak.

Vanaf $3.5\,\mathrm{km}$ tot grotere dieptes strekken lage-snelheidsanomalieën met variaties tussen -10 en -15% zich ruimtelijk uit in NW-ZO-richting binnen de caldera van de vulkaan. De anomalieën met variaties onder -10% van de gemiddelde snelheden kunnen wijzen op de aanwezigheid van warm materiaal, mogelijk gesmolten of gedeeltelijk gesmolten holtes en kanalen op alle onderzochte dieptes.

De hoge-snelheidsanomalieën correleren met een ringachtige structuur die de vorm en locatie van de calderaomtrek volgt. De sterke hoge-snelheidsanomalieën in de noordelijke en noordoostelijke kwadranten correleren goed met lava die aan het oppervlak is uitgevloeid.

Het model bestrijkt dieptes van 1.5 km to (numerical range) 6 km, heeft een horizontale resolutie van 4 km en een verticale resolutie van 500 m. De vervormingsmodellering wijst op tektonische extensie, corresponderend met de resterende verplaatsingspatronen na het fitten van een bolvormige magmabron op een diepte van ongeveer 5 km,

Contents vii

met een afmeting van 4.5×5 km en georiënteerd in NO-ZW-richting. In een kwalitatieve beoordeling komt de schatting van de brondiepte uit InSAR goed overeen met de lagesnelheidsanomalieën in het afgeleide 3D S-golf-snelheidsmodel.

Het opnemen van GNSS-gegevens in Eyjafjallajökull leidde tot een verfijnd deformatiemodel voor de post-eruptieve periode van de uitbarsting van Eyjafjallajökull in 2010, dat eerdere interpretaties ter discussie stelt. Geodetische inversies waarin GNSS-randvoorwaarden zijn opgenomen, zijn niet consistent met een tweedimensionale *sill* onder de top; in plaats daarvan geven ze de voorkeur aan een driedimensionale, ellipsoïde bron (lange as 2.7–4.2 km, korte as 0.55–0.74 km, azimutrichting van 60–73°) op 6.4–7.2 km diepte (volumeverandering van ongeveer 0.02–0.026 km³). Voorwaartse modellen gebaseerd op de eerder voorgestelde stapeling van sills reproduceren de InSAR-oppervlakteverplaatsingen niet, wat impliceert dat seismische relocaties die ogenschijnlijke stapelingen van sills volgen waarschijnlijk zones van bros falen en transiënte vloeistofpaden markeren binnen een heterogeen systeem. In combinatie met petrologisch bewijs ondersteunen deze geodetische resultaten een *mush*-gedomineerd magmareservoir onder Eyjafjallajökull, en versterken ze een bredere verschuiving in de vulkanologie van eenvoudige sill-/kamermodellen naar dynamische, kristalrijke netwerken.

Op het westelijke Reykjanes-schiereiland toont tomografie significante en goed afgebakende lage-snelheidszones, waarbij de sterkste anomalieën (onder -15%) liggen onder de geothermische velden van Svartsengi en Eldvörp. De lage-snelheidsanomalie bij Svartsengi valt samen met de bodemstijging die geassocieerd wordt met de Grindavíkuitbarstingsreeks van 2024. Vergelijkbare anomalieën worden aangetroffen onder de uitbarstingslocaties van Geldingadalur, Fagradalsfjall en Litli-Hrútur, hoewel interpretaties voor deze randzones met voorzichtigheid moeten worden benaderd, omdat *checkerboard*-tests daar een verminderde resolutie aantonen. Alles bij elkaar genomen suggereert de ruimtelijke samenloop tussen lage-snelheidszones en eruptieplaatsen dat deze anomalieën magma-rijke zones markeren die verband houden met de activiteit sinds 2024, maar hogere-resolutiebeelden en aanvullende, onafhankelijke datasets zijn nodig om een direct oorzakelijk verband te bevestigen.

Nomenclature

Acronyms

CO₂ Carbon dioxide

DRE Dense-rock equivalent (used to estimate volcanic eruption volume)

EGF Empirical Green's functions

H₂O Water

HF High-Frequency LF Low-Frequency

MPS Magmatic plumbing system
RI Radar interferometry
RMSE Root mean squared errors
SI Seismic Interferometry

LoS Line of Sight

IMO Icelandic Meterological OfficeUSGS Unites States Geological SurveyVEI Volcanic Explosivity Index

VIPS Volcanic and igneous plumbing systems

PS Persistent Scatterer

1

Introduction

1.1. Motivation

The characterisation of magmatic plumbing systems is important to understand local and global volcanism, but we lack direct observations. In this thesis, I investigate the use of satellite radar interferometry and seismic interferometry to enhance our knowledge of the location, size, and geometry of magmatic plumbing systems.

1.2. Background

Volcanic eruptions are the most direct manifestation of mantle processes on the Earth's surface, showcasing the dynamic interplay within the Earth's interior (Richards et al. 1989; Davaille 1999). While extruded volcanic rocks may say much about composition and conditions under which the rocks have formed, less is known about the pathways and reservoirs along which these rocks (magma) have travelled or rested before eruption (Spera 2000; Marsh 2006; Cashman and Sparks 2013). These interconnected systems of pathways and reservoirs are recently known as volcanic and igneous plumping systems (VIPS) (Burchardt et al. 2022) or simply magmatic plumbing systems (MPS) (Sigurdsson et al. 1999). Understanding these systems is crucial for unravelling the complexities of volcanic processes.

Improving our understanding of MPS serves three key purposes. First, it enhances our scientific comprehension of how magma is transported through the Earth's crust, where and how it is stored, in which volumes, and what triggers an eruption. This knowledge is fundamental to advance our understanding of volcanic phenomena and to improve our ability to forecast and mitigate volcanic hazards. Second, it will help minimise the impact of volcanic hazards, e.g., by predicting more accurately the type of volcanic eruption, its impact and its location. Third, a better understanding of MPS can be leveraged to maximise the utilisation of geothermal energy in volcanic areas (or high-enthalpy geothermal systems). By accurately mapping magma reservoirs, we can strategically identify suitable locations to harness geothermal power while avoiding the risks associated with drilling into active magma reservoirs.

The key to minimising the impact of volcanic eruptions, or maximising the energetic potential of a volcano, is to forecast 'where', 'how', and 'when' volcanic unrest will lead to an eruption. The location—the 'where'—is likely to be around the 1350 potentially active volcanoes worldwide (USGS 2006). Subduction and rift zones, areas with geothermal surface manifestations, active volcanic systems, and hot spots embrace most of these volcano locations. The 'how' question can benefit from information about the processes

2 1. Introduction

preceding the eruptions, such as: how is magma stored? how does magma flow occur through volcanic conduits and reservoirs? or how big are the magma chambers? It also defines whether volcanoes can produce super-eruptions, i.e. eruptions with a Volcanic Explosivity Index (VEI) above 8, with a bulk ejected volume greater than 1000 km³. With comprehensive knowledge of the volcano subsurface and continuous monitoring, the 'when' question can be addressed with a certain degree of likelihood. This is the case for some of the most active and densely populated volcanic regions, where various measurement methods and continuous monitoring are in place, such as Italy, Iceland, Hawaii, and Japan. However, it is worth acknowledging the limitations in predictive capabilities. For example, some volcanoes, such as Hekla in Iceland, exhibit seismic activity only a few hours before an eruption (Soosalu et al. 2005; Soosalu and Einarsson 2005).

Most of these questions revolve around a comprehensive understanding of MPSs. Better insights into a volcano's MPS could improve current models from a static perspective (i.e., geometry, depth, volumes, composition, and magma volatile content) and from a dynamic perspective (i.e., magma flow, duration, and periodicity of the eruption cycles). While the static perspective would be the basis for, e.g., magma volume estimation, snapshots of MPS can also be used to simulate magma flow dynamics and forecast the likely paths of magma emplacement or propagation prior to eruptions. A mapped volcano subsurface would allow us to test hypotheses on the mechanisms that can trigger an eruption, the size and impact of a volcanic outburst, or the influence on oceans, atmosphere, and possibly global climate.

1.2.1. Magma reservoir vs magma mush paradigm

MPS have long been thought to be a network of interconnected magma chambers ranging from tens of metres to several kilometres in size. These subsurface pathways would form as the magma rises and accumulates in a large magma reservoir or smaller reservoirs within the Earth's crust. Whenever these pathways are intruded by magma, the transport of magma in brittle rock can occur by vertical, subvertical, or steep dipping dikes (Rivalta et al. 2015). The magma can then accumulate in "magma domains" (Sigmundsson 2016), which have been assumed to have different geometries. Examples of these geometries include structures with a high length-to-depth thickness ratio, often referred to as 2D-like structures such as sheets and sills (Gudmundsson 1998; Tibaldi 2015). On the other hand, magma reservoirs are three-dimensional structures that exhibit a range of shapes and geometries. These reservoirs are known to accumulate substantial volumes of magma (Sigurdsson et al. 2015), and depending on its phase within the volcanic cycle, the magma reservoir's content can be fully or partially molten rock containing varying amounts of melt and gas bubbles.

Magma chambers or 3D-like reservoirs have been recognised for their ability to accumulate significant volumes of magma (Sigurdsson et al. 2015). This point of view originates from the notion that eruptions characterized by large outpourings of magma should be proportional to the capacity of magma storage. Therefore, in the last century, the prevailing consensus within the scientific community has been that super volcanic eruptions with a higher Volcanic Explosivity Index (VEI) of \geq 8 would require the presence of an exceptionally large magma chamber filled with molten material.

Following a similar proportionality reasoning: large volcano calderas are considered to be the surface expression of volcanoes with large magma chambers, as the size of the volcano caldera is proportional to its deflation after an eruption (Sigurdsson et al. 2015).

In recent years, petrology studies have reassessed the idea that there is a single long-lived molten magma chamber and described it as the magma chamber paradigm (Cashman et al. 2017; Sparks et al. 2019). The paradigm involves the maintenance and evolution of a sizeable melt-dominated reservoir in the crust capable of producing high VEI eruptions. Physical models suggest that magma chambers with molten rock are difficult to maintain or short-lived and that high rates of melt transfer would be required to maintain melt-dominated magma chambers in the upper crust (Degruyter and Huber 2014).

Conventional understanding has therefore shifted: large volcanic eruptions requiring voluminous magma chambers may not have originated in a long-lived fully molten magma reservoir but in a magmatic system highly dominated by mush areas (Hildreth 1981; Sinton and Detrick 1992; Bachmann and Huber 2016; Cashman and Giordano 2014; Cooper and Kent 2014; Burchardt 2018). Mush areas —or volumetrically dominant mush systems (Edmonds et al. 2019)— are parts of the reservoir that contain sufficiently high crystal contents forming a semi-rigid framework, a mixture of crystals with interstitial liquid magma (Sparks et al. 2019; Maclennan 2019).

According to Sparks et al. (2019), a magma reservoir is composed of three phases: melt, fluids, and crystals, for which magmatic systems may be divided into the magma, mush and surrounding host rock domains. Following these definitions and physical properties of magmatic systems, the same authors describe four main non-exclusive mechanisms for magma chamber formation while reviewing the arguments that magmatic plumbing systems are predominantly mush.

In principle, if such sizeable molten rock reservoirs existed, one could detect them through seismic imaging. Recent observations of magma storage from different regions indicate the presence of multiple melt lenses feeding single eruptions and rapid pre-eruptive assembly of large volumes of melt (Cashman and Giordano 2014). However, the resolution of seismic imaging is too low to define a detailed geometry or scale of melt distributions undermining the estimation of melt fractions (Sparks et al. 2019) and limited accuracy in estimating properties such as temperature and porosity (Maclennan 2019). To tackle this paradigm shift and improve our general knowledge on MPS, it is imperative to integrate multiple disciplines, employ a combination of methodologies, and establish a unified approach that harmonises the perspectives of various disciplines.

1.2.2. Understanding volcanic hazards and climate

Magmatic Plumbing Systems hold, carry, and emit volcanic products that generate volcanic hazards. Knowledge of MPS morphology is instrumental in identifying crustal reservoirs, assessing magma supply rates, elucidating migration processes during preand co-eruptive phases, and on post-eruptive cooling cycles. The morphology of the MPS can serve as an indicator of the anticipated eruption style and provide information on the potential volume of eruptive material. Although it may not directly contribute to precise eruption timing predictions, knowledge of the MPS morphology is crucial to forecasting the dynamics and mechanisms through which eruptions may unfold.

On a global scale, insights on MPS can impact across the solid, oceanic, and atmospheric Earth context due to the exchange of volcanic products along the three domains. On a local scale, understanding the conditions in which magma is stored (pressure, temperature, and state) can, e.g., indicate how quickly magma can be mobilised (Cooper and Kent 2014) or how high volcanic plumes can be (Hreinsdóttir et al. 2014). On both regional and global scales, volcanic hazards have a tremendous impact on our daily lives. The most common volcanic hazards can be pyroclastic flows, hot ash emission plumes, and fluid (e.g., Hawaii) or viscous lava streams. Glacier flows, avalanches, and earthquake activity may also stimulate outburst floods. Known as jökulhlaups (Björnsson 1992), these floods can be the most common hazard related to ice-covered volcanoes such as in Mt. St. Helens, Alaska, and Iceland (Major and Newhall 1989). Rainstorms and breakouts of crater lakes can reach extremes, dragging unconsolidated soils, sediments, and anthropogenic structures into the water path, e.g. the Lahars at Mount Pinatubo (Newhall and Punongbayan 1996; Lowe et al. 1986).

Volcanic eruptions also interact closely with the atmosphere and oceans, and shortand long-term effects also impact our safety and economy. The 2010 Eyjafjallajökull air traffic disruptions and the consequential high financial impacts (Mazzocchi et al. 2010; Casadevall 1994) are an example of short-term impacts. In the long-term, the injection of sulfur gases into the stratosphere and the oceans can result in the reduction of rainfall (Gillett et al. 2004), ecosystem ocean acidification through carbon dioxide vents (Hall-Spencer et al. 2008), and other responses in the Earth's climate system as indicated by Robock (2000). On the other hand, specific underwater eruptions can reduce ocean warming and, as a consequence, sea level rise as cooling effects on the ocean surface have been found to last for an extended period after an eruption (Church et al. 2005; Gleckler et al. 2006). To close the cycle, the current high temperatures due to global warming have been causing the ice on volcano glaciers to retreat. Pressure decrease due to the retreat and rebound of the surface may alter the capacity to store and enhance magma's capture within the crust and promote magma storage. Such phenomena have been observed by Hooper et al. (2011) during the intrusion without an eruption of a deep dyke at Upptyppingar, in Iceland.

1.2.3. Harvesting geothermal potential

In addition to their significance in understanding volcanic hazards, an in-depth exploration of the properties of MPS can also contribute to harnessing the geothermal potential found within volcanic environments (Rinehart 1980). The extreme geothermal gradients and high surface heat flow mainly present in volcanic areas are known as high-enthalpy systems/reservoirs, which can be used to produce electrical power from steam (Duffield and Sass 2003). In the context of the energy transition from fossil to renewable energy and as a long-term investment, geothermal resources in volcanic areas (high enthalpy) can help reduce the need for fossil fuels (Boyle 2004). In Europe, buildings and industry heat and cooling systems represent half of the EU's energy consumption (EU 2018). Alternatives may pass through biomass boilers and solar heating systems. However, geothermal resources offer a remarkable advantage over other renewable energies that require continuous, reliable production (365 days/year) by eliminating the need for energy storage (Bajpai and Dash 2012). Continuous energy

sources are more difficult to achieve than solar heating or wind energy. In addition to the benefits and prediction for a 18.5% rate of growth of geothermally generated electric power between 2020 and 2025 (Huttrer 2021), the full potential of geothermal sources is not fully explored. Attempts to explore deep geothermal sources, particularly the supercritical part of hydrothermal systems, hold great promise for enhancing energy efficiency and unlocking new potentials in geothermal energy harvesting. This growing interest in deep geothermal systems further underscores the importance of gaining a deeper understanding of MPS, as it plays a crucial role in the characterisation and exploitation of these geothermal resources. One of the most noticeable advantages of supercritical systems is that the increase of pressure (>221 bars) and heat (>374°C for seawater (Reinsch et al. 2017)) can potentially induce an estimated power output ~10 times higher than traditional Icelandic geothermal wells (Fridleifsson and Albertsson 2000; Albertsson et al. 2003). In Iceland, while customary geothermal systems usually reach down to 3 km depth with steam temperatures between 290°C and 320°C, predictions by Friðleifsson et al. (2014b) report that deep wells reaching depths between 4 km and 5 km may have temperatures between 400°C and 600°C. These results were tested and partially confirmed with the second Icelandic Deep Drilling Project (IDDP2) in Reykjanes (drilled between 2016 and 2017) with a measured temperature of 427°C and fluid pressure of 340 bar at ~4.5 km depth (Friðleifsson et al. 2017). The intention of exploiting deep geothermal sources and recent episodes of drilling into a magma reservoir also highlighted the need for MPS improved knowledge and imaging techniques to aid in drilling operations. For example, in 2009, during the first Icelandic Deep Drilling Project (IDDP), the drilling of the IDDP-1 well in the Krafla area of Iceland encountered rhyolitic magma at a depth of 2104 m (Hólmgeirsson et al. 2010). Magnetotelluric (MT) electromagnetic surveys performed at Krafla estimated a magma source at 4.5 km deep (Elders et al. 2011; Gasperikova et al. 2015), but the drilling pit encountered unexpected magma at shallower depths. Although MT surveys are the preferred geophysical measurement procedure to locate the water reservoirs required for the closed loop of geothermal production (e.g. (Newman et al. 2008; Árnason et al. 2010; Hersir et al. 2018)) and they have been utilised frequently in Iceland (e.g. (Hersir et al. 1984; Eysteinsson and Hermance 1985; Oskooi et al. 2005)), the magma pocket drilled at the Krafla IDDP-1 well location was possibly below the level of resolution of the area surveyed using MT (Árnason et al. 2007). In December 2016, the IDDP-2 well drilled at the WRP saline geothermal system in southwest Iceland successfully reached a depth of approximately 4.5 km (vertical) (Ómar Friðleifsson et al. 2017; Elders et al. 2014; Friðleifsson et al. 2018). For the location of the well, operators could consider results from resistivity measurements (Karlsdóttir et al. 2018; Friðleifsson et al. 2014a; Darnet et al. 2018), as well as travel-time seismic tomography (Jousset et al. 2017). The drilling into a magma pocket and the need for deep wells drilling unlocked new perspectives on (i) the presence of shallow magma pockets, and (ii) the need for higher-resolution imaging techniques to assist drilling operations.

1.3. Remote sensing for MPS imaging

The impossibility of measuring and looking directly into the Earth's subsurface boosted the deployment and investment in remote sensing techniques. Through indirect mea6 1. Introduction

surements, seismology and geodesy have provided valuable insights into the interior of the Earth and have equal potential to MPS characterisation (Magee et al. 2018). Whether acquired from Earth Observation satellites or from seismic and MT techniques, both passive and active remote sensing methods are the only way to map and understand the subsurface rheology and Earth's internal processes. Through indirect measurements, seismology and geodesy are two scientific fields that have provided the most significant insights into the Earth's interior and MPS characterisation. In the following, I discuss volcano seismology and volcano geodesy.

1.3.1. Volcano seismology

Seismic methods are crucial for probing MPS as they provide a unique tool by revealing the dynamics of magma injection and transport, mapping in situ properties, and constraining the extent and evolution of magma, which is essential for assessing eruptive behaviour and volcanic hazards (Chouet 2003). Understanding volcanic processes and estimating the properties of the subsurface is possible using seismic wave propagation techniques. Through waveform analysis of seismic activity, the distinction of seismic event types has been used to characterise volcanic mechanisms and derive models for, e.g. volcanic fluids (Kawakatsu and Yamamoto 2015).

Each type of seismic event, associated with a particular source mechanism, is used to estimate different physical phenomena. An event may be referred to as a source of 'illumination' because of its characteristic to shed light on the often obscure processes in the subsurface. In volcanically active areas, there are four main types of seismic events that are commonly identified and helpful for MPS understanding purposes (McNutt 2005; Sigurdsson et al. 2015; Kawakatsu and Yamamoto 2015): high-frequency (HF) earthquakes (or volcano-tectonic events), low-frequency (LF) earthquakes, explosions, and volcanic tremors.

HF events are usually associated with shear fractures (regional tectonics, hydrofracturing, volumetric extension due to magma intrusions or cooling) and are therefore not expected to initiate within magma chambers with partially molten material. For this reason, one of the most currently used methods to understand magma intrusions prior to an eruption is precise event positioning to identify areas of high event density instead of areas void of HF earthquakes. The distinction between both areas in time is essential. Seismic events that become shallower over time indicate that a magma intrusion is rising, and areas void of earthquakes may be due to partially molten sills or reservoirs. Stress orientations by focal mechanisms and stress tensor inversion are typically some of the primary usages of HF events (Fernández et al. 2002; Moran 2003; Sánchez et al. 2004). Once the locations of the HF events are known, using the arrival times of multiple events, it is possible to generate tomographic images of seismic wave velocity and seismic velocity anomalies. Velocity anomalies characterize the properties related to subsurface density, pressure, and temperature, indicating the presence of gas, fracture density, or even partial melt. Tomography and stress tensors can also help constrain intrusive mechanisms (Alparone et al. 2012). The precise locations of HF earthquakes can also help infer frequency-magnitude relations (cf. b-values by Gutenberg and Richter (1942) and Gutenberg and Richter (1956)).

LF events are another type of seismic events, which are considered to be more

complex. Although LF events are known to be caused by fluids, the definition of the radiating source is ambiguous. The question of whether LF signals originate solely from mechanical energy or are a combination of mechanical origin and fluid-filled conduits is still unknown (McNutt 2005). However, LF events have been inciting new research as, e.g. LF events may allow estimation of magma and gas flux (Neuberg 2000).

Volcanic explosions involve high speed and pressure of dense mixtures of gas and ash from a volcanic vent (Woods 1995). They have a characteristic signal that also allows subsurface characterisation. Woods (1995) summarises that the height of rising explosive eruption columns depends on (i) eruption rate, (ii) stratification of the atmosphere, (iii) degree of thermal disequilibrium between the particles and the air, and (iv) water vapour in the atmosphere. Infrasonic microphones, pressure sensors, and GNSS ionospheric disturbances are commonly used to study volcanic explosions. These methods allow a direct way of measurement rather than seismic waves, as the latter are more affected by propagation effects.

Volcanic tremors, or harmonic tremors, are ground vibrations that oscillate at different frequencies, which may be due to different physical processes. These resonance signatures indicate complex driving mechanisms due to their interaction between magmatic fluids, water, and the surrounding rock. Konstantinou and Schlindwein (2003) review some of these events worldwide, often occurring in conjunction with a volcanic eruption. Recently, other studies have shown that these events do not require an eruption to occur (Martins et al. 2022).

Ambient noise and seismic interferometry: a tool for subsurface imaging

In the 20th century, a form of exploiting new sources of signal arose from the concept of "turning noise into signal" (Wapenaar and Snieder 2007). Obtaining a signal from noise can be done by cross-correlating diffusive fields recorded at two different receivers. The cross-correlated signal returns the response at the position of one receiver as if the source was at the other receiver (Shapiro and Campillo 2004; Schuster et al. 2004; Roux et al. 2005a; Larose et al. 2005; Sabra et al. 2005a; Shapiro et al. 2005a; Draganov et al. 2007; Ruigrok et al. 2011).

The attractive alternative to using ambient noise as a source of illumination is seismic interferometry (SI), first proposed by Claerbout (1968) in the exploration community for 1D media. Later, Wapenaar (2004) extended the SI concept to arbitrarily heterogeneous 3D media. SI by time-domain cross-correlation is the process of generating new seismic responses between receivers using the cross-correlation and summation of (noise) recordings from surrounding (noise) sources (Wapenaar 2004). The concept of using SI with ambient noise for the retrieval of surface waves is consistent with the spatial autocorrelation method (SPAC) (Aki 1957; Aki 1965) as shown by Yokoi and Margaryan (2008). By comparing both approaches, Tsai and Moschetti (2010) also suggests that the results of each technique can be used in the other. SPAC can be used in a volcanic setting to estimate phase velocity curves (Nagaoka et al. 2012).

The subsequent application of SI to ambient noise and tomographic inversion to obtain a 3D velocity model is called ambient noise tomography (ANT). ANT has been used to image the Earth's subsurface over large areas (Sabra et al. 2005b; Yao et al. 2006; Kang and Shin 2006; Villasenor et al. 2007; Yang et al. 2007; Bensen et al. 2008). On a

1

local scale, ANT can be used to image volcanic magmatic systems, e.g. (Brenguier et al. 2007; Masterlark et al. 2010; Stankiewicz et al. 2010; Behr et al. 2011; Nagaoka et al. 2012; Villagómez et al. 2011; Luzón et al. 2011; Mordret et al. 2014; Jaxybulatov et al. 2014), or to estimate the temporal changes in seismic velocity before eruptions of active volcanoes (Sens-Schönfelder and Wegler 2006; Brenguier et al. 2011; Sens-Schönfelder et al. 2014). Using the ANT technique it is possible to retrieve an S-wave velocity field beneath the volcano. Estimating S-wave velocity anomalies with reference to an average velocity allows us to delineate high- or low-velocity anomalies, which may highlight the magmatic plumbing systems' location and geometry.

1.3.2. Volcano Geodesy

In the realm of volcano geodesy, the utilisation of conventional geodetic techniques provides valuable insights into the subsurface dynamics of MPS. Volcano geodesy starts with the first measurements of the raising and lowering of the Earth's surface, interpreted as a result of volcanic activity. The first published volcano-geodesy measurements were acquired in Japan using levelling (Omori 1913a; Omori 1913b). Sixteen years later, on the east side of Mauna Loa and Kilauea, Hawaii, Jaggar and Finch (1929) showed that surface deformation before and after an eruption was correlated with the changes in the measurement of tilt and leveling. This discovery shed light on the understanding of the monthly levelling measurements collected since 1819 at the Roman Market built near the Pozzuoli harbour close to Naples. A sinking pattern with an average rate of 15 mm/year until 1968 was interpreted as resultant of volcanic subsurface activity (Parascandola 1947; Oliveri del Castillo 1960; Berrino et al. 1984). In the 20th century, several levelling, spirit level tilting, trilateration, electronic distance meter (EDM) and tiltmeter campaigns with measurements with daily to biannual repetitions occurred over several active volcanoes throughout Japan, Russia, North-, Central-, and South America, Iceland, Italy, Indonesia, Africa, and New Zeeland.

Geodesy played a crucial role in two main application domains: (i) MPS imaging, by providing valuable insights into magma reservoir depth and geometry, and (ii) monitoring volcanic unrest. Within the geodetic MPS imaging domain, analytical solutions have been derived using inversion strategies to simulate simple source geometries such as sills, dikes, and spheres to explain and model the mechanics between surface measurements and subsurface processes. These mathematical analytical models are based on constitutive equations used to relate the stresses due to forces acting on the particles of a given material and the resulting strains or deformations (Mogi 1958; Okada 1985; McTigue 1987; Fukushima et al. 2005; Dzurisin 2006; Lisowski 2007; Segall 2010). Furthermore, many geodetic measurements confirmed that displacement rates, together with spatiotemporal displacement patterns, provide information on subsurface characteristics such as magma build-up rate and magma accumulation depth (Dvorak and Dzurisin 1997). Likewise, depending on the magnitude of the displacements, the estimated depths of magma accumulation (often constrained by gravity anomalies or gravity changes) have allowed different volcanic processes to be understood through volcano geodesy (Dzurisin 2000). Several applications in volcano monitoring have been reviewed by Dvorak and Dzurisin (1997), Dzurisin (2000), Fernández et al. (2017), and Poland and Zeeuw-van Dalfsen (2021), that is, volcanic unrest before eruptions (uplift and subsidence patterns) and the estimation of long-term displacements such as subsidence calderas.

Satellite geodesy: InSAR, a tool for volcano source modeling

In the early 1990s, geodetic techniques improved significantly with the advent of space-based measurements. Global navigation satellite systems (GNSS) improved positioning capabilities, providing a unique way to measure the tectonic and volcanic processes in the crust, e.g. (Segall and Davis 1997; Jónsson et al. 1997; Sagiya et al. 2000; Bartel et al. 2003). A dramatic improvement was due to the development of Synthetic Aperture Radar (SAR) satellite sensors, which stimulated research and monitoring of Earth's surface deformation processes (Massonnet and Feigl 1998). SAR sensors are composed of an active pulsed radar (RAdio Detection and Ranging) that penetrates the atmosphere and clouds, providing measurements regardless of weather conditions.

SAR satellite missions allow the estimation of surface displacements from interferometry (Interferometric SAR or InSAR) which, compared with the traditional levelling technique, has a higher spatial and temporal resolution with comparable accuracy coverage without the need for fieldwork. These capabilities allow the monitoring of volcanoes located in areas of difficult access or not accessible at all. The success of InSAR has been proven by the increased amount of applications using the past and present radar missions (e.g. ERS-1/2, ENVISAT, TerraSAR-X, RadarSat-1/2, Cosmo-Skymed, Sentinel-1, ALOS). Alongside, developments in the InSAR family of processing techniques using time series enable a more accurate displacement estimation due to atmospheric effect estimation and removal (Ferretti et al. 2000; Ferretti et al. 2001; Berardino et al. 2002; Schmidt and Bürgmann 2003; Kampes 2005; Hooper 2008; Ferretti et al. 2011). The surface deformation may be induced by natural phenomena—e.g., earthquakes (Wright et al. 2003; Ryder et al. 2007; Sudhaus and Sigurjón 2009), landslides (Hilley et al. 2004; Singh et al. 2005), volcanoes (Hooper et al. 2004; Pritchard and Simons 2002; Biggs et al. 2014), post-glacial rebound motion (Auriac et al. 2014)—or anthropogenic activities, e.g., induced subsidence by fluid extraction (Amelung et al. 1999; Nakagawa et al. 2000) and after mining effects (Cuenca et al. 2013); monitoring of bridges (Sousa and Bastos 2013; Lazecky et al. 2017), railways (Chang et al. 2017), pipeline failure (Arsénio et al. 2015) or building monitoring (Dheenathayalan et al. 2011; Rossi and Eineder 2015) based on high-precision positioning of radar scatterers (Dheenathayalan et al. 2016).

Advancements in InSAR technology have revolutionised the field of volcanology, enabling the monitoring and imaging of volcanic systems with unprecedented spatial and temporal resolutions. Numerous volcanoes around the world have benefitted from InSAR monitoring, including those in south (Fournier et al. 2010; Delgado 2021), central (Pinel et al. 2011; Ebmeier et al. 2013; Békési et al. 2019b) and north-America (Lu et al. 2010), Aleutian islands in the Pacific (Lu and Dzurisin 2014), Galapagos (Yun et al. 2006; Hooper et al. 2007; Jónsson 2009; Bagnardi and Amelung 2012; Galetto et al. 2019), Cape Verde (González et al. 2015), Canary islands (González et al. 2010), Iceland (Pedersen and Sigmundsson 2004; Ofeigsson et al. 2011; Sigmundsson et al. 2010; Sigmundsson et al. 2018), New Zeeland (Samsonov et al. 2011), Indonesia (Chaussard et al. 2013), Japan (Morishita et al. 2016; Kobayashi et al. 2018; Yamasaki et al. 2018), Italy (Neri et al. 2009; Solaro et al. 2010; Di Traglia et al. 2014; Di Traglia et al. 2015) or Africa

10 1. Introduction

(Hutchison et al. 2016) among other locations. These studies have provided valuable information on the dynamics of magmatic reservoirs and have been motivating the use of machine learning techniques to 'hint' at potentially erupting volcanoes from large databases of interferograms (Biggs et al. 2014; Anantrasirichai et al. 2018). Additionally, the frequent acquisitions of satellite data have facilitated the investigation of cyclic behaviour over certain volcanoes (Parks et al. 2012), the constraint of deep magma sources (Ofeigsson et al. 2011) or the estimation of the deformation behaviour during the pre-, co-, and post-eruptive moments. Recent satellite missions, such as Sentinel-1, have further expanded the capabilities of InSAR by enabling the study of volcanic deformation in highly vegetated areas, such as in the Azores archipelago, where the previous low coherence has hindered the results (Catita et al. 2005; Martins 2006).

1.4. Problem statement

Despite InSAR's impressive results, using it to image MPS has four main limitations.

First, while surface displacements estimated from radar interferometry (InSAR) can be used in geophysical modelling to constrain location, geometry, and pressure changes in magma systems, the resolution of the inferred modelled magma source is typically poor (regardless of the high resolution of SAR images), and we cannot resolve the actual shape of the inverted magma source when inverting from surface displacements to magma source geometry. Second, inversions of MPS sources from InSAR do not always provide unique solutions. Yun et al. (2006) have shown that despite the constraints of ascending and descending tracks over the Sierra Negra Volcano in the Galápagos Islands, the data are insensitive to the bottom and sides of the magma reservoir. In fact, the authors could fit any source with variable bottoms and peripheral shapes as long as its top was flat (sill-like). This result highlighted the need for other sources of constraints in InSAR magma source modelling. Third, geophysical modelling to invert magma source geometry from InSAR-derived surface displacements relies on elastic and rheological properties that are not accurately known. Finally, since magma source modelling based on surface displacements requires pressure changes in magmatic systems, if there are no surface displacements, magma source modelling is not possible.

These four limitations on the use of InSAR for imaging MPS's triggered the idea for a complementary approach utilising seismic observations.

Seismic tomographic methods, which provide a 3D image of the subsurface, can provide complementary information on MPS. High-resolution images from tomography can be computed through active-source reflection seismic (Draganov et al. 2007; Draganov 2007), as applied to hydrocarbon exploration. However, active seismic surveys are expensive. Seismic tomography using seismic waves generated by earthquakes is also widely used. However, this relies on the existence of earthquakes, requires a good spatial distribution of the earthquakes, and requires precise S-wave first-arrival picks. Therefore, the resolution of earthquake-based tomographic models of tomographic models is degraded whenever the seismicity is scarce. The ambient noise from microseismicity (sec. 1.3.1) tackles these limitations, and ambient noise tomography (ANT) could retrieve meaningful medium characteristics within the aperture of the used seismic network. Therefore, proceeding with Seismic Interferometry (SI) (Wapenaar

and Fokkema 2006) and deriving 3D subsurface tomographic images to constrain InSAR source modelling seems an appropriate choice.

Although InSAR and ANT techniques have been around for the last decade and have matured enough for specific applications, they still need to be fine-tuned and require addressing specific requirements. Additionally, these techniques presume location-dependent adaptation for optimised results. Consequently, I have identified six main research problems which are addressed in this study.

Research problem 1. Source of illumination – the origin of the ambient noise. When using ambient noise (or microseism) for seismic interferometry, the accuracy of the Green's function is affected by an inhomogeneous azimuthal distribution of seismic noise sources. This can lead to inaccurately estimated arrival times, affecting the reliability of isotropic and anisotropic tomographic inversions for both velocity and attenuation (Harmon et al. 2010). It is therefore necessary to study the origin of the noise and retrieve the Green's functions correctly between pairs of stations. In addition, analysing the amplitude factors between the causal and anti-causal parts of the cross-correlation can provide insight into the energy flux between stations (Tiggelen 2003; Paul et al. 2005), allowing us to measure the main direction of energy flow across the seismic network (Stehly et al. 2006). Therefore, accurately estimating the azimuth direction of ambient noise sources is location dependent and a critical requirement to apply ambient noise interferometry for tomographic studies.

Research problem 2. Estimation of phase velocity. Most of the ambient noise tomography studies have focused on retrieving group velocities. Yet, the main argument to justify extracting phase rather than group velocities is that phase velocity picks can be done at lower frequencies and, consequently, they better constrain higher depths, especially when using seismic campaigns with relatively short inter-station distances. The reliability of group measurements depends on amplitude information and could be impacted by any distortion present in the amplitude spectrum of the empirical Green's functions (EFG) (Yao et al. 2006). According to Yao et al. (2006), the phase information in the empirical Green's functions (EGF) estimated by noise cross-correlation functions is theoretically identical to that of the actual Green's functions. The main limitation is that phase velocity is more difficult to retrieve than group velocity.

Research problem 3. Non-uniqueness of the tomographic results. Inverse problems are often used in more than one branch of science. Within seismology, the main problems with discrete tomographic inversions are related to the properties of the design matrix G, which turns a simple linear inversion into an ill-posed problem. Problems can arise when the distribution and number of the ray paths are not optimal, when there are not enough ray paths for a fully ranked G (matrix G is rank-deficient), and when the solution depends not only on the data but also on the noise present, which means that there is not a unique solution. Solutions to regularise these problems are needed for a unique solution.

12 1. Introduction

Research problem 4. Resolution of the tomographic models. The vertical and horizontal resolution of the derived tomographic images depends on the spatial distribution of the ambient noise, the seismic wavelength of the surface wave, the wave source distance, and the coverage of the seismometers. All of these are case-study dependent. Furthermore, due to the novelty of the ANT methods, **the highest possible achievable resolution is not yet an exploited parameter**, which is especially needed in geothermal reservoirs.

Research problem 5. The rate of surface deformation is not always linear. When performing magma source modelling, it may be appropriate to use a linear deformation model over time as the input deformation model. However, this approach may not always accurately describe the phenomena, reducing the accuracy and reliability of the resulting model. This is the case for InSAR data sets processed over a volcanic event. Depending on the temporal resolution of the SAR acquisitions and coherence of the InSAR time series it may be difficult to identify non-linear rates from the time-series alone. In such cases, **improved deformation rates may need to be considered before modelling**, and GPS measurements can provide an alternative source of information whenever available.

Research problem 6. Unique character of each volcano. Studying specific volcanoes is valuable due to their unique characteristics and processes. Once these processes and conditions are individually understood, they will provide insights applicable to volcanoes in similar conditions. Factors such as tectonic setting, type of volcano, style of volcanic activity, erupted material, and eruptive phase influence seismic or InSAR data processing approaches and interpretation of results. Because of the uniqueness of each volcano due to the combination of these factors, adjustments to processing approaches are also required.

1.5. Research Objectives

To effectively image and comprehend MPS, interdisciplinary solutions must be employed. To this end, I hypothesize that combining independent observations obtained through seismic and radar techniques will enhance our understanding of MPS—particularly with regard to reservoir geometry—by providing a more precise determination of the location, shape, and depth of the magma reservoir. As such, these techniques have the potential to answer various questions concerning MPS, including those pertaining to its 'where', 'how', 'when', 'what', and 'why', see sec. 1.2.

The research problems discussed above on imaging MPS's with InSAR techniques alone motivated the main research question of this study:

What is the added value of the joint analysis of radar and seismic interferometry to image MPS (size, geometry, and location) over active volcanoes?

To address this research question, taking into account the limitations of each technique discussed in sec. 1.4, I present three subsequent research objectives, including the

respective methodological approach.

Research objective 1. Develop, process and validate an approach to extract phasevelocities from ambient seismic noise using Seismic Interferometry (SI) and optimise it for volcano 3D shear-wave tomographic studies. In this objective I aim to develop and apply a methodology to derive 3D tomographic subsurface images of active volcanoes from ambient noise. In order to ensure the successful implementation and application of the methodology, it is important to consider and meet certain requirements. The first requirements concern the prerequisites for retrieving the ballistic surface waves (BSW) portion of the Green's functions. Some of these prerequisites are related to the data acquisition. For example, to converge the retrieved signals towards the BSW portion of the Green's function, long duration of data collection are required, as well as high density and a good geometry of seismic stations. Then, other requirements should be met after the data acquisition. These concern data pre-processing corrections or filtering and requirements for the retrieval of velocities from seismic interferometry, e.g. to ensure the existence of an isotropic distribution of the illuminating sources. The methodology will be focused on the requirements post data acquisition, and will encompass instrument corrections, temporal and spatial normalisation, selection of the best frequency bandwidth given the purpose, and mapping of the preferential azimuthal direction of the ambient noise with beamforming techniques. Therefore, the first part of the methodology will involve preparing the waveforms to extract ambient noise and retrieving the empirical Green's function or ballistic surface waves (BSW) using SI ensuring that the requirements for ambient noise tomography are met. The remaining requirements relate to the tomographic inversion and the inversion from frequency to depth. The tomographic inversion uses the picked travel times of the retrieved ballistic to estimate slowness between stations. This tomographic inversion is ill-posed, so a regularisation must be applied. The resolution of the tomography also needs to be addressed. Resolution for this method primarily depends on the ray-path coverage and wavelength. The methodology will take into account Quality checks will be performed after each processing step.

Research objective 2. Design, process, validate, and evaluate the deformation estimated from the InSAR time series followed by modelling the geometry, size, and depth of the magmatic plumbing systems. The design and processing of the InSAR time series requires expert judgement to select of processing parameters and cannot be entirely automated. Specific parameters, which are case dependent, are typically associated with factors such as the choice of SAR images, the assessment of the atmospheric phase delay (Hanssen 2001), the estimation of phase ambiguity and other necessary corrections depending on the type of volcano and stage of the eruptive cycle. Whenever possible, the InSAR time series will be validated with GNSS measurements followed by the evaluation of the appropriate deformation model prior to magma source modelling. The MPS geometry, size, and depth will then be modelled using the estimated deformation rates and additional constraints whenever available.

To address this objective, I will process two sets of satellite radar images in C- and X-bands over two areas with distinct volcanic processes. InSAR processing aims to: (i)

14 1. Introduction

minimize the impact of error sources, (ii) increase the number of point-scatterers to reduce unwrapping errors in areas affected by ash coverage-induced decorrelation, and (iii) extract the desired deformation signal from other overlapping deformation signals.

Following InSAR processing, the deformation rate will be estimated to describe the physical processes occurring in each volcano. Bayesian methods, specifically the Markov Chain Monte Carlo (MCMC) approach, will be employed for the modeling of the magma source. This approach allows estimating a multivariate probability distribution for model parameters associated with the geometry, depth, and size of the magma chamber.

Research objective 3. Evaluate and interpret the results over active volcanoes for which the techniques are individually or mutually applied. Here, I will examine the benefits of using geodetic and seismic imaging techniques individually or combined in relation to three areas of interest: geothermal energy, volcanic hazards, and melt quantification. The practical implications of these imaging techniques can be understood by discussing the products resulting from each active volcano. The three active volcanic systems were chosen on the basis of selected characteristics and data access constraints, making them ideal for illustrating the power and practical implications of these imaging techniques. These characteristics are described below.

Torfajökull volcanic system is an ideal location to evaluate the performance of radar and seismic interferometric observations due to the availability of historical satellite data and a seismic campaign with a valuable network configuration for tomographic studies during the same period. Torfajökull volcano has not erupted in the last 500 years but has exhibited subsidence at linear rates for the last 30 years. Despite its location far from major cities, a future eruption could affect infrastructure and nearby hydroelectric plants due to tephra fall. Because it has been hypothesised that lateral magma propagation occurs between the fissure swarm of the Veidivötn's (Bárðarbunga) volcanic system and the Torfajökull volcanic system, both InSAR datasets will be focused from RAW images to obtain a larger frame covering Torfajökull and Veidivötn's volcanic system.

Eyjafjallajökull became known worldwide after the disruption of air traffic during the 2010 eruption. The nonlinear displacements in time and space for the 2010 pre-, co-, and post-eruptive moments suggest a complex set of sills and dikes. To study the magmatic sources associated with the co- and post-eruptive periods, I will process the InSAR time series, compare with GPS measurements acquired during the eruption, and use both InSAR and GPS measurements to image the source(s) associated with the co- and post-eruptive periods.

The third AOI is the Reykjanes peninsula, an area with a high enthalpy geothermal reservoir where geothermal energy has been produced since its first power plant at Svartsengi, which began operation in 1976. Geodetic measurements have previously detected subsidence as a result of geothermal exploration. However, there are only coarse-resolution tomographic studies around earthquake-dense areas that are not suitable for geothermal purposes. Furthermore, given the 2021-2024 volcanic activity, seismic tomographic imaging will allow mapping of the location, depth, and extension of low-velocity anomalies resulting from magma accumulation. In this area, I will perform an ANSI tomographic study to show the capabilities of ANT to characterize geothermal

15

reservoirs and map possible molten pockets of magma.

1.6. Outline

This thesis is organised in the following way. The current chapter introduced motivation followed by a background review on the role of magmatic plumbing systems within the social context. The seismic and radar techniques for MPS characterisation were then followed by the problem statement and research objectives.

Chapter 2 describes the concepts behind the applied methodology to extract the observations for MPS modelling and the modelling approaches for each of the applied techniques. It concludes with the tectonic and volcanic setting of the used case Icelandic studies.

Then, chapter 3 describes a systematic procedure developed to retrieve 3D shearwave tomographic models from ambient noise with seismic interferometry (Ambient noise seismic interferometry, ANSI) tomography. The developed methodology is applied to derive the first 3-D shear-wave tomographic model of Torfajökull volcano using seismic data recorded at 23 broad-band seismometers for 100 days. The content of this chapter has been published in the Journal of Geophysical Research (Martins et al. 2019).

Chapter 4 describes the feasibility of the methodology and implementation of the procedure chapter 3 on the derivation of a 3-D shear-wave tomographic model of the Reykjanes Peninsula, targeting three operating geothermal fields. Using a denser seismic network recorded at 30 broad-band seismometers for a longer period (1.5 years), I will also focus on the potential for increasing the horizontal resolution as a means to improve understanding of the local geothermal reservoirs. The content of this chapter has been published in the Journal of Volcanology and Geothermal Research (Martins et al. 2020).

Chapter 5 describes the processing and deformation modelling of the InSAR time series. The chapter further extends on the InSAR and GPS joint inversion for magmatic plumbing system modelling of the co- and post-eruptive periods of the 2010 Eyjafjallajökull volcano eruption.

Chapter 6 describes the use of RI and SI for imaging of magmatic plumbing systems. This chapter's content has partially been published in the *Proceedings of the World* Geothermal Congress (Martins et al. 2021).

Finally, the conclusions given the proposed objectives and further recommendations in Chapter 7.

1

Methods and data

Given the impossibility of directly observing the subsurface, remote sensing techniques can be used to indirectly image it and subsequently improve the rheological, geological, and geometrical knowledge of magmatic plumbing systems. In this chapter, I describe the remote sensing techniques and the modelling approach that link remote sensing data—either from satellites or seismometers—to the parameters of interest, in this case the geometry of magmatic plumbing systems of active volcanoes in Iceland. I start with the Gauss-Markov mathematical model, followed by a brief overview of the seismic and radar observations, the unknowns and the functional model. Finally, in sec. 2.4, I introduce the volcanic and tectonic setting of the Icelandic active volcanic zones used as case studies and the details of the used data sources.

2.1. Gauss-Markov model formulation

Analytical models to estimate the geometry of MPS involve the formulation of an inverse problem. The inversion procedure follows the form of the generic Gauss-Markov formulation combining a functional of observation equations(Gauss 1809) and a stochastic model describing the precision of the observations (Markoff 1912). Here, the functional model is

$$\underline{y} = A(x) + \underline{e},\tag{2.1}$$

or in its linearized form

$$y = Ax + \underline{e}. (2.2)$$

In Eq. 2.1 and Eq. 2.2, A is the design matrix that relates the observables, \underline{y} , to the unknowns, x, and \underline{e} is the noise that contaminates the measurements. The underline expresses the stochastic nature of the variable. Under the assumption that $E\{\underline{e}\} = 0$, where $E\{.\}$ is the expectation operator, we can write the functional model as $E\{\underline{y}\} = A \cdot x$. The stochastic part of the model is expressed by:

$$D\{\underline{y}\} = Q_y, \tag{2.3}$$

where $D\{.\}$ the dispersion operator and Q_y is the variance-covariance matrix of the observations.

Fig. 2.1 provides an overview of the sequential inversion approach used in this study, where he left column (inversions 1A-2A-3A) concerns the seismic dataset and the right column (inversions 1B-2B-3B) the radar dataset. The unknowns estimated in one inversion step serve as the observations for the subsequent one. Inversion 1 uses

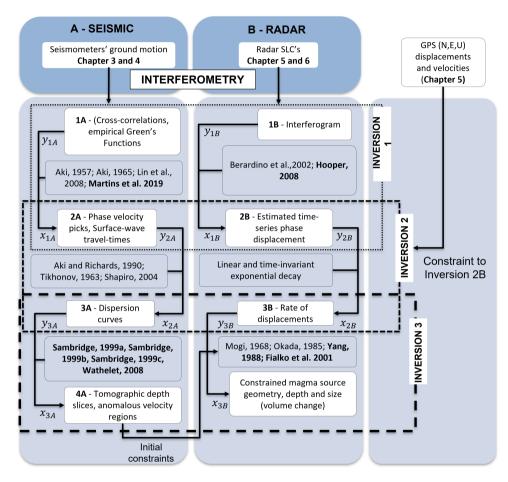


Figure 2.1: Overview of the sequential inversion methodology used in this study by employing the Gauss-Markov functional model formulation.

the interferograms derived from both methods as observations. In the case of seismic interferometry (1A), the phase velocity and surface wave travel times, i.e., the unknowns in the Gauss-Markov formulation, are derived from seismic cross-correlations of the observations in the Gauss-Markov formulation. The phase velocities are estimated from the retrieved surface waves of recorded ambient noise from the cross-correlation panel. In the case of radar interferometry (1B), the time series of displacements are the unknowns of inversion 1, which are estimated from the radar interferograms. Fig. 2.2a shows an example of inversion 1 observations, both for radar and seismic data.

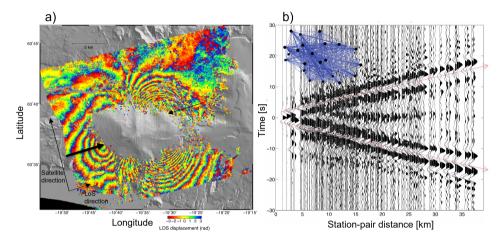


Figure 2.2: Interferograms from both radar and seismic interferometry techniques, respectively. a) SAR interferogram covering the 2010 Eyjafjallajokull eruption (chapter 5) on top of a digital elevation model. b) Interferogram of the EFG's obtained by ordering the cross-correlation of all station-pairs (blue lines connecting the seismic network in the top-left corner of the figure) by interstation-pair distance.

In Inversion 2, the parameters estimated in Inversion 1 are utilised as observations. In the case of seismic interferometry (2A), this inversion step is also known as tomography, i.e., retrieving frequency-dependent velocities and velocity anomalies from seismic travel times between station pairs. The results of Inversion 2 can be interpreted in relation to subsurface parameters due to the estimated velocity anomalies. However, these velocity anomalies are frequency-dependent, so an inversion from frequency to depth is needed to have a depth-dependent tomography. For this reason, the input for Inversion 3 is formed by the dispersion curves, which describe the velocity as a function of frequency in each tomographic grid cell. In radar interferometry (2B), the rates of displacements vary based on the time series observed for each specific case study. For the Eyjafjallajökull case study, additional GPS data are used to validate InSAR processing, inform the deformation modelling, and to delineate the magma source geometry.

Inversion 3 uses the parameters estimated in Inversion 2 as observations. Inversion 3A estimates the three-dimensional surface-wave tomography, subsequently deriving depth-dependent instead of frequency-dependent dispersion curves. This additional inversion allows the estimation of the velocity anomaly depths to be directly

compared, or used as an initial constrain in the InSAR modelling. Inversion 3B uses the previously obtained rates of displacements to invert for magma chamber geometry and volume change. In this inversion, the initial magma source parameters can be constrained by the tomographic results to estimate a so-called constrained geometry of the magma reservoir.

The following sections subsequently discuss the observations, the unknowns, and the functional models utilised in each inversion step.

2.2. The observations

The observations y in Eq. (2.1) are the estimated parameters sequentially derived from radar and seismic interferometry. In Fig. 2.1, the observations are named 1A, 2A, 3A, and 4A for seismic interferometry measurements and 1B, 2B, and 3B for radar interferometry products. This section discusses how these (derived) observations are sequentially obtained.

2.2.1. Interferometry

In this study, the concept of interferometry is the shared characteristic of the radar and the seismic methods. However, the corresponding signals differ fundamentally. Radar systems operate based on the propagation of electromagnetic waves, typically utilising wavelengths between 3 cm and 25 cm, depending on the sensor. Seismic waves are pressure waves that travel through the Earth, exhibiting wavelengths spanning from meters to hundreds of kilometres. While electromagnetic waves can propagate through vacuum and other media at the speed of light (3×10^8 m/s in vacuum), seismic waves are mechanical, require a medium to propagate, and their speed is dependent on the properties of the medium.

Fig. 2.2 illustrates the interference patterns produced from satellite radar and seismic measurements. The cross-correlation panel depicted in Fig. 2.2 b will be called a 'seismic interferogram'. Interferograms A and B serve as initial observations of the sequential inversion procedure. Inversions 1 to 3 aim to estimate the geophysical system properties from radar and seismic interferometry. Specifically, the rate of surface displacements and the seismic velocity variations along the crust are the estimated geophysical system properties which serve as inputs or observations for estimating the unknowns of the MPS in inversion 4.

Fig. 2.2a shows an interferogram covering Eyjafjallajökull volcano, obtained after complex multiplication of the electromagnetic phase signal between two SAR (Synthetic Aperture Radar) acquisitions and applying the appropriate corrections for topographic height, ellipsoid, and orbits (Hanssen 2001). The 'fringe' pattern represents the deformation that occurred between the two radar acquisitions. The outline of the interferogram indicates the radar acquisition footprint. The lack of coherence (i.e., areas without colours) in the middle and east of the interferogram is due to a glacier covering the summit volcano caldera of Eyjafjallajökull and Katla, respectively. Ice, snow, and water bodies, as well as vegetation-covered areas result in a coherence reduction due to temporal decorrelation of the InSAR echoes (Samiei-Esfahany 2017). The colour scale represents line-of-sight (LoS) displacements wrapped between $-\pi$ and π . The fringe

pattern in the interferogram allows for identification of displacements towards the satellite (indicated by the thick black arrow) and away from the satellite (indicated by the thin black arrow), suggesting possible inflation and deflation, respectively.

In Fig. 2.2b, the seismic cross-correlation panel or seismic interferogram shows a 'V' pattern. Each line results from the time-domain cross-correlation signal of ambient-noise of registered station pairs, ordered by the corresponding inter-station distance. The ordering of the cross-correlated lines by station-pair distance results in a constructive interference pattern, which allows for the estimation of the arrival times between each station-pair. Each line is the empirical Green's function (EGF) between two stations. The positive and negative time indication shows the order of the performed cross-correlation, i.e., whether the seismic station A isvcross-correlated with station B or the other way around. After interferogram generation, the final vector of observations results from a tomographic inversion, see Chap. 3. The following sections detail on the concept of interferometry as initial step of the sequential inversion procedure.

2.2.2. Seismic wave velocity

The seismic wave velocity or derived dispersion curves from tomographic methods are used as derived observables for inversion 3A in Fig. 2.1, and are derived through the sequential inversion scheme A. Seismic waves undergo acceleration or deceleration as they propagate through the Earth's subsurface, influenced by the varying materials encountered along their paths. With respect to a reference velocity model that accounts for depth it is possible to estimate the slowness of waves and their depth-dependent velocity variations. This way, different structures of the Earth's anatomy can be imaged.

Seismic signal

Velocity variations in seismometer data depend on the type of wave as well as the density and elasticity of the propagation medium (Stein and Wysession 2009). Any propagating wave with an arbitrary shape can be decomposed using Fourier analysis into different harmonic components. A function of the form $u(x, t) = f(x \pm vt)$, where u(x, t) is the displacement in a certain component (x, y, or z), is a propagating wave. Therefore, the seismic wave solution of planar waves has the following solution as a harmonic wave

$$u(x,t) = Ae^{i(\omega t \pm kx)} = A\cos(\omega t \pm kx) + Ai\sin(\omega t \pm kx). \tag{2.4}$$

This is a complex function for which the displacement is described as the real part of u(x,t) or $A\cos(\omega t - kx)$ representing the wave field as a function of time and space, where A is the amplitude, ω is the angular frequency, and k is the wavenumber.

From the wave equation, it follows that $v = \omega/k$, from which all relationships in Tab. 2.1 can be derived. Eq. (2.4) can be evaluated at a fixed position as function of time, to obtain relationships such as periodicity (from angular frequency and frequency). If u(x,t) is studied at a fixed time as function of position, it is possible to estimate the wavelength and wavenumber. Quantities like pressure, particle velocity, particle displacement and intensity describe seismic waves, and four important parameters can be extracted from each of the seismometer components: wavelength λ , period T, wave number k, and angular frequency ω .

Quantity	Units	Relationship
Velocity	distance/time	$v = \omega/k = f/\lambda = \lambda/T$
Period	time	$T = 2\pi/\omega = 1/f = \lambda/v$
Angular Frequency	$time^{-1}$	$\omega = 2\pi/T = 2\pi f = kv$
Frequency	$time^{-1}$	$f = \omega/(2\pi) = 1/T = v/\lambda$
Wavelength	distance	$\lambda = 2\pi/k = \nu/f = \nu T$
Wavenumber	$distance^{-1}$	$k = 2\pi/\lambda = \omega/\nu = 2\pi f/\nu$
Ray Parameter	time/distance	$p = 1/c_x = \sin(i/\nu) = k_x/\omega$

Table 2.1: Fundamental relationships of waves. Adapted from (Stein and Wysession 2009)

Ambient-noise

Microseisms, also known as ambient noise or the Earth's 'hum' (Nawa et al. 1998), refer to tenuous vibrations caused by swell waves in the ocean, sometimes referred to as oceanic microseism. The generation of ambient noise involves a three-stage process of atmosphere/ocean/seafloor coupling (Rhie and Romanowicz 2004): (i) conversion of atmospheric storm energy into short-period ocean waves, (ii) non-linear interaction of ocean waves producing longer-period, infra-gravity waves, and (iii) coupling of infra-gravity waves to the sea floor, through a process involving irregularities in the ocean floor topography. The recorded ambient seismic vibrations are primarily composed of Rayleigh waves and can propagate over large distances through the crust and mantle. Ambient noise travels as surface waves and typically exhibits a characteristic signature in the 0.1–1 Hz frequency band. The direct interaction of waves with the seafloor produces a signature in the range of 0.05–0.1 Hz, and in shallow water, where non-linear wave interactions occur, the frequency is doubled to the range of 0.1–0.25 Hz (Webb and Crawford 1999).

Using ambient noise, it is possible to retrieve direct surface waves between pairs of receivers. This is the basis of seismic interferometry (SI) through cross-correlation techniques. Here, one of the receivers acts as a source and the other as a receiver, i.e., it enables us to retrieve the response as if one of the receivers from a receiver pair measures the direct surface wave that was induced by a virtual source at the other receiver.

Seismic interferometry by cross-correlation

Seismic interferometry (SI) is the method by which we extract the Green's functions by the cross-correlation of recorded noise at two different locations. These functions are referred to as the empirical Green's functions. In the methodology flowchart of Fig. 2.2, this step is the result of the seismic interferometry process, which will serve as observations for inversion 1A.

SI by cross-correlation is possible because of reciprocity. The positive time retrieval of a cross-correlation provides an estimation of the fundamental mode Rayleigh wave, while the result at negative times offers an estimate of its time-reversed variant (Bensen et al. 2007). The reciprocity concept is an important aspect of the elastic wave equation, expressing that the wave propagation is reversible and that the equation is symmetric in

time

$$G_{ij}(x_B, x_A, t) = G_{ij}(x_B, x_A, -t),$$
 (2.5)

where G_{ij} are the Green's functions corresponding to a solution recorded in the i component (vertical) for a force in the j (horizontal) direction. x_A and x_B are the source and receiver positions, and t represents time. SI by cross-correlation of selected microseisms recorded at two stations aims at retrieving the coherent wavefield between this station-pair. The collection of such retrieved wave fields between the different station pairs allows us to characterise properties of the medium between station pairs. By cross-correlating seismic observations at two receiver locations x_A and x_B , we obtain a response at one of those receivers, x_B , as if there were a source at the other receiver x_A ; this process is also called Green's function retrieval (Wapenaar 2004). If we integrate all sources along an integration boundary $\partial \mathbb{D}$, we will retrieve the Green's function $G(x_B, x_A, t)$ and its time-reversed version $G(x_B, x_A, -t)$. The Green's function contains the direct wave, but also scattered waves (Wapenaar and Fokkema 2006). This relation is given by

$$G(x_B, x_A, t) - G(x_B, x_A, -t) \propto -\frac{d}{dt} \left(\oint_{\partial \mathbb{D}} G(x_B, x, -t) * G(x_A, x, t) d^2 x \right), \tag{2.6}$$

where $G(x_B, x_A, t)$ represents the Green's function between x_B and x_A , and t denotes time, while $G(x_B, x_A, -t)$ is its time-reversed version. The right-hand side of the equation shows the cross-correlations of wavefield observations at x_A and x_B , integrated along sources at x along $\partial \mathbb{D}$. In Eq. (2.6) the * denotes the temporal convolution.

Figure 2.3 presents an example demonstrating the cross-correlation analysis performed between two seismic stations across three distinct frequency bands. frequency bands examined include 0.1–0.5 Hz, 0.5–1 Hz, 1–3 Hz, and 3–10 Hz. The figure showcases the results of the cross-correlation conducted over a duration of one hour, as well as the outcomes obtained after stacking 50 hours. The cross-correlation analysis reveals a remarkable level of stability. This is evident from the clear arrivals observed after one hour of cross-correlation in the first two frequency bands (0.1-0.5 Hz and 0.5-1 Hz). However, in the higher frequency band of 3-10 Hz, the results obtained from one hour of cross-correlation exhibit significant noise. Only after stacking 50 hours of cross-correlations, coherent arrivals can be reliably detected. An additional aspect to note from this analysis is the concept of ambient noise directionality. In the intervals of 0.1–0.5 Hz and 0.5–1 Hz, a peak at approximately +0.3 seconds suggests a velocity of 4.4 km/s, which is exceptionally fast for a surface wave propagating parallel to the path between the two stations. Under a certain velocity assumption, the angle of a surfacewave arrival with respect to the direction between the two stations can be estimated. Moving to the 1-3 Hz range, there are two distinct wave arrivals observed at positive times. The second arrival at approximately +2.6 s exhibits a velocity of 0.5 km/s, which is remarkably slow for a direct surface wave between the stations. This suggests the possibility of it being a reflected wave.

2.2.3. Radar deformation rates

InSAR-derived deformation rates are used as observables for inversion 3B in Fig. 2.1, and are computed following the sequential inversion scheme B. Synthetic aperture radar

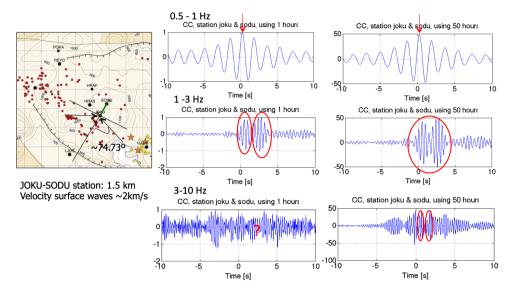


Figure 2.3: Cross-correlation example for surface wave arrival. The map view shows two seismic stations (JOKU and SODU) used in chapter 3. The cross-correlations panels show three frequency bands (0.5–1 Hz, 1–3 Hz and 3–10 Hz) to demonstrate the difficulty in identifying the wave arrival at higher frequencies.

(SAR) observations serve as primary input. The first scheme estimates the time-series displacements based on InSAR The second scheme estimates the displacement rate, which represents the volcano deformation. Below we briefly introduce the concept of interferogram creation and the methods employed for the time series estimation.

SAR Interferometry

The SAR imaging system used in this study is a side-looking moving radar sensor on board of a satellite (Wiley 1954; Skolnik 1980; Skolnik 2002). In Fig. 2.1 the dark blue box represents a single SAR acquisition, also called Single-Look Complex (SLC) image. SLC data have the finest spatial resolution and contain complex numbers from which it is possible to derive amplitude and phase

$$y_P = |y_P| \cdot e^{j\psi_P}. \tag{2.7}$$

The amplitude, $|y_P|$, provides information on scattering characteristics of objects at the surface. The phase ψ_P , of a radar resolution cell is a superposition of multiple scatterers or quasi-random scattering elements (Hanssen 2001). The index P refers to a certain image acquisition P (Primary), to distinguish it from Secondary (S) in the formation of the interferogram.

A radar interferogram contains the phase difference between two SAR satellite acquisitions. If Eq. (2.7) represents the phase of the primary image, the secondary image will be similarly represented by $y_S = |y_S| \cdot e^{j\psi_S}$. When two acquisitions are used, the

interferogram is computed by complex multiplication,

$$v = y_P y_S^* = |y_P| |y_S| \exp(j(\psi_P - \psi_S)),$$
 (2.8)

where * is the complex conjugate. The interferogram is the main input to estimate the change in distance between the satellite and the Earth's surface between acquisitions: if the Earth's surface deforms between the satellite passes, phase differences emerge in the interferogram, expressed as modulo- 2π cycles.

InSAR time-series

Persistent-scatterer time series techniques (Ferretti et al. 2001; Hooper et al. 2004; Kampes 2005) estimate the surface displacement of coherent point scatterers (PS) in time after coregistering many secondary images to a single primary (master) image and extracting phase-relevant point reflections in time. Within the same context, Berardino et al. (2002) introduced a procedure in which multiple interferograms are generated. using subsets with small temporal and geometrical baselines, referred to as Small BAseline Subset (SBAS) techniques. Areas selected by the SBAS technique have different scattering mechanisms than the PS and are therefore named distributed scatterers (DS). Hooper (2008) developed a merged approach technique using PS- and DS-InSAR to increase the number and density of coherent points, and Ferretti et al. (2011) introduced a methodology to use all the information from PS and DS in an optimal manner (SqueeSAR). A comprehensive literature review and comparison of the state-of-the-art InSAR time series methodologies can be found in Samiei-Esfahany (2017).

2.3. The unknowns and functional model: MPS Geometry Estimation

MPS geometry estimation is based on a modeling approach to relate observations to the parameters of interest. These modelling approaches distinguish numerical models (e.g., finite-element, boundary-element, finite-difference or finite-volume), and analytical models. Although numerical models offer the advantage of incorporating arbitrary volcano source geometries, boundary conditions, detailed mesh parametrisation and even reservoir properties, analytical models provide a first-order assessment of the modelled parameters and a quick and accurate way to retrieve low residual fits (Segall 2010). Because of the mathematical simplicity and efficiency of a first-order estimation, here we focus on analytical models through inversion procedures mimicking an elastic, homogeneous or layered (for seismic tomography) flat half-space.

2.3.1. MPS unknowns: geometry, size and location

The unknowns are the parameters of interest x in Eq. (2.1), which describe the source geometry, magmatic chamber shrinking and swelling, and magma migration in space. Due to a magma reservoir, a crack, a dike, or a combination of some of these sources aligned at different depths, pressure changes due to magma intrusions can be derived. We use geodetic and seismology modelling methods to estimate MPS geometry, size, and location incorporating constraints from other disciplines, cf. chapter 5.

2.3.2. Functional Model for Ambient Noise Tomography (ANT)

Ambient noise tomography (ANT) refers to the method that uses the empirical Green's functions from ambient noise to image the subsurface seismic velocity structure. ANT is an inversion problem that aims to find a velocity field from travel-time observations in three dimensions. In this context, Eq. (2.1) can be recast as

where \underline{y}_f is the travel-time vector per frequency, A is the design matrix relating slowness with the travel-times, x contains the model parameters, and \underline{e} represents the noise in the measurements. For each frequency interval there is an $m \times n$ design matrix A (of full rank equal to n), where n represents the number of ray paths found for that frequency interval and m is the number of grid cells. The number of non-zero elements in the design matrix is dependent on the number of ray paths previously selected. Because this inversion problem is ill-posed it requires a regularisation procedure. Here this is resolved by applying a Tikhonov regularisation (Tikhonov 1963). The regularisation adds a new term to the least-squares problem, also called the regularisation parameter or damping factor. The regularisation parameter is chosen using the cross-validation approach of Golub et al. (1979). The regularisation and the cross-validation's implementation is discussed in more detail in sec. 3.4 using the Torfajökull seismic network and afterwards applied in sec. 4.2.3 for the Reykjanes Peninsula data.

2.3.3. Functional Model for MPS geometry from InSAR

Surface deformation estimates are used as observables to estimate magma chamber geometry and depth parameters through geophysical modelling. As the Earth's surface inflates or deflates due to pressure changes, geodetic measurements can be used to estimate the deformation (strain) at the volcano surface during tensile or compressive internal forces (stress) in the subsurface. The functional model relating source geometry to surface displacements consists of analytical expressions which can simulate different geometries and deformation (inversion 4).

Various analytical expressions have been derived to estimate the unknown parameters for volcano applications, earthquakes, and gas or oil reservoir monitoring. These equations are mostly divided into point source models such as Mogi (1958), Yang et al. (1988) and dislocation models such as Okada (1985). The Mogi model is one of the most applied models to estimate the depth and size of a magma chamber. The geometry is a point source which can approximate a spherical source if the depth is significantly greater than the radius. Simple geometries like Mogi require a limited number of unknown parameters, as outlined in Table 2.2.

Okada (1985) inferred one of the most used analytical expressions for surface displacements for both point and rectangular sources in a half-space, and Okada (1992) inferred the analytical expressions to estimate the internal strains due to dislocations because of shear and tensile faults. This model is often used to estimate earthquake fault parameters, but the same principles can be applied to volcanoes where magma migrates through dikes on existing faults. In general, all these models start with the assumption that the physical structure of the Earth is an elastic half-space. Besides their

Table 2.2: Summary of commonly used functional models and corresponding unknown parameters

Functional	Source	# unknown	Medium	
model	shape	parameters	assumptions	
Point (Mogi 1958)	finite spherical	4 unknowns: location and depth (x_0, y_0, z_0) volume change δV	Elastic medium, homogeneous, isotropic in an half-space	
Ellipsoid (Yang et al. 1988)	Cigar-like prolate spheroid	7 unknowns: location and depth (x_0, y_0, z_0) volume change δV aspect ratio (A) dip angle (φ) strike angle (θ)	Elastic medium half-space double for centre of dila- tion solutions	
Sill (Okada 1985) (Fialko et al. 2001)	circular horizontal crack, penny-shaped crack	5 unknowns: location and depth (x_0, y_0, z_0) volume change δV radius (r)	Elastic medium Pressurised horizontal circular crack	
Dike (Okada 1985)	rectangular	8 unknowns: location and depth (x_0, y_0, z_0) length (L) Width (W) dip angle (φ) Opening Strike angle (θ)	homogeneous, isotropic in an elastic half-space	

mathematical simplicity, these models require previous knowledge of some geological parameters.

2.4. Areas of interest

Iceland is a young active system with a dynamic tectonic environment characterised by frequent volcanic eruptions, see Fig. 2.4. The island is located between the North American and the north Eurasian tectonic plates, which diverge along the Mid-Atlantic Ridge (MAR). The MAR extends over Iceland, beginning from the southwest at the Reykjanes Peninsula, continuing through the West Volcanic Zone (WVZ), and further north into the North Volcanic Zone (NVZ). The offshore regions include the Reykjanes Ridge (RR) to the southwest, forming part of the MAR, and the Kolbeinsey Ridge (KR) to the north.

The extension of the MAR across Iceland occurs at the main rift faults and connecting transform zones link these volcano-tectonic regions. The rift zones along the tectonic plate boundaries experience a spreading rate of $\sim 18-19.5$ mm/year in direction $\sim N(100-105)^{\circ}E \sim 100^{\circ}-105^{\circ}$ (Sella et al. 2002; Sigmundsson et al. 2020). As a result, magma fills in the cracks along these rift zones and this geological process leads to the formation of the youngest geological features near the rift and transform zone faults. Holocene volcanic activity in Iceland is concentrated primarily within the Neovolcanic Zones. These encompass distinct volcanic belts: the Reykjanes Volcanic Belt (RVB), West Volcanic Zone (WVZ), Mid-Iceland Belt (MIB), East Volcanic Zone (EVZ), and North Volcanic Zone (NVZ). Two minor lateral volcanic belts, namely the Öræfi Volcanic Belt (ÖVB) and Snæfellsnes Volcanic Belt (SVB), also contribute to the island's volcanic landscape.

At these locations, volcanic activity occurs within what is known as a volcanic system (VS). A VS typically comprises a central volcano and associated small craters that reflect the volcanic activity of the central volcano. These VS's are characterised by abnormally high temperatures extending over a width of approximately 40–50 km near the Earth's surface (Sæmundsson 1979; Einarsson 1991; Jóhannesson and Saemundsson 1998). The opening of cracks and the intrusion of magma often coincide with seismic activity, manifesting as earthquakes. The hypocenters of these earthquakes are predominantly located at the VS's, rift zones, and transform fault locations, as indicated by the coloured dots in Fig. 2.4. At one of the edges of the SISZ (South Icelandic Seismic Zone), the Torfajökull and the Eyjafjallajökull volcanoes and on the other side of the SIVZ, the Reykjanes Peninsula VS's are the case studies of this manuscript. These represent sites hosting dynamic volcanic systems, extensively monitored through satellite sensors and seismic campaigns to assess the efficacy of both approaches. This study centers on two specific volcanoes located within the South Icelandic Seismic Zone (SISZ) and the Reykjanes Peninsula Volcano System (VS), positioned diametrically across the SISZ.

2.4.1. Eyjafjallajökull volcano

The Eyjafjallajökull volcano is located in the southern part of the Eastern Volcanic Zone (EVZ), outside the central zone of the Icelandic propagating rift (red dashed line in Fig. 2.4). Eyjafjallajökull is a ~25 by 15 km central volcano, with a 2.5 km wide summit

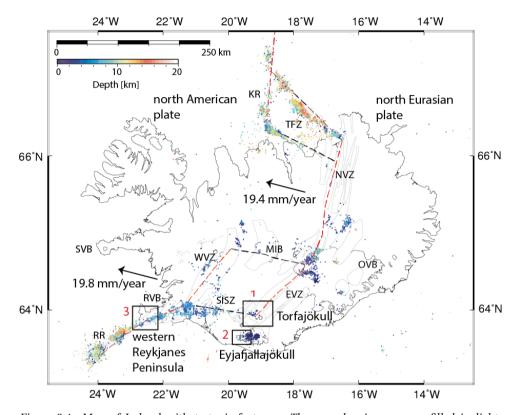


Figure 2.4: Map of Iceland with tectonic features. The neovolcanic zones are filled in light-shaded grey (Einarsson and Saemundsson 1987; Erlendsson and Einarsson 1996; Einarsson et al. 2002; Sturkell et al. 2006; Einarsson 2008; Sigmundsson et al. 2020) as a result of the MAR and North Atlantic mantle plume. The map's red dashed lines demarcate the plate boundary or the propagating rift zone, the extension of the Mid-Atlantic Ridge over Iceland, while black dashed lines delineate the transform fault system. To illustrate the region of heightened seismic activity, the coloured dots correspond to the depth of earthquakes recorded over seven years (1995 to 2012), primarily concentrated along the rift and transform zones. Additionally, the North Volcanic Zone (NVZ), the Western Volcanic Zone (WVZ), the Eastern Volcanic Zone (EVZ), and the South Iceland Seismic Zone (SISZ) are identified on the map. The black box 1 in the map locates the Torfajökull VS at the intersection of the SISZ and EVZ, immediately north of the Katla volcano. The black box 2 locates Eyjafjallajökull, immediately west of Katla volcano and the black box 3 locates the western Reykjanes Peninsula (WRP). The arrows show the total spreading rate of the North American plate (mm/yr) and direction estimated from the REVEL plate motion model (Sella et al. 2002) relative to stable north Eurasian plate.

caldera rising to 1,666 meters which is covered by a 50–200 m thick ice cap, which gives it its name. Eyjafjallajökull is a moderately active volcano, only erupting every few centuries, with three historical episodes: two effusive eruptions in the years (CE) 500, 920, 1612–1613 and explosive eruptions in 1821–1823 (Gudmundsson et al. 2008). Between eruptions, the average interval has been estimated to be 350–400 years in the last 1500 years.

In 1992, seismicity increased at Eyjafjallajökull volcano (Sturkell et al. 2003). In 1994 and 1999, geodetic measurements using optical tilt and GPS (Sturkell et al. 2003) and conventional InSAR (Pedersen and Sigmundsson 2006) suggested two sill intrusions. Although the two sill intrusions were at approximately the same depth (between 4.5 and 6.5 km), the sources' aerial extent and locations of the sources were different, indicating that there were two magma compartments. Using InSAR time series analysis, Hooper et al. (2009) constrained the location more accurately with estimated depths of 5.6 ± 0.1 km for the 1994 source and 5.7 ± 0.5 km for the 1999–2000 source. Furthermore, Hjaltadóttir et al. (2015) used GPS data from 1992 to 2009 and also estimated two sills associated with the 1994 and 1999 intrusions revealing a 4.5 to 5 km deep sill model for the 1994 intrusion and a depth of 5.0 ± 1.3 km for 1999 intrusion.

After quiescence since the sill intrusions in 1994 and 1999–2000, and already two decades of unrested geological activity, Eyjafjallajökull erupted in spring of 2010. This event led to a memorable disruption of air traffic attributed to the interaction between melted water from the glacier and the high-temperature magma and emission of finegrained ash into the jet stream (Gislason et al. 2011). The pre-eruptive unrest began in June 2009 with increased seismicity and surface displacements (Sigmundsson et al. 2010). The displacements were due to magma intrusions, and the unrest culminated in the first eruption, an effusive eruption of olivine basaltic andesite lava on 20 March 2010. The eruption occurred at Fimmvörðuháls mountain between the Eyjafjallajökull and Mýrdalsjökull glaciers and ended on 12 April 2010. This eruption was followed by an explosive event early in the morning of 14 April 2010 under the glacier covering the central summit caldera, which caused the air traffic disruption until 22 May. The 2010 Eyjafjallajökull's eruption, preceded by ~20 years of unrest, highlighted the need for research on the mechanisms behind moderately active volcanoes in Iceland and other volcanoes that erupt infrequently.

2.4.2. Torfajökull volcano

Torfajökull is a central volcano located at the Eastern Volcanic Zone (EVZ) and at the intersection of the propagating rift zone and the transform zone that connects to Reykjanes Peninsula/ridge, see Fig. 2.4. It erupts infrequently, with only two eruptions in the last 1200 years, the latest of which was over five centuries ago (870 and 1477 CE). It is the largest silicic volcanic centre in Iceland, covering 450 km² with most of its rhyolitic lava flows having erupted sub-glacially (Tuffen 2007). Two small ice caps partially cover the southeastern part of the large caldera of about 18×12 km. The caldera is cut by fissure swarms stretching to the NE and SW reaching an extension of 40 km long and 30 km wide (Soosalu et al. 2006). Gunnarsson et al. (1998) suggested that the large Torfajökull caldera collapsed after one or more eruptions, followed by younger extrusives which partially filled it in. These younger extrusives involve basaltic magmas mixing events

9

(Larsen 1984; Blake 1984; Mørk 1984; McGarvie 1984) formed after the tholeiitic basalts.

Torfajökull eruptions happened at the central volcano and along the fissure swarms. The Holocene eruptions are thought to be triggered by dyke intrusions from the two neighbour VS's which have fissure swarms intersecting Torfajökull caldera: to the west Hekla-Vatnafjöll (direction of the transform zone) and to the northeast, in direction of the rift zone, the Veidivötn's (Bárðarbunga) VS (EVZ in Fig. 2.4) (Sigurdsson 1970; Saemundsson 1972). The latter occurred with tholeiiric basalts entering into the Torfajökull's silicic centre active (Sigurdsson 1970; Saemundsson 1972). Blake (1984) and McGarvie et al. (1990) also conclude that the silicic and basaltic magma originating within the flank zone was mobilised by rifting injection of tholeiitic magma from the NE tholeiitic Veidivötn fissuring (McGarvie et al. 1990).

Low-frequency earthquakes (1–3 Hz with magnitude <2) argued to be related with active magma movements are detected at the south-east part of the caldera, extending downwards to about 15 km depth (Brandsdóttir and Einarsson 1992; Soosalu and Einarsson 2004). The epicentral area of the low-frequency earthquakes coincides with the area of highest temperature geothermal activity (> 340°C) (Bjarnason and Ólafsson 2000). At the western part of the caldera, high-frequency earthquakes (4-10 Hz with magnitude < 3), are located beneath the most recent eruptive sites; these earthquakes have been related to a brittle failure of the volcanic edifice (Einarsson 1991; Soosalu and Einarsson 1997; Lippitsch et al. 2005). Seismicity studies suggest a spherical aseismic volume centred at 8 km depth and a diameter of 4 km (Soosalu and Einarsson 1997; Soosalu and Einarsson 2004). Because this area is void of earthquakes, it has been interpreted as a magma chamber location. Because of the low impedance's throughout this area, the current working hypothesis is that the a-seismic volume is cooling magma, mostly solidified. Geodetic studies using InSAR and GNSS show vertical deflation of ~12 mm/year in the west part of the volcano caldera (Scheiber-Enslin et al. 2011), also suggesting a magma chamber contracting due to a decrease of temperature.

While the Torfajökull volcano has maintained an absence of eruptions over the past five centuries, it has consistently displayed subsidence at linear rates spanning the last quarter-century. Notably, the region lacks tomographic models, rendering it an optimal setting for evaluating the effectiveness of seismic interferometric techniques. The amalgamation of historical radar data and an existing seismic campaign conducted in 2005, which offers an invaluable array configuration suitable for tomographic investigations, underscores the Torfajökull volcano's eminence as an exceptional site for testing and refining both radar and seismic interferometric methodologies aimed at delimiting magma chamber geometries.

The conjecture of lateral magma migration between the fissure swarm of the Veidivötn's (Bárðarbunga) volcanic system and the Torfajökull volcanic system provides the backdrop for focusing both InSAR datasets on RAW images. This approach facilitates a more comprehensive perspective over both the Torfajökull and Veidivötn's volcanic systems.

Despite being the largest geothermal field in Iceland, Torfajökull's area is not subject to production. The volcano is one of the largest geothermal areas in Iceland, with geothermal surface manifestations covering an area of 150kg². Some studies have been performed to understand Torfajökull's potential for geothermal exploitation (e.g.

Ólafsson and Bjarnason (2000) and Palmason et al. (1970)). However, this area has also been suggested as a UNESCO World Heritage site for its unique geological features. The massive caldera (12x18 km) indicates the presence of a sizeable magma chamber and is located in a unique tectonic setting at the intersection of a rift and a transform zone. Torfajökull volcanic system is an ideal location for assessing the performance of radar and seismic interferometric observations. First, it is an active volcanic system within a complex tectonic setting, second due to the availability of historical satellite data and a seismic campaign with valuable network configuration for tomographic studies over the same period.

2.4.3. Reykjanes Peninsula

The Western Reykjanes Peninsula (WRP), located at the southwestern tip of Iceland (Fig. 4.1) is a transitional zone between a tectonic spreading centre and a transform zone (Pálmason and Sæmundsson 1974; Einarsson 1991; Sigmundsson et al. 2020). At this transitional zone, an extensional component with northeast–southwest trending normal faulting, and a transform component with strike-slip faulting oriented north–south can explain the observed displacements (Klein et al. 1973; Einarsson 2008). Inversion from deformation measurements to fault parameters using GPS and InSAR and microearthquake focal mechanisms studies (Keiding et al. 2008; Keiding et al. 2009) reinforce Einarsson (1991)'s results on the fracture locations and geothermal mechanisms along the transform zone.

Reykjanes Peninsula's tectonic setting facilitates the intrusion of magma in dikes along the NE-SW trending area of densely spaced fissures and faults. The presence of magmatic intrusions through dikes and fault swarms, in turn, promotes channels for down-flow of cooler "fresh" ground water followed by and thermal up-flow at the same locations (Franzson 1987). The high geothermal activity at the surface matches the location of the volcano-tectonic segments of the MAR extension over Iceland (Arnórsson For this reason, Reykjanes Peninsula is an excellent source of geothermal The Reykjanes peninsula has been subject to shallow and deep drilling for geothermal purposes, which makes it an appealing location to map the subsurface with seismic techniques. Given the fact that deep well measurements have been taking place at the tip of Reykjanes peninsula make it possible to correlate and calibrate the seismic with well measurements. Under the IMAGE (Integrated Methods for Advanced Geothermal Exploration) project framework, seismic interferometry of ambient noise for tomographic study of Reykjanes peninsula is exploited to study further capabilities for geothermal applications. The success of this seismic campaign has been broadly reported (Weemstra et al. 2016; Verdel et al. 2016; Darnet et al. 2018; Toledo et al. 2018; Blanck et al. 2019; Sánchez-Pastor et al. 2019; Martins et al. 2020).

Since 2021, Reykjanes Peninsula has been experiencing a volcanic crisis. The typical pre-eruption uplift and increased earthquake activity, common precursors to volcanic activity, have been measured before each recent eruption at Fagradalsfjall and Grindavik. First, at the Geldingadalur Valley in 2021, Fagradalsfjall, significant earthquake activity and surface deformation occurred due to magma intrusion and tectonic stress release. However, a notable decline in seismicity and deformation just before the eruption suggested that the magma was nearing the surface, encountering less resistance in

the weaker crust (Sigmundsson et al. 2022). The lava, rich in MgO, indicated a deep source, estimated to be around 17-20 km. The volcanic activity of the Fagradalsfjall eruption continued in 2022 at Meradalir Valley, evolving predominantly through one main crater but also with fissure formations and lava fountains reaching heights of 100-150m. From July 112th to early August 2023, another eruption occurred close to Litli-Hrútur volcanic fell, Fagradalsfjall, with a 200-meter-long fissure. From August 2nd onwards, the activity has transitioned into a new phase marked by shrinking the crater at Litli-Hrútur, decreasing lava extrusion rate, followed by a stable decline in volcanic tremor since midnight of August 42th. The lava field extended over an area of 1.5 km² with a total volume of 15.9 million m³ of lava released. In November 2023, a dike intrusion developed with an extremely high inflow rate (Sigmundsson et al. 2024). Following this event, there have been three eruptions at an approximate pace of one per month until January. In March 2024, a more vigorous eruption occurred, with lava flows reaching estimated rates of 1,100–1,500 m³ per second, followed by another eruption on May 29, 2024, with lava flow rates reaching even higher levels, indicating a significant buildup of magma beneath the surface. Ongoing magma accumulation, evidenced by measured uplift beneath the Svartsengi-Porbjörn area, has been a persistent concern, indicating that more eruptions are expected to come.

2.5. Data

In this study, seismic and geodetic data sources are used, see Table 2.3.

2.5.1. Seismic data

For Torfajökull, a network of broadband seismometers is used, deployed by the University of Cambridge during the summer of 2005. This network of 30 Güralp 6TD seismometers was initially installed around and inside the Torfajökull caldera by Soosalu et al. (2006) for seismicity location purposes and tomography given the good seismic stations distribution and density. For this study, data from 22 out of the 30 seismometers are used, avoiding intermittent operation, GPS clock timing errors reported in seven stations and unreliable cross-correlations detected from the interferometric processing at one station. To ensure continuous data acquisition, the vertical component of the 22 selected stations is used, recording noise over a 100-day period from June 19 to September 27 in 2005.

For the Reykjanes Peninsula, GFZ Potsdam and Iceland Geosurvey deployed 54 broadband seismometers on and around the Western Reykjanes Peninsula (WRP). These included 30 seismometers placed onshore and 24 ocean bottom stations (OBS) (Blanck et al. 2019; Jousset et al. 2017). The onshore instruments were operating from March 2014 until August 2015, while the OBS were deployed in August 2014 and collected in 2015. All equipment was collected in August 2015. In this study, the vertical component displacements of 30 onshore seismometers (20 broadband Trillium compact sensors and 10 short-period MarkSensors) are used for a duration of almost one year and five months.

Table 2.3: Summary of the seismic and radar data used in this study

Data type	Location	Sensors	Temporal coverage
Seismic	Torfajökull volcano	22 Broadband Güralp 6TD seismometers	06/2005 – 09/2005
	Reykjanes Peninsula	20 Trillium Broadband seismometers and 10 MarkSensors short-period seismometers	03/2014 – 08/2015
Radar	Eyjafjallajökull volcano	TerraSAR-X Level-1 Ascending track: 132 Descending track: 125	2009 – 2010
	Torfajökull volcano	ERS-1, ERS-2, Level-0 Descending track: 052 Ascending track: 359	1993 – 2000
	Torfajökull volcano	ENVISAT, Level-0 Descending tracks: 052, 152, 324 Ascending tracks: 087, 359, 488	2003 – 2010

2.5. Data 35

2.5.2. Radar data

For the Eyjafjallajökull 2010 eruption data from one ascending and one descending track of TerraSAR-X satellite operated by the German Aerospace Center (DLR) are used. The acquisitions were performed in the StripMap image mode with a spatial resolution of approximately 3 meters. Both tracks cover the eruptive period between 18 July 2009 and 1 September 2010, with images acquired every 11 days throughout the eruption (Fig. 5.2). Winter acquisitions are not used due to snow cover and therefore to ensure summer-to-summer coherence.

To estimate the deformation field over Torfajökull the complete scenes of six EN-VISAT tracks are processed: three descending and three ascending modes acquired between 2003 and 2010 as well as two ERS tracks covering the period between 1995 and 2009. The ERS processing is used only to confirm the rate of displacements in a different period. To study the whole SISZ (South Icelandic Seismic Zone) Fig. 6.1), RAW (Level 0) SAR images are used and refocused to Level 1 (SLC).

2

Imaging Torfajökull volcano with ambient noise seismic interferometry and tomography

Although most active volcanoes are continuously monitored, less is known about volcanoes that have not erupted recently. The Torfajökull volcano in Iceland has not erupted since 1477. However, intense geothermal activity, deformation, and seismicity suggest a long-lasting magmatic system. In this chapter, I investigate seismic tomography using ambient-noise seismic interferometry to generate the first seismic image of Torfajökull's magmatic plumbing system using one hundred days of ambient-noise data from 23 broad-band seismometers.

3.1. Introduction

Located in the eastern volcanic flank zone (see EVFZ in Fig. 3.1a) Torfajökull has, as direct neighbours, the Hekla volcano to the west and the Katla volcano to the south, which are among the top three most active Icelandic volcanoes (see Fig. 3.1b). Despite Torfajökull's infrequent eruptions, only two in the last 1200 years, ongoing seismicity, deformation, and geothermal activity within its caldera indicate the continued presence of a still hot magma chamber.

Low-frequency earthquakes (1–3 Hz with magnitude <2) argued to be related to active magma movements are detected only in the south-east part of the caldera, extending downward to about 15km depth (Brandsdóttir and Einarsson 1992; Soosalu and Einarsson 2004). The epicentral area of low-frequency earthquakes coincides with the area of highest-temperature geothermal activity (> 340°C) (Bjarnason and Ólafsson 2000). In the western part of the caldera, high-frequency earthquakes (4–10 Hz with magnitude < 3), are located below the most recent eruptive sites; these earthquakes have been related to a brittle failure of the volcanic edifice (Einarsson 1991; Soosalu and Einarsson 1997; Lippitsch et al. 2005). Seismicity studies reveal a spherical aseismic volume (void of earthquakes) with a centre at 8km depth and a diameter of 4km (Soosalu and Einarsson 1997; Soosalu and Einarsson 2004) interpreted as a cooling volume of magma mostly solidified. Geodetic studies show vertical deflation of ~12 mm/year in the west part of the volcano caldera (Scheiber-Enslin et al. 2011), also suggesting a magma chamber contracting due to a decrease in temperature.

In this study, we create the first image of Torfajökull's magmatic plumbing system

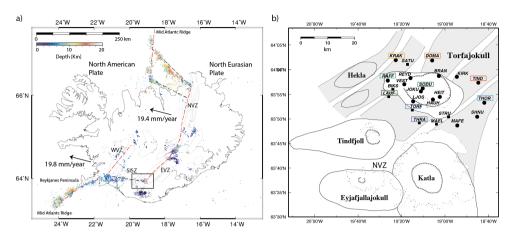


Figure 3.1: a) Map of Iceland with tectonic features (see Fig. 2.4 here repeated for convenience). The box in south-central of the map locates Torfajökull volcanic system at the intersection of the SISZ and EVZ, immediately north of Katla volcano. b) Location of Torfajökull and neighbouring volcanoes (square of a) zoomed in). The extent of each volcano and the corresponding caldera are represented by the black polygons. The glaciers are represented by the dashed polygons and the shadowed area represent the volcanic systems surrounding these volcanoes. Black circles and squares locate the acausal deployed in 2005. Coloured squares around station names identify the stations plotted in Fig. 3.2.

with ANT. We used SI with ambient noise for retrieval of the surface wave's phase. This is considered consistent with the spatial autocorrelation method (SPAC) (Aki 1957; Aki 1965) as shown by Yokoi and Margaryan (2008). In a volcanic setting, SPAC can be used to estimate phase velocity curves (Nagaoka et al. 2012). The comparative study of the two approaches (SPAC and SI) by Tsai and Moschetti (2010) also suggests that the results of each technique can be used to benefit the other.

We aim at imaging Torfajokull's subsurface to understand if there are low-velocity 1 zones beneath or outside the volcano caldera as a result of an existing magma chamber (molten or partially molten). Given the relatively short time acquisition of the seismic network for passive seismic purposes, we follow a methodology that aims at retrieving accurate surface wave phase-velocity estimations for tomographic inversion, as well as to control the quality of the inversion results.

 $^{^1}$ In geophysics, the term "low-/high-velocity" or "velocity anomaly" has been used due to historical convention, even though it would be more precise to call it a "speed anomaly". Since it is widely accepted, and everyone in the field understands that it refers to scalar wave speeds, I kept the convention. However, seismic wave velocity anomalies refer to variations in the speed (how fast) at which seismic waves travel through different parts of the Earth. These anomalies are typically expressed as either absolute speeds (e.g., S-wave velocity $v_S = 6.2$ km/s, or relative changes (e.g., velocity variation $\delta v/v = -10\%$ compared to a reference model, such as PREM, or a reference model derived from the dataset). The direction of wave propagation is known or modelled separately (ray paths, or beamforming, see sec. 3.2.4), but when we say "velocity anomaly" we mean a change in wave speed, not the full velocity vector as for the InSAR-derived velocities.

3.2. Retrieval of Surface Waves from Ambient Noise

From the possible seismic waves, surface waves, because these are usually the most energetic arrivals at the surface. As an alternative to using surface waves from earth-quakes, we extract surface waves with a high signal-to-noise ratio (SNR) using seismic ambient noise. Since the origin of the surface waves is not known, SI by cross-correlation allows us to retrieve the direct surface waves between pairs of receivers where one of the receivers acts as a source and the other as a receiver. That is, we retrieve the response as if one of the receivers from a receiver pair measures the direct surface wave — ballistic surface wave (BSW) — that was induced by a virtual source at the other receiver. In this section, we extract surface waves from ambient noise by using SI by cross-correlation.

3.2.1. Pre-Processing of the Ambient Noise

We used 22 of the 30 Güralp 6TD seismometers initially installed around and inside the Torfajökull caldera by Soosalu et al. (2006) (Fig. 3.2) in summer 2005 (station metadata listed Tab. 3.1). Although most seismometers were reported to have data recovery 100%, seven out of the thirty stations had intermittent operating periods (starting and stopping at irregular intervals) and were reported to have GPS clock timing errors. At a later stage, we also excluded the STRU station from our processing because of unreliable cross-correlations. Therefore, to avoid gaps during data acquisition, we use the vertical component of the 22 selected stations simultaneously recording noise during a period of 100 days (approximately fourteen weeks from June 19 until September 27). Details on station coordinates and data gathered during the seismic campaign can be found in Tab. 3.1.

After data acquisition, we preprocessed the recorded noise to prepare the waveforms for retrieval of surface waves by SI (Bensen et al. 2007), e.g., to remove trends, to eliminate instrumental irregularities and thus to enhance the broadband character of the noise, and to suppress strong transient arrivals. The instruments have a sampling rate of 50 samples per second, thus recording ambient noise up to 25 Hz. We remove the instrument response by complex deconvolution for all three components of the displacement to flatten the response down to 0.1 Hz.

We use time-domain normalisation to downweight high-amplitude arrivals (nuisance sources) in a continuous record by homogenising the amplitudes over a predefined window length. The running-absolute-mean normalisation described in Bensen et al. (2007), computes a running average of the absolute value of the waveform in a normalisation time window. This normalised time window has a fixed duration of 2 seconds and weights the waveform at the centre of the window by the inverse of the running average. The last step of the pre-processing is spectral normalisation (or whitening) with the goal of broadening the ambient-noise band for the cross-correlations. The whitening is implemented through running-absolute-mean normalisation in the frequency domain, with a window of 0.5 Hz.

3.2.2. Frequency Selection

Table 3.1: Broad-band station coordinates placed at Torfajökull volcano and corresponding volume of data gathered during the seismic campaign, Summer 2005 (Soosalu and White 2006)

Station	Latitude	Longitude	Elevation	Installed	Pick-up	Operation	Recovered data
Name	[°N]	[°W]	[m]	[day]	[day]	[days]	[%]
LAUF	63.90916	19.43146	658	09/Jun	05/Oct	117.95	100
BIKS	63.94943	19.41237	779	09/Jun	05/Oct	117.9	100
RAFF	63.96364	19.43877	911	09/Jun	05/Oct	117.86	100
KRAK	64.03248	19.37757	682	10/Jun	05/Oct	117.06	100
SATU	63.01809	19.28747	671	10/Jun	04/Oct	116.18	100
DOMA	64.03158	19.09841	652	10/Jun	04/Oct	116.18	100
BRAN	63.97903	19.04707	620	10/Jun	04/Oct	116.07	100
POKA	63.98442	19.26821	917	11/Jun	05/Oct	116.09	~100
HRAF	63.95618	19.21494	897	11/Jun	05/Oct	116.08	94
REYD	63.97201	19.26449	917	11/Jun	05/Oct	116.03	100
VEST	63.95115	19.31254	872	11/Jun	05/Oct	115.74	100
SODU	63.93718	19.17151	1078	14/Jun	19/Oct	127.09	100
HRAS	63.93641	19.20482	1018	14/Jun	05/Oct	113.03	~100
JOKU	63.92701	19.18447	1109	14/Jun	19/Oct	126.95	100
TORF	63.86405	19.24982	547	15/Jun	07/Oct	113.96	100
LJOS	63.8933	19.24454	697	15/Jun	07/Oct	113.86	100
MAEL	63.8164	19.01667	619	15/Jun	06/Oct	113.09	~78
KGIL	63.85869	18.97325	603	15/Jun	06/Oct	112.98	100
STRU	63.84095	18.97253	576	15/Jun	06/Oct	112.91	95
THRA	63.82057	19.19711	580	16/Jun	06/Oct	112.32	100
SVAR	63.83705	19.06336	605	16/Jun	07/Oct	112.98	~100
KKLO	63.87033	19.05419	655	16/Jun	07/Oct	112.93	~100
MAFE	63.8117	18.90571	552	16/Jun	06/Oct	111.97	100
HALL	63.97064	18.83239	601	20/Jun	06/Oct	107.78	~100
KIRK	63.97617	18.90944	605	20/Jun	06/Oct	107.7	~98
TIND	63.95618	18.74455	682	21/Jun	06/Oct	107.06	100
THOR	63.88849	18.69845	490	21/Jun	06/Oct	107.03	100
SHNU	63.8414	18.75374	591	21/Jun	06/Oct	107	100
HAUH	63.89973	19.09278	963	22/Jun	20/Oct	120.1	100
HEIT	63.90829	19.03936	971	22/Jun	20/Oct	120.05	100

Power Spectral Density

To select the bandwidth of the microseisms, we analyse the Power Spectral Density (PSD) of the recorded signal, which shows where the average power is distributed as a function of frequency. We compare the measurements on stations spatially well spread over the acausal with global measurements of ambient noise. We computed the PSD of the selected stations and compared the PSD with the models obtained by Peterson (1993), the New Low Noise Model (NLNM) and the New High Noise Model (NHNM).

Fig. 3.2 shows the variation of the amplitudes in different frequency bands for nine stations on the edges and one at the middle of the acausal for day 221 of the year.

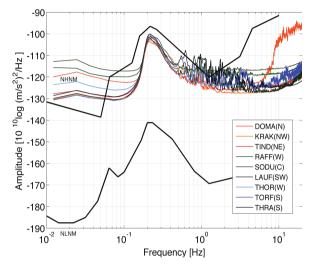


Figure 3.2: Variation of the PSD at the different selected stations for the day 220 (for station locations see Fig. 3.1). Orange to red colours represent the northernmost stations. The stations located in the middle of the array are shown in green, and the southernmost stations in blue, respectively. The black lines show the lower and upper limits given by the NLNM and NHNM models.

The PSD of all the stations analyzed follows the same trend as the models except for frequencies below 0.1 Hz, at which frequency the instruments rapidly lose their sensitivity. The recorded noise is closer to the NHNM indicating that the area is dominated by a high-noise level within almost all frequencies, as would be expected given the proximity to the ocean. The amplitudes between 0.1 Hz and 1 Hz follow the NLNM and NHNM models, reaching a peak of the higher power spectrum at double frequency microseism (Haubrich et al. 1963). Substantial changes in the amplitude values of particular stations occur close to 1 Hz and above. Two stations, TORF and THRA, reach a peak of noise around 2 Hz which could be due to local geological characteristics, perhaps connected with the local history of volcanic activity (Martins et al. 2022). From approximately 8 Hz to the maximum recorded frequency (25 Hz), stations DOMA, KRAK and RAFF exhibit higher levels of energy. At the DOMA station, this is probably related to car traffic given the proximity to local roads. At KRAK and RAFF stations it might be caused by earthquakes, which are not included in the NHNM

model.

Spectrogram Analysis

For an overview of the distribution of the noise in frequency and time, we compute the PSD of the whole time period for one station located in the centre of the array, station JOKU. We divide the selected time period into 5 min windows and then compute the PSD using the ensemble average for different segments of 11 shorter time windows. The spectrogram for the JOKU station is shown in Fig. 3.3. We identified two bandwidths: one between 0.1–0.5 Hz (the band) and the other between 10–25 Hz that exhibit a consistent presence of high-amplitude noise throughout the recording period. There is a third frequency band between 2.0–2.5 Hz which shows steady noise presence, but with lower amplitudes.

We selected the frequency band between 0.1 Hz and 0.4 Hz not only because of its high PSD, but also because of the depth range of the surface waves to which these frequencies are sensitive. Within this frequency band, it is clear that the energy levels are significant. However, in time, power does not always reach the upper and lower limits of this frequency band (close to 0.1 Hz and 0.4 Hz), especially during the first half of the recording time period. This means that the frequencies at the edge of the bandwidth might not have enough energy to retrieve acceptable surface waves. Nevertheless, at this selection stage, we are more permissive, and we select a frequency band comprising the detected limits of high energy. In the second half of the recording time period (from August 20 onward) the power is much higher than during the first half, most likely due to an increase of storms in the ocean, leading to an increase of microseism generation near the seabed.

3.2.3. Crosscorrelation and Temporal Stacking

To retrieve the surface-wave part of the Green's function, we bandpass filter the microseisms (from 0.1~Hz to 0.4~Hz) of the ambient noise recorded during the selected 100 days, divide the ambient noise recorded at each station in portions of 1~h and cross-correlate those portions for each station-pair combinations. To recover the BSW, we cross-correlated the vertical components of the station pairs, averaged the cross-correlated results over a long time period, and then took the time derivative multiplied by -1, see Eq. (2.6). In total, we apply SI to 253 pair of stations (see Fig. 2.3~hz) for example between two stations and Fig. 3.4a~hz for all the stations stacked over time).

We averaged (sum) the one-hour correlations over the chosen 100 days of recordings. What we gain by the time averaging/stacking is a convergence of the retrieved signal to the surface-wave part of the Green's function. In Fig. 3.4b we see the results of averaging 100 days of cross-correlations as a function of receiver-pair distance at positive and negative correlated lags. Each of the vertical lines corresponds to a retrieved trace between a certain station-pair (Fig. 3.4a).

The retrieval at positive times is an estimation of the fundamental-mode Rayleigh wave, whereas the result at negative times is an estimate of its time-reversed variant (Bensen et al. 2007). The arrivals at positive and negative time lags are not symmetric, indicating that the illumination is not isotropic: the illumination from one station to another is not the same as in the opposite direction. Fig. 3.4c, d and e show the

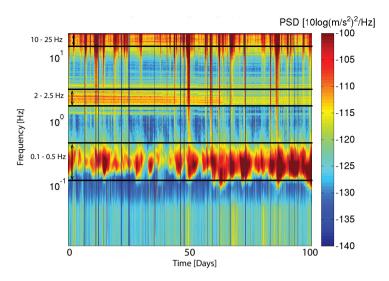


Figure 3.3: Spectrogram for JOKU station for the whole recording period (100 days) after removing the instrument response. We recognize three frequency bands with higher power identified by the horizontal black lines. Hours without data result in vertical blue lines spanning the entire frequency range.

retrieved Green's functions, band-pass filtered in narrower bands centered at 0.14, 0.28 and 0.38 Hz, respectively. The plots show well-retrieved results; however, for short intra-station distances, the retrieved arrivals at positive and negative time lags start interfering, resulting in less precise surface-wave arrivals. We take this into consideration later when extracting the travel times from these waveforms.

3.2.4. Direction and Slowness of the Microseism Noise

SI requires an isotropic distribution of the illuminating sources to retrieve the complete Green's function (Weaver and Lobkis 2004; Wapenaar 2004; Roux et al. 2005b). However, noise sources such as microseisms are usually characterized by preferential source locations (Bromirski and Duennebier 2002). As a result of this directionality, the accuracy of Green's function estimates will be affected, which can afterward affect isotropic and anisotropic tomographic inversions (Harmon et al. 2010).

Analysis of the time lags over the array of incoming surface-wave noise unveils the directionality of the illumination. This information can be used to decide to use some pair of stations and not others. If there is a lack of microseism noise travelling in a particular azimuthal direction, the SI result for station pairs oriented in that direction will contain an erroneous retrieved BSW. We apply a beamforming analysis to determine the azimuthal distribution of the noise sources and also the apparent velocity of the microseisms surface-wave noise. The procedure for beamforming can be found, for example, in (Lacoss et al. 1969; Rost and Thomas 2002; Gerstoft and Tanimoto 2007; Tanimoto and Prindle 2007). We used the previously selected frequency band, from 0.15 Hz to 0.25 Hz, and we apply beamforming to one entire day of recordings to see the

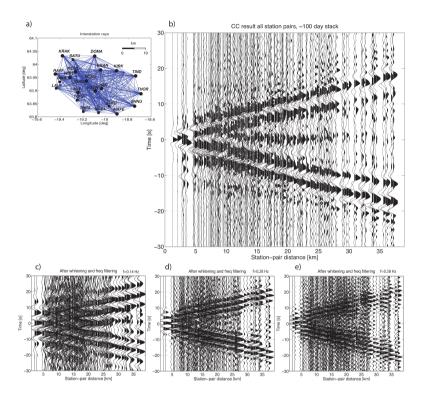


Figure 3.4: a) Combinations of all station pairs for retrieval of surface-wave arrivals. b) The retrieved surface-wave arrivals at positive and negative times in the frequency band between 0.1 and 0.5 Hz. In the abscissa represents the station-pair distance considering R the vector of distances between each station-pair sorted by its magnitude. The ordinate represents the time, positive and negative according to the direction of surface-wave propagation. c), d) and e) are the retrieved surface-wave arrivals separated into three narrow frequency bands centered around 0.14 Hz, 0.28 Hz, 0.38 Hz, respectively.

illumination characteristics (direction, pulse structure, apparent velocity) of the noise in a short time scale. In Fig. 3.5, we observe during day 226 (August 14), persistent stronger noise from the NW/SE directions travelling with apparent velocities near 2.8 km/s.

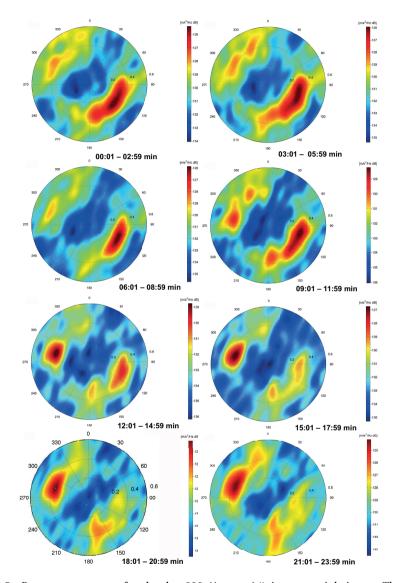


Figure 3.5: Beampower output for the day 226 (August 14) in sequential times. This output represents three parameters: the estimated ray-parameter or derivative of travel time tt with horizontal distance (radius), the estimated azimuth of the dominant beam (where 0° indicates north), and the estimated amplitude of the dominant beam.

To obtain an estimate of the illumination over the entire 100-day period we apply

beamforming directly to the stack of cross-correlations (Figure 4a). This procedure is described in Ruigrok et al. (2017). The beam power results show the directionality of stronger noise sources, which are centred around the west and south-east (Fig. 3.6a). When selecting the primary and secondary peak after beamforming the 1-day recordings (Fig. 3.6b), we also found weaker sources. We identify predominant directions from back-azimuth intervals between $\sim 15^{\circ}-35^{\circ}$, $\sim 60^{\circ}-75^{\circ}$, $\sim 90^{\circ}-180^{\circ}$ and $\sim 210^{\circ}-300^{\circ}$, showing roughly that no microseism noise is coming from directions between 300° and 15°. This shows an anisotropic noise distribution, which means that for some pair of stations, reliable BSW would be retrieved only at positive or only at negative times. In Fig. 3.6a) there appears to be an illumination hole between $\sim 210^{\circ}$ and $\sim 220^{\circ}$ degrees. However, Fig. 3.6b) shows that weaker sources are still covering these azimuths. We detect sufficient illumination, meaning that the BSW would be retrieved at both positive and negative times, or at least at one of the times, which can then be used as well. For this reason, after the beamforming analysis, we do not exclude any station pair for the dispersion-curve extraction.

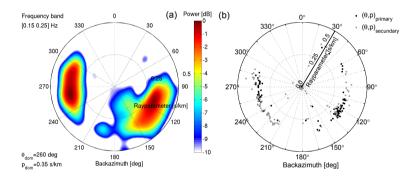


Figure 3.6: Beamforming analysis as a function of back-azimuth and apparent velocity for approximately 100 days over the entire seismic array using a narrower frequency band (between 0.15 to 0.25). a) Interpolation of the primary sources as a function of back-azimuth and ray-parameter. b) Primary and secondary sources as a function of back-azimuth and ray-parameter.

As Iceland is an island, it is expected to have ocean waves coming from all directions; however, storms, especially west and south-east of Iceland, could result in microseism noise predominantly from these directions. The sources of more powerful noise from the west direction are likely to be related to the polar air effect over the ocean originating in Greenland (Båth 1953) and eventually storms between Greenland and Iceland. The source of noise arriving from the south-east can be related to depressions heading for NW Europe. In both cases, the estimated directions of stronger microseism noise are consistent with the noise source locations from Stutzmann et al. (2012) for the period band 5–7 s of data acquired during summertime.

3.3. Velocity Variations at Depth from Surface Waves

3.3.1. Average Dispersion Curve

The average dispersion curve is estimated from the time-distance slope of the retrieved BSWs. The average phase velocity c(f) could be found in the time-space domain by filtering the data in a narrow band around f and picking a best-fitting line through the BSW's and determining its slope by:

$$c(f) = \frac{\mathrm{d}R}{\mathrm{d}Rt},\tag{3.1}$$

where *R* is the distance between the receiver pairs. A more robust implementation is achieved in the wavenumber-frequency domain, where the phase velocity is estimated from the frequency-wavenumber slope:

$$c(f) = \frac{f}{k(f)},\tag{3.2}$$

where k(f) is the wavenumber function describing the BSWs.

The picking in the wavenumber-frequency domain follows the approach of the multichannel surface wave method (MASW) of Park et al. (1998) and Park et al. (1999). In this approach, the dispersion curve (phase velocity as a function of frequency) is extracted from the amplitude spectrum preserving the information about the phase spectrum (dispersion properties). Implementing a multichannel analysis has several advantages, mainly in effectively identifying noise that contaminates the estimation of fundamental-mode Rayleigh-wave dispersion (higher-mode Rayleigh waves, refracted and reflected body waves, scattered and non source-generated surface waves).

From the retrieved BSWs (Fig. 3.4b), we take either the positive times or the timereversed negative times, depending on the side with the highest signal-to-noise ratio. The resulting panel is transformed to the wavenumber-frequency domain. Fig. 3.7 shows the amplitude spectrum.

For each frequency, the wavenumber with the maximum amplitude is picked, yielding the function k(f) and the dispersion curve from Eq. 3.2. Fig. 3.8 shows the resulting dispersion curve as a dashed black line.

The amplitude spectrum is not affected much by aliasing. Using 232 station pairs with maximum station-pair distance R_{max} and minimum station-pair distance R_{min} , the average spacing (dR)between subsequent station pairs (n_{pairs}) is 153 m from:

$$dR = \frac{(R_{\text{max}} - R_{\text{min}})}{n_{\text{pairs}} - 1}$$
(3.3)

This spacing yields the following approximate Nyquist wavenumber (k_{NY}) of $0.0032 m^{-1}$ from

$$k_{NY} = \frac{1}{2dR} \tag{3.4}$$

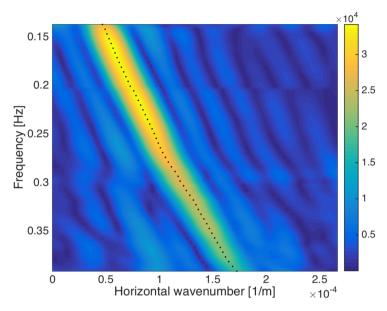


Figure 3.7: Frequency-wavenumber amplitude spectrum of the retrieved surface waves (Fig. 3.4b). The black dots denote the wavenumber with the maximum amplitude picked for each frequency. The picked wavenumber-frequency function is used to derive an average dispersion curve over the array.

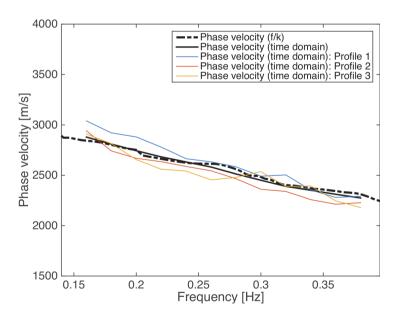


Figure 3.8: Average phase velocities over the seismic network. The dashed and continuous black line are phase velocities from pickings in frequency and time domain, respectively. Coloured lines are the phase-velocity dispersion curves of three random station pairs.

where k_{NY} is significantly larger than the extent of the wavenumber axis in Figure 3.7. However, the irregularity in station distance distribution does result in spurious mappings of the BSWs to the frequency-wavenumber domain. In Fig. 3.7, the aliased-like features can be identified as low-amplitude frequency-shifted repetitions of k(f). There are no indications of higher modes or retrievals other than surface waves that are consistent over the entire array.

3.3.2. Path Dispersion

In the time domain, we extracted the averaged dispersion curve over the paths connecting the different pair of stations. The picks in the time-domain are performed in narrow frequency bands, between 0.12 Hz and 0.44 Hz, with steps of 0.02 Hz. Assuming the filtered response to be monochromatic with frequency f_i (where $i \in [0.12, 0.4]$ with the defined 0.02 step), the time domain BSW is written as a phase-shifted cosine:

$$u(t, f_i) = \cos(2\pi \cdot f_i \cdot t - \frac{2\pi \cdot R}{c} - \phi_{\text{VS}}), \tag{3.5}$$

where *R* is the distance between the two receivers, $c(f_i)$ is the phase velocity and ϕ_{VS} is the phase term of the virtual source.

The phase shift is composed of a distance term $\frac{2\pi R}{c}$ and a source term ϕ_{VS} . For perfect illumination, the phase of the virtual source (reconstructed source) is $\frac{\pi}{4}$. For perfect illumination, the phase of the virtual source (reconstructed source) is $\frac{\pi}{4}$. This additional phase term stems from the two-dimensional wave propagation of surface waves. For imperfect illumination and/or additional interference with spurious terms, ϕ_{VS} will be a frequency-dependent deviation from $\frac{\pi}{4}$. Lin et al. (2008) introduced the parameter λ to express the phase deviation due to imperfections and coined it the source phase ambiguity. λ and ϕ_{VS} are related as

$$\phi_{\rm VS} = \pi/4 + \lambda,\tag{3.6}$$

where λ is the wavelength.

Isolating the phase velocity from Eq. 3.5 yields

$$c(f_i) = \frac{R}{t(f_i) - \frac{\phi_{\text{VS}}}{(2\pi \cdot f_i)}}.$$
(3.7)

Hence, we estimate the dispersion curve by first picking $t(f_i)$ from the bandpass-filtered BSW's and subsequently correcting for the virtual-source phase term.

To pick $t(f_i)$, we use the guidance from the average phase velocities using the MASW algorithm to circumvent timing mismatches due to the interference of retrieved arrivals at positive and negative times and to avoid picking at an incorrect cycle. Fig. 3.9 (top) shows examples of retrieved BSWs bandpass frequency filtered using narrow bands around f_i . Due to the narrow band remaining, the signal is still somewhat localised in time. For most frequencies and station pairs, $t(f_i)$ corresponds to $t_{\max}(f_i)$, the time at which the maximum amplitude occurs. However, sometimes a velocity closer to the

MASW estimate is obtained by picking the next cycle: $t(f_i) = t_{\max}(f_i) + 1/f_i$. In theory, also the cycle before t_{\max} could lead to a velocity closer to the MASW estimate. This case does not occur for this dataset, probably due to the fact that reducing $t(f_i)$ in Eq. 3.7 leads to significantly higher velocities for the small station distances involved in this dataset (R < 40km). The travel-time picks are made after taking the time derivative of the cross-correlations multiplied by -1, see Eq. (2.6). This differentiation is required to interpret the interferometric result as part of a Green's form.

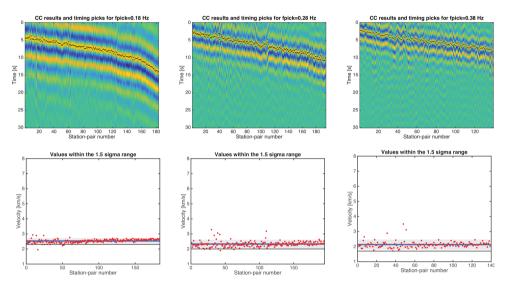


Figure 3.9: Top: Travel time picking for the frequency values 0.14 Hz, 0.28 Hz, and 0.38 Hz. Colourbar indicates the coherence of the retrieved surface waves and the black dots are the actual pickings. Bottom: Final velocity values obtained from the picked times. We select for the tomographic inversion only those values, which fall inside the 2σ interval (grey zone) from the mean value (the blue line).

The quality of the retrieved BSW degrades when the inter-station distances (R) are too short or too long (Fig. 3.4). For short distances there is interference between acausal and causal times, and therefore we cannot pick an accurate timing. Some authors define this minimum distance as $3\lambda_{f_i}$ (Bensen et al. 2007), others as $2\lambda_{f_i}$ (Shapiro et al. 2005a). At larger distances, especially when the wavelength of the surface wave is shorter, direct waves start to interfere with scattered waves. The maximum distance between station pairs should also be set, as such scattered wave arrivals complicate the pickings of BSW at larger distances. The thresholds we use to discard station pairs based on the minimum and maximum inter-station distances $(R_{i,\min})$ and $R_{i,\max}$) are, respectively:

$$R_{i,\min} = \frac{2}{3} \lambda_{i,0},$$
 (3.8)

$$R_{i,\text{max}} = 2.8 \cdot \lambda_{i,0}, \text{ with } \lambda_{i,0} = \frac{\nu_{i,0}}{f_i}$$
 (3.9)

where $0.12 \le f_i \le 0.4$ Hz with a step of 0.02 Hz, $v_{i,0}$ is the average reference velocity for each frequency value, and $\lambda_{i,0}$ is the wavelength obtained from the average velocity, per frequency value. Here, we are less conservative in defining the minimum distance than previous studies. However, we select only retrieved surface waves with high SNR and no serious interference to allow accurate travel-time picking. The maximum distance was defined empirically by visual inspection of the distance, where a clear identification of the direct wave becomes problematic. We select either the causal or the acausal side, based on the side with the highest amplitudes. We make this choice before taking the time derivative of the retrieved SI results multiplied by -1.

In our dataset, we restrict the path-dispersion estimation to waves that travel in less than three cycles from source to receiver, see Eq. (3.9). With this restriction, it is unlikely that a wrong cycle is chosen when using the MASW velocity as a guide. For datasets with larger station distances and/or for higher frequencies, there is a risk of underestimating or overestimating the path dispersion if our approach were used.

Finally, we do an additional outlier check as a way to determine outliers that are caused by poorly retrieved fundamental-mode Rayleigh waves or by interference of retrieved fundamental-mode Rayleigh waves with other retrieved waves. While picking the travel times, we discard values falling outside the 2σ deviation from the mean. In Fig. 3.9 (top) we show the picked points (on either the causal or time-reversed acausal interferometric result) for the different station pairs for the same three frequency values shown in Fig. 3.4. In Fig. 3.9 (bottom) we show the picked travel-time values converted into velocities using the intra-station distances. Below each picked point figure, we show the corresponding 2σ confidence interval around the mean velocity value per frequency band. After removing the outliers and applying the correction with the theoretical value of $\pi/4$ we obtain a dispersion curve for each station pair.

Fig. 3.8 shows the phase-velocity dispersion curves for three station pairs (coloured lines). The black lines are the average dispersion as found by averaging over all station-pair paths. Both the average dispersion as estimated in the time domain (black continuous line) figure and the average dispersion as estimated in the frequency-wavenumber domain (black dashed line) show similar velocity variations. Moreover, the first-order similarity of both dispersion curves shows that the phase-correction term we use for the time-domain picks is a fair estimation.

3.3.3. Source Phase Estimation

As a quality measure of the illumination, we make an estimate of the frequency-dependence of the virtual-source phase term $\phi_{VS}(f_i)$, see Eq. (3.5). For a given frequency f_i , we plot the travel-time picks $t(f_i)$ for multiple station pairs as a function of distance and fit a linear function through the points. From the intersection of this line with the time axis $t_o(f_i)$ we estimate the average virtual-source phase term:

$$\phi_{\text{VS}} = 2\pi \cdot f_i \cdot t_o. \tag{3.10}$$

Phase values closer to $\pi/4$ indicate a higher quality of the retrieved surface waves and time picking for the respective frequency. In Fig. 3.10 we show the estimated virtual source phase per frequency (a) and the number of ray paths per frequency (b). The latter parameter is largely governed by the wavelength-based thresholds (Eq. 3.8 and

Eq. 3.9). By analysing the two graphs, we can see that $\phi_{\rm VS}$ for 0.12 Hz is more than double the expected value. For 0.4 Hz the number of ray paths starts to decrease and to be conservative at the limits of the frequencies, so we decided to select a narrower frequency band of the picked travel-times, $0.16 \le f_i \le 0.38$ Hz, in the subsequent tomographic analysis.

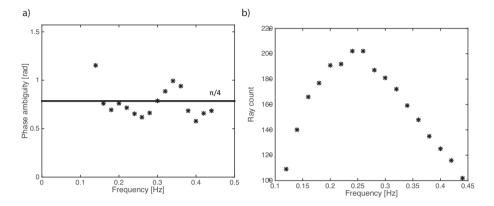


Figure 3.10: a) Estimated phase term of the virtual-source (ϕ_{VS}) per frequency. The phase term of the virtual source values are close to $\frac{\pi}{4}$. Frequencies 0.3 Hz and 0.32 Hz show the second highest variation from the expected $\frac{\pi}{4}$ value. b) Number of ray-paths per frequency. The lowest number of ray paths is, as expected, at the limits of the frequency band from 0.12 Hz to 0.44 Hz.

Lin et al. (2008) describe an alternative way to estimate the source phase $\lambda = \phi_{VS}(f_i) - \pi/4$. Their method is based on comparisons of travel times of station triples that are nearly aligned along the same great circle. The advantage of our method is that such station triples do not need to be present. Our method can be implemented for more arbitrarily array configurations. However, the requirement is that for one f_i there is enough pair of stations present to confidently fit a time-distance curve.

3.3.4. Azimuthal Velocity Variations

Using the estimated travel times, we check the azimuthal velocity variations to identify trends or possible inconsistencies of the estimated velocities in frequency and direction. Fig. 3.11 depicts the derived azimuthal velocity variation. There is a trend, over the complete frequency range, of the highest speeds being near 40 degrees and near 220 degrees. The lowest velocities are between 100° and 170°. Note that these azimuths are close to the ranges where we had lower illumination (sec. 3.2.4) due to weaker sources (Fig. 3.6b). Nevertheless, because the source-phase estimation indicates that there was sufficient illumination (sec. 3.3.3), it is more likely that a possible anisotropy causes the azimuthal dependence on the velocities. The inferred fast axis (30 degrees) corresponds well with the strike of the rifting as well as the orientation of the erupted lavas on a NE-SW fissure swarm (Ivarsson 1992).

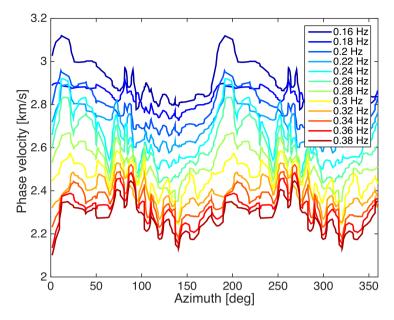


Figure 3.11: Variation of the phase velocity with azimuth and frequency.

3.4. Tomography

To constrain the geometry and location of the magma system beneath Torfajökull volcano, we invert the travel-times between each station pair to estimate surface-wave velocity variations. The following forward problem is inverted:

$$\begin{bmatrix} tt_1 \\ tt_2 \\ \vdots \\ tt_{n-1} \\ tt_n \end{bmatrix} = \begin{bmatrix} s_1 \\ s_2 \\ \vdots \\ s_{n-1} \\ s_n \end{bmatrix}^T \begin{bmatrix} l_{1,1} & l_{1,2} & \cdots & l_{1,j-1} & l_{1,j} \\ l_{2,1} & l_{2,2} & \cdots & l_{2,j-1} & l_{2,j} \\ \vdots & \vdots & \vdots & \vdots & \vdots \\ l_{k-1,1} & l_{k-1,2} & \cdots & l_{k-1,j-1} & l_{k-1,j} \\ l_{k,1} & l_{k,2} & \cdots & l_{k,j-1} & l_{k,j} \end{bmatrix}.$$
(3.11)

where tt_n (n = 1,...,N) are the travel-times previously determined for each ray, $l_{k,j}$ is a matrix of the path length of the k-th ray in the j-th grid cell where k = 1,...,N; j = 1,...,M.

This problem formulation is solved in a linear least-squares context $d_f = G \cdot m + e$, where d_f is the travel-time vector per frequency, G is the design matrix relating slowness with the travel-times, m contains the model parameters, and e is the noise contaminating the measurements. For each frequency value, we built the $N \times M$ design matrix G (of full rank equal to N), where N represents the number of ray paths found for a certain frequency (Fig. 3.10) and M is the number of grid cells. The number of nonzero elements of the design matrix is dependent on the number of ray paths previously selected. The model parameters are estimated independently for each f_i .

As we are interested in slowness perturbation with respect to a background model, we first remove the velocity at each frequency by:

$$\Delta d_f = d_f - G_f \cdot s_{0,f},\tag{3.12}$$

where Δd are the travel-time estimated with respect to the reference velocity at frequency f (the reference slowness $s_{0,f}$). The reference velocity we use in this formula is not the velocity derived from the dispersion curve but the average velocity from the picked travel times.

3.4.1. Tikhonov Regularization

We regularize the ill-conditioned inversion problem by adding a new term to the least squares problem (Tikhonov 1963):

$$min_x\{||d - Gm||^2 + \mu||m||^2\},$$
 (3.13)

where $\mu \ge 0$ is the regularisation parameter, also known as the damping factor. The accuracy of the inversion procedure is directly affected by the choice of the regularisation parameter (Kusche and Klees 2002). If μ is too small, the solution is contaminated by noise as it overfits d, if μ is too large, the solution becomes smooth and it is a poor approximation of m. To choose a reliable regularisation parameter, we use the cross-validation methodology (Golub et al. 1979). A different regularisation parameter is selected per frequency value as the ray paths per frequency are inverted independently.

3.4.2. Checkerboard Tests

We perform a checkerboard sensitivity test (Lévěque et al. 1993) to check the ability of our inversion methodology to solve the geometric details for the chosen grid size of 4 km. First, we create a regular 2-D checkerboard of opposite polarities with perturbations over an 8 km grid and with velocity perturbations in the same range as the data. Then we simulate the same number and combination of ray-paths as used for the tomographic inversion. We also add noise to the modelled surface wave arrivals to simulate realistic errors during travel time picking. Finally, we invert the simulated data applying Tikhonov regularization with the previously estimated regularisation parameter (μ) per frequency. Fig. 3.12 shows the simulated checkerboard velocity model and the tomographic results. The simulated inversion can fully recover the principal geometry of the perturbed model, especially for frequency values used in this study (0.16–0.38 Hz), indicating a good number of simulated ray-paths and distribution of receivers. Because we impose a regularisation parameter that decreases the variability of the velocity values, quantitatively, the inversion result does not fully describe expected velocity variations.

3.5. Results

3.5.1. Surface-wave Tomography

Using Tikhonov regularisation, we invert the picked travel times of the retrieved ballistic Rayleigh waves for phase-velocity variations at depth. Prior to the depth inversion, we first invert each frequency independently over a 4 by 4 km grid, using grid cells crossed by at least six ray paths. We choose this resolution based on a compromise

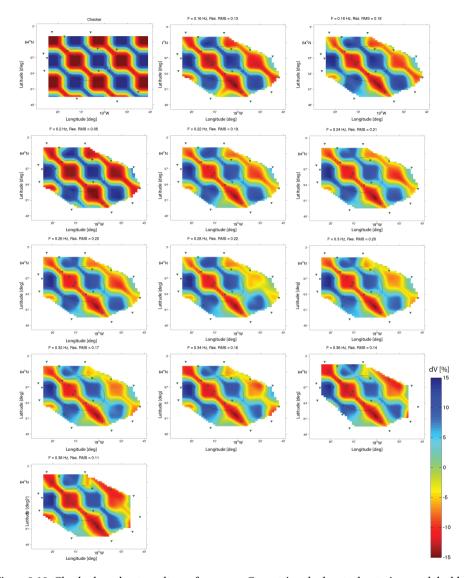


Figure 3.12: Checkerboard test results per frequency. Green triangles locate the stations and the black line the caldera, both at the surface.

between a desirable high spatial resolution and a threshold of at least five ray-paths per grid cell. Fig. 3.13 shows the Rayleigh wave phase-velocity variation maps for different frequencies.

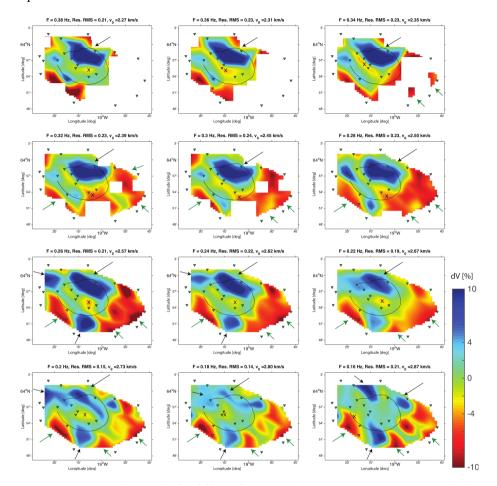


Figure 3.13: Tomographic results for different frequency values representing variations of velocity with respect to a reference velocity. Blue and red denote higher and lower velocity, respectively. The black line indicates the caldera outline, the green inverted triangles are the location of the seismic stations at the surface. The green and black arrows indicate low-velocity and high-velocity features, respectively. The crosses locate the areas of lower velocities within the caldera outline. White areas locate grid cells where the number of ray-paths is not enough to estimate a constrained velocity variation.

The inverted results show velocity variations that reach up to 15% from the average velocity for each frequency. For display purposes, we plot the results on a scale of -10% to 10% to highlight anomalies greater than 5% deviation from the mean velocity. The velocity deviations vary remarkably smoothly as a function of frequency even though each frequency is inverted individually, indicating solid travel-time picks and stable

3.5. Results 57

inversion results. In the current inversion implementation we did not take into account anisotropic variations nor ray bending for phase-velocity estimation; therefore, the results could eventually be improved.

3.5.2. 3D S-wave Velocity

With the following procedure, we produce a 3-D shear-velocity model (Fig. 3.14 displayed with variations between -15% and 15%) from the phase-velocity maps. Per grid cell, we build a dispersion curve using the phase velocity estimated from the 2-D tomographic results at different frequencies (Shapiro et al. 2004). We individually invert a total of ~ 50 dispersion curves using the neighbourhood algorithm (NA) in a Monte Carlo approach, described by Sambridge (1999a) (Sambridge (1999b)a and Sambridge (1999a)b), later implemented and improved by Wathelet (2008).

The approach follows a stochastic searching method assuming that the dispersion characteristics of surface waves are mostly dependent on layer parametrization (depth, thickness, and densities) and body-wave velocities (ν_p and ν_s linked by Poisson ratio). The optimum model is the velocity depth model for which the forward-modelled dispersion curve has a minimum misfit with the measured dispersion curve (Wathelet et al. 2004).

As a result of the smoothness in the forward computation of the dispersion curves, it is difficult to identify sharp velocity jumps, e.g., when stiff rocks are juxtaposed with low-velocity zones (LVZ) at depth. To address the identification of complex boundaries, we tried to detect different layers by first parametrising the model in three layers without fixing depths. The boundary layer does not differ much between adjacent grid cells, but changes between grid cells where frequency-dependent tomographic results (Fig. 3.13) show contrast between velocity variations. This confirms irregular boundary layers within the area of interest.

We parametrise our model into five fixed horizontal layers, allowing the velocities $v_{\rm p}$ and $v_{\rm s}$ to change with depth within these layers. We assign an ample interval for the $v_{\rm p}$ input velocities (~4000 m/s between the lower and upper bounds) allowing a higher range of solutions and because the presence of rigid rocks can influence v_s as reported by Wathelet (2008). We assumed a fixed density of $2600 kg/m^3$, a varying Poisson ratio between 0.24 and 0.28, and estimated the S-wave velocities from two independent runs with different boundary layers. We run the model first for depth limits between 1.5kmand 5.5km and then for depth limits between 2km and 6km, both with 1km vertical resolution. For each of the runs, the methodology we follow is similar to that of Kao et al. (2013) and Mordret et al. (2014). Per grid cell, from a total of ~30000 models, we choose the depth model with minimum misfit. In Fig. 3.14 we show the variations of the S-wave velocity with reference to a 1-D velocity model (the mean of the estimated velocities per depth) for the two model runs (a, c, e, g and i are the result of the first run and b, d, f, h, j of the second run). The reference 1D velocity model (asterisks in Fig. 3.14 k) is the average of all grid cell inverted models. To check the quality of the reference velocity model, we compare two other 1D S-wave velocity models. The first is the model with the minimum misfit using all the dispersion curves as targets with the corresponding parameter space and inverting for a single average dispersion curve (circles in Fig. 3.14 k). The second is the 1D velocity model obtained by Lippitsch et al.

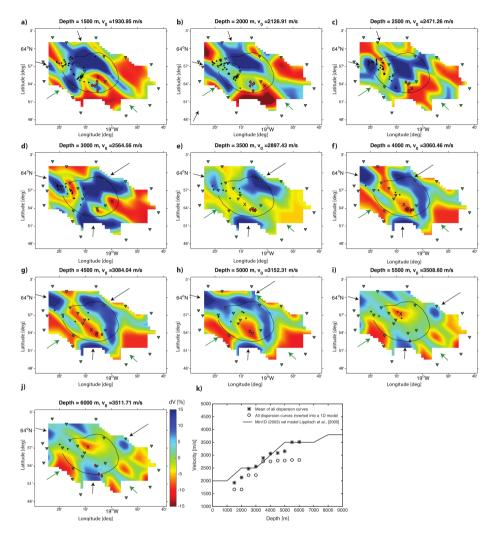


Figure 3.14: 3-D shear velocity model of the waves velocity variations w.r.t. an average 1-D velocity model at depth. Blue and red denote high and low velocity, respectively. The filled black line represents the caldera outline at the surface, the green inverted triangles are the location of the seismic stations at the surface. Black dots represent high-frequency earthquakes, while red diamonds low-frequency earthquakes. The green and black arrows indicate low-velocity and high-velocity features, respectively. Figure k) shows the average velocity profiles at depth from three sources. The average of all the grid-cells per depth, which is the reference average for which the anomalies are plotted (asterisks). A velocity model derived using all the dispersion curves and the adopted parametrization (circles). And the 1D S-wave velocity profile from Lippitsch et al. (2005) over Torfajökull.

3.5. Results 59

(2005) for the same area with a different seismic campaign (Fig. 3.14k identified by the black line). The first shows no difference between the two parameter spaces, meaning that the model derived with the minimum misfit using all the dispersion curves as targets is exactly the same for the two model runs. This model also has estimated velocities lower than the mean of all the dispersion curves for all depths. The adopted reference velocity model (Fig. 3.14k identified by asterisks) shows a remarkable fit for most depths with the 1D model of Lippitsch et al. (2005).

Fig. 3.15a and b depict the standard deviation of the estimated velocity of the best 10% models at each grid cell. The maximum velocity standard deviation detected is of 146 m/s at 2.5 km depth (Fig. 3.15a) in an isolated pixel on the periphery of the model. This corresponds to \sim 5 % from the mean velocity at the same depth. Most of the standard deviation values are on the order of 20 m/s, approximately between \sim 0.5 % and \sim 1 % depending on the analysed depths. The standard deviation from the best In the same figure we show an example of a dispersion curve with the corresponding 30000 models misfits and the final selected model with the minimum misfit. The dispersion curve that serves as an example is the grid cell identified in a) by a red vertical line.

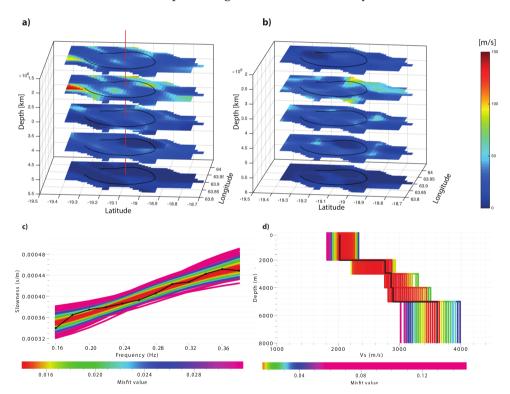


Figure 3.15: a) and b) standard deviation of the velocity estimated from the 10% models with lowest misfit for the depths $[1.5\,\mathrm{km},\,2.5\,\mathrm{km},\,3.5\,\mathrm{km},\,4.5\,\mathrm{km},\,5.5\,\mathrm{km}]$ and $[2\,\mathrm{km},\,3\,\mathrm{km},\,4\,\mathrm{km},\,5\,\mathrm{km},\,6\,\mathrm{km}]$, respectively. c) and d) shows the input dispersion curve and depth velocity of a grid-cell (red line in a) with the corresponding 30000 models and misfit. The black line in c) and d) locates the model with minimum misfit.

3.6. Discussion

3.6.1. Quality Control

The quality of tomographic inversion depends on the three fundamental properties of the data and their interdependence: the noise in the observations, the seismic network configuration, and the model resolution.

The way we deal with noisy observations is by rejecting them throughout the whole processing chain. We selected the microseismic frequency band with the highest SNR. After the cross-correlation, we make sure that we have used high-amplitude microseisms noise to retrieve coherent causal or acausal surface waves. Using the most reliable waveforms from the cross-correlation, we perform the travel-time picking avoiding too long or too short intra-station distances (Eq. 3.8 and Eq. 3.9). First, we compute an average dispersions curve before picking station-pair dispersion curves. In an initial approach, we use MASW to deal with a suboptimal seismic network configuration towards seismic tomography applications (our array is slightly skewed in the NW-SE direction), as well as to address local noise sources, scattered waves and correct phaseambiguity estimation. In a second approach, we use MASW results to guide the timedomain picking. As we see a degradation of the dispersion measurements related to the spacing of the array above and below certain frequencies, we narrow the frequency band used from 0.1-0.4 Hz to 0.14-0.38 Hz. After the travel-time picking, we only select the velocity variations within 2σ from the mean to avoid noisier observations and picks made on an erroneous cycle. During the travel-time picking process, we estimate the surface-wave phase velocity term from the estimated pickings instead of assuming the derived $\pi/4$ value (Snieder 2004). In this way, we have a measure to validate, using all the travel times per frequency, how the estimation reproduces the expected $\pi/4$ phase shift. We remove the frequency values for which this estimation is far from the expected value, for example for the travel-times measured at 0.14 Hz.

The resolution of tomographic results depends primarily on the wavelength of the signal (v/f where v is the velocity of the seismic wave). At higher frequencies, the modelled results extract more detail, whereas at lower frequencies, the results are smoother. The regularisation during the inversion automatically deals with this, as we can see that the results for lower frequencies are more smeared. The other parameter on which the resolution is dependent is the number of ray-paths covering a particular area. We used a regular grid of 4 km, and the ray coverage was more than sufficient to invert the slowness for this resolution, as shown by the checkerboard test. The ray-path count is much higher within the caldera outline, indicating that the estimation is more redundant. Due to the number of ray paths, the degradation of the dispersion measurements and the performance of the checkerboard for different depths, we decided to remove the edge frequencies (0.12 Hz, 0.14 Hz, and 0.40 Hz) for the inversion to S-wave velocities as we have less confidence in the inverted results for these frequencies.

Because we are dealing with ambient noise interferometry, another component can worsen the quality of the travel-time estimation before inversion — the direction of the ambient noise with respect to the orientation of a station-pair combination. We addressed the topic of surface wave directionality in sec. 3.2.4, where it does not seem to be an issue for this data set.

3.7. Conclusions 61

3.7. Conclusions

We applied surface-wave tomography to Rayleigh waves estimated with ambient noise seismic interferometry to the image of the subsurface of Torfajökull volcano. We applied this methodology using only 100 days of ambient noise data but with an approach that relies on a solid quality selection of inter-station travel times and reliable phase-velocity estimation from retrieved surface waves. We removed frequencies for which the best-fitting phase term of the virtual source does not come close to a physical source term. We successfully detected velocity variations between approximately 1.5 km and 6 km depth, with a horizontal resolution of 4 km.

North-east along the caldera outline, we identified high-velocity structures that might correspond to cold (rhyolitic) dikes. Outside the caldera, to the southwest and east, there are low-velocity anomalies that may indicate the presence of warm bodies. Although we detect low-velocity anomalies inside the caldera deeper than 4 km depth, the low anomalies outside the volcano caldera are more prominent. As none of the identified features resembles a hot, established magma chamber beneath the caldera, we suggest that if a crustal magma chamber does exist beneath Torfajökull's caldera, it must be located below 6 km depth. However, the shallowest part of it may, however, start from 3.5 km depth onward, as suggested by the detected low-velocity anomalies inside the volcano caldera. Our results suggest new opportunities for applying ambient-noise seismic interferometry even to short acquisition-time campaigns, especially in oceannoise-prone areas like Iceland.

3

4

3D S-wave velocity imaging of Reykjanes Peninsula high-enthalpy geothermal fields with ambient-noise tomography

In addition to MPS characterisation of active volcanoes, ambient noise techniques are attractive for geothermal applications, which require economic subsurface characterisation and monitoring while avoiding shooting. This attractiveness holds especially in areas like Iceland, where the microseism illumination seems excellent for ambient noise applications, as shown in the previous chapter. Although ambient noise correlation techniques have been recently explored for geothermal operations, ambient noise tomography is still poorly used at the operational level because of resolution limitations and imaging depths. In this chapter, I produce a 3D S-wave tomographic image over the western Reykjanes Peninsula high-enthalpy geothermal fields using 30 broadband stations operating for approximately one-and-a-half years.

4.1. Introduction

The seismic tomographic image obtained in the course of this chapter was estimated from a seismic campaign developed under the European-funded program Integrated Methods for Advanced Geothermal Exploration (IMAGE). The Jousset et al. (2017) tomographic study confirms the previous results of Bjarnason et al. (1993) and of Tryggvason et al. (2002) in the same area with enhanced details around well locations. The authors interpret the low-ratio anomaly of compressional- over shear-velocity as being due to the absence of a sizeable magmatic body at the tip of Reykjanes Peninsula, which was confirmed by Friðleifsson et al. (2018).

The unexpected drilling into a magma source in Krafla in 2009 highlighted the need to explore high-resolution imaging techniques as a complement to current measurement methods and to improve the existing ones. Seismic tomographic techniques and recent advances using ambient noise-based methodologies can play a role in assessing the necessary depth and resolution information and in constraining other geophysical estimations. In this regard, ambient noise seismic interferometry (ANSI) techniques can offer additional advantages by avoiding the cost of active seismic methods (which makes ANSI techniques economically more attractive) and circumventing limitations

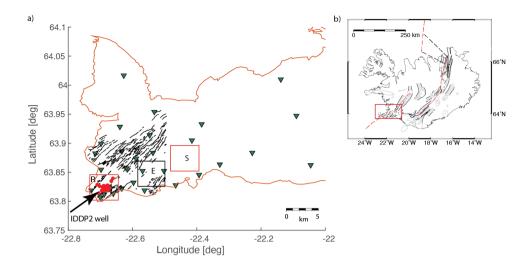


Figure 4.1: Map of WRP seismic campaign, faults, fractures and location in Iceland. a) WRP coastal outline. The green triangles denote the onshore broadband stations. The red dots identify wellsheads in Reykjanes geothermal fields, and the black lines the identified faults and fractures in the vicinity of the geothermal production areas. The squares locate high temperature areas (mapped by the Icelandic GeoSurvey ISOR (Guðnason 2014)) from west to east, Reykjanes (R), Eldvörp (E), Svartsengi (S), of which the red squares indicate the location of the two existing power plants. b) Icelandic coastal boundary with Reykjanes peninsula within the red rectangle (here repeated for convenience, see legend in Fig. 2.4).

such as the limited number of earthquakes and irregular earthquake distribution. The straightforward data acquisition and theoretical concepts, extended from 1D media (Claerbout 1968) to arbitrarily heterogeneous 3D media by Wapenaar (2004), make ANSI attractive for tomography applications. The ANSI concept relies on a virtual source that is generated at the location of one of the two receivers by cross-correlation and summation of (noise) recordings from surrounding ambient noise sources. The tomographic results are subsequently derived from Rayleigh (or Love) waves retrieved between the virtual sources and the receivers. The number of applications of ambient noise tomography (ANT) studies has increased in recent years, especially in Iceland ((Obermann et al. 2016; Benediktsdóttir et al. 2017; Jeddi et al. 2017; Green et al. 2017) and chapter 3 in this thesis). Along with the direct advantage of characterising the subsurface within the depth range of Icelandic geothermal operations, ANT can contribute to constraining other geophysical measurements or interpretations that have previously been acquired over the same area and vice versa. ANT can be used to improve a subsurface image with complementary seismic studies ((Verdel et al. 2016; Blanck et al. 2019; Jousset et al. 2017)).

In this study, I derive a 3D S-wave velocity tomographic image of the WRP's subsurface by applying ANT to the seismic survey deployed under the IMAGE project framework. On top of assessing the reliability of the retrieved dispersion curves, I devote particular attention to the model resolution given the deployed network configuration

and to obtain results that allow one to constrain other geophysical measurements.

4.2. Data and Methodology

Within the IMAGE project framework, the German Research Center for Geosciences (GFZ Potsdam) and Iceland Geosurvey (ISOR) deployed 54 broadband seismometers on and around the WRP. Of these, 24 are ocean bottom stations (OBS), and 30 are seismometers placed onshore ((Blanck et al. 2019; Jousset et al. 2017)). The onshore instruments were operating from March 2014, and the OBS's were placed in August 2014 (see Tab. 4.1 for instrument details). All equipment was collected in August 2015. The OBS deployed during the IMAGE project were not used in this study due to a phase shift in the instruments (Weemstra et al. 2016). We used the 30 onshore 3 components seismometers (20 broadband Trillium compact sensors and 10 short-period MarkSensors) with a corner frequency as low as 0.005 Hz and a sampling rate of 200 Hz for a duration of almost one year and five months. We only use the vertical-component displacements and to reduce computation time, we down-sampled the records to 25 samples per second (Nyquist of 12.5 Hz).

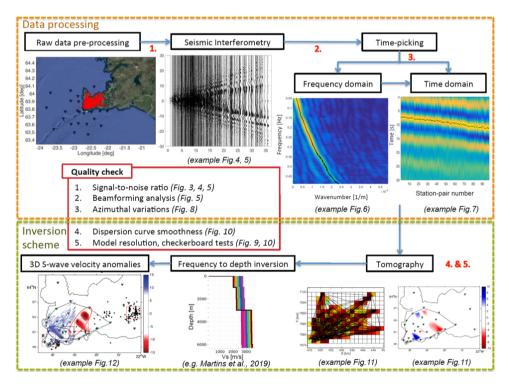


Figure 4.2: Illustrative processing-chain flowchart. Each step is identified with the corresponding reference or figure of this study.

The applied methodology follows the integral processing approach of Martins et al. (2019) and the processing chain is depicted in Fig. 4.2 with a division between the data

processing and inversion schemes (identified in Fig. 4.2 by the orange and green dashed squares, respectively). We divide the processing chain into two steps: data processing of the retrieved surface waves and the inversion procedure. The pre-processing includes deconvolution of the instrument responses, spectral whitening, temporal averaging (Bensen et al. 2007) and frequency filtering. The next step is Empirical Green's Functions (EGF) retrieval with seismic interferometry. The tomographic inversion scheme makes use of the estimated Ballistic Surface Waves (BSW) arrival times from the EGF to estimate frequency-dependent spatial velocity anomalies. Finally, we estimate the depth-dependent 3D S-wave velocity anomalies.

In the rest of this section, we describe the data pre-processing, EGF retrieval, BSW arrival time picking, tomography, and inversion to S-wave velocity. Between these steps, we perform quality checks to ensure that: 1) the signal-to-noise ratio is high enough to allow acceptable surface-wave arrival time estimation. 2) The illumination is sufficiently uniform (taking into account that a lack of causal illumination can be compensated by the acausal part of the cross-correlated signal). 3) The estimated time picks are consistent. 4) Smooth velocity variations between the tomographic frequency dependent results while inverted independently, and 5) We are choosing the most appropriate resolution.

4.2.1. BSW From Cross-correlations

The instrument response is removed by complex deconvolution, after which we apply a spectral domain normalisation (i.e. whitening) (Bensen et al. 2007). We extract coherent EGFs between 0.1 and 0.5 Hz after a spectrogram examination of the ambient noise. This bandwidth is dominated by the microseisms. In the raw spectrogram (Fig. 4.3 a) we identify a higher time-dependent (seasonal) power spectral density (PSD) band around 0.2 Hz. In the same figure, the sharp lines covering the entire frequency spectrum with large PSD mark the occurrence of earthquakes. The seasonal effect with increased PSD from mid-August to April (top Fig. 4.3) occurs due to the higher number of ocean storms and larger waves in autumn and winter (Ardhuin et al. 2011). From the spectrograms we see that there is sufficient energy up to 0.8 Hz.

We computed the cross-correlations per hour and stack the computed cross-correlations using approximately one year and five months of recorded seismic data. Fig. 4.4 shows the resulting EGF's obtained between the 435 unique station pairs, using data between 0.1 and 0.5 Hz. The extracted EGF's are highly coherent and show a non-symmetrical (in amplitude) 'V' shape of the BSW arrivals indicating, as expected, a non-isotropic azimuthal distribution of ambient noise sources (Froment et al. 2010).

Strictly speaking, the retrieved BSWs only coincide with the surface wave part of the Green's function and its time-reversed version under the condition that (i) the receiver pairs are illuminated uniformly from all angles (Wapenaar and Fokkema 2006), (ii) a single surface wave mode dominates the recorded ambient vibrations (Halliday and Curtis 2008), and (iii) the medium is lossless. In practice, and therefore also in our case, these conditions are not fulfilled, leading to deviations of the extracted surface wave velocities from the true surface wave velocities, (e.g., (Tsai 2009; Froment et al. 2010)). If the illumination pattern is sufficiently uniform over an angle-range of at least 180 degrees, it suffices to use only the causal or acausal BSW. It has been shown that this

Table 4.1: IMAGE Seismic Network over Reykjanes Peninsula — broad-band station coordinates placed on Reykjanes Peninsula Seismic Network from IMAGE Project http://www.image-fp7.eu

Station code	Latitude [°N]	Longitude [°N]	Sensor
BER	63,818466	-22,562944	Trillium Comp
EIN	63,856934	-22,619266	Trillium Comp
GEV	63,828094	-22,466464	Trillium Comp
HAH	63,928601	-22,638602	Trillium Comp
HAS	63,882949	-22,715219	Trillium Comp
HOS	63,947675	-22,089654	Trillium Comp
KEF	64,016213	-22,627548	Trillium Comp
KUG	64,009625	-22,139352	Trillium Comp
LFE	63,883868	-22,535548	Trillium Comp
ONG	63,818635	-22,727764	Trillium Comp
PAT	63,953996	-22,532067	Trillium Comp
PRE	63,886239	-22,633336	Trillium Comp
RAH	63,852855	-22,567946	Trillium Comp
RAR	63,825801	-22,678328	Trillium Comp
RET	63,806745	-22,700812	Trillium Comp
SDV	63,821768	-22,633443	Trillium Comp
SKG	63,863371	-22,32921	Trillium Comp
SKH	63,904584	-22,414933	Trillium Comp
STA	63,854302	-22,697544	Trillium Comp
SUH	63,852128	-22,502155	Trillium Comp
ARN	63,862844	-22,04607	Mark sensor
HOP	63,845073	-22,39242	Mark sensor
KHR	63,832367	-22,596432	Mark sensor
KRV	63,812744	-22,660527	Mark sensor
MER	63,883236	-22,228253	Mark sensor
NEW	63,932983	-22,385217	Mark sensor
SKF	63,811912	-22,687761	Mark sensor
STF	63,913445	-22,547067	Mark sensor
STK	63,899571	-22,697866	Mark sensor
VSR	63,873686	-22,588137	Mark sensor

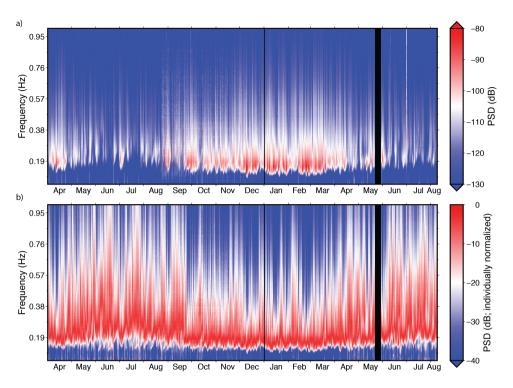


Figure 4.3: Power spectral density (PSD) of the recordings (April 2014 - August 2015) by the station EIN located in the centre of the seismic network. Power spectra are averaged over four hours and 1.38×10^{-3} Hz. a) shows the (non-normalized) PSD and b) the power spectra individually normalized (i.e., with respect to the maximum power in a four-hour period). Black bars indicate no data acquisition.

still allows us to obtain meaningful tomographic (surface wave) images (e.g., (Shapiro et al. 2005b; De Ridder et al. 2015)).

Fig. 4.5 a), b) and c) show three of the filtered EGFs around 0.18 Hz, 0.28 Hz and 0.38 Hz, respectively, and cross-correlations filtered with a small frequency window around specified frequency values (± 0.01 Hz). The coherent 'V'-shaped wave pattern of the BSW indicates that it is well possible to pick arrival times. From Fig. 4.5, we can recognise that lower frequencies travel faster. Moreover, it can be seen that at short interstation distances there is interference between the BSW at causal and acausal times.

We estimate the azimuthal directions of the illumination, using a beamforming analysis applied to the cross-correlation results (Ruigrok et al. 2017). Fig. 4.5 shows the beamforming results (d, e and f) for three frequency bands covering the highest SNR of the BSW bandwidth [0.16,0.22], [0.22,0.32] and [0.32,0.44], respectively. Persistent BSW arrive within most directions of three azimuthal quadrants, between 90° and 360°. In addition to the backazimuth, the beamforming also yields the horizontal ray parameter (inverse of the velocity for surface waves) of the incoming waves.

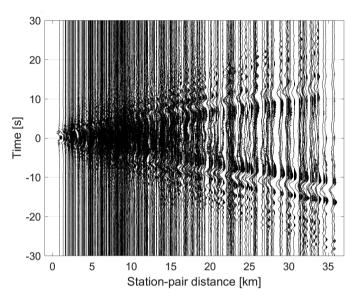


Figure 4.4: EGF with ambient noise seismic interferometry applied to vertical-component data. Each seismic trace corresponds to a station-pair combination ordered by interstation distance. Forming unique station pairs with 30 broad-band stations results in 435 seismograms. Approximately 1.5 years of data Fig. 4.3 was used between 0.1 and 0.5 Hz.

The beamforming results indicate that no station pair should be dropped because of the lack of illumination. The quadrant lacking surface wave arrivals (between 0° and 90°) can be compensated for by the opposite quadrant (between 180° and 270°). These results are in agreement with similar analyses in Iceland for the three analysed frequency bands (Stutzmann et al. 2012; Martins et al. 2019).

4.2.2. Surface-wave Phase Velocity Picking

The high coherence of the BSW between adjacent inter-station distances (Fig. 4.4) allows us to estimate well the timing at local maxima of the correlation waveform (considered to be the correct phase cycle). To obtain individual (i.e. per station pair) phase-velocity estimates, we first extract an average phase-velocity dispersion curve for the fundamental mode Rayleigh wave c(f) (where f is frequency) in the frequency domain using the multichannel analysis of surface waves (MASW) algorithm ((Park et al. 1998; Park et al. 1999)). The average dispersion curve as a function of frequency (Fig. 4.6) serves as further guide to avoid phase cycle jumps in the phase picking of individual frequencies (f_i) with a short interval around f_i (where $f_i \in [0.1, 0.5]$ Hz). Realistic velocities are only estimated for frequencies higher than 0.14 Hz.

Fig. 4.6 shows both MASW picking and the average phase velocity dispersion curve (left and right panels, respectively). On top of the average phase velocity, we plot the resulting phase velocity if different cycles were to be picked (green, red, and black asterisks Fig. 4.6 right side). Selecting a correct cycle is straightforward with the MASW

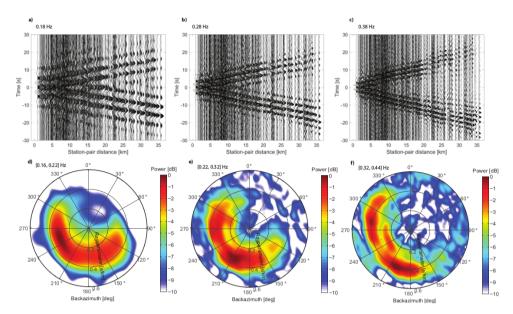


Figure 4.5: EGF for 3 frequency bands (top) and corresponding illumination (bottom). a), b) and c) represent the EGF after whitening and frequency filtering around (± 0.01 Hz) 0.18, 0.28 and 0.38 Hz, respectively. d), e) and f) represent the beamforming results for three frequency bandwidths covering the highest SNR of the BSW, bandwidth [0.16, 0.22], [0.22, 0.32] and [0.32, 0.44], respectively.

velocity reference. For one cycle velocities are obtained that are close to the MASW velocities. Picking the maxima of other cycles yields unrealistic velocities (Fig. 4.6 right).

We impose a threshold to withdraw station pairs with distances where too much destructive interference (or low SNR) occurs, with consequent loss of waveform coherence. Higher coherent cross-correlations allow an accurate time-picking arrival. Considering

$$\lambda_{i,0} = \frac{\nu_{i,0}}{f_i},\tag{4.1}$$

we use the frequency-dependent thresholds estimated by Eq. 3.9 and Eq. 3.8 to define the minimum and the maximum admissible inter-station distances, respectively. The "0" subscript refers to the reference (average) phase velocity obtained from MASW. For each station combination, there is (potentially) a causal and an acausal BSW retrieval. We used the BSW that has the highest amplitude. Fig. 4.7 shows the picks in the time domain. As an additional evaluation, the figure also shows the selected outliers, the values outside the 2σ deviation from the mean.

With estimated time picks for every f_i between 0.1 Hz and 0.5 Hz in steps of 0.02 Hz, we calculate the azimuthal variation of the phase velocity. Azimuthal variations per frequency can be seen as a quality check to detect non-smoothness of timepicks and, in cases of success, together with sufficient illumination can also indicate velocity anisotropy. We observe higher azimuthal velocities between 40 and 80 degrees, approximately in a northeast–southwest direction, and lower velocities between 100 and

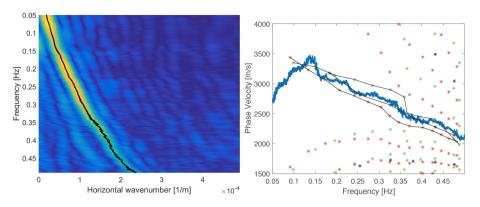


Figure 4.6: Left panel: picking in frequency-wavenumber domain using MASW algorithm. Right panel: blue filled line represents the time domain average dispersion curve as result of MASW picking. The green, red and black asterisks show the travel-time picks (reworked to velocities) of three random station pairs for different phase unwrapping integers. The black lines connecting the asterisks indicate the selected phase velocity curve c(f).

200 degrees (Fig. 4.8). Higher velocities may be correlated with the orientation of the main faults and ridge that cut the WRP (Fig. 4.1), but more research would be required to verify this observation. Azimuthal variations are consistent for all frequencies and have a smooth differential from lower to higher frequencies. These also indicate reliable time picks (the picks are made independently for each f_i). As a reference for frequency-depth correspondence, we add to Fig. 4.8, the depth of maximum sensitivity of the Rayleigh waves, as well as the maximum penetration depth, both as a function of frequency.

4.2.3. Tomography

Seismic tomography is an inversion problem that aims to find a slowness field from travel-time observations in three dimensions. The forward problem can be written as:

$$d = G \cdot m + e, \tag{4.2}$$

where d the data vector (or observations) containing the picked frequency-dependent travel times; m the model vector describing the (unknown) frequency-dependent slowness values of each grid cell; G is the operator matrix containing the ray path lengths of each ray path (first dimension) through each grid cell (second dimension) and; e is a term expressing noise.

We use the same methodology as described in chapter 3, a first-order Tikhonov regularisation (Tikhonov 1963) to regularise this inversion problem, which minimises the double objective function:

$$\min_{m \in \mathbb{R}^n} \{ ||d - Gm||^2 + \mu ||m||^2 \} \tag{4.3}$$

The term $\mu ||m||^2$ denotes the norm of the model, multiplied by the so-called regularisation parameter μ_i . The added objective of minimising the norm of the

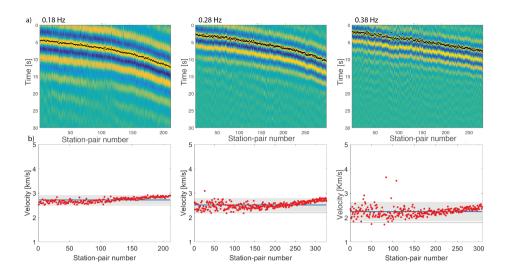


Figure 4.7: a) Cross-correlated results and corresponding time-picks for frequencies (left to right) 0.18, 0.28 and 0.38 Hz. b) Time-picks (reworked to velocities) within 2 sigma velocity variation from the mean for frequencies (left to right) 0.18, 0.28 and 0.38 Hz

estimated parameters avoids over-fitting of the data by enforcing smoothing:

$$\hat{m} = (G^T G + \mu I)^{-1} G^T d, \tag{4.4}$$

where I is the identity matrix and where the superscript T denotes the transpose of a matrix. We use the cross-validation methodology (Golub et al. 1979) to choose a regularisation parameter (μ) per frequency value (f_i) . For each frequency, we start by removing one observation tt_j where tt represents the travel-time between two stations. Then we use Eq. (4.4) to fit a solution without the removed observation (\hat{m}_j) . We predict the neglected travel time using the resolved m_j and compare it with the dropped observation itself: $r_j = d_j - G_j.\hat{m}_j$, where G_i lacks the row associated with the station couple j. We perform this for all observations and sum the squares of the residuals to check the robustness of μ_i . We repeat this for multiple μ and select the μ_i that minimises $P = \frac{1}{n} \sum_{j=1}^n (G_j \hat{m}_j - d_j)^2$, where n is the number of observations, i.e., the number of station couples for which the phase velocity was estimated.

The linear tomographic inversion is repeated for different frequencies to produce phase-velocity maps. The frequency can be approximated to depth using the theoretical relations in Xia et al. (1999) and Haney and Tsai (2015) (Fig. 4.8 right). However, for a more accurate frequency-depth conversion it is advised to perform a second inversion using the Rayleigh wave sensitivity kernels (Zhou et al. 2004). This method is described in sec. 4.2.5. As the ray paths per frequency are inverted independently, we also estimate a different regularisation parameter per frequency value, μ_i and $f_i \in [0.18, 0.44]$ with 0.02 Hz steps. Fig. 4.9 shows the tomographic results for each frequency

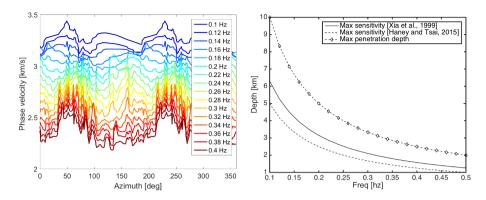


Figure 4.8: Left: Azimuthal phase velocity per frequency. Right: Estimate of the depth of maximum sensitivity as function of frequency by both Xia et al. (1999) and Haney and Tsai (2015) theoretical relations and the maximum penetration depth also as function of frequency.

(steps of 0.02 Hz) used for the inversion from frequency to depth. As can be observed, the anomalies identified for each frequency are smooth compared to the adjacent frequencies. Considering that each frequency is inverted independently, the observed smoothness reinforces the reliability of the tomographic results.

4.2.4. Checkerboard Resolution

An adequate resolution of the model can help identify the geometries of subsurface anomalies, which is relevant for subsurface characterisation and geothermal purposes. We used checkerboard forward modelling to test the ability of the seismic network geometric coverage to reproduce a simulated checker for each of the tested resolutions versus anomaly size. We tested combinations of spatial resolutions (ranging from 1 to 4 km), and size of simulated perturbations (with perturbation sizes ranging from 2 to 6 km). As the number and spatial distribution of the ray paths changes with frequency, we reproduce a checkerboard for each frequency f_i . Similarly to the procedure for the field-data inversion, the checkerboard inversion is done independently for each f_i using the estimated Tikhonov regularisation parameter of the field-data inversion μ_i . In this section, we discuss only the lateral resolution. The depth resolution is briefly discussed in sec. 4.2.5.

Fig. 4.10 shows some of the most relevant combinations. A feature we extract from these figures is the capability to reproduce the simulated checker inside the area limited by the black polygon. We define the polygon by selecting the areas with lower root mean square error (RMS), where the vertices are locations of seismic stations. The area inside the polygon is trensected by a large number of ray paths with varying orientations for all the analysed frequencies. Although in some areas outside the polygon (especially along the southwest–northeast direction), the number of ray paths suffices to estimate slowness values, the lack of multidirectional sampling prevents accurate retrieval of the velocity structure. The poor performance in reproducing the checker outside the polygon is due to the broad-band seismic network configuration. Based on these results,

we drop grid cells outside the polygon for further tomography comparison between resolutions. For the frequency-to-depth inversion we keep the grid cells outside the polygon if there are enough frequency values to perform the inversion. In Fig. 4.10 results are shown for 0.18, 0.28 and 0.38 Hz as sampled examples from the used bandwidth. However, we independently invert all frequencies from 0.18 Hz to 0.44 Hz with a spacing of 0.02 Hz and use all of these frequencies for further inversion to depth.

The regularisation parameter (μ_i) can also be a measure of how well the regularisation fits the data given the noise. A small μ_i can indicate that the noise contaminates the solution as it overfits d (meaning that nearly no regularisation is applied), and a high μ_i can increase the smoothness of the solution and indicate a possible (not reasonable) estimation of m. Fig. 4.11 shows the variation of the regularisation parameter as a function of resolution and frequency.

As higher resolutions consistently result in lower regularisation parameters for all frequencies, we divide the regularization parameter (dx) by the corresponding spatial resolution to provide a fair comparison $(\frac{\mu_i}{dx})$ with $1 \le dx \le 4$ km).

We see that there are no large discrepancies between the estimated regularisation parameters at the same frequencies for different resolutions (when normalised by the spatial resolution of each parameter). Nonetheless, between 0.2 Hz and 0.34 Hz, the preferred regularisation parameter is approximately double the value derived from frequencies between 0.16 and 0.18 Hz, and 0.36 and 0.44 Hz. The estimated regularisation parameter seems to be higher for the frequency interval with better quality SNR and a larger number of ray path coverage.

We invert to frequency-dependent Rayleigh wave velocity dispersion curves for different resolutions (1, 2, 3 and 4 km) which we depict in Fig. 4.11 b. Each line represents the tomographic result for each grid cell with estimated velocities for different grid cell sizes (1 to 4 km). The dispersion curves are smooth for almost all frequencies, with the exception of a few grid cells for 1 and 2 km resolution. In theory, if the ray-path coverage was the same for each frequency, we would expect the regularization parameters to be the same for all frequencies, indicating that the suitability of the data for use in this inversion problem is equivalent between frequencies. The regularization parameter with the lowest standard deviation is the one of 1~km resolution. From Fig. 4.11 we observe that the depth-dependent velocity estimation using the 3 km resolution is the higher resolution with monotonically decreasing dispersion curves, a requirement for phase velocities (Liu et al. 1976). The depth-dependent velocities for 1 km resolution also seem less noisy, with only a few dispersion curves that do not monotonically decrease.

4.2.5. Depth Velocity Estimation

We estimate the depth-dependent S-wave velocity tomography using the methodology of Wathelet (2008), an improved implementation of the neighbourhood algorithm (NA) described by Sambridge (1999a) and Sambridge (1999b). This estimation is another illposed problem, as it relies on the inversion of smooth dispersion curves into abrupt depth-dependent velocity changes, imposed by a given depth parametrisation. For each estimated dispersion curve (each grid cell) we run ~30000 inversions from which we extract the best model with minimum misfit. We run the models to calculate the S-wave velocity at five fixed horizontal layers, ranging from 1000 to 6000 m depth to achieve 1 km

4.3. Results 75

resolution depth. We assume a Poisson ratio that linearly varies with depth between 0.24 and 0.28 and a fixed density of $2600 \ kg/m^3$.

4.3. Results

We use the fundamental mode Rayleigh wave arrival time produced by ANSI in a tomographic inversion scheme to obtain frequency-dependent velocities. Fig. 4.12 depicts the results of the tomography inversion for the four grid cell tested resolutions (1 to 4 km). Positive and negative anomalies are estimated from an inverted average velocity V_0 per frequency derived from the tomographic inversion. To facilitate the comparison of resolution results in Fig. 4.12 we show two of the 14 inverted phase-velocity maps (from 0.18 Hz to 0.44 Hz with a 0.02 Hz spacing).

We retrieve velocity anomalies with variations with maxima around 15% from an estimated average velocity V_0 . In Fig. 4.12 these variations are plotted between -10% and 10% to facilitate visualisation. All the variations above 5% are highlighted and compared between resolutions. We observe that the location of the main anomalies does not differ much between resolutions within the same frequencies (see red and blue circles in Fig. 4.12), even though higher resolutions (1 km) detect smaller anomalies which lower-resolution grid cells fail to recognise (3 and 4 km) (see sec. 4.2.4 and sec. 4.4.1 for more details). The root mean square error (RMS), measures of imperfections between the fit of the estimator and the data, which is lower in the tomographic results with 1 km resolution indicating a better fit to the data. The similarity of anomaly locations between different resolutions is especially interesting considering that each of the sub-figures is inverted independently (with a single design matrix G and regularisation parameter for each frequency value f_i as described in sec. 4.2.3).

A comparison between both 1 km and 3 km resolution (the resolutions with smoother dispersion curves) allows us to do an additional independent check on the inversion to depth performance while trying to retrieve a higher horizontal spatial resolution. In Fig. 4.13 we show the depth-dependent S-wave velocity in a 3D field estimated through the procedure described in sec. 4.2.5. The velocity variations are shown with respect to the average dispersion of the inverted results at each depth. We identified low- and high-velocity anomalies with matching locations between the 1 km and 3 km resolutions. The red and blue circles show the locations with good matches for both resolutions and the red and blue arrows in Fig. 4.13 identify the locations where the match between the anomalies using 1 and 3 km resolution is not good. Most of the seismicity indicated in Fig. 4.12 occurred to the east of the investigated area.

4.4. Discussion

4.4.1. Resolution

The spatial resolution of the tomography is determined by location, the number of seismic stations (grid spacing and seismic network aperture as a function of azimuth) and the frequency content of the data. These parameters define the number of possible ray paths that cross each grid cell and how well the ray paths are sampling each cell area. Additionally, frequency-dependent interstation distance filtering (see sec. 4.2.2 for details), adds a relation between the highest achievable resolution and frequency

bandwidth. Higher resolutions will require shorter inter-station distances for higher frequencies while larger inter-station distances for lower frequencies. The effect on the resolution will be the loss of ray coverage at the edge of the seismic network for high frequencies and at the middle of the seismic network for low frequencies.

From the checkerboard tests, it seems reasonable to use 1, 2 or 3 km resolution as the checkers are well reproduced, at least inside the defined polygon. Note that the estimated RMS shown in Fig. 4.10 is maximized as it also takes into account the area outside the polygon, and this bias is the same for all reproduced checkers. We observe that preferable resolutions depend on the size of the simulated checker anomalies. The larger the simulated anomalies, the better the checkerboard test recreates the checker. Based on these findings, we estimate the depth-dependent velocities using the 3 km resolution (which is the higher resolution without noisy dispersion curves), and for 1 km resolution, while dropping out the dispersion curves which are not monotonically decreasing. The choice of inverting for two resolutions allows an additional independent check on the consistency of the inversion from frequency to depth between resolutions.

The 1 km resolution samples a larger area around the Reykjanes geothermal field, which is not possible to detect with coarser resolutions, which is a region of interest given the location of most of the geothermal wells in the peninsula. However, while trying to achieve a higher resolution, the direct-wave approximation is inherently violated, and for resolutions below 3-4 km the quality of the velocity variation estimations may be reduced. This implies that the direct-wave assumption only holds if the wavelength of the waves is larger than the scale of the medium heterogeneities. Although the observed mismatch between both resolutions (arrows in Fig. 4.13) could be due to the anomaly size (the resolution should be higher than twice the anomaly size), this would also only hold if the direct wave approximation did not play a role. Implications on the deterioration of the tomographic results for resolutions below 3 km would need further research, which is outside of the scope of this study. Therefore, we are careful to interpret the 1 km resolution results and focus our interpretation on the 3 km resolution tomographic image.

4.4.2. Insights on the Geothermal Fields

The retrieved S-wave velocity variations can occur as a result of wave propagation through different geological media, specific tectonic features or rock state (solid, melting or partial melting). Conditions such as crack alignment (isotropic or anisotropic fault swarms), composition (e.g., relation between minerals, shale content, fluid content), saturation (porosity, permeability, water content), pressure and temperature determine the speed of seismic waves (Biot 1956a; Biot 1956b; Gassmann 1951).

The main contribution due to effective pressure can be observed in Fig. 4.13, the deeper structures show higher velocities (e.g., mean velocity v_0 at higher depths), since velocity usually increases with effective pressure. However, that is not always the case. Because effective pressure is defined by the difference between the confining pressure and pore pressure, pore pressure determines effective pressure at the same depths. This is under the assumption of the same confining pressure for the same depths, which is not the case for the WRP tectonic setting (see description in sec. 4.1), as expected in a tectonically and magmatically active site. In the study area, there are three zones of fault

4.4. Discussion 77

swarms (Clifton and Kattenhorn 2006): 1. within the Reykjanes (R) geothermal field, 2. within the Eldvörp (E) and Svartsengi (S) geothermal fields 3. North of Reykjanes (R) and Eldvörp (E).

In addition to the aforementioned contributions, in geothermal areas it is well known that alteration in hydrothermal systems, salinity, shale content and water saturation (O'Connell and Budiansky 1974) interfere with wave speed, as well as with changes in the rock state (solid/melting/partial melting). Variations in fluid content and temperature are likely to be the most determining parameters for velocity anomalies in geo- and hydro-thermally active areas (Nakajima et al. 2001b), and while partial melting areas might not exist, inclusions filled with H_2O (Nakajima et al. 2001a) seem reasonable to exist in the Reykjanes Peninsula. Therefore, the present study should be interpreted in conjunction with constraints from other measurements.

The derived velocity anomalies using 3 km resolution do not cover the Reykjanes geothermal field, preventing us from any possible interpretation. With the 1 km resolution, the observed local low-velocity anomalies in the Reykjanes geothermal field match the location of the intensively exploited part of the geothermal reservoir. This could potentially indicate that the observed low-velocity anomalies might be related to a heat source, water inclusion, or both (O'Connell and Budiansky 1974; Mavko 1980). The same location is described by Friðleifsson et al. (2018) as the upflow area targeted by IDDP-2 interpreted as hotter and more permeable. And a resistivity model based on the 3D inversion of MT data (Karlsdóttir et al. 2018) indicates that the IDDP-02 well was drilled into a low resistivity anomaly, which coincides with the low S-wave velocities observed in Fig. 4.13 (red arrow in a to d at the location of the Reykjanes geothermal field). However, we would need to verify the influence of the direct wave assumption for such high resolution to be able to confirm such an interpretation.

We identified low-velocity anomalies that in volcanic areas are usually associated with partially molten magma pockets (or reservoirs depending on their size) or highly fractured conduit systems with possible molten rock (e.g. (Benz et al. 1996; Sudo and Kong 2001; Villasenor et al. 1998)) as interpreted by Nakajima and Hasegawa (2003). These anomalies are present mainly in the high-density fractured area north of Eldvörp field (between 2 and 5 km depth) and at the location of the Svartsengi geothermal field (between 3 to 6 km depth) Fig. 4.13 from e) to g). The geology in this area is composed of post-glacial lavas, with late Pleistocene hyaloclastites at the location of the Svartsengi geothermal field. At the same location of high-temperature thermal areas and highpositive magnetic anomalies (Jakobsson et al. 1978). Given the depth of the Svartsengi anomalies, these could be related with molten or partially molten magma pockets, which may be the heat source of surface geothermal manifestations (e.g., the Blue Lagoon, located within the red square of the Svartsengi geothermal field in Fig. 4.1). In the Eldvörp geothermal field, we do not identify any low-speed anomalies within the studied depths, but north of Eldvörp field we detect low-speed anomalies between 3 to 5 km depth in the area of high fracture density. Franzson (1987) suggests that the dense fissure swarm around Eldvörp provides downflow channels of cold groundwater, while within the central part of the "swarm" an upflow of the hydrothermal system occurs along the same fractures. The derived 3D S-wave could eventually help to support this hypothesis with a detailed comparison with the existing borehole data from the area.

In general, there is an increase in low velocities from west to east, indicating that the temperature may be higher toward the interior of the peninsula. Between 4 and 6 km depth a high-velocity anomaly appears to separate the Reykjanes geothermal field from the remaining fields of the peninsula. The high S-wave velocity structure that might indicate the presence of solidified rocks that have been cooled down possibly because of the proximity of the ocean.

4.4.3. Future Applications

If we could focus on the higher resolution results of ANT, it would be possible to have enough ray-path coverage over the Reykjanes geothermal field and interpret 3D S-wave velocity cross-sections for this geothermal field. Here, as an example, and because the 1 km horizontal resolution results showed consistency with the 3 km resolution, we use the 3D- S-wave velocity field with 1 km resolution results under the strong assumption that the straight-ray approximation holds for the retrieved surface waves. Although the assumption of direct propagation between stations holds for homogeneous media, it may not hold for extreme velocity variations, where the waves may suffer refraction. The practical reason to assume that direct wave propagation still holds for 1 km resolution is to have enough coverage over the Reykjanes geothermal field and to be able to draw possible applications of the methodology over a more studied geothermal field. However, while the authors were conservative in not interpreting the 1 km results for the reasons mentioned above, the derived results in the publication show a remarkable spatial correspondence between the velocity anomalies of 1 km and 3 km resolution results.

The 1 km horizontal and vertical resolution S-wave velocity model is presented in Fig. 4.14 with the corresponding identified cross-sections. The extension of the model goes beyond the polygon for the grid cells with enough frequency values to estimate a velocity-depth profile. In the same figure, we display the identified vertical cross-sections with the NW-SE (Fig. 4.14 a-b) and the SW-NE orientation (Fig. 4.14 c) over the three individual geothermal fields. The longer cross-sections identify the S-wave tomography result along the line of seismometers, outside the defined polygon, but where some of the checkerboard tests could still be reasonably reproduced. In a general view, the derived 3D S-wave velocity model shows higher velocity structures at the southwestern tip of the Peninsula, and lower velocity areas towards the interior of the Peninsula, below the Svartsengi geothermal area and between 3 and 6 km in depth (e.g. Fig. 4.14 c1 and c3). This is generally the case except for the middle of the SW tip of the Reykjanes Peninsula (Fig. 4.14 c1 and c3).

In Fig. 4.14 a, the observed local low-velocity anomalies in the Reykjanes geothermal field match the location of the intensively exploited part of the geothermal reservoir. Such spatial correspondence may indicate that the observed low-velocity anomalies might be related to a heat source, water inclusion, or both (O'Connell and Budiansky 1974; Mavko 1980). The cross sections displayed in Fig. 4.14 (a1 to a3) show the 3D S-wave velocities in the Reykjanes geothermal field from 1 to 6 km depth of the highly explored area. The cross-sections from b1 to b2 cross the Eldvörp (E) geothermal field and b3 to b4 the Svartsengi (S) geothermal field. The cross-sections from c1 to c2 cross the three geothermal fields in the SW-NE direction, and c1 only the Reykjanes

4.5. Conclusions 79

geothermal field (R). For all the displayed cross-sections, we observe velocities lower than outside the locations of surface geothermal manifestations. Immediately outside the central area of geothermal exploration (Fig. 4.14 a4), the detected low-velocity anomalies are no longer present, possibly indicating a colder system.

Surface displacements in the area of the Reykjanes geothermal field estimated from Envisat SAR data show surface subsidence of up to 10~cm, which is correlated with the beginning of production in the field in May 2006 (Keiding et al. 2010a). Parks et al. (2018), used Envisat, TerraSAR-X and GNSS data to estimate the cumulative ground displacements between 2003 and 2016. The estimated locations of the contracting sources and depths correlate well with the low-velocity cavity imaged by ANT. The same holds for the results of Receveur et al. (2018) using more recent deformation data from the Sentinel-1 satellite.

This study shows the potential of ambient noise tomography as a complementary reservoir characterization tool for field operations. From a seismic network design point of view, the performed resolution tests can also elucidate the optimization of seismic station locations by using the methodology of Toledo et al. (2018) extended for ambient noise. Similarly, our results also show potential to complement the interpretation of deformation studies over the same area by (e.g.) i. interpreting how the estimated horizontal displacements of Hreinsdóttir et al. (2001) or 3D surface motion of Gudmundsson et al. (2002) can be observed by spatial changes in S-wave velocity field as a result of shear strain; ii—constraining the solutions on the local sources of man-derived subsidence derived by Keiding et al. (2010b) and Parks et al. (2018)

4.5. Conclusions

We have retrieved surface waves from ambient noise for approximately one year and five months using seismic interferometry and applied tomographic imaging of the subsurface covering the southwestern area of the Reykjanes Peninsula. We tested tomographic inversion with four spatial horizontal resolutions. We further inverted to a depth-dependent S-wave velocity model the tomographic result with the highest resolution and the resolution with more stable dispersion curves (1 km and 3 km, respectively). We detect high S-wave velocity structures that might indicate the presence of old intrusions that are now solidified and stiffer, or cooling-down effects due to ocean proximity. The low S-wave velocity anomalies can be interpreted as pockets of possible partial melt, for which the Vp/Vs ratio could give further insight. We detect S-wave velocity anomalies with variations between -15% and 15% with reference to an estimated average velocity between 2 and 6 km depth with 3 km of lateral resolutions and 1 km of vertical resolution. However, we refrain from interpreting the 1 km resolution tomography as real effects, as the assumption inherent in the straight-ray approximation could cause a deterioration in the quality of the results for higher resolutions (see Fig. 4.14 for an overview of the 1km results cross-sections). Although the seismic network used was not designed for ANT alone, it accommodates different seismic imaging techniques, and the results underline the capabilities of ANSI in Iceland. Furthermore, if the OBS deployed during the IMAGE project could be used, we would be able to extract more subsurface information over a broader area and have complementary constraints as a result of an increased number of ray paths and station covered area.

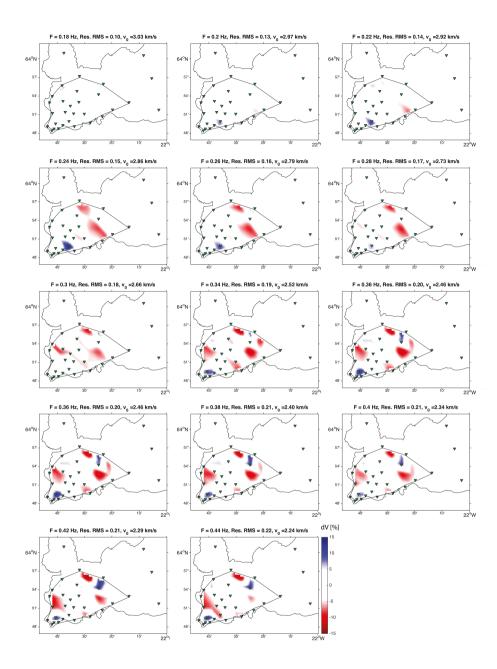


Figure 4.9: Tomographic results of all frequencies for 3 km resolution. The polygon outlines the area where there is enough ray-path coverage 4.10. In this figure the colorscale shows variations from -15% to 15% from the average velocity per frequency. Tomographic results of all frequencies for 3 km resolution. The polygon outlines the area where there is enough ray-path coverage

4.5. Conclusions 81

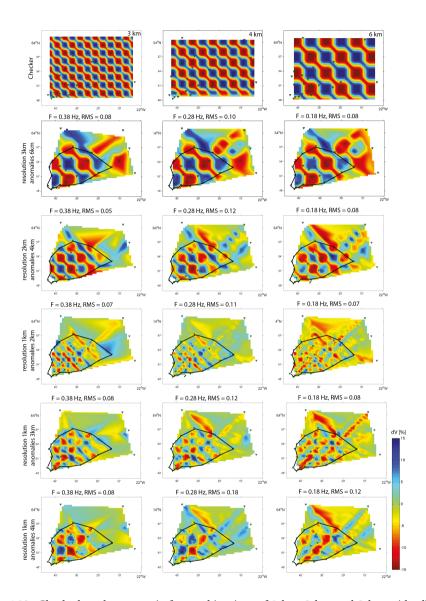


Figure 4.10: Checkerboard test matrix for combinations of 1 km, 2 km and 3 km grid cells and anomalies sizes between 2 and 6 km. The black polygon identifies the area in which the checker is recovered best.

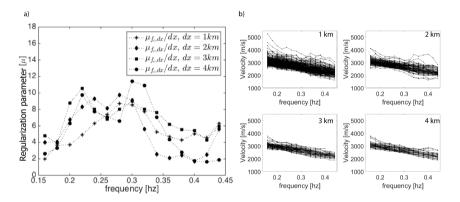


Figure 4.11: Left: Regularisation parameter normalized by the corresponding resolution, as function of frequency. Right: dispersion curves of the inverted surface-wave travel times for the corresponding 1, 2, 3 and 4 km resolutions identified in the left figure.

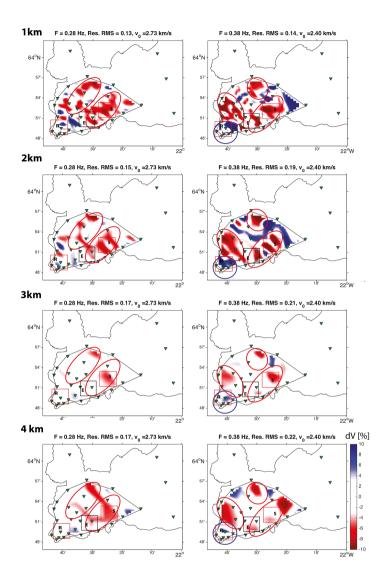


Figure 4.12: Phase-velocity maps after tomographic inversion using 0.28 Hz (left) and 0.38 Hz (right) for the four tested spatial resolutions with edited colour-bar between -10 and 10 percentage deviation from the average velocity (V_0) . The results are interpolated to the same grid cell size for figure comparison. Green triangles identify the seismic stations and the squares show the location of the geothermal fields identified in 4.1. The black polygon outlines the area where there is enough ray-path coverage to better recreate the simulated checkers of Fig. 4.10. Red ellipses identify similar low-velocity anomalies at different resolutions in the same frequency band. Blue circles identify similar high-velocity anomalies at different resolutions in the same frequency band.

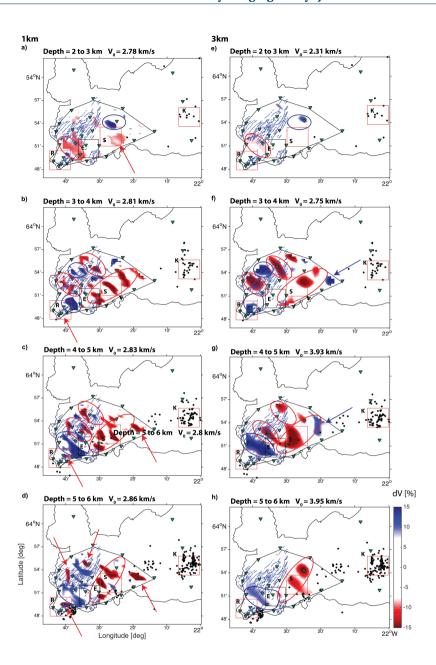


Figure 4.13: 3D S-wave velocity variations [%] from the average velocity (v_0) between 2 and 6 km depth. Spatial resolution tomographic inversion for all the identified depths: 1 km (left) and 3 km (right). Velocity anomalies low(red) to high (blue). Black dots: locations of detected earthquakes from 1993 to 2015 (IMO). Blue lines: fault system within the defined polygon. Green triangles: seismic stations. Squares: geothermal fields (Fig. 4.1). Red circles and arrows: areas where anomalies match between resolutions. Blue circles and arrows: no match is observed.

4.5. Conclusions 85

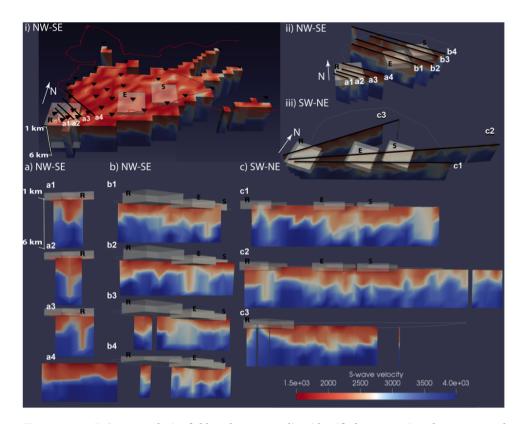


Figure 4.14: 3D S-wave velocity field and corresponding identified cross-sections between 1 and 6 km depth. The model has a 1 km spatial resolution and a 1 km depth resolution. i) General view of the 3D S-wave velocity model extension. The red line delimits the WRP coastal outline, with an inner previously defined polygon also in red. Black triangles indicate the on-shore broadband station locations and the black lines are the cross-sections displayed in a). The cubes denote the high-temperature areas (mapped by ISOR) from west to east, the Reykjanes (R), Eldvörp (E), and Svartsengi (S) geothermal fields. ii) The NW-SE location of the cross-sections displayed in a) and b) and the location of the geothermal fields. iii) The SW-NE location of the cross-sections displayed in c). a, b and c show the cross-sections identified in i, ii and iii and also display the geothermal field whenever the cross-section crosses the geothermal field location.

The Eyjafjallajökull's 2010 post-eruptive deformation and MPS modelling with InSAR, GNSS and seismic constraints

Geodetic measurements that capture volcanic events in action have become valuable in inferring magma movements through magmatic plumbing systems at depth. Eyjaf-jallajökull's 2010 eruption—preceded by ~20 years of unrest— highlights the need for research on the mechanisms behind moderately active volcanoes in Iceland and volcanoes that erupt infrequently. As volcanoes may erupt again, understanding the volcanic plumbing system will not only aid in predicting when unrest will end in a new eruption, but will also pinpoint the location around the volcano where such eruption is likely to occur. In this chapter, I extended the previous analysis of deformation linked to the 2010 Eyjafjallajökull's eruption by using InSAR and GNSS time series measurements over the pre, -co and post-eruptive periods. Because robust source modelling demands mutually coherent observations, I first cross-check between the InSAR and GNSS data sets. Once the consistency is established, I applied a two-step modelling: (i) run a forward model of the latest hypothesised magmatic plumbing system concept; (ii) jointly invert the InSAR and GNSS observations to retrieve the best fit of the co- and post-eruptive magma source.

5.1. Introduction

After a period of quiescence since sill intrusions in 1994 and 1999–2000, the Eyjafjalla-jökull volcano erupted in Spring 2010, causing the largest disruption of air traffic since World War II (Ulfarsson and Unger 2011). The seismicity and surface displacements induced by magma intrusions since mid-2009 culminated in the first eruptive event: an effusive eruption of olivine basaltic andesite lava on 20 March 2010, which took place at Fimmvörðuháls between the Eyjafjallajökull and Mýrdalsjökull glaciers, indicated by the red star in Fig. 5.1. This eruption ended on 12 April 2010. On 14 April 2010, an explosive event of trachyandesite took place under the glacier that covers the central summit caldera/ indicated by the black star in Fig. 5.1. The thick black arrow in the figure shows the location of the lava flow associated with the explosive eruption. The explosive eruption lasted until 22 May, causing a remarkable disruption of air traffic due to the

 \sim 0.27 km³ of tephra expelled by the volcano (equivalent to 0.18 \pm 0.05 km³ of dense rock equivalent (DRE) (Gudmundsson et al. 2012).

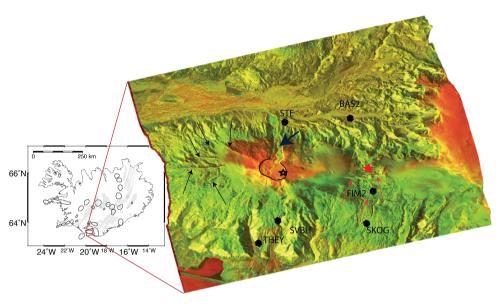


Figure 5.1: Left: Iceland map with an inset overview; the red square marks the zoomed region, the location of the processed area with Eyjafjallajökull volcano. The background shading represents the volcanic systems between the Eurasian and American plates, and the black polygons indicate the volcanic centres (Einarsson 2008). Right: Enlargement of the boxed area showing a multi-temporal RGB composition of two TerraSAR-X amplitude images used in this study. The RGB bands are composed as follows Red= 22/04/2010, Green= 14/05/2010, Blue= 22/04/2010. Two lava fields after the eruption at Fimmvörðuháls mountain (red star) are identified, alongside with few craters at the summit volcano formed after the volcano caldera eruption (black star), the lava flow during the summit eruption (black thick arrow). From this RGB composition, it is also possible to identify the previously mapped (Jakobsson and SP 1979; Magnússon et al. 2012; Einarsson and Hjartardottir 2015) eruptive fissures with a preferential E-W orientation (black arrows) and possible faults around the location of Fimmvörðuháls eruption (red arrows). Black hexagons identify the GNSS stations.

Significant displacements associated with magma movement in the subsurface and seismic events before and during these eruptions are described in (Sigmundsson et al. 2010). The authors used GNSS data and individual interferograms as constraints for the pre-eruptive period and the initial eight days of the explosive eruption. Here, we extend the InSAR/GNSS observations to 16 months covering the pre-, co-, and post-eruptive periods (from June 2009 to September 2010). The TerraSAR-X satellite images have a temporal sampling of 11 days and a spatial resolution of 3 x 3 m. The continuous and semi-continuous GNSS time series cover the same period.

In this chapter, we extend the previous analysis of deformation linked to the 2010 Eyjafjallajökull eruption by using InSAR and GNSS time series measurements over the pre-, co- and post-eruptive periods. Our approach considers recent results from petrological, geochemical, and seismic studies to constrain models of the complex

5.1. Introduction 89

plumbing system in different periods. The following subsections present the preceding unrest and the 2010 eruption, and discuss insights from other disciplines that helped delineate the modelling strategy adopted later in this research.

5.1.1. The 20 years of Unrest

In 1992, seismicity at Eyjafjallajökull volcano increased from previously low activity (Sturkell et al. 2003). In 1994 and 1999, geodetic measurements using dry tilt and GNSS (Sturkell et al. 2003) and conventional InSAR (Pedersen and Sigmundsson 2006) suggested two sill intrusions. Although the two sill intrusions were at approximately the same depth (between 4.5 and 6.5 km), the areal extents and locations of the sources were different, indicating that there were two separate magma compartments. Using InSAR time series analysis, Hooper et al. (2009) refined the investigation of the two deformation episodes (1994 and 1999). By reducing InSAR-related error, the authors were able to constrain the location more accurately with estimated depths of 5.6 ± 0.1 km for the 1994 source and 5.7 ± 0.5 km for the 1999–2000 source. Using GNSS data from 1992 to 2009 Hjaltadóttir et al. (2015) also estimated two sills related to the 1994 and 1999 intrusions, a 4.5 to 5 km deep sill model for the 1994 intrusion and a 5.0 ± 1.3 km deep sill model for the 1999 intrusion.

5.1.2. The 2010 Eruption

The GNSS station THEY (Fig. 5.1) was the first station to show displacements prior to the 2010 eruption, moving 10-12 mm southwards in mid-2009. In December 2009, increased seismicity and GNSS rates suggested deep-sourced magma injection. Single interferograms did not capture these displacements, as the measurements are within the magnitude of the InSAR errors. However, the rate of deformation increased at ≥5mm per day from 4 March until 20 March when a flank eruption opened a 500m fissure at Fimmvörðuháls producing two lava fields (Fig. 5.1). Sigmundsson et al. (2010) explain the observations from December until the end of February and the March pre-eruptive deformation with two sills at different depths, together with a south-east tilted dyke reaching to a few hundred metres or less below the surface (see 5.1 for previously modelled sources). Based on microearthquake locations, Tarasewicz et al. (2012a) suggest several northeast-southwest striking sub-vertical dykes at 2-6 km depth with a lateral extent of~6 km east-west and~3 km north-south preceding the flank eruption. This first eruptive period produced relatively primitive mildly alkaline basalt and continued until 12 April (Sigmarsson et al. 2011a) with no significant deformation until 9 April. The lack of (1) deformation for approximately 20 days while the volcano was still erupting (Sigmundsson et al. 2010) with seismic activity at depth (Tarasewicz et al. 2012a), and (2) relatively primitive erupted basalt (Sigmarsson et al. 2011a), suggested that the magma was flowing directly from the Earth's mantle (or crust/mantle interface) into the crust, feeding the Fimmvörðuháls eruption.

Early in the morning of 14 April, the first explosive eruption started in the summit caldera. This eruption was preceded by a one- and a half-day gap in eruptive activity, an increase in seismic activity, and a new inflation registered at GNSS station STE2. The ice-magma interaction during this occurrence caused the wide dispersal of ash throughout northeastern Europe. The eruption lasted 39 days with a decaying discharge of the

Table 5.1: Magma source models for Eyjafjallajökull associated with first detected unrest (1994) and 2010 eruption.

Date	Technique	Shape	Depth	Estimated
			[km]	volume [10 ⁶ m ³]
1994 ^{a)}	Moment ten-	E–W striking	_	_
· b)	sor	dike		
$1994^{b)}$	InSAR/GNSS	sill	5.5	15
1994 ^{c)}	GNSS	sill	4.5–5	11
$1999^{d)}$	GNSS/Tilt	mogi source	3.5 ± 0.6	_
$1999^{b)}$	InSAR/GNSS	sill	6.5	25
$1999^{c)}$	GNSS	sill	5.5 ± 2	30 ± 7
Until 28/2/2010 ^{e)}	InSAR/GNSS	pre-eruptive: Initial sill opening	4.1–5.5	9–15
2010: Feb–Mar ^{<i>e</i>)}	InSAR/GNSS	pre-eruptive: continued sill opening	4.7–6.0	15–20
2010: 14–12 April ^{e)}	InSAR/GNSS	pre-eruptive: tilted dike	4.6	19-41
2010: 11–22 April ^{e)}	InSAR/GNSS	Deflation: contracting sill	4.2-4.9	-15 to -12
2010: 02–07 May ^{f)}	earthquake location	Deflation: contracting sill	10–15	-
2010: 10 May ^{f)}	earthquake location	seismic swarms as melt escapes from sills	19	-
2010: 15 May ^{f)}	earthquake location	seismic swarms as melt escapes from sills	24	-

 $[\]overline{a^0}$ Dahm and Brandsdóttir (1997); b^0 Pedersen and Sigmundsson (2006); c^0 Hjaltadóttir et al. (2015); d^0 Sturkell et al. (2003); e^0 Sigmundsson et al. (2010); f^1 Tarasewicz et al. (2012b)

erupted magma from $\pm 10^6$ km/s to $\pm 10^4$ – 10^5 km/s until early May (Sigmarsson et al. 2011a). Only after the first summit eruption was deflation detected in the volcano's west flank at the GNSS stations STE2 and THEY, and no deformation was detected in the volcano's eastern flank at the station SKOG. Sigmundsson et al. (2010) fitted a horizontal deflating sill at $\sim 4.0-4.7$ km depth using the first 8 days of InSAR and GNSS observations.

The second explosive eruption in the summit caldera started on 5 May, reaching a maximum discharge rate of $\pm 10^6$ km/s and then decreased steadily until the eruption ended, on 22 May. GNSS stations STE and SKOG measured the renewed inflation pulse around 3-6 May, and the existing seismicity at 18-23 km depth suggested that the magmatic system was being recharged from the mantle (Karlsdóttir et al. 2012). These observations fit petrology studies; Sigmarsson et al. (2011a) suggested that the magma expelled in the first summit eruption was an influx of primitive hotter magma mixed with partial melts of the magma chamber carapace. After the residual silicic magma body beneath the summit of the volcano was consumed, in early May, Mg-rich basalt rose from depth and the magma became more primitive. The Tarasewicz et al. (2012b) study on possible magma sources of deflation suggested that the progressive deepening of seismic activity after the second eruption is due to a decompression wave propagating down through the crust causing sequential depressurization of vertically separated magma reservoirs. These authors supported their findings with microearthquake locations (Tarasewicz et al. 2012a) and petrology studies (Sigmarsson et al. 2011a). Tab. 5.1 summarises all the described modelled magma sources.

5.2. Data and Methodology

To assess the magma-induced ground motion associated with the pre-, co- and post-eruptive phases, I processed TerraSAR-X StripMap data and used a regional GNSS network. This section details the TerraSAR-X InSAR time series processing workflow and its cross-check against the GNSS time series of continuous and semi-continuous stations.

5.2.1. **SAR** data

I processed one ascending and one descending track of the TerraSAR-X satellite operated by the German Aerospace Center (DLR) and acquired in StripMap image mode (with a spatial resolution of \sim 3m). Both tracks cover the period between 18 July 2009 and 1 September 2010, with images acquired every 11 days over the co-eruptive from the beginning to the end of the eruption (Fig. 5.2). Outside the eruption period, the acquisitions during winter were interrupted due to snow cover and therefore to retain the coherence of the summer-to-summer acquisitions.

5.2.2. Interferograms

For the processing of the interferograms, I used DORIS, the TU Delft Object-oriented Radar Interferometric Software (Kampes and Usai 1999). In the ascending mode (track 132), I used 28 images, and in the descending mode (track 125), I used 16 images. The temporal distribution of the radar images is shown in Fig. 5.2 and further data and processing parameters are given in Appendix A.

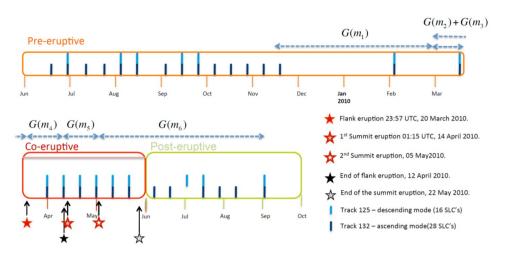


Figure 5.2: Time coverage of the available images of three TerraSAR-X tracks, from 18 June 2009 to 01 September 2010. Time classification regarding the three eruptive phases: orange pre–eruptive; red co-eruptive; green post-eruptive. G_{m_i} where i=1:6 represents the modelled magma source geometries related with different stages of the eruption. The modelled sources G_{m_1} to G_{m_4} previously modelled by Sigmundsson et al. (2010) are described in Tab. 5.1.

Using the precise orbits of DLR and a 25m digital elevation model (DEM) from the Iceland National Land Survey, I corrected for the reference phase (flat earth phase) and other geometric components of the interferometric phase,

Following the formalism of Brouwer and Hanssen (2023), the line-of-sight (LoS) component of a three-dimensional displacement vector $d = (d_E, d_N, d_U)^{\mathsf{T}}$ is obtained through an orthogonal projection through:

$$d_{\text{LoS}} = a^{\mathsf{T}} d = \begin{bmatrix} -\sin\theta_{\text{inc}} \sin\alpha_d & -\sin\theta_{\text{inc}} \cos\alpha_d & \cos\theta_{\text{inc}} \end{bmatrix} d, \tag{5.1}$$

where a is the LoS unit-vector and $P_{\text{LoS}\perp} = a^{\top}$ is the corresponding orthogonal projector onto the LoS (Brouwer and Hanssen 2023).¹ For the TerraSAR-X frames analysed here, $\theta_{\text{inc}} = 28.14^{\circ}$, $\alpha_d = 347.4^{\circ}$ (track 132, ascending) and $\theta_{\text{inc}} = 37.32^{\circ}$, $\alpha_d = 190.8^{\circ}$ (track 125, descending). Consequently, the LoS unit vectors are

$$a_{132} = (-0.46, -0.10, 0.88)^{\top}, \qquad a_{125} = (0.60, -0.11, 0.80)^{\top}.$$

The LoS components of a three-dimensional displacement vector are used throughout to project GNSS and model displacements into the radar geometry.

In general, the interferograms over Iceland are highly coherent. For this specific area, the exceptions are as follows:

- · over the ice caps.
- whenever there is snow during winter because of seasonal decorrelation.

 $^{^1\}alpha_d$ is the azimuth of the zero-Doppler plane (ZDP) at the target—not the satellite heading α_h . Using α_h instead of α_d introduces a range-dependent bias, as discussed by Brouwer and Hanssen (2023).

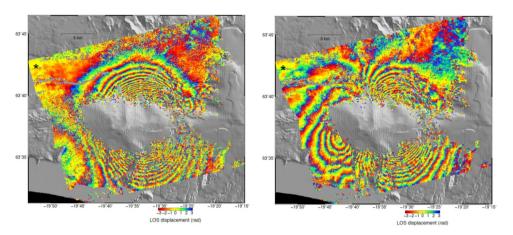


Figure 5.3: Left figure: Interferogram covering the pre- and part of the co-eruptive phases from 03-Sep-2009 to 25-May-2010. Right figure: Interferogram covering the pre-, co- and post-eruptive phase from 03-Sep-2009 to 19-Jul-2010. Both interferograms are from ascending track 132.

• during the explosive eruption, covering the co- and post-eruptive periods, because of the ash expelled and spread around the volcano flanks.

In Fig. 5.3 two interferograms show the complete deformation cycle: pre-eruption inflation, co-eruption activity, and post-eruption relaxation. The high coherence can be identified outside the central area of the interferograms. The central area has no observations because the summit caldera is covered by the glacier. The interferogram on the left shows the deformation pattern during the pre-eruptive and part of the co-eruptive phase marked by inflation, or a decrease in the satellite–surface distance between two acquisition times, from 3 September 2009 to 25 May 2010. The interferogram on the right covers the pre-, co-, and post-eruptive phases and shows the same inflation depicted in the left interferogram with a superimposed subsidence due to deflation (western fringe patterns) after the flank eruption.

5.2.3. InSAR Time Series

InSAR time-series techniques allow the picking of coherent backscattered points through different interferograms, for which it is possible to estimate time-series of surface displacements. I coregistered all images to a single primary acquisition (3 September 2009 for the ascending track and 14 April for the descending track), which was chosen not only to minimize the perpendicular, temporal, and Doppler baselines to ensure coherence stability over time (Fig. 5.4) but because it had fewer atmospheric artifacts.

The persistent scatterers (PS) selection method applied is StaMPS (Stanford Method for Persistent Scatterers) (Hooper 2006; Hooper et al. 2007; Hooper 2008). Minh et al. (2020) describe that StaMPS has the advantage over other Interferometric Synthetic Aperture Radar (InSAR) time series approaches (e.g., 'Permanent Scatterers' (Ferretti et al. 2001) and Delft's approach (Kampes 2005) because it does not rely on a prior deformation model in time, it instead relies on a correlation in space (Hooper et al.

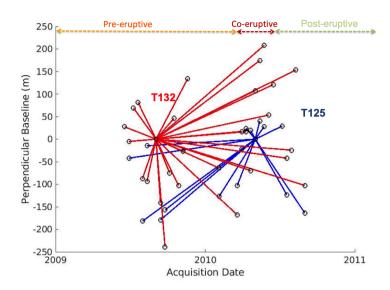


Figure 5.4: Perpendicular baselines coloured by track. This figure illustrates the distribution of the acquisition dates by the corresponding perpendicular baseline. The red lines represent track 132 in ascending orbit, and the blue lines represent track 128 in descending orbit.

2004) and because of the three-dimensional phase unwrapping approach of Hooper and Zebker (2007). Furthermore, StaMPS allows DEM error estimation, whereas other sources of errors can be reduced by the use of filters in space and time. These advantages of StaMPS's approach rely on a good choice of the parameters underlying the processing. While most of these parameters are tuned to commonly used data sets, if different sensors are used (e.g. C-band regarding the wavelength, resolution, etc.), or external interferences causing unwrapping errors (snow, ash, atmosphere) or even the use of default processing parameters, the deformation estimation may be biased (see Appendix A for further details).

PS Time Series

After interferogram generation, the error budget of the resulting interferometric phase (Hooper et al. 2007) is given by the following:

$$\phi_{w,x}^i = W \left\{ \phi_{\mathrm{Def},x}^i + \phi_{\mathrm{Atm},x}^i + \Delta \phi_{\mathrm{Topo},x}^i + \Delta \phi_{\mathrm{Orb},x}^i + \phi_{\mathrm{N},x}^i \right\}, \tag{5.2}$$

where ϕ_{Def} is the difference of phase due to deformation in the satellite line-of-sight, ϕ_{Atm} represents the difference of the atmospheric phase, $\Delta\phi_{\mathrm{Top}}$ is the residual phase due to DEM inconsistencies or the look angle error, $\Delta\phi_{\mathrm{Orb}}$ is the residual phase due to orbital errors, ϕ_N is the phase noise².

²Here, I refer to noise as 'random noise', or what is considered to be of nuisance contrasting with the ambient 'noise' from chapter 3 and chapter 4 of the interferogram

The resultant phase of this function $\phi^i_{w,x}$ for each pixel x, in a given interferogram i, is proportional to the effective difference in range and, therefore, will depend on satellite geometry, topography, soil moisture, or atmospheric conditions. Therefore, the resulting interferometric phase is the sum of all phase contributions as a function of the wrapped phase W. $\phi^i_{\mathrm{Def},x}$ is the component of the deformation estimated for each point x in each n interferogram.

Using a PS time series approach, we may reduce atmospheric effects (Hanssen 2001) under the assumption that small arcs have a similar atmosphere and, therefore, the atmospheric phase delays will cancel out when subtracted. However, the PS results still present a residual term of the atmospheric phase delay. The term that describes the remaining atmospheric phase difference can be expressed as the sum of the ionospheric phase delay and the tropospheric phase delay with

$$\Delta \phi_{\text{Atm},x}^{i} = \Delta \phi_{\text{Atm}_{\text{Ion},x}^{i}} + \Delta \phi_{\text{Atm}_{\text{Irop},x}^{i}}.$$
 (5.3)

The ionospheric phase delays ($\phi_{\mathrm{Atm}_{\mathrm{lon},x}^{i}}$) depend on the frequency of the signal. Given the TerraSAR-X centre frequency of 9.65 GHz, the path delay is estimated to be 2 cm for an average Total Electron Content (TEC) (Breit et al. 2010). By default, a constant average TEC already compensates for the delay in the ionospheric path (Breit et al. 2010).

To correct for the tropospheric component of the phase delay ($\phi_{Atm^i_{Trop,x}}$), I applied a correction described in Bekaert et al. (2015a), calculated from the data of the ERA interim model, which contains reanalysis data from the European Center for Medium-Range Weather Forecasts (ECMWF). The weather model is evaluated four times a day and is interpolated with the date of radar acquisitions. Using the TRAIN toolbox (Bekaert et al. 2015b), each SAR acquisition, both zenith tropospheric dry and wet delays, are computed and subtracted from the final unwrapped phase.

The residual topographical error $(\phi^i_{\text{Topo},x})$ is partially spatially correlated, so what remains is the uncorrelated spatial component of this error. To estimate the uncorrelated part of the look angle, the residual error of the look angle, it is assumed that there is a linear relationship between the remaining look angle error and the perpendicular baseline (Hooper et al. 2007). Because volcanic eruptions can change the volcano's topography, I removed the acquisitions of the co- and post-eruptive phases for the topographic residual error estimation.

I did not apply any correction for orbital errors $\phi^i_{{\rm Orb},x}$, under the assumption that $(\triangle\phi^i_{{\rm Orb},x})$ is insignificant for images TerraSAR-X Yoon et al. (2009).

After the applied PS processing, the error budget of each PS phase at a given interferogram is given by the following expression:

$$\psi_{\text{uw},x}^{i} = \psi_{\text{Def},x}^{i} + \Delta \psi_{\text{TopoUncorr},x}^{i} + \psi_{\text{N},x}^{i} + 2\pi n.$$
 (5.4)

Here ψ stands for the unwrapped phase, and the terms on the right-hand side of the equation Eq. 5.4 follow the same logic as Eq. 5.2. ψ_{Def} is the difference in phase due to deformation in the satellite LoS, $\Delta \psi_{\mathrm{TopUncorr},x}^i$, is the spatially uncorrelated phase due to errors in the DEM, ψ_N is the interferogram phase noise and πn is the term for the ambiguities of the wrapped phase. Since not all sources of errors in the final unwrapped

phase can be separated from the deformation component, we estimate the remaining source of errors stochastically in sec. 5.4.2 with a variogram model.

The interferogram coherence in Fig. 5.3 looks good due to the clear observed fringes, except for the glacier area surrounding the volcano caldera. However, at the location of the Fimmvörðuháls eruption, the connection of the fringe patterns between the north and south of the volcano flanks is lost. As a result, and after a consistency check with the GNSS time series sec. 5.2.4, unwrapping errors tend to occur at locations of high to low coherence (e.g., GNSS station STE or FIM2). The unwrapping errors are likely due to the loss of coherence due to ash coverage, snow, or the non-linear nature of the measured displacements.

Small Baselines

A common approach to minimise the influence of unwrapping errors caused by decorrelation between acquisitions is to apply the small-baseline subset strategy (see Fig. 5.5 for initial small baseline interferogram pairs), retaining only interferogram pairs whose perpendicular and temporal separations are ≤ 1 km and ≤ 1500 days, respectively. The resultant combinations, colour-coded by track, are plotted in the perpendicular versus temporal baseline domain. The red lines represent track 132 in ascending orbit and the blue lines represent track 125 in descending orbit.

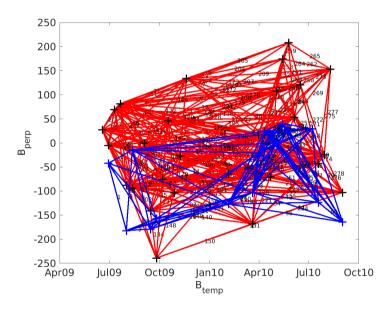


Figure 5.5: Perpendicular versus temporal baselines coloured by track using SBAS. Possible interferogram combinations using a minimum theoretical coherence threshold based on the perpendicular and temporal baselines, which by default are set to 1000~m and 1500 days. The red lines represent track 132 in ascending orbit and the blue lines represent track 125 in descending orbit.

The initial interferograms revealed high decorrelation at the Fimmvörðuháls eruption site, raising concern about the unwrapping reliability. To address this issue, I

experimented with the small baseline algorithm (SB) described by Hooper (2008). The main challenge was to select an interferogram network that would bridge two eruption intervals despite an acquisition hiatus caused by winter snow coverage, thus preserving phase coherence where it mattered most. This means connecting the early pre-eruptive period (from June 2009 to November 2009) with the period after the first eruption (20 March 2010 to 01 September 2010) with interferograms that would retain coherence around the Fimmvörðuháls eruption site.

StaMPS unwraps the SB interferograms by mapping residuals between the observed SB phases and those predicted from the single-master model.

Acceptable maps show only speckled noise or isolated residuals much less than π in magnitude, while spatially correlated residuals indicate a problem with unwrapping. Usually, it is possible to remove the interferogram showing the highest residuals from the estimation; however, since multiple interferograms overlap in each residual map, it is not easy to assess which interferogram causes the highest residuals. I dealt with this problem by adopting a trial-and-error approach: drop the suspect pair, re-unwrap, inspect again, and repeat until the spatial pattern has disappeared from the residuals.

Unfortunately, from the initial network (Fig. 5.5) only few interferograms connected both periods due to temporal decorrelation between the pre-and co-eruption moments (Fig. 5.6), and with the lowest coherence estimations. After dropping interferograms with higher spatially correlated residuals, only one pair survived the residual test, leaving no redundancy—a key advantage of SBAS—so the SB solution proved noisier than its PS counterpart when compared to GNSS time series. Consequently, I only used the PS-InSAR solutions for all subsequent modelling.

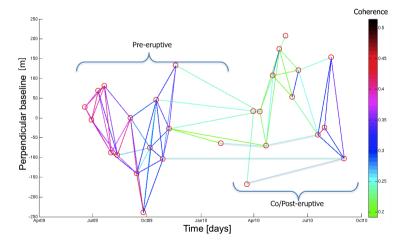


Figure 5.6: Perpendicular baselines coloured by the average coherence of each interferogram (after a pre-selection of the best interferograms) for track 132. During winter and the co-eruptive period, the coherence drops abruptly due to snow and ash coverage, respectively.

Station	Latitude [°N]	Longitude [°E]	Ellipsoidal height [m]	Start date	End date
STE1	63.677062	-19.608515	290.44	17 Jun 2009	07 Feb 2010
STE2	63.677033	-19.608547	290.44	22 Feb 2010	31 Aug 2010
THEY	63.561468	-19.643420	195.27	18 Jun 2009	01 Sep 2010
SOHO	63.552475	-19.246644	857.49	18 Jun 2009	26 Aug 2010
FIM2	63.610055	-19.433789	961.78	19 Mar 2010	01 Sep 2010
SKOG	63.576449	-19.445499	669.52	18 Jun 2009	01 Sep 2010
BAS2	63.675737	-19.476219	369.55	20 Mar 2010	01 Sep 2010
HAMR	63.622447	-19.985675	160.35	18 Jun 2009	31 Aug 2010
SVBH	63.580283	-19.618711	654.25	15 Apr 2009	16 Aug 2010
DAGF	63.627628	-19.799620	800.59	02 Jun 2009	10 Oct 2010

Table 5.2: GNSS Stations around Eyjafjallajökull volcano for the period covering the InSAR dataset.

5.2.4. Consistency check with GNSS

InSAR and GNSS measurements are complementary: GNSS provides precise three-component point displacements, while InSAR offers dense spatial coverage of relative LoS deformation but with higher uncertainty. Validating the consistency between the two techniques is therefore essential before combining them in a joint inversion framework. In this section, InSAR results were first benchmarked against GNSS time series to ensure reliability and to identify potential artifacts. Subsequently, the GNSS observations were integrated into the inversion.

GNSS Time Series

A vast continuous GNSS network in Iceland is operated by the Institute of Earth Sciences in cooperation with the Icelandic Meteorological Office (IMO). Covering the 2010 volcanic event, the GNSS stations listed in Tab. 5.2 werer operating in the following temporal sequence:

- Four continuous stations (THEY, SOHO, HAMR, SKOG) operated throughout the period covered by the InSAR dataset.
- Two stations (STE1 and SKOG) operated semi-continuously during winter, in the pre-eruptive period.
- Eight semi-continuous GNSS stations were installed during the pre- and coeruptive stages of the 2010 eruption, in addition to the continuous THEY and SOHO stations.
- On 19 February 2010, a permanent site (STE2) was installed next to STE1.
- Additional sites were installed at Fimmvörðuháls (BAS2 and FIM2) on 19 March 2010, one day before the flank eruption, followed by DAGF and SVBH.

The GNSS stations on and around Eyjafjallajökull volcano were processed with GYPSY-OASIS software (Lichten and Border 1987) by the University of Iceland (Institute of Earth Sciences 2023) and provided by Dr. Sigrun Hreinsdottir. A linear correction term was estimated to project the time series into the ITRF08 Eurasia stable reference frame using data from a continuous GNSS station (THEY) from April 2009 to September 2010 (Altamimi et al. 2007). The time series were de-trended by estimating annual and semi-annual terms with respect to data available from 2002 to 2009 from THEY station, a continuous GNSS station, and were removed from all the remaining stations' signals. GNSS heights were corrected for the geoid, and monuments were anchored in bedrock to ensure signals represent deep crustal processes.

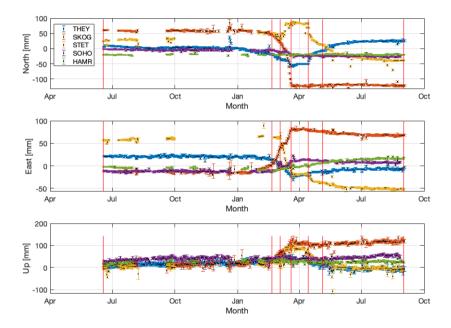


Figure 5.7: Displacements of GNSS stations THEY, SKOG, STET, SOHO and HAMR in the north (top), east (middle) and up (bottom) components of displacement with error bars showing 1σ uncertainty. Red lines mark the moments of deformation rate change used to model the different magma sources (also identified in Fig. 5.2).

Fig. 5.7 and Fig. 5.8 show the displacements in the north, east, and the up directions of all continuous and semi-continuous GNSS stations. Fig. 5.9 shows a finer zoom in on the co- and post-eruptive phases extracted from Fig. 5.7. In each of the figures, the vertical red lines indicate the periods of change in the deformation rate corresponding to the equivalent $G(m_1)$, (...), $G(m_6)$ in Fig. 5.2. The complete time series for each station covering the eruptive periods is in Appendix A.

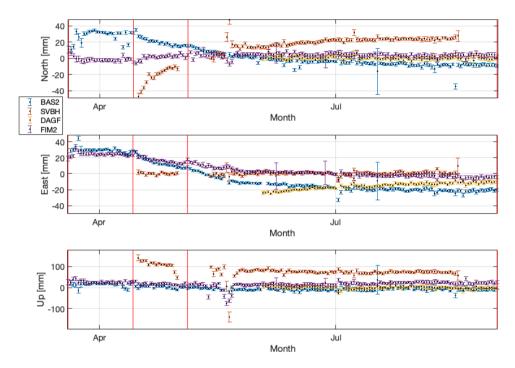


Figure 5.8: Displacements of GNSS stations BAS2, SVBH, DAGF, and FIM2 in the north (top), east (middle) and up (bottom) directions with error bars showing 1 σ uncertainty. Red vertical lines mark the times used in modelling the magma sources (also identified in Fig. 5.2).

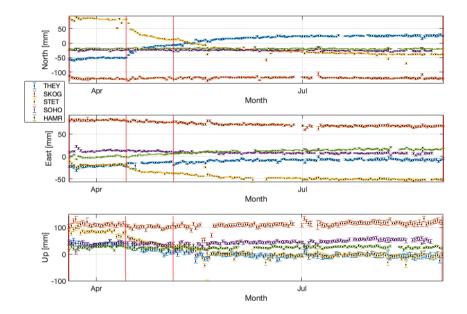


Figure 5.9: Displacements of GNSS stations THEY, SKOG, STET, SOHO and HAMR in the north (top), east (middle) and up (bottom) directions with error bars showing 1σ uncertainty. Figure similar to Fig. 5.7 but here covering only the co- and post-eruptive periods.

Consistency Check Between GNSS and InSAR

To first check the consistency of InSAR displacements against GNSS time series, I used three continuous stations (THEY, STEI/STE2, SKOG) operating during the entire period covered by InSAR and covered by ascending and descending tracks. For the co- and post-eruptive periods, I used data from all the continuous and semi-continuous GNSS stations for modelling purposes.

Validation involves three steps: (i) projection of GNSS displacements into the radar LoS, (ii) reference frame alignment using double differences (DD), and (iii) weighted least squares averaging of nearby PS points to mitigate scatter noise.

(i) Projection to LoS. I projected the daily GNSS *north–east–up* (NEU) solutions of stations THEY, STEI/2, and SKOG into the radar line of sight (LoS) using Eq. 5.1. Let the GNSS daily solutions (north, east, up) be represented by:

$$d_{\text{GNSS}}^{j}(u) = \left(d_{N}^{j}(u), d_{E}^{j}(u), d_{U}^{j}(u)\right)^{\top}, \qquad j = 1, \dots, N_{\text{GNSS}}, \tag{5.5}$$

where $(d_N^{\ j}(u), d_E^{\ j}(u), d_U^{\ j}(u))$ denote the three components (north, east, and up, respectively) of displacement recorded at a GNSS location u=(x,y) on day j, with GNSS recording daily observations. For each SAR acquisition (i) the unwrapped persistent–scatterer (PS) phase at the same location is $\phi_{\rm PS}^{\ i}(u)$. Its slant–range displacement $d_{\rm PSLoS}^{\ i}(u)$ follows from

$$d_{\text{PS,LoS}}^{i}(u) = \frac{\lambda}{4\pi} \phi_{\text{PS}}^{i}(u), \qquad i = 1, ..., N_{\text{SAR}},$$
 (5.6)

with radar wavelength λ . Fig. 5.10 shows the displacements of InSAR and GNSS in the LoS direction for the ascending track.

(ii) **Double differences.** To circumvent the difference between the reference frame of each geodetic technique, I compared double differences between pairs of GNSS stations u_1, u_2 and InSAR PS points:

$$DD_{GNSS}^{j}(u_2 - u_1) = d_{GNSSLoS}^{j}(u_2) - d_{GNSSLoS}^{j}(u_1),$$
(5.7)

$$DD_{InSAR}^{i}(u_2 - u_1) = d_{InSAR,IoS}^{i}(u_2) - d_{InSAR,IoS}^{i}(u_1).$$
 (5.8)

Assuming both techniques capture the same deformation signal (apart from a possible offset), the Gauss-Markov model, 2.1, can be applied here as a general linear functional and stochastic relationship between observations (in this case InSAR and GNSS) and parameters of interest (double difference displacements). Here, the functional model, or design matrix (A), is the linear vector (from \mathbb{R}^N to \mathbb{R}^M) that relates the displacements of GNSS and InSAR (y) with the displacements of double difference (x). I use Eq. (2.3) under the assumption that the GNSS and InSAR double differences should be equal (following the approach of, for example, Marinkovic et al. (2007) or Mahapatra et al. (2013)). Therefore, the functional model takes the form of the following:

$$A^{T}E\left\{ \begin{bmatrix} d_{\text{GNSS,LoS}} \\ d_{\text{PS,LoS}} \end{bmatrix} \right\} = \begin{bmatrix} I & 1 \\ I & 0 \end{bmatrix} E\left\{ \begin{bmatrix} dd_{\text{GNSS,InSAR}} \\ c_{\text{GNSS,InSAR}} \end{bmatrix}$$
 (5.9)

while the stochastic model looks like:

$$Q_d = \begin{bmatrix} Q_{d_{\text{GNSS}}} & 0\\ 0 & Q_{d_{\text{InSAR}}} \end{bmatrix}$$
 (5.10)

Here, A is the condition equation design matrix, $y_{\rm GNSS,LoS}$ and $y_{\rm PS,LoS}$ are the observables, the GNSS (transformed to LoS for each track) and the InSAR measurements respectively, $dd_{\rm GNSS,InSAR}$ and $c_{\rm GNSS,InSAR}$ are the calibrated deformation signal and the offset between the two technique measurements, respectively, I is the identity matrix, Q_y is the overall variance-covariance matrix of the observations, $Q_{d_{\rm GNSS}}$ is the precision of the GNSS double difference measurements, and $Q_{d_{\rm InSAR}}$ is the precision of the InSAR double difference measurements.

(iii) Weighted averaging of PS. I assumed that at the eruption site the GNSS and InSAR measured the same deformation process. To minimise local scatter noise, I used the inverse of the distance between each PS and the location of the GNSS as a weighting factor in a weighted least-squares formulation to estimate the average phase of the selected PS points by minimizing:

$$\min_{r} \|d - G \cdot m\|_{W}^{2}, \tag{5.11}$$

where m is the weighted average of the selected PS points around the GNSS station, G is the design matrix, d is the phase translated into displacement for each PS within the pre-defined radius, and W is the weight matrix, defined as the inverse of the distance to the GNSS station. The solution is given by

$$\hat{\bar{m}} = (G^T \cdot W \cdot G)^{-1} \cdot G^T \cdot W \cdot d. \tag{5.12}$$

The radius was defined to ensure at least three PS points around each GNSS location. This criterion reduces the influence of single-scatter noise and ensures that the distribution of phase displacements within the radius remains within one standard deviation.

Let $\phi_{x1}^i...\phi_{xn}^i$ denote the set of phases of the selected points x_n in the defined circle, where i is the number of each interferogram. Although both InSAR and GNSS measure surface deformation in one or more directions, these techniques may measure different deformation processes due to their spatial and temporal sampling differences and the installation conditions of the GNSS monument. InSAR measures relative LoS displacements over a spatially distributed scatterer network, while GNSS gives absolute 3D displacements at a single point, influenced by monument stability.

Fig. 5.11 shows the time series GNSS (black diamonds) and InSAR (blue diamonds) with their corresponding error bars. Note the difference in magnitude between the GNSS and InSAR error bars. GNSS is generally more precise, has smaller errors (mm-cm), while InSAR uncertainties (cm-level) reflect atmospheric noise, unwrapping errors, and decorrelation. The first column presents pairs of stations (double differences), while the second presents single differences between GNSS and InSAR to visualise the LoS displacement of a single station. The red dots indicate displacements of $\pm \lambda/2$ which may indicate phase jumps induced by the unwrapping.

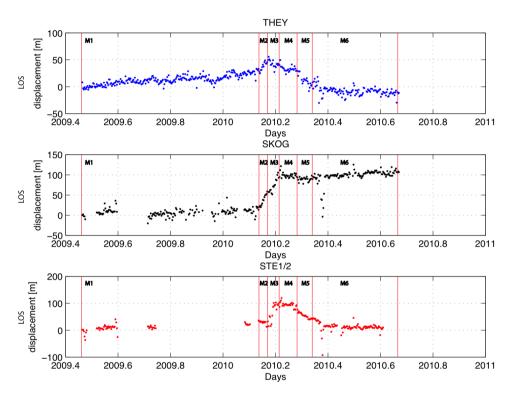


Figure 5.10: Displacements of GNSS stations THEY, SKOG and STE in LoS direction of ascending track 132.

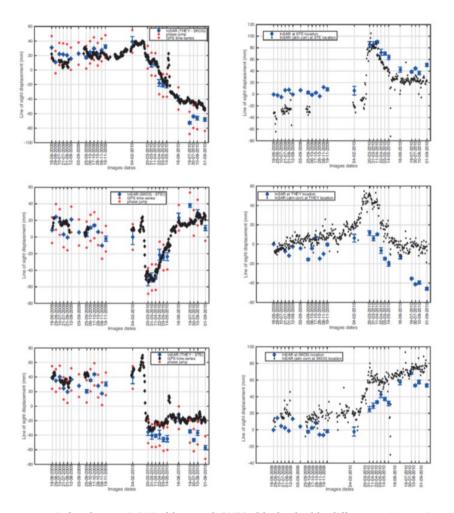


Figure 5.11: Left column: InSAR (blue) and GNSS (black) double differences time series. Red dots indicate the displacements due to a phase cycle up and down (λ /2) from the unwrapped displacement, possibly indicating a phase jump due to unwrapping. right column: InSAR and GNSS time-series converted to InSAR LoS.

A comparison across all stations is shown in Fig. 5.12, where double differences are colour-coded (THEY–SKOG in blue, SKOG–STET in magenta, and THEY–STET in green). The overall fit is good, although some individual observations exhibit misfits (some examples marked with red ellipses). The THEY–SKOG pair shows the best agreement, with an RMS of ~12 mm, except after 19 July during the post-eruptive phase. By contrast, the SKOG–STET and THEY–STET pairs show poorer fits, with RMS values of ~14.4 mm and ~14.5 mm, respectively. This suggests that the InSAR observations at STEI may suffer from unwrapping errors caused by coherence loss or decorrelation due to ash or snow cover; however, atmospheric effects may also contribute.

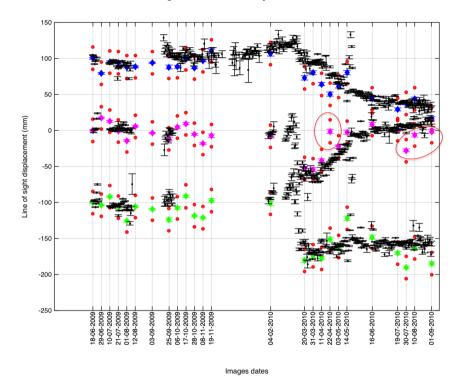


Figure 5.12: Comparison of double-difference time series between InSAR (coloured points) and GNSS converted to InSAR LoS (black). Red dots indicate displacements corresponding to phase cycle shifts (λ /2), likely due to unwrapping errors. Colours represent station pairs: THEY–SKOG in blue (RMS ~12 mm), SKOG–STET in magenta (RMS ~14.4 mm), and THEY–STET in green (RMS ~14.5 mm). To visualise all time series in the same figure, the blue and green series are plotted with artificially added vertical offsets of +50 mm and -50 mm, respectively.

5.3. Eruptive Deformation Cycle: InSAR and GNSS results **5.3.1.** Pre-Eruptive Inflation Phases

The InSAR time-series displacements in the early pre-eruptive phase (from June 2009 to February 2010) do not show relevant signals until the interferogram of February 4 2010.

A signal reached a line-of-sight shortening of up to 1.8 cm on the southwestern flank. The closest GNSS station to the area of the detected inflation, station THEY, shows a consistent displacement reaching ~2 cm in the LoS direction from early January until the date of the February 4 interferogram (see Fig. A.1). The late pre-eruptive phase can be identified in a single interferogram in which the slave image was acquired on March 20, 2010, a few hours before the first eruption. The satellite captured this image approximately 5 hours before the eruption, and the PS results show an inflation signal centred at Fimmvörðuháls mountain. This interferogram highlights the inflation signal and an increase in seismic events.

Fig. 5.13 and Fig. 5.14 show the general view of the deformation patterns covering the eruption from 18 June 2009 to 1 September 2010 for tracks 132 and 125, respectively. We can recognise the three relevant epochs also identified in the figure: the pre-, co-, and post-eruptive phases.

5.3.2. Co-Eruptive Deformation Pause and Post-eruptive Subsidence

The co-eruptive phase is identified in Figures 5.13 and 5.14 from March 31 to May 14, spanning the Fimmvörðuháls flank eruption (20 March–12 April) and the summit eruption under the glacier (beginning 14 April). See Fig. 5.2 for the satellite imagery and eruption timeline. During the short hiatus (12-14 April), interferograms and GNSS showed no deflation pattern relative to the prior interval, implying that the shallow system remained pressurised immediately before the explosive summit eruption (Sigmundsson et al. 2010). This sustained inflation likely facilitated the transition to the explosive phase on April 14, after which clear subsidence is observed. The interferograms between 20 March and 11 April show negligible deformation rates, indicating that for approximately 20 days the volcano remained inflated even while erupting. These rates are in line with the GNSS time series at the THEY station.

The second eruption was preceded by a short gap in eruptive activity between 12 and 14 April. Coinciding with the start of the explosive eruption on April 14, the onset of subsidence is visible, centred on the caldera on the 22 April interferograms for both tracks (Fig. 5.13 and Fig. 5.14). We interpret this as depressurization of the shallow plumbing system as discharge exceeded recharge during sustained explosive activity, consistent with InSAR/GNSS inversions for this eruption (Sigmundsson et al. 2010).

'Post-eruptive' refers to deformation after 14 May in our SAR time series (the last pre-cessation image), although eruptive activity at the summit waned through late May and was declared over later in 2010. The interferograms in Fig. 5.13 and Fig. 5.14 show an increase in cumulative subsidence until the last interferogram on 1 September. After eruptive activity ceased, this continued subsidence is expected and has been observed in other volcanoes as well, due to thermoelastic contraction during cooling and crystallization of intruded magma and near-surface lavas (Wang and Aoki 2019; Townsend 2022). These processes are widely invoked in post-eruptive deformation analyses and are consistent with our time series.

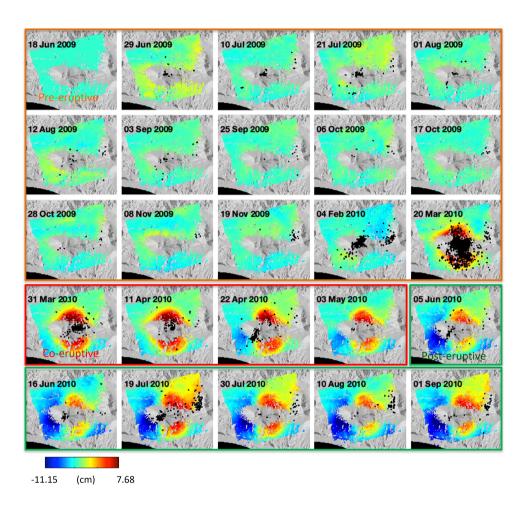


Figure 5.13: Cumulative line-of-sight displacement of track 132 ascending mode from 18 June 2009 to 01 September 2010, w.r.t. the first image. Background maps give shaded topography, with the ice cap showing no PS cover. Black dots are earthquake epicentres for each epoch (Icelandic Meteorological Office). The images corresponding to the 3 phases of the eruption are identified accordingly.

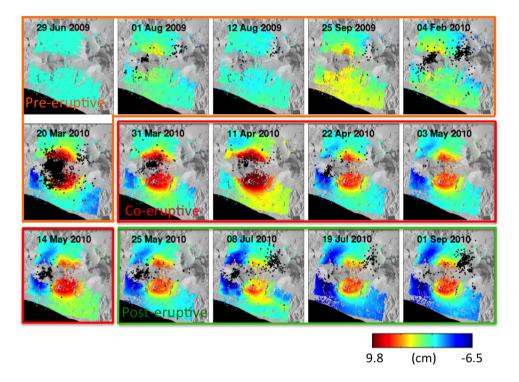


Figure 5.14: Cumulative line-of-sight displacement of track 125 descending mode from 29 June 2009 to 01 September 2010. Background maps give shaded topography, with the ice cap showing no PS cover. Black dots are earthquake epicentres for each epoch (Icelandic Meteorological Office).

5.4. Modelling Magma Sources: Co- and Post-Eruptive Results

Previous studies offered interpretations of the magmatic plumbing system associated with the co- and post-eruptive moments of the 2010 Eyjafjallajökull eruption. Sigmundsson et al. (2010) modelled a contracting sill at ~4.0–4.9 km depth, active during the co- and early post-eruptive phase (11–22 April), constrained by two interferograms. In addition to these results, Tarasewicz et al. (2012b) using precise earthquake relocations over a longer period, hypothesised a set of four vertically aligned sills beneath the volcano, sequentially activated by a downward-propagating decompression wave that triggered the explosive summit eruption. Although one of the sills in Tarasewicz et al. (2012b) is consistent with the shallow sill inferred by Sigmundsson et al. (2010), an open question remained: could the deformation after 22 April (not included in that initial modelling) also be explained by the same multi-sill configuration?

5.4.1. Geomechanical Forward Model with Seismicity Constraints Model Description

To test the seismic hypothesis of stacked sills of (Tarasewicz et al. 2012b), I computed surface displacements for pressurised sill-like sources using the finite penny-crack formulation of Fialko et al. (2001). This approach provides the 3-D Green's function solution for horizontal circular cracks embedded in a homogeneous, isotropic, elastic half-space, parameterised by crack radius, over/under-pressure, depth, and elastic moduli (μ, ν) . The physics involved in Fialko et al. (2001)'s model are based on the principle of elasticity and mechanics, simulating how the Earth's crust deforms in response to the stress exerted by magma intrusions/extrusions. The model considers the material properties of the crust, intrusion/extrusion geometry, and the stress-displacement mechanics in an elastic medium. The model evaluates integrals numerically and estimates surface displacements due to a pressurised sill-like source using the finite penny-crack model, where a certain radius, hydrostatic overpressure and location are predefined for the arbitrary crack. Even though analytical models have limitations, such as the limited geometries and boundary conditions, assumptions on linearity, and isotropic material behaviour, they allow for understanding and testing of whether the hypothesised magma sources can reproduce the estimated surface displacements and are computationally efficient, and suitable to test candidate source geometries.

Following Tarasewicz et al. (2012b), I simulated the four pressurised horizontal circular crack (sills) at depths of 5 km, 10–15 km, 19 km and 24 km. The volume change associated with each sill was estimated following the finite penny-shaped crack formulation of Fialko et al. (2001):

$$\Delta V = \frac{16(1-\nu)}{3\pi\mu} P a^3, \tag{5.13}$$

where ΔV is the volume change, P is the excess pressure, a is the sill radius, μ is the shear modulus, and v is Poisson's ratio. A uniform pressure change of 4 MPa in magnitude was assigned to each (sign convention: negative for deflation), shear modulus of $\mu = 30$ GPa, and Poisson's ratio was fixed at v = 0.25. For clarity and

Source	Depth [km]	Pressure [Pa]	Radius [km]	Volume change [km ³]	Shear modulus μ [GPa]
Sill 1	5	-4×10^{6}	5	-0.0489	30
Sill A	12	-4×10^{6}	4	-0.0174	30
Sill B	19	-4×10^{6}	4	-0.0171	30
Sill C	24	-4×10^{6}	3	-0.0054	30

Table 5.3: Previously modelled source parameters. A constant shear modulus of μ = 30 GPa was assumed for all sills, a standard for crustal rocks.

consistency, all pressures are in MPa, the excess pressure was defined as the ratio P/μ , and other source parameters are listed in Tab. 5.3.

The spatial displacement pattern associated with the post-eruptive deformation exhibits a near-circular symmetry. This can be seen from the concentric fringes in the interferograms centred on the volcano caldera Fig. 5.3. For this reason, I assume the centre of the volcano caldera to be the centre of the forward model.

Results

Using the TerraSAR-X ascending track geometry (incidence angle of 27° and a heading of 347°), I simulated the displacements of the four penny-shaped crack models and compared them with the observed LoS cumulative displacements. The model output is the vertical (up) and horizontal (north and east) deformation components and the volume change.

Fig. 5.15 shows the unwrapped solutions for the total LoS displacement estimated from the three (Sill A, B, and C of Tab. 5.3) and four (all listed sills in Tab. 5.3 modelled sills with the corresponding profiles. The displacement profiles show the vertical, eastward, and LoS estimated displacements for the modelled sills as well as the data and averaged data estimated from the interferograms for the post-eruptive period. The estimated cumulative surface displacements associated with the co- and post-eruptive phases from PS InSAR processing are one order of magnitude higher than the displacements estimated by forward modelling the hypothesised sills. Therefore, the forward-modelled stack of four sills suggested by earthquake relocation studies does not fit the estimated surface displacements.

For context, Fig. 5.16 and Fig. 5.17 show the spatial and temporal context of the deformation with the volcano topography as a reference. In Fig. 5.16, a spatial map and a west–east slice through the edifice are shown twice. In (a) the shaded relief with the topographic cross section, and in (b) the linear rate of displacements of the full co- and post-eruptive phases with the corresponding cross-section. In Fig. 5.17a, the time series of the Fig. 5.16 cross-section shows the evolution of surface displacements from the beginning of the eruption (20 March 2010) to September 2010. These traces represent the time-dependent counterpart of the cumulative displacements plotted in Fig. 5.15. Fig. 5.17b presents a zoomed-in view of the same series.

5.4.2. Inverse Modelling: Post-eruptive phase

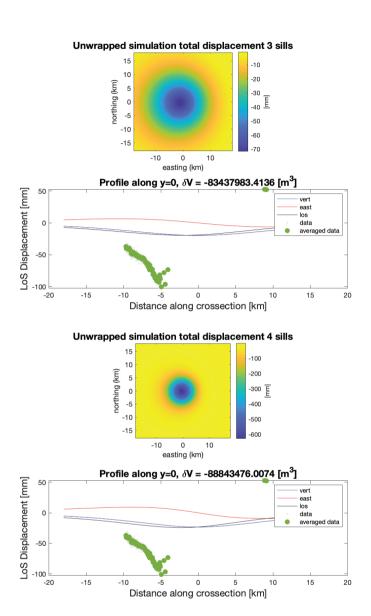


Figure 5.15: Total LoS displacement estimated from the three (top) and four (bottom) modelled sills with the corresponding profiles (y=0). The displacement profiles show the vertical, eastward, and LoS estimated displacements for the modelled sills as well as the data and averaged data estimated from the interferograms for the post-eruptive period

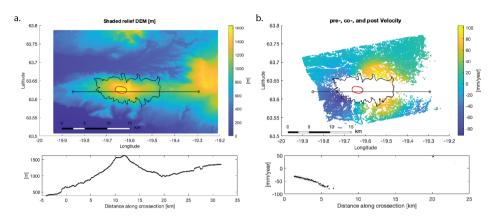


Figure 5.16: Spatial map and west–east cross-section showing (a) the shaded relief derived from a 25 m resolution DEM and (b) the pre-, co-, and post-eruptive velocity fields processed from TerraSAR-X Track 132. In the spatial map, the black polygon outlines the glacier overlying the volcano, while the red polygon delineates the caldera.

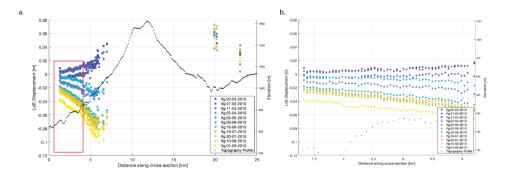


Figure 5.17: Time series of west–east cross-section displacements located in Fig. 5.16 showing (a) ground motion between 20/03/2010 and 01/09/2010, processed from TerraSAR-X Track 132, along with the topographic profile derived from a 25~m resolution DEM. The red rectangle highlights the portion of the time series that is enlarged in (b).

Modelling Approach

In addition to the forward modelling, here we extended the analysis to the full deflation period and performed a joint inversion of the InSAR and GNSS time series from 11 April to 1 September (intervals m_5 and m_6).

Let $\hat{d} = G(m)$ denote the forward mapping from the model parameters, where \hat{d} is the estimator, G is the physical model (it can be Mogi, crack, etc). For the modelled parameters m (source geometry and pressure change), it is possible to model different source parameters for different periods of measured deformation (m_1 to m_6). The inversion was implemented within a Bayesian framework, estimating posterior distributions of source parameters via a Monte Carlo Markov chain (MCMC) method with a Metropolis-Hastings algorithm. We estimated the probability distribution of the model parameters at each iteration step with pre-defined small steps between each tested parameter as follows. For each parameter tested, a first-best guess is provided for the initial model parameters with lower and higher bounds and small size steps, for which the sensitivity value for each model parameter is then calculated. Then with the estimated probability for each model parameter variation, the best model is chosen at each iteration using the MCMC. Atmospheric artefacts were incorporated into the covariance structure through variogram modelling. This approach offers two advantages: (i) it provides full probability distributions for each parameter, and (ii) it allows the use of prior constraints from independent observations.

The objective function of the modelling approach is based on Bayesian methods, which allows us to estimate a multivariate probability distribution for the model parameters (given the data), defined as

$$P(m/d) = K \cdot P(d/m) \cdot P(m), \tag{5.14}$$

where K is a normalised function so that the integral of the likelihood function is equal to 1 as follows:

$$K = \frac{1}{\int_{-\infty}^{\infty} p(d \mid m) \cdot p(m) dm},$$
(5.15)

where $p(d \mid m)$ is the likelihood function or the probability distribution function of a d given m and P(m) is the prior probability.

Results

The post-eruptive gradual deflation of a source in the western flanks of the volcano characterises the post-eruptive phase. The subsidence proceeds in an approximately steady-state fashion until the end of the eruption. We used the two tracks of the InSAR time series and GNSS data as observations and modelled the entire deflation period (11 April to 01 September). The inversion results favoured an ellipsoidal source, with a long axis $2.7-4.2 \, \text{km}$, short axis $0.55-0.74 \, \text{km}$ and strike of the long axis is $60-73^{\circ}$, located at $6.4-7.2 \, \text{km}$ depth and equivalent to a volume reduction of $\sim 0.02-0.026 \, \text{km}^3$ (Fig. 5.18).

This geometry reproduces the spatial and temporal characteristics of the observed subsidence better than the hypothesised four stacked sills.

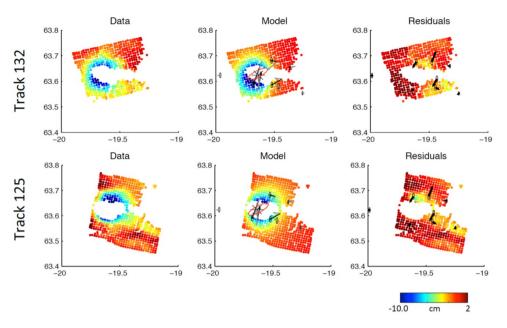


Figure 5.18: Modelled ellipsoidal source using linear velocity. Arrows locate the GNSS stations

5.5. Discussion and conclusions

The dense geodetic and seismic datasets acquired during the 2010 Eyjafjallajökull eruption, provide strong constraints on the magma pathways of an active volcano. Petrological analyses indicate that the explosive summit phase (trachyandesite) had low crystallinity and short crustal residence times, with crystals interpreted as remnants of earlier intrusions. Geochemical data are consistent with binary mixing between fractionated basalt and a dacitic melt, possibly a remnant of the 1821–1823 eruption of Eyjafjallajökull, which produced dacite (Keiding and Sigmarsson 2012; Gislason et al. 2011). The remnants of the old magma continuously erupted with the new magma until the summit eruption's end, implying a pre-existing reservoir beneath the summit.

Using GNSS and InSAR time series, we have focused on the deflation (subsidence) associated with the co-eruptive and post-eruptive phases of the 2010 Eyjafjallajökull eruption. Forward models based on the four stacked sills hypothesised from seismic relocations under-predict the InSAR amplitudes by approximately an order of magnitude. In contrast, a single ellipsoidal source at $\sim\!6-7$ km depth explains both spatial and temporal patterns of subsidence. This differs from earlier deformation models invoking multiple shallow sources and instead points to a dominant three-dimensional reservoir controlling the co- and post-eruptive signal.

The deflation observed between 11 and 22 April was previously modelled as a sill source at 4.0—4.9 km depth beneath the summit (Sigmundsson et al. 2010). Our analysis shows that this geometry cannot reproduce the deformation throughout the deflation period, from 11 April to 1 September, while a single ellipsoidal source at 6–7 km depth

provides a much better fit.

Seismic relocation studies had earlier favoured stacked sill sources, in part because of lens-shaped seismicity patterns and apparent seismic gaps (Tarasewicz et al. 2012b). A 3D source is therefore required to explain the post-eruption subsidence, yet if this source were entirely molten, the observed seismicity within its volume would be difficult to reconcile. Instead, the coexistence of deformation and seismicity may point to a mush-like reservoir: a long-lived, crystal-rich body with interconnected melt domains. In such a framework, seismicity can occur in the rigid crystal framework even as magma withdrawal drives subsidence.

Petrological and geochemical evidence supports this interpretation. The 2010 trachyandesite contained crystals inherited from earlier intrusions, while geochemical signatures suggest binary mixing between fractionated basalt and a probable remnant of dacitic melt from the 1821-1823 eruption (Keiding and Sigmarsson 2012; Gislason et al. 2011). This implies that parts of the older magma were preserved in the mush. During the decade before the eruption, shallow intrusions, including those in 1994 and 1999, may have reheated and recharged this mush, adding volatiles and promoting partial remelting. This rejuvenation explains both the mixed compositions that erupted in 2010 and the variable crystal residence times observed (Sigmarsson et al. 2011b; Moune et al. 2012).

Overall, the integration of geodetic, seismic and petrological data converges on a model where the active source during the 2010 eruption was not a stack of discrete molten sills but may be better explained by a vertically extensive that may be periodically reactivated. Our results support the mush paradigm by reconciling the geodetic, seismic, and petrological constraints on the 2010 Eyjafjallajökull eruption.

Lastly, we note a significant discrepancy between the estimated volume of eruptive products (approximately $0.17~\rm km^3~DRE$) and the modelled contraction volume of the ellipsoidal deflation source $\sim\!0.022-0.026~\rm km^3$. These results imply that volume contraction is 7 to 8 times less than the erupted volume. Following the work of Rivalta and Segall (2008), we propose that this discrepancy can be attributed to the compressibility of the magma and the inherent compliance of the fractures, which behave differently than the equidimensional chambers previously assumed.

The Magmatic Plumbing System of Torfajökull volcano by Geodetic and Seismic Imaging

In the context of this thesis and the objectives stated in sec. 1.5, this chapter delves into the potential of the two techniques applied for MPS's imaging. Focusing on the case study of the Torfajökull volcano, I provide a summary of the processed InSAR time-series data followed by the estimated rate of deformation to deduce MPS geometry and depth. Finally, I summarise the capabilities and limitations of both radar and seismic techniques within the context of the three applications of MPS knowledge described in sec. 1.2: geothermal energy, volcanic hazard and possible amount of melt.

6.1. Introduction

Deepening our understanding of MPS has a wide range of implications, from improving hazard assessment and forecasting eruptions to optimising and ensuring safer geothermal energy use. Enhanced subsurface MPS imaging uncovering the residing depths and shapes of magma chambers or pockets of magma, together with how the surface reacts to changes in magma pressure and depth, could aid in inferring magma-driving mechanisms. This knowledge has a dual benefit. First, it helps reduce the immediate and long-term impacts of volcanic eruptions and the risks associated with high-enthalpy geothermal drilling sites, such as minor earthquakes and ground subsidence. Second, strategic MPS assessments can help optimise energy extraction by guiding drilling operations away from magma zones or towards areas of enhanced geothermal potential (Elders et al. 2011).

This dual benefit can be achieved by having a detailed knowledge of the static and dynamic processes of the subsurface, which is usually expensive to obtain. Significant improvements in the cost, efficiency, methodologies, and feasibility of geophysical measurements, such as ambient noise tomography, are described in chapter 1 sec. 1.3.1. In geothermal applications, ambient noise techniques have been used to characterise the subsurface S-wave velocity field and to understand the temporal evolution of the velocity models from field operations in producing fields. Among other examples, ambient noise has been explored in both sedimentary and magmatic environments such as the Soultz-sous-Forêts (Calò et al. 2013; Calò and Dorbath 2013) St. Gallen geothermal site in Switzerland (Obermann et al. 2015), Alsace in France (Lehujeur et al.

2015), Mexico (Jousset et al. 2019; Martins 2018; Verdel et al. 2020; Granados et al. 2018; Verdel et al. 2019; Martins et al. 2020) and Iceland ("Ambient seismic noise monitoring and imaging at the Theistareykir geothermal field (Iceland)" 2022; Weemstra et al. 2016; Martins et al. 2019; Martins et al. 2020; Sánchez-Pastor et al. 2019).

As also reviewed in sec. 1.3.2 of chapter 1, SAR sensors coupled to satellites became a unique tool to measure deformation over large areas now with high temporal resolution. Compared with in situ leveling, the spatiotemporal resolution and coverage of SAR satellite missions, together with the reduction or elimination of fieldwork, are encouraging arguments to further investigate InSAR techniques. Among other applications, InSAR is used to infer the size, shape and depth of a volcano magma chamber through geophysical deformation modelling (e.g. Mogi (1958), Okada (1985), Fukushima et al. (2005), and Segall (2010)). In geothermal applications, the monitoring of geothermal production through InSAR techniques is growing fast, mostly used in volcanic environments to associate production with volume change given modelled sources, e.g. Jónsson et al. (2003), Fialko et al. (2001), Simons et al. (2002), Keiding et al. (2010b), Xu et al. (2017), Parks et al. (2018), Maghsoudi et al. (2018), Békési et al. (2019a), E. Martins et al. (2013), and Martins and Hooper (2012) or to estimate fault parameters of induced seismicity after stress development and fault reactivation due to production e.g., Pedersen et al. (2003), Jónsson et al. (2003), Hole et al. (2007), Yang et al. (2018), and Takada and Furuya (2010).

In this chapter, we investigate the potential of both techniques over the Torfajökull volcano. We used the Reykjanes Peninsula tomography of chapter 3 purely as an example of seismic imaging successes and limitations at volcanic-origin high-enthalpy geothermal sites. The locations of both the areas and the seismic campaigns used are displayed in Fig. 6.1. A complete description of the tectonic, geological, and seismic setting of the Torfajökull volcano can be found in sec. 2.4.2, and of the Reykjanes Peninsula in sec. 2.4.3 of chapter 1.

6.2. Data and Methodology

In this section we report on the processing of the deformation field over Torfajökull volcano. For the discussion section on the Reykjanes Peninsula, we refer to the InSAR results derived by Keiding et al. (2010b) and Parks et al. (2018) (see sec. 6.6).

Torfajökull 's Source of Subsidence by InSAR Time Series

To estimate the deformation field over the entire SISZ (South Icelandic Seismic Zone, Fig. 6.1), we processed the complete scenes of six ENVISAT tracks (three descending and three ascending modes) acquired between 2003 and 2010 and four ERS tracks covering the period between 1995 and 2009. The ERS data were mainly used to estimate historical displacements and to verify consistency in long-term displacement rates. They showed the same long-term rates as ENVISAT, and therefore our focus is on the ENVISAT results, which overlap with the seismic tomography period.

The temporal distribution of the six tracks is shown in Fig. 6.2. The omission of winter acquisitions was a deliberate strategy to preserve coherence, allowing us to maintain continuous interferometric coverage from summer to summer. The high latitude of Iceland provides the rare advantage of having six ENVISAT tracks covering the same

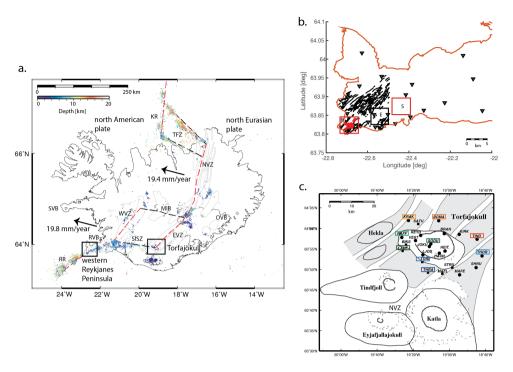


Figure 6.1: a) Map of Iceland with corresponding seismicity (1995–2015) and zoom of Reykjanes Peninsula and Torfajökull Volcano. b) West Reykjanes peninsula. Green triangles: onshore broadband stations for ~1.5 years chapter 4. Black lines: faults and fractures; squares: high-temperature areas: west to east, Reykjanes (R), Eldvörp (E), Svartsengi (S). c) Torfajökull seismic network and neighbouring volcanoes. Circles and squares: seismic network deployed in 2005 for about three months chapter 3. Box in south-central of map locates Torfajökull volcanic system at the intersection of the SISZ and EVZ, immediately north of Katla volcano.

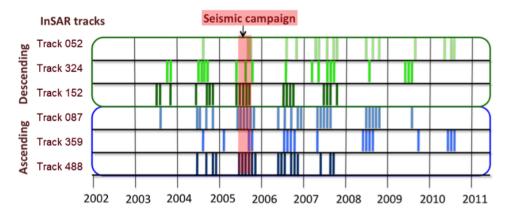


Figure 6.2: Time coverage of the available images of six ENVISAT tracks and time coverage of the 2005 seismic campaign (Fig. 6.1 c). Note the absence of winter acquisitions due to snow cover, which reduces coherence.

region. This dense coverage, combined with the differing acquisition geometries, allows better constraints on the estimation and decomposition of surface displacement vectors. The coverage of the total EVZ (Fig. 6.1) using ENVISAT and ERS required processing RAW (Level 0) SAR images.

We processed these using ROIPAC software (Repeated Orbit Interferometric Package) (Schmidt 2002) and generated interferograms with the Delft Object-oriented Radar Interferometric Software DORIS (Kampes et al. 2003). For time series, we applied the small-baseline approach of StaMPS (Stanford Method for Persistent Scatterers), including atmospheric correction extensions and supporting dependencies (Rosen et al. 2012; Foumelis 2018; Werner et al. 2002; Bekaert et al. 2015a; Bekaert et al. 2015b; Rosen et al. 2004). We corrected for the reference phase (flat-earth phase) and other geometric contributions to the interferometric phase, such as topography and orbits, using a 25 m digital elevation model (DEM) from the National Land Survey of Iceland and ESA DORIS orbits. We also corrected for drift in the local oscillator frequency of the ENVISAT satellite (Marinkovic and Larsen 2015). Ionospheric effects were not relevant for the C-band acquisitions. A multi-look of 5 in range and 4 in azimuth was applied for the small-baseline approach.

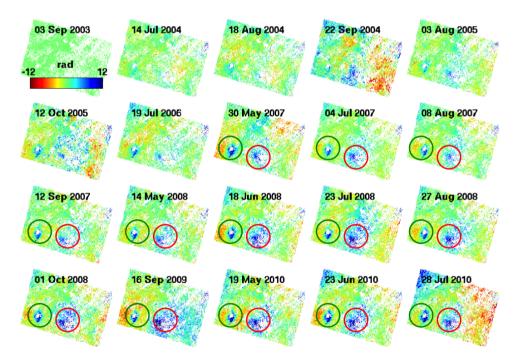


Figure 6.3: Cumulative LoS displacement in radians with respect to the first image 03 September 2003. Red circles locate Torfajökull volcano and green circles locate Hekla volcano both with increased distance from the satellite, therefore indicating subsidence.

Fig. 6.3 and Fig. 6.4 show two representative products of the ENVISAT 35-day repeat cycle. Fig. 6.3 presents the cumulative time series of LOS deformation in radians

6.3. Modelling 121

between 2003 and 2010 for descending track 324. Two coherent subsidence signals are visible: one under Hekla and one stronger beneath the Torfajökull volcano. The first scene, 03 September 2003, is used as the reference (zero displacement). The surface signal at Hekla is generally attributed to the thermal contraction of recent lava flows (Ofeigsson et al. 2011). Figure 6.4 summarises the LOS displacement rates derived from all six processed ENVISAT tracks; acquisition counts and timespans for each track are listed in Figure 6.2. The strongest deformation is a subsidence signal of up to 12 mm/yr, centred within the black outline of the Torfajökull caldera. Fig. 6.4 also shows the footprint of the six ENVISAT tracks around the Torfajökull volcano, recognised by its caldera. Not all tracks capture the subsidence signal (e.g., track 488, which has shorter temporal coverage; see Fig. 6.2). However, the most critical limitation is the lack of coherence within the caldera Torfajökull, caused by the presence of small glaciers and snow cover even during summer. The method of Samiei-Esfahany et al. (2016) improved coherence over this area, therefore it should be considered for future processing over this area. In this study, because of low coherence for two tracks, only four of the six tracks were used for subsequent modelling. These four tracks provided sufficient spatial and temporal coverage to constrain the 3D source modelling of the deformation field, discussed further in Section 7.1.2.

6.3. Modelling

6.3.1. Seismic Imaging

We use the methodology and results of ANT described for the Torfajökull volcano chapter 3 for seismic imaging.

The distribution of both seismic networks is shown in Fig. 6.1. The adopted procedure described in both chapters follows the following summarised approach: 1. Division of the ambient noise recorded at two stations in portions of one hour. 2. Cross-correlation of the corresponding portions and summation of the correlated results between all pairs of stations from which the surface-wave part of the Green's function is retrieved. 3. Tomographic inversion of the dispersion curves retrieved between pairs of stations. 4. Frequency-to-depth inversion to obtain the 3D S-wave velocity field.

6.3.2. Geodetic Imaging

To obtain the parameters of the source of the deformation, we use a forward model to find the source parameters that better fit the observed displacements. Then, guided by the forward modelling results, we inverted the displacements to solve for the parameters of a Yang magma source (Yang et al. 1988), a dipping prolate ellipsoid in an elastic half-space. The inversion is done using four tracks and using a nonlinear least-squares approach. The corresponding horizontal U_{xy} and vertical U_u displacements of the Yang prolate ellipsoid are calculated by the following relations:

$$U_{xy} = \frac{ab^2}{3\mu} r \left[\frac{2(1-2v)P^* - 2vP^{\bullet}}{R^3} + 3\frac{z_0^2 P^{\bullet}}{R^5} \right], \tag{6.1}$$

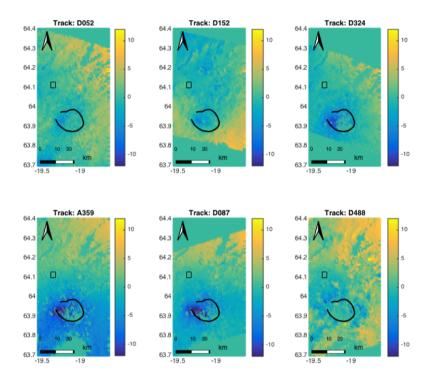


Figure 6.4: Velocity in mm/year of the six ENVISAT tracks. The small rectangle indicates the reference area and the black line outlines Torfajökull's volcano caldera.

6.4. Results 123

and,

$$U_{u} = \frac{ab^{2}}{3\mu} z_{0} \left[\frac{2(1-2\nu)P^{*} - 2\nu P^{\bullet}}{R^{3}} + 3\frac{z_{0}^{2}P^{\bullet}}{R^{5}} \right]$$
(6.2)

where $R = \sqrt{(x-x_0)^2 + (y-y_0)^2 + (z-z_0)^2}$, r is the horizontal distance from the centre of the spheroid to the observation point, λ and μ are the Lame parameters, and (x_0, y_0, z_0) are the coordinates of the centre of the ellipsoid.

6.4. Results

6.4.1. InSAR Time Series

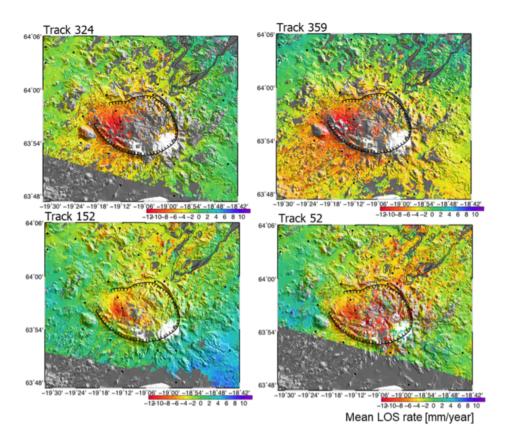
Using InSAR time series analysis from the two satellite missions covering approximately 13 years, we were able to detect a linear displacement within the Torfajökull caldera and estimate the displacement and velocity of each backscattered distributed point in time. We found a pattern of subsidence beneath the SW part of the caldera. This deformation signal has been ongoing since the start of ERS measurements – 1993 – and has been occurring until the end of the ENVISAT lifetime – 2010 – at rates of up to 13 mm/year. These results confirm the findings of Scheiber-Enslin et al. (2011) but with the use of four additional ENVISAT satellite tracks and a more extended time series. Although significant surface deformation was observed in the NE corner of the studied area, our modelling was limited to the Torfajökull region, which is outlined in Fig. 6.1. The estimated mean Line-of-Sight (LoS) velocity of four of the six processed tracks is shown in Fig. 6.5, with the volcano caldera outlined in black.

The trend of displacements in the NE-SW direction is attributed to glacial isostatic adjustment (GIA) due to the melting of the largest glacier in Iceland (Vatnaj"okull) and the rebound of the Earth's crust (Árnadóttir et al. 2009; Schmidt et al. 2012). Another uplift signal can be identified in Fig. 6.5 in the SE-most corner, which is also due to crustal movements due to Iceland's shrinking ice caps mimicking a magma inflow signal at Katla volcano (Spaans et al. 2015).

6.4.2. Modelling

In order to explain the estimated displacements from InSAR data, a model of a spheroidal body undergoing a uniform pressure decrease in space and time was used Eq. 6.1 and Eq. 6.2. The estimated InSAR displacements can be fit with low residuals using a model of a NE-SW oriented spheroidal body at \sim 5 km depth, undergoing a pressure decrease that is uniform in space and time. The best-estimate source of displacements is an ellipsoidal source starting at \sim 5 km depth, sized 4.5 x 5 km.

An example of the modelled source can be seen in Fig. 6.6 for track 324, with a preferential NW-SE orientation and located in the southern area within the volcano caldera. The residuals suggest that the modelled source can account for most of the deformation signal. However, a residual uplift or horizontal (moving westward) signal is left on the west side in opposition to a residual subsidence or horizontal (moving eastwards) signal in the east side of the modelled area, signalling a possible contribution of other superimposed source of deformation. A horizontal component of displacement, which may be associated with tectonic spreading, vertical displacement associated with GIA, or both, may explain the observed residuals.



 $Figure \, 6.5: Estimated \, mean \, LoS \, velocity \, of four \, out \, of \, the \, six \, processed \, tracks. \, The \, black \, line \, outlines \, the \, volcano \, caldera.$

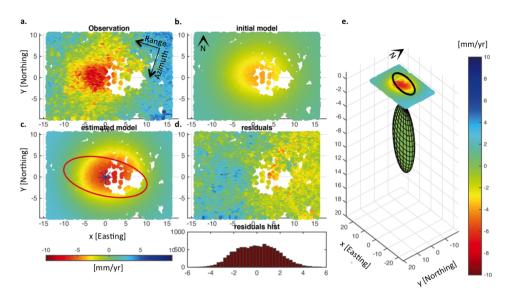


Figure 6.6: Modelling of the estimated displacements of Track 324 (a) with the corresponding initial model, final model and residuals (b, c, and d). In e) the estimated prolate spheroid in a 3D view.

Seismic ANT results from Fig. 6.7 do not show any anomalies below -10% of velocity variations from the mean velocity at the location of the subsidence signal. Fig. 6.6 shows the ANT results in a 3D model, with the vertical axis exaggerated for visualisation purposes. A low-velocity anomaly is detected, as expected for a magma chamber with molten or partially molten rock. The anomalies range from 7 to 15% for high-velocity anomalies and -7 to -15% for low-velocity anomalies, shown in blue and orange, respectively. The subsidence area is located between three prominent low-velocity anomalies detected by ANT in the south, southeast, and southwest, outside the volcano caldera and below 3 km depth. No abnormally low- or high-velocity anomaly was detected within the volcano caldera at the location of the modelled subsidence source.

6.5. Conceptual Model of Torfajökull Magmatic System

From ANT, we successfully identified velocity variations between approximately 1.5 km and 6 km depth. We find two areas with velocity anomalies between -10% and -15% located in the eastern and south-western investigation areas, outside the volcano caldera. These low-velocity anomalies are consistently present at depth in both the frequency and depth domains (green arrows in Fig. 3.13 and Fig. 3.14). In the eastern case, the velocity anomalies below -10% seem part of a larger hot body that extends in the SE and SW direction. Even with a more demanding selection of the number of ray-paths at each grid cell (minimum of 10 ray-paths per grid cell) at the edges of the horizontal layers, these low-velocity anomalies persist. Up to 4.5 km depth, we identify velocity variations below -10% in the NW quadrant outside the volcano caldera. The anomalies detected below -10% may indicate warmer material for all the depths

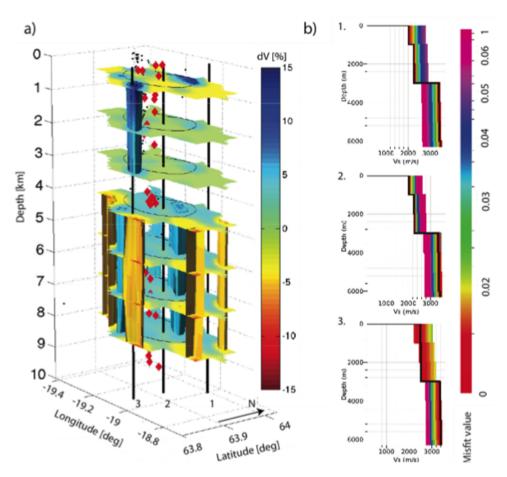


Figure 6.7: a) 3-D shear velocity model with reference to a 1-D velocity model at depth after Martins et al. (2019). The vertical axis is exaggerated for visualisation purposes. The circular-shaped black line represents the caldera outline at the surface. Black dots represent high-frequency earthquakes, and red diamonds are low-frequency earthquakes relocated by Lippitsch et al. (2005). Black vertical lines represent the centre of the grid cells of the profiles at b). b) Depth velocity of the 30000 models with the corresponding misfit. 1, 2 and 3 show examples of the inversion models for grid cells at the edges and centre of the modelled space. The black line represents the model with the minimum misfit.

explored.

Beneath the volcano caldera, we detected small areas with low-velocity anomaly reaching \sim -6% variation at most frequencies (marked with crosses in Fig. 3.13). Some of these features become more pronounced after the conversion from frequency to depth (Fig. 3.14 marked with crosses). This occurs because some grid cells with the lowest velocities at the model's edges are dropped out from the frequency-to-depth conversion because of information lacking at some frequencies. Even though the anomalies inside the caldera are less prominent than outside, the model is constrained by a higher number of ray paths. At shallower depths (up to ~3 km depth), velocity variations down to $\sim -10\%$ over small areas may also indicate hot material or possibly even the presence of small amounts of magma. These lower variations may be the origin of the high-temperature geothermal field at the surface (Bjarnason and Ólafsson 2000) as the location of both correlates well. From 3.5 km to higher depths, we detected a low velocity anomaly between -10 and -15% variation beneath the volcano caldera (Fig. 3.14e-j) extending spatially in a NW-SE fashion. In the same figure, we also plot the low- and high-frequency earthquakes. The events are displayed within 500 m above and below each inverted depth with reference to sea level. Low-frequency earthquakes, located beneath the caldera in the south-east quadrant, are interpreted to be related to the existence of viscous magma linked to a cryptodome formation (Soosalu et al. 2006). Low-frequency events occur near the zones of low S-wave velocity anomalies (Fig. 3.14 and Fig. 6.8 d2) that support the hypothesis of Soosalu et al. (2006). High-frequency earthquakes, interpreted as a brittle failure of the volcanic edifice, occur in areas where we see high or average velocity anomalies. These earthquakes, possibly related to fracturing due to thermal cracking (Soosalu and Einarsson 1997) or crystallisation processes (Scheiber-Enslin et al. 2011), are expected to be around average to high Swave velocity anomalies. The cross sections of the S-wave velocity field depicted in Fig. 6.8 (a2 to d2) provide additional insight into the spatial distribution of the discussed anomalies. Vertical cross sections crossing the south area beneath the caldera show lower S-wave velocities than elsewhere within the caldera outline (e.g., cross-sections a2 and d2 crossing the south part beneath the caldera as opposed to b2 and c2 crossing the northern area).

High-velocity anomalies with a ring-shaped structure, and following the shape and location of the caldera outline, contour the low-velocity anomaly (Fig. 3.14 NE quadrant between 4 and 5 km depth). Strong high-velocity anomalies following the north and northeast quadrants correlate well with lavas erupted at the surface (black arrows in Fig. 3.13 and Fig. 3.14). We interpret these as solidified eruption-feeding dikes, possibly corresponding to the Brandsgil (115,000 to 130,000 years before present) and Jokulgil (65,000 to 115,000) series of erupted rhyolites identified by Ivarsson (1992) (Fig. 6.8e). A feature catching the eye in the corresponding cross-sections (Fig. 6.8) is the abrupt change in velocity at the location of the caldera outline (vertical lines from a2 to d2), possibly due to the caldera collapse structure. Approaching the caldera outline from the outside to inside, we observe an increase in the S-wave velocity until it reaches the caldera outline location and then an immediate decrease. The speed change occurs with an S-wave velocity peak in the neighbourhood of the caldera outline. This is the case for most of the cross-sections we observe except for the cross-section in Fig. 6.8

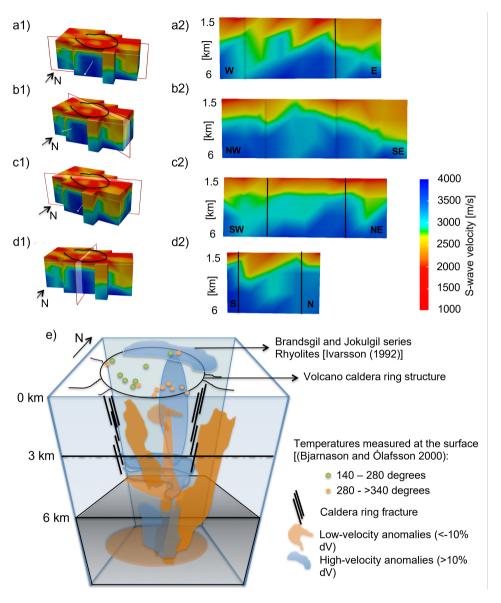


Figure 6.8: a to d: vertical cross-sections of S-wave velocities with corresponding locations (a1 to d1) and directions (a2 to d2). The black circle locates the volcano caldera which is projected to depth by the vertical black lines from a1 to d1. e: Conceptual model of Torfajökull volcano. The circle at 0 km depth conceptualises the volcano caldera with the remaining features identified in the legend figure (vertical exaggeration of approximately 4x).

c2. This exception may be because of different reasons. In the NE part of the caldera, we observe higher velocities interpreted as old dike intrusions. Therefore, the high-velocity anomalies might overlap the described caldera feature. In the western area, the described caldera feature might not be identified because in this area the caldera does not have surface manifestation. Note that the vertical lines are projected vertically at depth. Therefore, the (probably existing) dipping angle of the caldera fracturing at depth is not well represented here.

The overall S-wave velocity field (Fig. 6.8 from a to d) reveals anisotropy, which is typical for volcanic environments and can be accentuated by the magma mixing style of Torfajökull's eruptions (Blake 1984; McGarvie 1984). We propose a conceptual model of Torfajökull's magmatic system based on the tomographic results of this manuscript (Fig. 6.8e). The area where high-temperature geothermal activity is concentrated (> 140°C) (Bjarnason and Ólafsson 2000) is mainly located at the southeastern site within the volcano caldera and correlates well with a dip in s-wave velocities in the cross-section d1-d2 of the same figure. At this stage, we interpret the Torfajökull plumbing system up to 6 km depth as composed of possible molten or partial molten cavities and channels (orange features in Fig. 6.8e) relatively small compared to Torfajökull's caldera size. We display the location of the most prominent high-velocity anomaly in the northeast site (blue ellipse) beneath the volcano caldera, interpreted to be the dike intrusion in the origin of the Brandsgil and Jokulgil rhyolite eruptions.

These results indicate that if there is an established magma chamber within Torfajökull's caldera, it is likely to be deeper than the depths analysed. However, the shallowest part of it can also start at 4 to 5 km depth, as indicated by detected low-velocity anomalies. In case the low-velocity areas (velocity variations lower than $-10\,j\%$) are related to the presence of molten or partially molten rock at the estimated depths, three areas may be prone to eruption once the system is pressurised: the eastern and south-west sites outside the caldera outskirts and the south-east area beneath the volcano caldera.

6.6. Summary and Discussion

While the Earth's surface inflates or deflates as a result of tensile or compressive internal forces (stress) in the subsurface, geodetic measurements are used to quantify the amount of deformation (strain) at the surface. Surface displacements in geothermal areas can be a result of coupling processes such as flow, pressure build-up/release during pore volume increase/reduction, reservoir cooling; or in case there is no production, natural processes such as contracting due to cooling, regional extension, crystallization, expansion due to gas exsolution, and ongoing hydrothermal activity. If, on the one hand, these are time-dependent processes that can be modelled dynamically, on the other hand, surface displacements can also be used to solve for subsurface characterisation (e.g., fault-plane solutions or magma reservoir) through geodetic imaging. As seismic waves travel through the Earth's interior, they can be accelerated or decelerated depending on the different materials encountered along the seismic propagation path. With respect to a reference velocity model as a function of depth, it is possible to estimate velocity anomalies and distinguish different subsurface structures (static model) by seismic imaging. Other ambient noise seismic interferometric methodologies can also

identify temporal changes in wave propagation due to processes in the subsurface, namely geothermal production Donaldson et al. (2019).

Table 6.1: Summary of the main characteristics concerning the two techniques used in this thesis: Geodetic imaging with respect to InSAR time-series and Seismic Imaging using Ambient Noise Tomography.

	Geodetic imaging (InSAR based)	Seismic Imaging (ANT based)	
Input Data	Satellite SAR images: RAW (level- 0) or SLC (Single Look Complex images)	Network of seismometers: Vertical or/and horizontal (for anisotropy studies) component of displacements.	
Intermediate and final products	Surface deformation, surface morphology and reflectivity	Retrieval of surface waves from seismic interferometry. Azimuthal velocity variations, S-wave velocity field, S-wave velocity anomalies.	
Spatial Coverage	Scene size (ground footprint) depending on the satellite: 20x20 km or up to 250 km swath (length along a track)	Dependent on the station- network configuration and interstation distances. Can be applied for local, regional or global networks.	
Temporal coverage	Dependent on satellite sensor and location on Earth surface. Earliest in 1991 (ERS-1/2) up to current date (Sentinel-1)	Dependent on availability of seismic data	
Temporal sampling	Depending on satellite revisiting time and desired resolution. With Sentinel-1 it is possible up to 6.days. Future satellites (e.g., CubeSats) may provide an even higher temporal sampling.	Dependent on the type of seismic instrument, only applicable for tomography if tomographic inversion is performed using different temporal seismic acquisitions	
Spatial reso- lution	Depentent on the satellite: from 1 to 20 m	Dependent on the station- network configuration and interstation distances.	
Sensitivity at depth	Dependent on the radius-to- depth source ratio	Dependent on the bandwidth, interstation distance and sensitivity kernels.	
Main error sources	Phase unwrapping especially in areas of low coherence, variation in atmospheric properties, topography, orbital errors.	Limited ambient noise (source) energy, limited number of stations, non-uniform source distribution, presence of multiple surface wave modes, wrong phase/group velocity picks.	

Final and Intermediate products

Final: Source geometry, volume change, depth, location. Intermediate: Rate of displacements, time-series of displacements Final: 3D S-wave velocity field, S-wave velocity anomalies. Intermediate: Empirical Green's functions, Ballistic Surface waves, azimuthal velocity estimation, time-dependent

Advantages over similar techniques

Limitations

Cost-effective, large area coverage, of centimetre to millimetre levels of accuracy, depending on the AOI possible to go back to 1992 deformation measurements, measurements regardless weather conditions, no fieldwork requires

Possible to recover past seismic acquisitions, no need for active sources or earthquakes therefore economical.

Locating heat sources, complementary to understanding MT results, general subsurface characterisation (lithological variations with depth), the estimated S-wave velocity field can be used to constrain induced event location.

3D S-wave velocity derived but not P-wave, long acquisition periods are required.

Applications

Reservoir pressure change estimation (with the corresponding spatial extent), monitoring of production after effects (e.g., subsidence), locating structures controlling the geothermal fluid movement (e.g.,faults, calderas, basement and lateral permeability controls)

Locating heat sources, complementary to understanding MT results, general subsurface characterisation (lithological variations with depth), the estimated S-wave velocity field can be used to constrain induced event location.

Iceland is an excellent location to test both techniques due to the high SNR achieved using radar and passive seismic interferometry. Except for snow cover periods, InSAR interferograms are usually highly coherent due to low-density vegetation coverage and extensive rock coverage, which provides consistency in the backscattered signal between SAR acquisitions. The empirical Green functions derived from the seismic interferometry of the ambient noise are equally coherent, and the ambient noise sources are highly energetic, arriving from the ocean in almost every direction (chapter 3 and chapter 4).

In Tab. 6.1, we summarise some of the most relevant characteristics of both described techniques. Note that in this study, we focus only on generating geodetic or seismic imaging products based on the chosen imaging methods. The same holds for the parameters described in Tab. 6.1. However, both datasets ('Input data' in Tab. 6.1) can be processed differently to access other subsurface processes such as, e.g. fault solutions

after induced seismicity events modelled from single interferograms using InSAR or temporal changes due to production, from coda waves. Additionally, for both case study applications, seismic images of shallower depths would be preferred for a possible confrontation with production data. For this, using higher recorded frequencies of ambient noise or a combination of group and phase velocity picks and further inversion from frequency to depth would allow a more comprehensive knowledge of the shallow subsurface.

These results confirm that both InSAR and seismic tomography perform reliably in the Icelandic geological setting. This demonstrates the potential for broader application. A systematic deployment of seismic tomography in all volcanic systems in Iceland, coupled with routine InSAR monitoring, could substantially improve volcano monitoring, early warning capabilities, and long-term hazard assessment. Similarly, integrating InSAR, GNSS and seismic tomography with geothermal well measurements enables joint recovery of reservoir and geomechanical parameters, such as fluid extraction and injection rates, pressure evolution, reservoir compaction and expansion, subsurface structural geometry, and temperature—permeability distributions. Although well measurements provide most of the required parameters for geothermal operations, this integrated approach can offer a powerful framework to improve our understanding of fluid flow and heat transport processes, as well as mapping partially molten areas, serving both resource management and risk mitigation strategies.

Summary And Conclusions

The main research objective of this study was to assess the added value of the individual and synergistic use of radar and seismic interferometry for imaging MPS's on active volcanoes in Iceland. This objective was addressed through the implementation of the methodologies and a feasibility assessment over three active volcanic areas: Eyjafjallajökull, Reykjanes Peninsula, and Torfajökull volcano. In this chapter, I revisit and provide conclusions on the research objectives outlined in sec. 1.5. I also provide a summary of the study, discuss its limitations, and highlight key recommendations and key contributions.

7.1. Scientific contribution

In this study, I have demonstrated the potential of using geodetic and seismic imaging techniques to improve our understanding of magmatic plumbing systems (MPS). To achieve this, I defined three sub-goals. First, I developed and applied ambient noise tomography to image MPS, and created a newly derived phase velocity estimation method. Second, I estimated InSAR time series deformation rates and constrained deformation rates and volcano source modelling with other space-based or in situbased techniques. Third, investigate the MPS associated with volcanic activity or unrest in three volcanic systems: Eyjafjallajökull, during its 2010 eruption, Torfajökull, which shows unrest, and the west part of the Reykjanes Peninsula, which is subject to geothermal exploitation and where two volcanoes recently erupted. Below, I provide a summary of the findings and a discussion of the results related to these sub-goals.

7.1.1. Seismic imaging: 3D Volcano Subsurface Tomography with Ambient Noise Seismic Interferometry

Objective: Develop, process, and validate an approach to extract phase-velocities from ambient seismic noise using seismic interferometry (SI) and optimise it for volcano 3D shear-wave tomographic studies.

The strategy to retrieve ballistic surface-waves (BSW) from ambient noise using SI and optimise it for 3D subsurface tomographic studies was summarised in Fig. 4.2 (page 65). The developed approach encompassed several steps: first, the retrieval of BSW by seismic interferometry, followed by the estimation of phase-velocities from the BSW, ultimately leading to the estimation of the 1D, 2D, and 3D shear-wave velocity models. For phase-velocity estimation, a new method was introduced. The approach also took into account a quality control procedure, which involved selecting inter-station

travel-times, selecting reliable frequencies for phase-velocity estimation of the retrieved surface waves, and quality checks during the tomographic inversions. Within the context of the tomographic image, the resolution was exploited as a way to detect anomalies within the extent of the high-enthalpy geothermal field. In the following sections, key conclusions of the adopted and developed methodology are outlined.

Retrieval of Ballistic Surface Waves from ambient noise

Using two different seismic networks for Torfajökull (for 100 days, chapter 3) and the western part of the Reykjanes Peninsula (for 1.5 years, chapter 4), it was possible to retrieve empirical Green's functions from ambient-noise. The empirical Green's functions obtained from ambient noise, particularly the BSW, exhibit remarkable clarity and coherence in Iceland's seismic networks.

This quality is evident from several indicators. First, the analysis of the power spectral density and the spectrograms highlighted a notably high signal-to-noise ratio in the frequency range of 0.1 to 0.4 Hz. This broader bandwidth, compared to other locations, allowed the extraction of signals sensitive to a wider range of depths.

Moreover, the conventional practice of extensive temporal averaging or stacking, often employed to converge retrieved signals toward the BSW portion of the Green's function, proved challenging for Torfajökull. Yet, even with only 100 days of seismic recordings (as detailed in sec. 3.2.1), coherent empirical Green's functions were obtained. It is worth noting that the potential to reduce the number of days for temporal stacking opens up the possibility of repurposing historical seismic networks originally designed for earthquake tomography to facilitate ambient-noise retrieval.

Finally, beyond the highly coherent retrieved BSW, the beamforming results reinforce ambient noise quality particularly in terms of azimuthal coverage. The beamforming results of both seismic networks indicated an apparent surface-wave velocity of 3 km/s and exhibited evidence of anisotropic noise distribution. Despite the non-isotropic nature of the noise distribution, both seismic networks showed sufficient illumination from at least two quadrants (spanning an angular range of at least 180°). This enabled us to choose between the causal or the a-causal BSW arrivals.

Surface-wave phase velocity estimation

The method developed in this thesis to estimate phase velocities initially involves phase picking in the frequency domain and subsequently in the time domain. The average phase velocity was first extracted using the multichannel surface-wave method (MASW). This enabled the extraction of phase velocity from the amplitude spectrum, preserving the phase-spectrum information. MASW performed well despite several challenges, including suboptimal seismic network configurations, ¹ local noise sources, scattered waves, and phase ambiguity estimation problems. The results also revealed a clean retrieval of surface waves with no higher modes or unexpected arrivals.

The number of ray-paths per frequency is dependent on the inter-station distance as the quality of the retrieved ballistic surface waves degrade when inter-station distances are too short or too large. For short inter-station distances, the retrieved arrivals at

¹The Torfajökull array is slightly skewed in the NW-SE direction, while the Reykjanes Peninsula array is skewed in the NE-SW direction

positive and negative time lags interfere with each other, resulting in less accurate timing picks. For large inter-station distances, the direct waves interfered with scattered-wave arrivals, which complicated the phase picks. Therefore, a minimum and a maximum inter-station distance threshold was set.

With the method newly developed in this thesis for phase-velocity extraction (sec. 3.3.3), it was possible to reject frequencies for which the average virtual source phase term deviates from the expected value $\pi/4$. Frequencies for which the best-fitting phase term of the virtual source does not come close to a physical source term were dropped for further analysis. The advantage of this method over other source-phase estimation methods is its applicability to arbitrary array configurations. The downside is that the presented method requires enough pairs of stations to fit a time-distance curve reliably. As demonstrated for the case studies in this thesis (Chapters 3 and 4), even for the case with fewer seismic stations, the minimum number of station pairs is enough to extract consistent phase-velocities with this method.

The estimation of phase velocities also demonstrated consistency in the azimuthal phase velocity. For both volcanic areas studied, the azimuthal phase velocities showed a smooth variation between adjacent frequencies, keeping consistent velocity variations. Thus, the evaluation of phase velocities confirmed their consistent increase in a monotonous manner with the inverse of the frequency.

1D, 2D, and 3D shear wave velocity, accuracy, and model resolution

The 1D to 3D velocity models were derived through the sequential seismic workflow (A) (cf. Fig. 2.1, p. 18). The 1D phase velocity was estimated in the wavenumber-frequency domain using MASW and then in the time domain inversion step 1A). The 2D shearwave velocities were estimated with the 1D velocity as a reference and by development and application of tomography in the frequency domain, known as inversion step 2A. The 3D tomography in the frequency domain was derived in step 3A, and the 3D-shearwave velocity model was estimated after the inversion from frequency to depth, known as inversion step4A.

In the tomographic inversion process, specifically in step 2A, a first-order statistical Tikhonov regularisation was effectively incorporated to account for the ill-posedness nature of the problem. Using a cross-validation approach ensured that the regularisation parameter was finely tuned even when estimated independently for each frequency. This was evidenced by the low RMSE across 2D frequency-dependent outcomes, affirming the robustness of the estimator, and by the smoothly transitioning velocities decreasing monotonically with increasing frequency, underpinning the reliability of the velocity estimates.

In inversion 3A, a neighbourhood algorithm (NA) was applied in a Monte Carlo approach to the dispersion curves of each grid cell derived from inversion step 2A, the 3D V_S model. The estimated 3D model standard deviation from the 10% best models (out of 3000 models) had a minimum misfit between 0 and 150 m/s. For Torfajökull (sec. 3.5.2), the standard deviation of the 3000 models is in the order of 20 m/s indicating a minimal misfit. This deviation reflects a change in wave speed between $\sim 0.5\%$ and $\sim 1\%$ depending on the analysed depths. The results obtained over the Reykjanes network displayed a similar order of magnitude.

Regarding the resolution of the final 3D shear-wave velocity estimation, a tradeoff exists between resolution and reliability. Due to the characteristics inherent to the application sites and corresponding seismic networks, the depth resolution of the tomography was exploited using Torfajökull's network and the horizontal resolution using the Reykjanes Peninsula network.

In the tomography of chapter 3 a resolution was fixed to 4 km and checkerboard tests successfully reproduced the simulated checkers for the chosen resolution. Afterwards, in the inversion from frequency to depth (inversion 3A), the S-wave velocities were estimated from two independent runs with interspersed boundary layers using the same modelling setup. One model runs with depth limits between 1.5 and 5.5 km, while the second model runs for depth limits between 2 and 6 km, both with 1 km vertical resolution. The results of both model runs, now with 500 m depth resolution, describe a smooth velocity variation and the resultant averaged 1D model exhibits consistency with previously published studies. In theory, a higher resolution could be achieved by iterating model runs with different depth interfaces as unknowns during the inversion to depth (inversion 3A). However, this approach has the potential to introduce artificial features in practice.

For the Reykjanes Peninsula network (chapter 4), since the network is denser than for Torfajökull, it made sense to test different combinations of horizontal resolutions and anomaly sizes. For each of these combinations, checkerboard sensitivity tests were used, constrained by the Tikhonov regularisation parameter previously estimated (inversion 2A) for each frequency value. The resultant dispersion curves of the four tested horizontal resolutions (1 to 4 km with steps of 1 km) exhibit similarities, indicating stable outcomes even at higher resolutions, such as 1 km. This observation is further supported by the consistent values of the regularisation parameter for each frequency and resolution, which were estimated independently.

While ANT techniques are suitable to derive 3D shear-wave velocity fields, the straight-ray approximation often employed holds under the assumption that the retrieved surface waves follow a direct path between stations. This assumption is valid only in uniform media. As soon as the waves cross, e.g., a 'fast body' or a medium-contrast of finite size, the use of tomographic cells with a smaller size violates the direct wave assumption. Therefore, despite the excellent fit between the dispersion curves and the resulting velocity anomalies obtained at both lower (4 km) and higher (1 km) horizontal resolutions, there should be caution when interpreting higher-resolution solutions. For further Reykjanes Peninsula interpretation, the 3 km resolution was selected. In chapter 6, the 1 km resolution solution was exploited to comment on the possible added value for volcano monitoring and geothermal applications.

7.1.2. Geodetic Imaging with constraints: MPS's geometry from deformation modelling and seismics

Objective: Design, process, validate, and evaluate the deformation estimated from InSAR time-series followed by modelling the magmatic plumbing systems' geometry, size, and depth.

To achieve this objective, the first step involved processing SAR acquisitions into InSAR time-series products for two volcanoes. TerraSAR-X time-series data spanning a year were processed to cover the 2010 Eyjafjallajökull volcanic eruption. For Torfajökull, nearly 25 years of ERS and Envisat acquisitions were processed. Different approaches for geodetic imaging of MPS were chosen for the two case studies, depending on the deformation rate and available constraints.

Processing

The processing of SAR imagery for deformation estimation was influenced by several interconnected variables, including sensor characteristics (spatio-temporal resolution, image availability, and wavelength), characteristic of the Area of Interest (AOI) (i.e., surface cover, topography), and the nature of deformation (linear/non-linear in time and space). The processing aimed to reduce error sources (such as atmospheric and orbital errors) and increase the number of point-scatterers to minimise unwrapping errors caused by snow, glaciers, and large magnitude displacements associated with the eruption. Additionally, the processing was focused on extracting the deformation signal of interest from other superimposed signals. The temporal resolution of TerraSAR-X data was particularly valuable for capturing changes in displacement during the pre-, co-, and post-volcanic phases of the 2010 Eyjafjallajökull eruption, providing insights at GPS locations at higher spatial resolution (chapter 5). However, for volcanic eruptive-related displacements, smaller wavelengths (such as X-band) may not be ideal due to the likelihood of phase unwrapping errors associated with high magnitude and non-linearity of the displacement patterns during the eruptive cycle. Given the AOI characteristics, which included glaciers and snow cover, winter acquisitions were excluded to retain coherence in the interferograms.

The displacements accompanying the 2010 eruption were also captured and detected in ENVISAT data processing aimed at the Torfajökull volcano, although only two coherent acquisitions were available after removing winter scenes. The main added value of using the ERS and Envisat acquisitions was to cover the period of the seismic network used. Almost 25 years of acquisitions were processed from RAW format (level 0) to allow a wider swath over the study area, supporting longer-term deformation analysis.

Deformation modelling from InSAR and GNSS time-series

In the Eyjafjallajökull case study, chapter 5, GNSS data was used to enhance and complement the results obtained from the InSAR analysis. The high temporal resolution of the GNSS time series served three crucial purposes. First, for validation of the InSAR time series. By comparing InSAR and GNSS data, after conversion to the Line of Sight (LOS), it became possible to identify unwrapping errors in the InSAR time series. Second, as a constraint for magma chamber estimation. The displacement rates estimated from GNSS, when jointly considered with the InSAR displacement rates, allowed for a more precise determination of the size, shape, and depth of the magma source as well as indications of when the model is a better or worse fit by analysing the residuals.

The use of InSAR measurements to monitor volcanic unrest has consistently demonstrated the benefit of including at least one GNSS station for external data validation. This integration proves to be especially crucial in the context of monitoring ice- and snow-covered volcanoes, where the exclusion of winter acquisitions is necessary to

maintain interferogram coherence. The existing GNSS stations provide essential prior knowledge of the anticipated deformation, which informs the geodetic measurement acquisition strategy and guides the selection of suitable InSAR processing parameters.

Geodetic Imaging with seismic and GPS constraints

With the estimated displacement rates, the magma source depth, shape, and volume change were modelled for Torfajökull and Eyjafjallajökull volcanoes.

For Torfajökull, a forward inversion of the InSAR and GNSS displacements indicated a best-fit ellipsoidal source at \sim 5 km depth. This depth coincides with the low-velocity anomaly imaged in chapter 3, suggesting that the deformation source and the seismic anomaly are physically linked. However, the full Bayesian inversion using a Markov chain Monte Carlo (MCMC) framework was not performed in this study; instead, this is proposed as future work. Such a framework would allow the incorporation of prior knowledge from seismic tomography and provide a probabilistic assessment of uncertainties.

For Eyjafjallajökull, the integration of seismic and geodetic observations provided an instructive methodological example. A forward model based on the four vertically aligned sills hypothesised from seismicity (Tarasewicz et al. 2012b) failed to reproduce the observed surface displacements, yielding residuals an order of magnitude larger than the InSAR and GNSS measurements. In contrast, the joint inversion of the InSAR and GNSS time series favoured a three-dimensional ellipsoidal source at 6–7 km depth, with a gradual volume reduction throughout the post-eruptive phase. This demonstrates the added value of combining seismic and geodetic datasets, where joint inversions can better constrain source geometry and evolution compared to forward models based solely on seismicity.

7.1.3. Icelandic MPS: Modelling and interpretation

Objective: Evaluate and interpret the results over each AOI for which the techniques were individually or mutually applied.

Torfajökull: At the Torfajökull volcano I applied both seismic imaging (chapter 3) and geodetic imaging (chapter 6). I successfully identified V_S variations between approximately 1.5 km and 6 km depth, with low-velocity anomalies ranging from -10% to -15%. These anomalies are observed in two distinct areas: the eastern and southwestern regions outside the volcano caldera, where they persist at different depths and frequencies. Beneath the caldera, we detected small low-velocity anomalies that reached approximately -6% at most frequencies. Some of these anomalies become more pronounced after frequency-to-depth conversion, despite loss of edge data. At shallow depths (up to ~ 3 km), velocity variations down to $\sim -10\%$ in small areas suggest hot material or potentially even small amounts of magma, which may be responsible for the high-temperature geothermal field on the surface. From 3.5 km depth and deeper, we observe a low-velocity anomaly between -10% and -15%, which spatially extends in a direction NW-SE below the caldera.

Seismicity patterns support these interpretations. Low-frequency earthquakes are concentrated beneath the southeastern quadrant of the caldera, coinciding with low V_S anomalies and indicating viscous magma, possibly linked to cryptodome formation. High-frequency earthquakes, attributed to the brittle failure of the volcanic edifice, occur in regions of high or average velocity, possibly due to thermal cracking or crystallization processes.

High-velocity anomalies outlining the caldera form a ring-like structure, with stronger anomalies in the north and northeast quadrants. These correlate with surface-exposed lavas, likely representing solidified eruption-feeding dikes from the Brandsgil (115,000–130,000 years before present) and Jökulgil (65,000–115,000 years before present) rhyolite eruptions. The abrupt velocity changes at the caldera outline suggest a structural feature associated with caldera collapse.

Based on these tomographic results, we proposed a conceptual model of Torfajökull's magmatic system. High-temperature geothermal activity (above 140°C) is mainly concentrated in the southeastern caldera, which correlates with a decrease in V_S . The plumbing system, extending to 6 km depth, consists of relatively small molten or partially molten cavities and channels. Although a large and established magma chamber within the caldera is not directly evident, the shallowest part of such a structure may begin at 4–5 km depth, as indicated by the low-velocity anomalies. Surface displacements show a consistent subsidence pattern within the volcano caldera, with the most prominent subsidence occurring in the southwestern region of the caldera. Inverse and forward models of surface displacement indicate that the magma chamber can be fitted with a spheroid at ~5km depth. By seismic imaging, an area of potential melt or partial melt within the volcano caldera at ~5 km might be the source modelled by InSAR.

If the observed low-velocity areas (< -10% variation) correspond to molten or partially molten rock, three regions are particularly prone to future eruptions in the event of system pressurization:

- The **eastern** site outside the caldera outskirts,
- The **southwestern** site outside the caldera outskirts,
- The southeastern site beneath the volcano caldera.

These findings provide crucial insights into Torfajökull's magmatic system, its geothermal implications, and potential eruption scenarios. However, as with InSAR, ambient noise tomography alone cannot conclusively identify mush zones: low-velocity anomalies may equally reflect high temperatures, partial melt, or altered lithologies. Robust confirmation of a mush zone in Torfajökull would require joint constraints from petrology, attenuation studies, reliable variations in $V_{\rm P}$ for $V_{\rm P}/V_{\rm S}$ estimates or receiver function analyses.

Eyjafjallajökull's 2010 co- and post-eruptive source modelling The results of TerraSAR-X and GPS analysis showed that the 2010 eruption of Eyjafjallajökull cannot be explained

by a simple sill beneath the summit, as earlier models suggested. Instead, a three-dimensional ellipsoidal source at 6–7 km depth better accounts for the observed deformation. Seismic event relocations had suggested a stack of four depressurising sills (Tarasewicz et al. 2012b), but these models fail to explain the geodetic data.

This discrepancy highlights that the plumbing system is unlikely to consist of fully molten, pressurised sills and instead requires a three-dimensional magma reservoir. However, a fully molten chamber would not explain the observed seismicity, since earthquakes cannot nucleate within a homogeneous melt. Combined with petrological evidence for mixing of older and newly intruded magma, a more plausible interpretation is that both seismic and geodetic constraints point to a partially molten, crystal-rich mush system. In such a framework, seismic events occur within a heterogeneous mixture of melt, crystals, and volatiles rather than within discrete magma chambers. The Eyjafjallajökull case, therefore, may be reinforcing a broader shift in volcanology: magmatic plumbing systems are increasingly recognised as dynamic, mush-dominated networks rather than simple, fully molten reservoirs.

Seismic event relocations had previously suggested a vertically aligned stack of four sills depressurising with time (Tarasewicz et al. 2012b). However, forward models based on this hypothesis failed to reproduce the observed surface displacements, yielding residuals much larger than the geodetic uncertainties. This discrepancy indicates that while seismicity effectively traced zones of brittle failure and transient fluid migration, these features are unlikely to represent fully molten pressurised sills. Instead, they can be more plausibly interpreted as seismic activity within a partially molten, crystal-rich mush system.

Taken together, the geodetic and seismic observations support an interpretation of the Eyjafjallajökull plumbing system as mush dominated rather than composed of discrete sill-shaped chambers. This perspective aligns with broader developments in volcanology, where magmatic systems are increasingly recognised as dynamic networks of melt, crystals, and volatiles rather than simple reservoirs.

Reykjanes Peninsula The observed V_S anomalies exhibit variations ranging from 0.85 to 1.15 times the estimated 1D velocity model within the depth range of 2 to 6 km. Tomography achieved a lateral resolution of 3 km and a vertical resolution of 1 km. The lower V_S anomalies could be indicative of pockets that potentially contain partially molten material, where the V_p/V_s ratio offers further insight into this interpretation. The higher V_S anomalies suggest the possible existence of older intrusions that have solidified and became more rigid. In addition, these structures may also result from cooling effects associated with proximity to the ocean.

The geological setting of the Reykjanes Peninsula is more sensitive to magma intrusion through dikes along the NE-SW trending region, exemplified by the high density of fissures and faults. However, this tectonic context does not appear to favour the presence of large magma chambers. This observation is consistent with the findings of this study chapter 4 using seismic ambient noise tomography over Reykjanes Peninsula. Relatively small extensions of low-velocity anomalies, resembling lenses or possibly sills were detected, some of which at shallow depths 1 to 3 km. One of these low-velocity anomalies was located below the location where the volcanic eruptions of

Geldingadalur, Fagradalsfjall, and Litli-Hrutur occurred in 2021, 2022, and 2023, respectively. The largest low-velocity anomaly is located below the most recent series of volcanic eruptions from December 2023 to December 2024, near Grindavík and the Blue Lagoon. Overall, the study area in the western part of the Reykjanes Peninsula indicates the presence of low-velocity anomalies, which after spatial correspondence with the location of the recent volcanic series seem to be the magma source related to the eruptions. There is no evidence for a large mush-dominated reservoir, consistent with a tectonic-dike-dominated setting. However, similar to the Torfajökull volcano, ANT alone cannot unambiguously prove mush, only low-velocity anomalies that may be linked to partial melt.

7.2. Recommendations

Clearly, the results from this study, based on choices and assumptions related to data and methodology can be subject of academic discussion, and lead to recommendations for future research. Thirteen main recommendations are listed below.

- A different approach involving the *extraction of both group and phase velocities*, followed by joint inversion from frequency to depth, may yield tomographic results at shallower depths. This may be valuable for sites with seismic campaigns since it can potentially enhance our understanding of the hydrogeological system.
- 2. In terms of inversion methods, the Gauss-Markov formulation used in this study for depth-dependent seismic tomography primarily focused on deterministic aspects. In addition to using the neighbourhood algorithm (NA) in a Monte Carlo approach to estimate the 3D model standard deviation from the 10% best models, the uncertainties of the estimated dispersion curves can also be formulated stochastically, as variance of the observations. Recent methods, such as transdimensional tomography, are promising in this context.
- 3. The *adoption of reflection seismic techniques*, as initially explored for Torfajökull seismic network, may offer a complimentary perspective. Further exploration of reflection seismic methods may shed light on the expected behaviour of S and P waves, potentially aiding in interpreting cross-correlation panels and providing insight into shallow reflections.
- 4. Incorporating *time-dependent analysis into seismic interferometry* may enable comparisons with InSAR displacements, potentially revealing dynamic changes in the subsurface.
- 5. This study has explored the relationship between heterogeneity dimensions of the medium and the selected cell size for inversion, using checkerboards and forward models in seismic configurations. Full-waveform modelling in 2D synthetic velocity models may achieve more reliable results, which can be tested to specific seismic acquisition configurations. The relationship between medium heterogeneity and cell size can also be assessed by comparing the velocity model obtained through straight-ray tomographic inversion of observed travel times to the

- *synthetic velocity model.* These results may lead to valuable recommendations for the practical use of ANT over geothermal reservoirs, focusing on uncertainties concerning model resolution.
- 6. It is recommended to exploit the complementary nature of ambient noise tomography and earthquake tomography by using the 3D V_S models obtained from ANT as initial input for precise earthquake relocation. This integrated approach could enhance the accuracy of the earthquake depth estimation and provide details where earthquake tomography lack illumination.
- 7. Leveraging *more recent Synthetic Aperture Radar (SAR) data*, such as Sentinel-1 over Torfajökull, can be used to extend the available time series data, allowing for the confirmation or assessment of changes in subsidence rates over time.
- 8. Given the demonstrated insights on the spatial and temporal coverage that TerraSAR-X provided covering the Eyjafjallajökull eruption, volcanic eruptions should have have acquisition privilege over competing requests during crises. This holds especially when no other non-commercial satellite acquisitions are available that would be fit for purpose, as it was for the 2010 Eyjafjallajökull eruption.
- 9. ESA could consider providing access to the algorithms utilised to transition from RAW Level 0 to level 1. Such step would benefit the users enabling them to process wider geographic areas using historical data more effectively and easier to compare with Sentinel-1.
- 10. A better deformation rate model should be used in chapter 5. A model using an exponential decay may provide a better magma source geometry and volume change estimation of the post-eruptive deflation source. An inversion scheme with a better deformation rate estimation should be revisited.
- 11. To better understand the linear subsidence observed at Torfajökull, a crystallisation model should be employed to investigate whether the subsidence rates align with the cooling or crystallisation of a magma chamber at depth. These models can be either analytical or of the Finite Element Modelling type.
- 12. In relation to chapter 6, continuous or semi-continuous GPS observations could have constrained the decomposition of the residual horizontal component of the deformation signal (which seems to be of tectonic origin) and magma source geometry.
- 13. Finally, I also recommend to explore the potential of machine learning algorithms to integrate InSAR and seismic data. Approaches such as neural networks or ensemble learning could automate the identification of patterns or correlations between datasets at certain time instances.

7.3. Main Contributions

7.3.1. Summary of Contributions

The main contributions of this research are:

- 1. The generation of the first 3D subsurface image of Torfajökull volcano, resolving ring-shaped high-velocity and discrete low-velocity anomalies. I detected high-and low-velocity anomalies, which we correlate with old dike intrusions and small pockets of possible molten rock, respectively. I identified a potential start for a magma chamber at 5 km depth. Methodologically, I showed that the retention of coherent EGFs from relatively short temporal stacks (approximately 100 days) allows the repurposing of historical seismic networks for ANSI tomography (chapter 3).
- 2. Derivation of a 3D V_S model of the Reykjanes peninsula from ANSI tomography covering the Geldingadalur, Fagradalsfjall and Litli-Hrutur eruptions and three geothermal fields. Low- V_S zones (strongest < -15%) coincide spatially with uplift and eruptive centres active in 2024. Anomalies are most robust in regions of high path density and multi-azimuth coverage with cautious interpretation near model edges due to reduced checkerboard amplitude recovery (chapter 4).
- 3. Introduction a method to efficiently estimate phase speeds, resolve the phase ambiguity term, and quantify the reliability of the retrieved surface waves (developed in chapter 3 and used in chapter 4).
- 4. Regularisation of the ill-posed tomographic inversion with a Tikhonov regularization with a cross-validation method to solve the choice of regularisation parameters (derived in chapter 3 and used in chapter 4).
- 5. Inversion of dispersion curves using a Monte-Carlo neighbourhood algorithm to obtain depth-dependent V_S profiles and ensemble uncertainty (developed in chapter 3 and used in chapter 4).
- 6. Design of a quality control workflow to assess the ANSI tomographic results by combining (i) beamforming-based azimuthal diagnostics, (ii) temporal coherency screening of empirical Green's functions, and (iii) resolution/sensitivity analyses (chapter 3 and chapter 4).
- 7. Forward-modelling of surface displacements for hypothesised stack of sills associated with the 2010 summit eruption of Eyjafjallajökull, and results showing that such models fail to reproduce the observed InSAR displacements (chapter 5).
- 8. Application of a Bayesian inversion (Gauss-Markov framework with Monte Carlo Markov Chain) to jointly invert GNSS and InSAR for Eyjafjallajökull 2010 eruption source parameters. The data favoured a 3-D ellipsoidal source at 6.4–7.2 km depth and $\Delta V \approx 0.02$ –0.026 km³, contradicting a 2-D sill beneath the summit. (chapter 5).

- 9. Demonstration of the potential of ANSI tomographic models to identify present-day eruption sites on the Reykjanes Peninsula chapter 4).
- 10. Invertion of four InSAR tracks over Torfajökull volcano, and surface deformation modeling suggested a spheroidal source at \sim 5 km depth (4.5×5 km, NE–SW), spatially coincident with low V_S anomalies within the caldera (chapter 6).

7.3.2. List of Publications

Peer-reviewed articles

- 1. **Joana E Martins**, Miguel Caro Cuenca, Bart Davids, Guang Zhai, Elena González-Alonso, John PM Boncori, Lene Kristersen, Joan Sala, Lorenzo Solari, "Validation of the European Ground Motion Service with Global Navigation Satellite Systems and Corner Reflectors Over Deforming Areas". In IGARSS 2024-2024 IEEE International Geoscience and Remote Sensing Symposium, pp. 7537-7541. IEEE, 2024.
- Calero, Joan Sala, Amalia Vradi, Malte Vöge, Daniel Raucoules, Marcello de Michele, Joana E. Martins, Miguel Caro Cuenca, Filippo Vecchiotti, Marian Neagul, and Henrik Steen Andersen. "European Ground Motion Service Validation: InSAR Big Data Analytics". In IGARSS 2023-2023 IEEE International Geoscience and Remote Sensing Symposium, pp. 7537-7541. IEEE, 2023.
- 3. Ted Manders, **Joana E. Martins**, "Identification of Potential Sinkhole Signatures: Employing Time Series Clustering for Anomaly Detection in InSAR Time Series Over Limburgs Mining District". In IGARSS 2024-2024 IEEE International Geoscience and Remote Sensing Symposium, pp. 7415-7419. IEEE, 2024.
- 4. Dirk Kraaijpoel, **Joana E. Martins**, Sander Osinga, Bouko Vogelaar, and Jaap Breunese. "Statistical analysis of static and dynamic predictors for seismic b-value variations in the Groningen gas field". Netherlands Journal of Geosciences, 2022
- 5. T. Toledo, A. Obermann, A Verdel, **J. E. Martins**, P Jousset, AK Mortensen, K Erbas, and CM Krawczyk. "Ambient seismic noise monitoring and imaging at the Theistareykir geothermal field (Iceland)". Journal of Volcanology and Geothermal Research, page 107590, 2022.
- 6. Békési, E., Békési, Fokker, Peter A, **Martins, J. E.**, Norini, G., van Wees, JD. "Source parameters of the 8 February 2016, Mw= 4.2 Los Humeros earthquake by the inversion of InSAR-based ground deformation". Geothermics, 94, 102133, Elsevier, 2021.
- 7. **J. E. Martins**, A. J. Hooper, and R. F. Hanssen. "Towards geothermal reservoir characterization and monitoring through seismic (ambient noise) and geodetic (InSAR) imaging: Torfajökull volcano and Reykjanes peninsula, Iceland". In World Geothermal Congress 2020+1. Stanford University, 2021.
- 8. Harmen F. Mijnlieff, Bart Kempen, Caja Vries, Sjoerd Tolsma, **Joana E. Martins**, Mark Vrijlandt, Hans Veldkamp, and JD. van Wees. "The Dutch Geothermal

- Resource Base: Classified Using UNFC Resource Classification System and Its Potential to Meet the Dutch Geothermal Ambition". In World Geothermal Congress 2020+1. Stanford University, 2021.
- 9. Eszter Békési, **Joana E. Martins**, Jan Diederik van Wees, Jon Limberger, et al. "Ground deformation at the Los Humeros geothermal field (Mexico) inferred by InSAR". In World Geothermal Congress 2020+1. Stanford University, 2021.
- Martins, J. E., Weemstra, C., Ruigrok, E., Verdel, A., Jousset, P., and Hersir, G. P. (2020). "3D S-wave velocity imaging of Reykjanes Peninsula high-enthalpy geothermal fields with ambient-noise tomography". Journal of Volcanology and Geothermal Research, 391, 106685.[Invited Research Article]
- 11. Kay Koster, Arnoud Frumau, Jan Stafleu, Joris Dijkstra, Arjan Hensen, Ilona Velzeboer, Joana E. Martins, and Willem Jan Zaadnoordijk. "Greenhousepeat: a model linking CO2 emissions from subsiding peatlands to changing groundwater levels". Proceedings of the International Association of Hydrological Sciences, 382:609–614, 2020
- 12. **Martins, J. E.**, Ruigrok, E., Draganov, D., Hooper, A., Hanssen, R. F., White, R. S., and Soosalu, H. (2019). "Imaging Torfajökull's magmatic plumbing system with seismic interferometry and phase velocity surface wave tomography". Journal of Geophysical Research: Solid Earth, 124(3), 2920-2940.
- Békési, E., Fokker, P. A., Martins, J. E., Limberger, J., Bonté, D., and Van Wees, J. D. (2019). Production-induced subsidence at the los Humeros geothermal field inferred from PS-InSAR. geofluids, 2019.
- 14. Arie Verdel, Boris Boullenger, Joana E. Martins, Anne Obermann, Tania Toledo, and Philippe Jousset. "Ambient noise seismic reflection interferometry at the Los Humeros geothermal field, Mexico". In European Geothermal Congress 2019, 11-14 June 2019, The Hague, The Netherlands, 2019.
- 15. Eszter Békési, Peter A Fokker, **Joana E. Martins**, and Jan-Diederik van Wees. "Inversion of coseismic deformation due to the 8th February 2016, Mw 4.2 earthquake at Los Humeros (Mexico) inferred from dInsar". In Proceedings of the European Geothermal Congress, 2019.
- Samiei-Esfahany, S., Martins, J. E., van Leijen, F., and Hanssen, R. F. (2016). "Phase estimation for distributed scatterers in InSAR stacks using integer least squares estimation". IEEE Transactions on Geoscience and Remote Sensing, 54(10), 5671-5687.

- Aki, K. (1957). "Space and time spectra of stationary stochastic waves, with special reference to microtremors". In: *Bull. Earth. Res. Inst.* 35, pp. 415–456 (cit. on pp. 7, 38).
- Aki, K. (1965). "A note on the use of microseisms in determining the shallow structures of the earth's crust". In: *Geophysics* 30.4, pp. 665–666 (cit. on pp. 7, 38).
- Albertsson, A., J. Ö. Bjarnason, T. Gunnarsson, C. Ballzus, K. Ingason, et al. (2003). "The Iceland Deep Drilling Project: fluid handling, evaluation, and utilization". In: 000599234 (cit. on p. 5).
- Alparone, S., G. Barberi, O. Cocina, E. Giampiccolo, C. Musumeci, and D. Patanè (2012). "Intrusive mechanism of the 2008–2009 Mt. Etna eruption: Constraints by tomographic images and stress tensor analysis". In: *Journal of volcanology and geothermal research* 229, pp. 50–63 (cit. on p. 6).
- Altamimi, Z., X. Collilieux, J. Legrand, B. Garayt, and C. Boucher (2007). "ITRF2005: A new release of the International Terrestrial Reference Frame based on time series of station positions and Earth Orientation Parameters". In: *Journal of Geophysical Research: Solid Earth* 112.B9 (cit. on p. 99).
- "Ambient seismic noise monitoring and imaging at the Theistareykir geothermal field (Iceland)" (2022). In: *Journal of Volcanology and Geothermal Research* 429, p. 107590 (cit. on p. 118).
- Amelung, F., D. L. Galloway, J. W. Bell, H. A. Zebker, and R. J. Laczniak (1999). "Sensing the ups and downs of Las Vegas: InSAR reveals structural control of land subsidence and aquifer-system deformation". In: *Geology* 27.6, pp. 483–486 (cit. on p. 9).
- Anantrasirichai, N., J. Biggs, F. Albino, P. Hill, and D. Bull (2018). "Application of machine learning to classification of volcanic deformation in routinely generated InSAR data". In: *Journal of Geophysical Research: Solid Earth* 123.8, pp. 6592–6606 (cit. on p. 10).
- Ardhuin, F., E. Stutzmann, M. Schimmel, and A. Mangeney (2011). "Ocean wave sources of seismic noise". In: *Journal of Geophysical Research: Oceans* 116.C9 (cit. on p. 66).
- Árnadóttir, T., B. Lund, W. Jiang, H. Geirsson, H. Björnsson, P. Einarsson, and T. Sigurdsson (2009). "Glacial rebound and plate spreading: results from the first countrywide GPS observations in Iceland". In: *Geophysical Journal International* 177.2, pp. 691–716 (cit. on p. 123).
- Árnason, K. et al. (2007). "A study of the Krafla volcano using gravity, micro earthquake and MT data". In: 001045504 (cit. on p. 5).
- Árnason, K., H. Eysteinsson, and G. P. Hersir (2010). "Joint 1D inversion of TEM and MT data and 3D inversion of MT data in the Hengill area, SW Iceland". In: *Geothermics* 39.1, pp. 13–34 (cit. on p. 5).
- Arnórsson, S. (1995). "Geothermal systems in Iceland: structure and conceptual models—I. High-temperature areas". In: *Geothermics* 24.5-6, pp. 561–602 (cit. on p. 32).

Arsénio, A. M., P. Dheenathayalan, R. Hanssen, J. Vreeburg, and L. Rietveld (2015). "Pipe failure predictions in drinking water systems using satellite observations". In: *Structure and Infrastructure Engineering* 11.8, pp. 1102–1111 (cit. on p. 9).

- Auriac, A., F. Sigmundsson, A. Hooper, K. Spaans, H. Björnsson, F. Pálsson, V. Pinel, and K. Feigl (2014). "InSAR observations and models of crustal deformation due to a glacial surge in Iceland". In: *Geophysical Journal International* 198.3, pp. 1329–1341 (cit. on p. 9).
- Bachmann, O. and C. Huber (2016). "Silicic magma reservoirs in the Earth's crust". In: *American Mineralogist* 101.11, pp. 2377–2404 (cit. on p. 3).
- Bagnardi, M. and F. Amelung (2012). "Space-geodetic evidence for multiple magma reservoirs and subvolcanic lateral intrusions at Fernandina Volcano, Galápagos Islands". In: *Journal of Geophysical Research: Solid Earth* 117.B10 (cit. on p. 9).
- Bajpai, P. and V. Dash (2012). "Hybrid renewable energy systems for power generation in stand-alone applications: A review". In: *Renewable and Sustainable Energy Reviews* 16.5, pp. 2926–2939 (cit. on p. 4).
- Bartel, B. A., M. W. Hamburger, C. M. Meertens, A. R. Lowry, and E. Corpuz (2003). "Dynamics of active magmatic and hydrothermal systems at Taal Volcano, Philippines, from continuous GPS measurements". In: *Journal of Geophysical Research: Solid Earth* 108.B10 (cit. on p. 9).
- Båth, M. (1953). "Comparison of microseisms in Greenland, Iceland, and Scandinavia". In: *Tellus* 5.2, pp. 109–134 (cit. on p. 46).
- Behr, Y., J. Townend, S. Bannister, and M. Savage (2011). "Crustal shear wave tomography of the Taupo Volcanic Zone, New Zealand, via ambient noise correlation between multiple three-component networks". In: *Geochemistry, Geophysics, Geosystems* 12.3 (cit. on p. 8).
- Bekaert, D., A. Hooper, and T. Wright (2015a). "A spatially variable power law tropospheric correction technique for InSAR data". In: *Journal of Geophysical Research: Solid Earth* 120.2, pp. 1345–1356. ISSN: 2169-9313 (cit. on pp. 95, 120).
- Bekaert, D., R. Walters, T. Wright, A. Hooper, and D. Parker (2015b). "Statistical comparison of InSAR tropospheric correction techniques". In: *Remote Sensing of Environment* 170, pp. 40–47 (cit. on pp. 95, 120).
- Békési, E., P. A. Fokker, J. E. Martins, J. Limberger, D. Bonté, and J.-D. van Wees (2019a). "Production-Induced Subsidence at the Los Humeros Geothermal Field Inferred from PS-InSAR". In: *Geofluids* 2019. ISSN: 1468-8115 (cit. on p. 118).
- Békési, E., P. A. Fokker, J. E. Martins, J. Limberger, D. Bonté, and J.-D. van Wees (2019b). "Production-Induced Subsidence at the Los Humeros Geothermal Field Inferred from PS-InSAR". In: *Geofluids* 2019 (cit. on p. 9).
- Benediktsdóttir, Á., Ó. Gudmundsson, B. Brandsdóttir, and A. Tryggvason (2017). "Ambient noise tomography of Eyjafjallajökull volcano, Iceland". In: *Journal of Volcanology and Geothermal Research* 347, pp. 250–263 (cit. on p. 64).
- Bensen, G., M. Ritzwoller, M. Barmin, A. Levshin, F. Lin, M. Moschetti, N. Shapiro, and Y. Yang (2007). "Processing seismic ambient noise data to obtain reliable broad-band surface wave dispersion measurements". In: *Geophysical Journal International* 169.3, pp. 1239–1260 (cit. on pp. 22, 39, 42, 50, 66).

Bensen, G., M. Ritzwoller, and N. Shapiro (2008). "Broadband ambient noise surface wave tomography across the United States". In: *Journal of Geophysical Research: Solid Earth (1978–2012)* 113.B5 (cit. on p. 7).

- Benz, H., B. Chouet, P. Dawson, J. Lahr, R. Page, and J. Hole (1996). "Three-dimensional P and S wave velocity structure of Redoubt Volcano, Alaska". In: *Journal of Geophysical Research: Solid Earth* 101.B4, pp. 8111–8128 (cit. on p. 77).
- Berardino, P., G. Fornaro, R. Lanari, and E. Sansosti (2002). "A new algorithm for surface deformation monitoring based on small baseline differential SAR interferograms". In: *Geoscience and Remote Sensing, IEEE Transactions on* 40.11, pp. 2375–2383 (cit. on pp. 9, 25).
- Berrino, G., G. Corrado, G. Luongo, and B. Toro (1984). "Ground deformation and gravity changes accompanying the 1982 Pozzuoli uplift". In: *Bulletin volcanologique* 47.2, pp. 187–200 (cit. on p. 8).
- Biggs, J., S. Ebmeier, W. Aspinall, Z. Lu, M. Pritchard, R. Sparks, and T. Mather (2014). "Global link between deformation and volcanic eruption quantified by satellite imagery". In: *Nature communications* 5, p. 3471 (cit. on pp. 9, 10).
- Biot, M. (1956a). "Theory of elastic waves in a fluid-saturated porous solid. 1. Low frequency range". In: *The Journal of the acoustical Society of America* 28.2, pp. 168–178 (cit. on p. 76).
- Biot, M. A. (1956b). "Theory of propagation of elastic waves in a fluid-saturated porous solid. II. Higher frequency range". In: *The Journal of the acoustical Society of America* 28.2, pp. 179–191 (cit. on p. 76).
- Bjarnason, I. T., W. Menke, Ó. G. Flóvenz, and D. Caress (1993). "Tomographic image of the mid-Atlantic plate boundary in southwestern Iceland". In: *Journal of Geophysical Research: Solid Earth* 98.B4, pp. 6607–6622 (cit. on p. 63).
- Bjarnason, J. and M. Ólafsson (2000). "Chemical composition of geothermal steam and hot water at Torfajökull". In: *National Energy Authority of Iceland, Report OS-2000* 30, p. 91 (cit. on pp. 31, 37, 127, 129).
- Björnsson, H. (1992). "Jökulhlaups in Iceland: prediction, characteristics and simulation". In: *Annals of Glaciology* 16, pp. 95–106 (cit. on p. 4).
- Blake, S. (1984). "Magma mixing and hybridization processes at the alkalic, silicic, Torfajökull central volcano triggered by tholeiitic Veidivötn fissuring, south Iceland". In: *Journal of volcanology and geothermal research* 22.1, pp. 1–31 (cit. on pp. 31, 129).
- Blanck, H., P. Jousset, G. P. Hersir, K. Ágústsson, and Ó. G. Flóvenz (2019). "Analysis of 2014–2015 on-and off-shore passive seismic data on the Reykjanes Peninsula, SW Iceland". In: *Journal of Volcanology and Geothermal Research* (cit. on pp. 32, 33, 64, 65).
- Boyle, G. (2004). "Renewable energy". In: *Renewable Energy, by Edited by Godfrey Boyle, pp. 456. Oxford University Press, May 2004. ISBN-10: 0199261784. ISBN-13: 9780199261789*, p. 456 (cit. on p. 4).
- Brandsdóttir, B. and P. Einarsson (1992). "Volcanic tremor and low-frequency earthquakes in Iceland". In: *Volcanic seismology*. Springer, pp. 212–222 (cit. on pp. 31, 37).
- Breit, H., T. Fritz, U. Balss, M. Lachaise, A. Niedermeier, and M. Vonavka (2010). "TerraSAR-X SAR processing and products". In: *Geoscience and Remote Sensing, IEEE Transactions on* 48.2, pp. 727–740 (cit. on p. 95).

Brenguier, F., D. Clarke, Y. Aoki, N. M. Shapiro, M. Campillo, and V. Ferrazzini (2011). "Monitoring volcanoes using seismic noise correlations". In: *Comptes Rendus Geoscience* 343.8, pp. 633–638 (cit. on p. 8).

- Brenguier, F., N. M. Shapiro, M. Campillo, A. Nercessian, and V. Ferrazzini (2007). "3-D surface wave tomography of the Piton de la Fournaise volcano using seismic noise correlations". In: *Geophysical research letters* 34.2 (cit. on p. 8).
- Bromirski, P. D. and F. K. Duennebier (2002). "The near-coastal microseism spectrum: Spatial and temporal wave climate relationships". In: *Journal of Geophysical Research: Solid Earth (1978–2012)* 107.B8, ESE–5 (cit. on p. 43).
- Brouwer, W. S. and R. F. Hanssen (2023). "A treatise on InSAR geometry and 3-D displacement estimation". In: *IEEE Transactions on Geoscience and Remote Sensing* 61, pp. 1–11 (cit. on p. 92).
- Burchardt, S. (2018). "Introduction to volcanic and igneous plumbing systems—Developing a discipline and common concepts". In: *Volcanic and Igneous Plumbing Systems*. Elsevier, pp. 1–12 (cit. on p. 3).
- Burchardt, S., C. J. Annen, J. L. Kavanagh, and S. Hilmi Hazim (2022). "Developments in the study of volcanic and igneous plumbing systems: outstanding problems and new opportunities". In: *Bulletin of Volcanology* 84.6, p. 59 (cit. on p. 1).
- Calò, M. and C. Dorbath (2013). "Different behaviours of the seismic velocity field at Soultz-sous-Forêts revealed by 4-D seismic tomography: case study of GPK3 and GPK2 injection tests". In: *Geophysical Journal International* 194.2, pp. 1119–1137. ISSN: 0956-540X (cit. on p. 117).
- Calò, M., X. Kinnaert, and C. Dorbath (2013). "Procedure to construct three-dimensional models of geothermal areas using seismic noise cross-correlations: application to the Soultz-sous-Forêts enhanced geothermal site". In: *Geophysical Journal International* 194.3, pp. 1893–1899. ISSN: 1365-246X (cit. on p. 117).
- Casadevall, T. J. (1994). *Volcanic ash and aviation safety: proceedings of the first international symposium on volcanic ash and aviation safety.* Vol. 2047. US Government Printing Office (cit. on p. 4).
- Cashman, K. V. and G. Giordano (2014). "Calderas and magma reservoirs". In: *Journal of Volcanology and Geothermal Research* 288, pp. 28–45 (cit. on p. 3).
- Cashman, K. V. and R. S. J. Sparks (2013). "How volcanoes work: A 25 year perspective". In: *Bulletin* 125.5-6, pp. 664–690 (cit. on p. 1).
- Cashman, K. V., R. S. J. Sparks, and J. D. Blundy (2017). "Vertically extensive and unstable magmatic systems: a unified view of igneous processes". In: *Science* 355.6331, eaag3055 (cit. on p. 3).
- Catita, C., K. Feigl, J. Catalão, J. Miranda, and L. Victor (2005). "InSAR time series analysis of the 9 July 1998 Azores earthquake". In: *International Journal of Remote Sensing* 26.13, pp. 2715–2729 (cit. on p. 10).
- Chang, L., R. P. Dollevoet, and R. F. Hanssen (2017). "Nationwide railway monitoring using satellite SAR interferometry". In: *IEEE Journal of Selected Topics in Applied Earth Observations and Remote Sensing* 10.2, pp. 596–604 (cit. on p. 9).
- Chaussard, E., F. Amelung, and Y. Aoki (2013). "Characterization of open and closed volcanic systems in Indonesia and Mexico using InSAR time series". In: *Journal of Geophysical Research: Solid Earth* 118.8, pp. 3957–3969 (cit. on p. 9).

Chouet, B. (2003). "Volcano seismology". In: *Pure and applied geophysics* 160.3, pp. 739–788 (cit. on p. 6).

- Church, J. A., N. J. White, and J. M. Arblaster (2005). "Significant decadal-scale impact of volcanic eruptions on sea level and ocean heat content". In: *Nature* 438.7064, pp. 74–77 (cit. on p. 4).
- Claerbout, J. F. (1968). "Synthesis of a layered medium from its acoustic transmission response". In: *Geophysics* 33.2, pp. 264–269 (cit. on pp. 7, 64).
- Clifton, A. E. and S. A. Kattenhorn (2006). "Structural architecture of a highly oblique divergent plate boundary segment". In: *Tectonophysics* 419.1-4, pp. 27–40 (cit. on p. 77).
- Cooper, K. M. and A. J. Kent (2014). "Rapid remobilization of magmatic crystals kept in cold storage". In: *Nature* 506.7489, pp. 480–483 (cit. on pp. 3, 4).
- Cuenca, M. C., A. J. Hooper, and R. F. Hanssen (2013). "Surface deformation induced by water influx in the abandoned coal mines in Limburg, The Netherlands observed by satellite radar interferometry". In: *Journal of Applied Geophysics* 88, pp. 1–11 (cit. on p. 9).
- Dahm, T. and B. Brandsdóttir (1997). "Moment tensors of microearthquakes from the Eyjafjallajökull volcano in South Iceland". In: *Geophysical Journal International* 130.1, pp. 183–192 (cit. on p. 90).
- Darnet, M., P. Wawrzyniak, N. Coppo, S. Nielsson, E. Schill, and G. Ó. Friðleifsson (2018). "Monitoring geothermal reservoir developments with the Controlled-Source Electro-Magnetic method A calibration study on the Reykjanes geothermal field". In: *Journal of Volcanology and Geothermal Research* (cit. on pp. 5, 32).
- Davaille, A. (1999). "Simultaneous generation of hotspots and superswells by convection in a heterogeneous planetary mantle". In: *Nature* 402.6763, pp. 756–760 (cit. on p. 1).
- De Ridder, S., B. Biondi, and D. Nichols (2015). "Elliptical-anisotropic eikonal phase velocity tomography". In: *Geophysical Research Letters* 42.3, pp. 758–764 (cit. on p. 68).
- Degruyter, W. and C. Huber (2014). "A model for eruption frequency of upper crustal silicic magma chambers". In: *Earth and Planetary Science Letters* 403, pp. 117–130 (cit. on p. 3).
- Delgado, F. (2021). "Rhyolitic volcano dynamics in the Southern Andes: Contributions from 17 years of InSAR observations at Cordón Caulle volcano from 2003 to 2020". In: *Journal of South American Earth Sciences* 106, p. 102841 (cit. on p. 9).
- Dheenathayalan, P., M. C. Cuenca, and R. Hanssen (2011). "Different approaches for PSI target characterization for monitoring urban infrastructure". In: 8th International Workshop on Advances in the Science and Applications of SAR Interferometry, FRINGE 2011 (cit. on p. 9).
- Dheenathayalan, P., D. Small, A. Schubert, and R. F. Hanssen (2016). "High-precision positioning of radar scatterers". In: *Journal of Geodesy* 90.5, pp. 403–422 (cit. on p. 9).
- Di Traglia, F., M. Battaglia, T. Nolesini, D. Lagomarsino, and N. Casagli (2015). "Shifts in the eruptive styles at Stromboli in 2010–2014 revealed by ground-based InSAR data". In: *Scientific reports* 5.1, pp. 1–11 (cit. on p. 9).

Di Traglia, F., L. Cauchie, N. Casagli, and G. Saccorotti (2014). "Decrypting geophysical signals at Stromboli Volcano (Italy): Integration of seismic and Ground-Based InSAR displacement data". In: *Geophysical Research Letters* 41.8, pp. 2753–2761 (cit. on p. 9).

- Donaldson, C., T. Winder, C. Caudron, and R. S. White (2019). "Crustal seismic velocity responds to a magmatic intrusion and seasonal loading in Iceland's Northern Volcanic Zone". In: *Science Advances* 5.11, eaax6642 (cit. on p. 130).
- Draganov, D. (2007). "Seismic and electromagnetic interferometry: retrieval of the earth's reflection response using crosscorrelation". PhD thesis. TU Delft (cit. on p. 10).
- Draganov, D., K. Wapenaar, W. Mulder, J. Singer, and A. Verdel (2007). "Retrieval of reflections from seismic background-noise measurements". In: *Geophysical Research Letters* 34.4 (cit. on pp. 7, 10).
- Duffield, W. A. and J. H. Sass (2003). *Geothermal energy: Clean power from the earth's heat.* Vol. 1249. US Geological Survey (cit. on p. 4).
- Dvorak, J. J. and D. Dzurisin (1997). "Volcano geodesy: The search for magma reservoirs and the formation of eruptive vents". In: *Reviews of Geophysics* 35.3, pp. 343–384 (cit. on p. 8).
- Dzurisin, D. (2000). "Volcano geodesy: challenges and opportunities for the 21st century". In: *Philosophical Transactions of the Royal Society of London. Series A: Mathematical, Physical and Engineering Sciences* 358.1770, pp. 1547–1566 (cit. on p. 8).
- Dzurisin, D. (2006). *Volcano deformation: new geodetic monitoring techniques*. Springer Science & Business Media (cit. on p. 8).
- E. Martins, J., A. Hooper, D. Draganov, and E. Ruigrok (2013). "Imaging the magmatic system beneath Torfajökull volcano, Iceland: A combination of radar and seismic interferometry". In: *Living Planet Symposium, Edinburgh, United Kingdom*, http-livingplanet2013 (cit. on p. 118).
- Ebmeier, S. K., J. Biggs, T. A. Mather, and F. Amelung (2013). "Applicability of InSAR to tropical volcanoes: insights from Central America". In: *Geological Society, London, Special Publications* 380.1, pp. 15–37 (cit. on p. 9).
- Edmonds, M., K. V. Cashman, M. Holness, and M. Jackson (2019). *Architecture and dynamics of magma reservoirs* (cit. on p. 3).
- Einarsson, P. (2008). "Plate boundaries, rifts and transforms in Iceland". In: *Jökull* 58.12, pp. 35–58 (cit. on pp. 29, 32, 88).
- Einarsson, P. (1991). "Earthquakes and present-day tectonism in Iceland". In: *Tectono-physics* 189.1, pp. 261–279 (cit. on pp. 28, 31, 32, 37).
- Einarsson, P. and A. R. Hjartardottir (2015). "Structure and tectonic position of the Eyjafjallajokull volcano, S-Iceland". In: *JOKULL* 65, pp. 1–16 (cit. on p. 88).
- Einarsson, P. and K. Saemundsson (1987). *Earthquake Epicenters 1982-1985 and Volcanic Systems in Iceland: Upptok Jardskjalfta 1982-1985 Og Eldstodvakerfi a Islandi.* Menningarsjodur (cit. on p. 29).
- Einarsson, P., S. Þorbjarnarson, and M. Böttger (2002). *Faults and fractures of the South Iceland seismic zone near Þjórsá*. Landsvirkjun (cit. on p. 29).
- Elders, W., G. Friðleifsson, and A. Albertsson (2014). "Drilling into magma and the implications of the Iceland Deep Drilling Project (IDDP) for high-temperature geothermal systems worldwide". In: *Geothermics* 49, pp. 111–118 (cit. on p. 5).

Elders, W. A., G. Ó. Friðleifsson, R. A. Zierenberg, E. C. Pope, A. K. Mortensen, Á. Guðmundsson, J. B. Lowenstern, N. E. Marks, L. Owens, D. K. Bird, et al. (2011). "Origin of a rhyolite that intruded a geothermal well while drilling at the Krafla volcano, Iceland". In: *Geology* 39.3, pp. 231–234 (cit. on pp. 5, 117).

- Erlendsson, P. and P. Einarsson (1996). "The Hvalhnúkur Fault, a strike-slip fault mapped within the Reykjanes Peninsula oblique rift, Iceland". In: *Seismology in Europe, XXV ESC General Assembly, Reykjavık Iceland, September*, pp. 9–14 (cit. on p. 29).
- EU (2018). Heating and cooling: Overview of support activities and projects of the European Union on energy efficiency and renewable energy in the heating and cooling sector. (https://ec.europa.eu/energy/topics/energy-efficiency/) (cit. on p. 4).
- Eysteinsson, H. and J. F. Hermance (1985). "Magnetotelluric measurements across the eastern neovolcanic zone in south Iceland". In: *Journal of Geophysical Research: Solid Earth* 90.B12, pp. 10093–10103 (cit. on p. 5).
- Fernández, C., J. de la Nuez, R. Casillas, and E. García Navarro (2002). "Stress fields associated with the growth of a large shield volcano (La Palma, Canary Islands)". In: *Tectonics* 21.4, pp. 13–1 (cit. on p. 6).
- Fernández, J., A. Pepe, M. P. Poland, and F. Sigmundsson (2017). "Volcano Geodesy: Recent developments and future challenges". In: *Journal of Volcanology and Geothermal Research* 344, pp. 1–12 (cit. on p. 8).
- Ferretti, A., A. Fumagalli, F. Novali, C. Prati, F. Rocca, and A. Rucci (2011). "A new algorithm for processing interferometric data-stacks: SqueeSAR". In: *IEEE Transactions on Geoscience and Remote Sensing* 49.9, pp. 3460–3470 (cit. on pp. 9, 25).
- Ferretti, A., C. Prati, and F. Rocca (2000). "Nonlinear subsidence rate estimation using permanent scatterers in differential SAR interferometry". In: *IEEE Transactions on geoscience and remote sensing* 38.5, pp. 2202–2212 (cit. on p. 9).
- Ferretti, A., C. Prati, and F. Rocca (Jan. 2001). "Permanent Scatterers in SAR Interferometry". In: *TGARS* 39.1, pp. 8–20 (cit. on pp. 9, 25, 93).
- Fialko, Y., Y. Khazan, and M. Simons (2001). "Deformation due to a pressurized horizontal circular crack in an elastic half-space, with applications to volcano geodesy". In: *Geophysical Journal International* 146.1, pp. 181–190 (cit. on pp. 27, 110, 118).
- Foumelis, M. (2018). "Vector-based approach for combining ascending and descending persistent scatterers interferometric point measurements". In: *Geocarto international* 33.1, pp. 38–52. ISSN: 1010-6049 (cit. on p. 120).
- Fournier, T., M. Pritchard, and S. Riddick (2010). "Duration, magnitude, and frequency of subaerial volcano deformation events: New results from Latin America using InSAR and a global synthesis". In: *Geochemistry, Geophysics, Geosystems* 11.1 (cit. on p. 9).
- Franzson, H. (1987). "The Eldvorp High-Temperature Area, SW-Iceland. Geothermal Geology of First Exploration Well". In: *Proceedings of the 9th New Zealand Geothermal Workshop*, pp. 179–185 (cit. on pp. 32, 77).
- Friðleifsson, G. Ó., W. A. Elders, R. A. Zierenberg, A. P. Fowler, T. B. Weisenberger, K. G. Mesfin, Ó. Sigurðsson, S. Níelsson, G. Einarsson, F. Óskarsson, et al. (2018). "The Iceland Deep Drilling Project at Reykjanes: Drilling into the root zone of a black smoker analog". In: *Journal of Volcanology and Geothermal Research* (cit. on pp. 5, 63, 77).

Friðleifsson, G. Ó., Ó. Sigurdsson, D. Þorbjörnsson, R. Karlsdóttir, Þ. Gíslason, A. Albertsson, and W. Elders (2014a). "Preparation for drilling well IDDP-2 at Reykjanes". In: *Geothermics* 49, pp. 119–126 (cit. on p. 5).

- Friðleifsson, G., W. Elders, and A. Albertsson (2014b). "The concept of the Iceland deep drilling project". In: *Geothermics* 49, pp. 2–8 (cit. on p. 5).
- Friðleifsson, G., W. A. Elders, R. A. Zierenberg, A. Stefánsson, A. P. Fowler, T. B. Weisenberger, B. S. Harðarson, and K. G. Mesfin (2017). "The Iceland Deep Drilling Project 4.5 km deep well, IDDP-2, in the seawater-recharged Reykjanes geothermal field in SW Iceland has successfully reached its supercritical target". In: *Scientific Drilling* 23, pp. 1–12 (cit. on p. 5).
- Fridleifsson, G. Ó. and A. Albertsson (2000). "Deep geothermal drilling at Reykjanes Ridge: opportunity for an international collaboration". In: *Proceedings of the World Geothermal Congress*, F7–5 (cit. on p. 5).
- Froment, B., M. Campillo, P. Roux, P. Gouédard, A. Verdel, and R. L. Weaver (2010). "Estimation of the effect of nonisotropically distributed energy on the apparent arrival time in correlations". In: *Geophysics* 75.5, SA85–SA93 (cit. on p. 66).
- Fukushima, Y., V. Cayol, and P. Durand (2005). "Finding realistic dike models from interferometric synthetic aperture radar data: The February 2000 eruption at Piton de la Fournaise". In: *Journal of Geophysical Research: Solid Earth (1978–2012)* 110.B3. ISSN: 0148-0227 (cit. on pp. 8, 118).
- Galetto, F., M. Bagnardi, V. Acocella, and A. Hooper (2019). "Noneruptive unrest at the Caldera of Alcedo Volcano (Galápagos Islands) revealed by InSAR data and geodetic modeling". In: *Journal of Geophysical Research: Solid Earth* 124.4, pp. 3365–3381 (cit. on p. 9).
- Gasperikova, E., G. K. Rosenkjaer, K. Arnason, G. A. Newman, and N. J. Lindsey (2015). "Resistivity characterization of the Krafla and Hengill geothermal fields through 3D MT inverse modeling". In: *Geothermics* 57, pp. 246–257 (cit. on p. 5).
- Gassmann, F. (1951). "Elastic waves through a packing of spheres". In: *Geophysics* 16.4, pp. 673–685 (cit. on p. 76).
- Gauss, C. F. (1809). *Theoria motus corporum coelestium in sectionibus conicis solem ambientium*. Vol. 7. Perthes et Besser (cit. on p. 17).
- Gerstoft, P. and T. Tanimoto (2007). "A year of microseisms in southern California". In: *Geophysical Research Letters* 34.20, p. L20304 (cit. on p. 43).
- Gillett, N., A. Weaver, F. Zwiers, and M. Wehner (2004). "Detection of volcanic influence on global precipitation". In: *Geophysical Research Letters* 31.12 (cit. on p. 4).
- Gislason, S. R., T. Hassenkam, S. Nedel, N. Bovet, E. S. Eiriksdottir, H. A. Alfredsson, C. P. Hem, Z. I. Balogh, K. Dideriksen, N. Oskarsson, et al. (2011). "Characterization of Eyjafjallajökull volcanic ash particles and a protocol for rapid risk assessment". In: *Proceedings of the National Academy of Sciences* 108.18, pp. 7307–7312 (cit. on pp. 30, 115, 116).
- Gleckler, P., T. Wigley, B. Santer, J. Gregory, K. AchutaRao, and K. Taylor (2006). "Volcanoes and climate: Krakatoa's signature persists in the ocean". In: *Nature* 439.7077, pp. 675–675 (cit. on p. 4).

Golub, G. H., M. Heath, and G. Wahba (1979). "Generalized cross-validation as a method for choosing a good ridge parameter". In: *Technometrics* 21.2, pp. 215–223 (cit. on pp. 26, 54, 72).

- González, P. J., M. Bagnardi, A. J. Hooper, Y. Larsen, P. Marinkovic, S. V. Samsonov, and T. J. Wright (2015). "The 2014–2015 eruption of Fogo volcano: Geodetic modeling of Sentinel-1 TOPS interferometry". In: *Geophysical research letters* 42.21, pp. 9239–9246 (cit. on p. 9).
- González, P. J., K. F. Tiampo, A. G. Camacho, and J. Fernández (2010). "Shallow flank deformation at Cumbre Vieja volcano (Canary Islands): Implications on the stability of steep-sided volcano flanks at oceanic islands". In: *Earth and Planetary Science Letters* 297.3-4, pp. 545–557 (cit. on p. 9).
- Granados, I., M. Caló, A. Soto, L. Oregel, T. A. Toledo Zambrano, J. Martins, P. Jousset, and M. Perton (2018). "Structure of the Los Humeros geothermal field, Mexico, using seismic noise tomography". In: *10th Cities on Volcanoes Conference* (cit. on p. 118).
- Green, R. G., K. F. Priestley, and R. S. White (2017). "Ambient noise tomography reveals upper crustal structure of Icelandic rifts". In: *Earth and Planetary Science Letters* 466, pp. 20–31 (cit. on p. 64).
- Gudmundsson, A. (1998). "Magma chambers modeled as cavities explain the formation of rift zone central volcanoes and their eruption and intrusion statistics". In: *Journal of Geophysical Research: Solid Earth* 103.B4, pp. 7401–7412 (cit. on p. 2).
- Gudmundsson, M., G. Larsen, A. Hoskuldsson, and Á. Gylfason (2008). "Volcanic hazards in Iceland". In: *Jökull* 58, pp. 251–68 (cit. on p. 30).
- Gudmundsson, M. T., T. Thordarson, Á. Höskuldsson, G. Larsen, H. Björnsson, F. J. Prata, B. Oddsson, E. Magnússon, T. Högnadóttir, G. N. Petersen, et al. (2012). "Ash generation and distribution from the April-May 2010 eruption of Eyjafjallajökull, Iceland". In: *Scientific reports* 2 (cit. on p. 88).
- Gudmundsson, S., F. Sigmundsson, and J. M. Carstensen (2002). "Three-dimensional surface motion maps estimated from combined interferometric synthetic aperture radar and GPS data". In: *Journal of Geophysical Research: Solid Earth* 107.B10, ETG–13 (cit. on p. 79).
- Guðnason, E. Á. (2014). "Analysis of seismic activity on the western part of the Reykjanes Peninsula, SW Iceland, December 2008-May 2009". PhD thesis. University of Iceland (cit. on p. 64).
- Gunnarsson, B., B. Marsh, and H. Taylor Jr (1998). "Generation of Icelandic rhyolites: silicic lavas from the Torfajökull central volcano". In: *Journal of Volcanology and Geothermal Research* 83.1, pp. 1–45 (cit. on p. 30).
- Gutenberg, B. and C. F. Richter (1956). "Earthquake magnitude, intensity, energy, and acceleration: (Second paper)". In: *Bulletin of the seismological society of America* 46.2, pp. 105–145. ISSN: 1943-3573 (cit. on p. 6).
- Gutenberg, B. and C. F. Richter (1942). "Earthquake magnitude, intensity, energy, and acceleration". In: *Bulletin of the Seismological Society of America* 32.3, pp. 163–191. ISSN: 1943-3573 (cit. on p. 6).
- Hall-Spencer, J. M., R. Rodolfo-Metalpa, S. Martin, E. Ransome, M. Fine, S. M. Turner, S. J. Rowley, D. Tedesco, and M.-C. Buia (2008). "Volcanic carbon dioxide vents show ecosystem effects of ocean acidification". In: *Nature* 454.7200, pp. 96–99 (cit. on p. 4).

Halliday, D. and A. Curtis (2008). "Seismic interferometry, surface waves and source distribution". In: *Geophysical Journal International* 175.3, pp. 1067–1087 (cit. on p. 66).

- Haney, M. M. and V. C. Tsai (2015). "Nonperturbational surface-wave inversion: A Dixtype relation for surface waves". In: *Geophysics* 80.6, EN167–EN177 (cit. on pp. 72, 73).
- Hanssen, R. F. (2001). *Radar interferometry: data interpretation and error analysis*. Vol. 2. Springer Science & Business Media (cit. on pp. 13, 20, 24, 95).
- Harmon, N., C. Rychert, and P. Gerstoft (2010). "Distribution of noise sources for seismic interferometry". In: *Geophysical Journal International* 183.3, pp. 1470–1484 (cit. on pp. 11, 43).
- Haubrich, R., W. Munk, and F. Snodgrass (1963). "Comparative spectra of microseisms and swell". In: *Bulletin of the Seismological Society of America* 53.1, pp. 27–37 (cit. on p. 41).
- Hersir, G. P., K. Árnason, A. M. Vilhjálmsson, K. Saemundsson, P. Ágústsdóttir, and G. Ó. Friðleifsson (2018). "Krýsuvík high temperature geothermal area in SW Iceland: Geological setting and 3D inversion of magnetotelluric (MT) resistivity data". In: *Journal of Volcanology and Geothermal Research* (cit. on p. 5).
- Hersir, G. P., A. Björnsson, and L. B. Pedersen (1984). "Magnetotelluric survey across the active spreading zone in southwest Iceland". In: *Journal of volcanology and geothermal research* 20.3-4, pp. 253–265 (cit. on p. 5).
- Hildreth, W. (1981). "Gradients in silicic magma chambers: implications for lithospheric magmatism". In: *Journal of Geophysical Research: Solid Earth* 86.B11, pp. 10153–10192 (cit. on p. 3).
- Hilley, G. E., R. Bürgmann, A. Ferretti, F. Novali, and F. Rocca (2004). "Dynamics of slow-moving landslides from permanent scatterer analysis". In: *Science* 304.5679, pp. 1952–1955 (cit. on p. 9).
- Hjaltadóttir, S., K. S. Vogfjörd, S. Hreinsdóttir, and R. Slunga (2015). "Reawakening of a volcano: Activity beneath Eyjafjallajökull volcano from 1991 to 2009". In: *Journal of Volcanology and Geothermal Research* 304, pp. 194–205 (cit. on pp. 30, 89, 90).
- Hole, J., C. Bromley, N. Stevens, and G. Wadge (2007). "Subsidence in the geothermal fields of the Taupo Volcanic Zone, New Zealand from 1996 to 2005 measured by InSAR". In: *Journal of volcanology and geothermal research* 166.3-4, pp. 125–146. ISSN: 0377-0273 (cit. on p. 118).
- Hólmgeirsson, S., A. Gudmundsson, B. Pálsson, H. Bóasson, K. Ingasson, and S. Thorhallsson (2010). "Drilling operations of the first Iceland deep drilling well (IDDP)". In: *Proceedings of the World Geothermal Congress 2010*, p. 10 (cit. on p. 5).
- Hooper, A. (2008). "A Multi-Temporal InSAR Method Incorporating Both Persistent Scatterer and Small Baseline Approaches". In: *Geophysical Research Letters* 35, p. L16302. DOI: 10.1029/2008GL03465 (cit. on pp. 9, 25, 93, 97).
- Hooper, A., R. Pedersen, and F. Sigmundsson (2009). "Constraints on Magma Intrusion at Eyjafjallajökull and Katla Volcanoes in Iceland, From Time Series SAR Interferometry". In: *The VOLUME Project, VOLcanoes: Understanding subsurface mass moveMEnt (eds. C.J.Bean et al.)*, pp. 13–24 (cit. on pp. 30, 89).

Hooper, A. (2006). "Persistent Scatterer Radar Interferometry for Crustal Deformation Studies and Modeling of Volcanic Deformation". PhD thesis. Stanford University (cit. on p. 93).

- Hooper, A., B. Ófeigsson, F. Sigmundsson, B. Lund, P. Einarsson, H. Geirsson, and E. Sturkell (2011). "Increased capture of magma in the crust promoted by ice-cap retreat in Iceland". In: *Nature Geoscience* 4.11, pp. 783–786 (cit. on p. 4).
- Hooper, A., P. Segall, and H. Zebker (2007). "Persistent scatterer interferometric synthetic aperture radar for crustal deformation analysis, with application to Volcán Alcedo, Galápagos". In: *Journal of Geophysical Research: Solid Earth* 112.B7 (cit. on pp. 9, 93–95).
- Hooper, A., H. Zebker, P. Segall, and B. Kampes (2004). "A new method for measuring deformation on volcanoes and other natural terrains using InSAR persistent scatterers". In: *Geophysical research letters* 31.23 (cit. on pp. 9, 25, 93).
- Hooper, A. and H. A. Zebker (2007). "Phase unwrapping in three dimensions with application to InSAR time series". In: *JOSA A* 24.9, pp. 2737–2747 (cit. on p. 94).
- Hreinsdóttir, S., P. Einarsson, and F. Sigmundsson (2001). "Crustal deformation at the oblique spreading Reykjanes Peninsula, SW Iceland: GPS measurements from 1993 to 1998". In: *Journal of Geophysical Research: Solid Earth* 106.B7, pp. 13803–13816 (cit. on p. 79).
- Hreinsdóttir, S., F. Sigmundsson, M. J. Roberts, H. Björnsson, R. Grapenthin, P. Arason, T. Árnadóttir, J. Hólmjárn, H. Geirsson, R. A. Bennett, et al. (2014). "Volcanic plume height correlated with magma-pressure change at Grímsvötn Volcano, Iceland". In: *Nature geoscience* 7.3, pp. 214–218 (cit. on p. 4).
- Hutchison, W., J. Biggs, T. A. Mather, D. M. Pyle, E. Lewi, G. Yirgu, S. Caliro, G. Chiodini, L. E. Clor, and T. P. Fischer (2016). "Causes of unrest at silicic calderas in the East African Rift: New constraints from InSAR and soil-gas chemistry at Aluto volcano, Ethiopia". In: *Geochemistry, Geophysics, Geosystems* 17.8, pp. 3008–3030 (cit. on p. 10).
- Huttrer, G. W. (2021). "Geothermal Power Generation in the World 2015-2020 Update Report". In: *World Geothermal Congress* 2020+ 1 (cit. on p. 5).
- Institute of Earth Sciences (2023). Crustal Deformation (cit. on p. 99).
- Ivarsson, G. (1992). "Geology and petrochemistry of the Torfajokull central volcano in central south Iceland, in association with the Icelandic hot spot and rift zones". PhD thesis. University of Hawaii (cit. on pp. 52, 127).
- Jaggar, T. and R. Finch (1929). "Tilt records for thirteen years at the Hawaiian Volcano Observatory". In: *Bulletin of the Seismological Society of America* 19.1, pp. 38–51 (cit. on p. 8).
- Jakobsson, S. P., J. Jónsson, and F. Shido (1978). "Petrology of the western Reykjanes peninsula, Iceland". In: *Journal of Petrology* 19.4, pp. 669–705 (cit. on p. 77).
- Jakobsson, S. P. and J. SP (1979). "Petrology of recent basalts of the Eastern Volcanic Zone, Iceland". In: *Icelandic Museum of Natural History* (cit. on p. 88).
- Jaxybulatov, K., N. Shapiro, I. Koulakov, A. Mordret, M. Landès, and C. Sens-Schönfelder (2014). "A large magmatic sill complex beneath the Toba caldera". In: *science* 346.6209, pp. 617–619 (cit. on p. 8).

Jeddi, Z., O. Gudmundsson, and A. Tryggvason (2017). "Ambient-noise tomography of Katla volcano, south Iceland". In: *Journal of Volcanology and Geothermal Research* 347, pp. 264–277 (cit. on p. 64).

- Jóhannesson, H. and K. Saemundsson (1998). "Jardfraedikort af Islandi". In: *Hoggun (Geological Map of Iceland. Tectonics)*. *Náttúrfraedistofunu Islands (Icelandic Institute of Natural History), Reykjavık* (cit. on p. 28).
- Jónsson, S. (2009). "Stress interaction between magma accumulation and trapdoor faulting on Sierra Negra volcano, Galápagos". In: *Tectonophysics* 471.1-2, pp. 36–44 (cit. on p. 9).
- Jónsson, S., P. Einarsson, and F. Sigmundsson (1997). "Extension across a divergent plate boundary, the Eastern Volcanic Rift Zone, south Iceland, 1967–1994, observed with GPS and electronic distance measurements". In: *Journal of Geophysical Research: Solid Earth* 102.B6, pp. 11913–11929 (cit. on p. 9).
- Jónsson, S., P. Segall, R. Pedersen, and G. Björnsson (2003). "Post-earthquake ground movements correlated to pore-pressure transients". In: *Nature* 424.6945, p. 179. ISSN: 1476-4687 (cit. on p. 118).
- Jousset, P., K. Agustsson, E. Barison, G. Böhm, M. Caló, I. Chavarria, B. Farina, E. Gaucher, K. Loer, J. Martins, et al. (2019). "Seismic structures of the Acoculco and Los Humeros geothermal fields". In: *GEMex Deliverable D* 5 (cit. on p. 118).
- Jousset, P., K. Ágústsson, H. Blanck, M. Metz, S. Franke, G. Pàll Hersir, D. Bruhn, Ó. Flovenz, and G. Friðleifsson (2017). "Travel time seismic tomography on Reykjanes, SW Iceland". In: EGU General Assembly Conference Abstracts. Vol. 19, p. 17398 (cit. on pp. 5, 33, 63–65).
- Kampes, B. M. (Sept. 2005). "Displacement Parameter Estimation using Permanent Scatterer Interferometry". PhD thesis. Delft, the Netherlands: Delft University of Technology (cit. on pp. 9, 25, 93).
- Kampes, B. and S. Usai (1999). "Doris: The delft object-oriented radar interferometric software". In: *2nd international symposium on operationalization of remote sensing, enschede, the netherlands.* Vol. 16. Citeseer, p. 20 (cit. on p. 91).
- Kampes, B. M., R. F. Hanssen, and Z. Perski (2003). "Radar interferometry with public domain tools". In: *Proceedings of FRINGE*. Vol. 3 (cit. on p. 120).
- Kang, T.-S. and J. S. Shin (2006). "Surface-wave tomography from ambient seismic noise of accelerograph networks in southern Korea". In: *Geophysical Research Letters* 33.17 (cit. on p. 7).
- Kao, H., Y. Behr, C. A. Currie, R. Hyndman, J. Townend, F.-C. Lin, M. H. Ritzwoller, S.-J. Shan, and J. He (2013). "Ambient seismic noise tomography of Canada and adjacent regions: Part I. Crustal structures". In: *Journal of Geophysical Research: Solid Earth* 118.11, pp. 5865–5887 (cit. on p. 57).
- Karlsdóttir, R., A. M. Vilhjálmsson, and E. Á. Guðnason (2018). "Three dimensional inversion of magnetotelluric (MT) resistivity data from Reykjanes high temperature field in SW Iceland". In: *Journal of Volcanology and Geothermal Research* (cit. on pp. 5, 77).
- Karlsdóttir, S., Á. G. Gylfason, Á. Höskuldsson, B. Brandsdóttir, E. Ilyinskaya, M. T. Gudmundsson, Þ. Högnadóttir, and B. Þorkelsson (2012). "The 2010 Eyjafjallajökull eruption, Iceland". In: *Report to ICAO*, *209p* (cit. on p. 91).

Kawakatsu, H. and M. Yamamoto (2015). "Volcano seismology". In: *Earthquake Seismology*, pp. 389–419 (cit. on p. 6).

- Keiding, J. K. and O. Sigmarsson (2012). "Geothermobarometry of the 2010 Eyjaf-jallajökull eruption: Constraints on magma storage and mixing". In: *Journal of Geophysical Research: Solid Earth* 117.B11, B11202. DOI: 10.1029/2011JB008829 (cit. on pp. 115, 116).
- Keiding, M., T. Árnadóttir, S. Jonsson, J. Decriem, and A. Hooper (2010a). "Plate boundary deformation and man-made subsidence around geothermal fields on the Reykjanes Peninsula, Iceland". In: *Journal of Volcanology and Geothermal Research* 194.4, pp. 139–149. ISSN: 0377-0273 (cit. on p. 79).
- Keiding, M., T. Árnadóttir, S. Jonsson, J. Decriem, and A. Hooper (2010b). "Plate boundary deformation and man-made subsidence around geothermal fields on the Reykjanes Peninsula, Iceland". In: *Journal of Volcanology and Geothermal Research* 194.4, pp. 139–149 (cit. on pp. 79, 118).
- Keiding, M., T. Árnadóttir, E. Sturkell, H. Geirsson, and B. Lund (2008). "Strain accumulation along an oblique plate boundary: the Reykjanes Peninsula, southwest Iceland". In: *Geophysical Journal International* 172.2, pp. 861–872 (cit. on p. 32).
- Keiding, M., B. Lund, and T. Árnadóttir (2009). "Earthquakes, stress, and strain along an obliquely divergent plate boundary: Reykjanes Peninsula, southwest Iceland". In: *Journal of Geophysical Research: Solid Earth* 114.B9 (cit. on p. 32).
- Klein, F. W., P. Einarsson, and M. Wyss (1973). "Microearthquakes on the Mid-Atlantic Plate Boundary on the Reykjanes Peninsula in Iceland". In: *Journal of Geophysical Research* 78.23, pp. 5084–5099 (cit. on p. 32).
- Kobayashi, T., Y. Morishita, and H. Munekane (2018). "First detection of precursory ground inflation of a small phreatic eruption by InSAR". In: *Earth and Planetary Science Letters* 491, pp. 244–254 (cit. on p. 9).
- Konstantinou, K. I. and V. Schlindwein (2003). "Nature, wavefield properties and source mechanism of volcanic tremor: a review". In: *Journal of Volcanology and Geothermal Research* 119.1-4, pp. 161–187 (cit. on p. 7).
- Kusche, J. and R. Klees (2002). "Regularization of gravity field estimation from satellite gravity gradients". In: *Journal of Geodesy* 76.6-7, pp. 359–368 (cit. on p. 54).
- Lacoss, R., E. Kelly, and M. Toksoz (1969). "Estimation of seismic noise structure using arrays". In: *Geophysics* 34.1, pp. 21–36 (cit. on p. 43).
- Larose, E., A. Khan, Y. Nakamura, and M. Campillo (2005). "Lunar subsurface investigated from correlation of seismic noise". In: *Geophysical Research Letters* 32.16 (cit. on p. 7).
- Larsen, G. (1984). "Recent volcanic history of the Veidivötn fissure swarm, southern Iceland—an approach to volcanic risk assessment". In: *Journal of Volcanology and Geothermal Research* 22.1-2, pp. 33–58 (cit. on p. 31).
- Lazecky, M., I. Hlavacova, M. Bakon, J. J. Sousa, D. Perissin, and G. Patricio (2017). "Bridge displacements monitoring using space-borne X-band SAR interferometry". In: *IEEE Journal of Selected Topics in Applied Earth Observations and Remote Sensing* 10.1, pp. 205–210 (cit. on p. 9).
- Lehujeur, M., J. Vergne, J. Schmittbuhl, and A. Maggi (2015). "Characterization of ambient seismic noise near a deep geothermal reservoir and implications for interfero-

metric methods: a case study in northern Alsace, France". In: *Geothermal Energy* 3.1, p. 3. ISSN: 2195-9706 (cit. on p. 117).

- Lévěque, J.-J., L. Rivera, and G. Wittlinger (1993). "On the use of the checker-board test to assess the resolution of tomographic inversions". In: *Geophysical Journal International* 115.1, pp. 313–318 (cit. on p. 54).
- Lichten, S. M. and J. S. Border (1987). "Strategies for high-precision Global Positioning System orbit determination". In: *Journal of Geophysical Research: Solid Earth* 92.B12, pp. 12751–12762 (cit. on p. 99).
- Lin, F.-C., M. P. Moschetti, and M. H. Ritzwoller (2008). "Surface wave tomography of the western United States from ambient seismic noise: Rayleigh and Love wave phase velocity maps". In: *Geophysical Journal International* 173.1, pp. 281–298 (cit. on pp. 49, 52).
- Lippitsch, R., R. White, and H. Soosalu (2005). "Precise hypocentre relocation of microearthquakes in a high-temperature geothermal field: the Torfajökull central volcano, Iceland". In: *Geophysical Journal International* 160.1, pp. 371–388 (cit. on pp. 31, 37, 57–59, 126).
- Lisowski, M. (2007). "Analytical volcano deformation source models". In: *Volcano deformation*. Springer, pp. 279–304 (cit. on p. 8).
- Liu, H.-P., D. L. Anderson, and H. Kanamori (1976). "Velocity dispersion due to anelasticity; implications for seismology and mantle composition". In: *Geophysical Journal International* 47.1, pp. 41–58 (cit. on p. 74).
- Lowe, D. R., S. N. Williams, H. Leigh, C. B. Connort, J. B. Gemmell, and R. E. Stoiber (1986). "Lahars initiated by the 13 November 1985 eruption of Nevado del Ruiz, Colombia". In: *Nature* 324.6092, p. 51 (cit. on p. 4).
- Lu, Z. and D. Dzurisin (2014). "InSAR imaging of Aleutian volcanoes". In: *InSAR imaging of Aleutian volcanoes*. Springer, pp. 87–345 (cit. on p. 9).
- Lu, Z., D. Dzurisin, J. Biggs, C. Wicks Jr, and S. McNutt (2010). "Ground surface deformation patterns, magma supply, and magma storage at Okmok volcano, Alaska, from InSAR analysis: 1. Intereruption deformation, 1997–2008". In: *Journal of Geophysical Research: Solid Earth* 115.B5 (cit. on p. 9).
- Luzón, F., J. Almendros, and A. García-Jerez (2011). "Shallow structure of Deception Island, Antarctica, from correlations of ambient seismic noise on a set of dense seismic arrays". In: *Geophysical Journal International* 185.2, pp. 737–748 (cit. on p. 8).
- Maclennan, J. (2019). "Mafic tiers and transient mushes: evidence from Iceland". In: *Philosophical Transactions of the Royal Society A* 377.2139, p. 20180021 (cit. on p. 3).
- Magee, C., C. T. Stevenson, S. K. Ebmeier, D. Keir, J. O. Hammond, J. H. Gottsmann, K. A. Whaler, N. Schofield, C. A. Jackson, M. S. Petronis, et al. (2018). "Magma plumbing systems: a geophysical perspective". In: *Journal of Petrology* 59.6, pp. 1217–1251 (cit. on p. 6).
- Maghsoudi, Y., F. van der Meer, C. Hecker, D. Perissin, and A. Saepuloh (2018). "Using PS-InSAR to detect surface deformation in geothermal areas of West Java in Indonesia". In: *International journal of applied earth observation and geoinformation* 64, pp. 386–396. ISSN: 0303-2434 (cit. on p. 118).
- Magnússon, E., M. Gudmundsson, M. Roberts, G. Sigurðsson, F. Höskuldsson, and B. Oddsson (2012). "Ice-volcano interactions during the 2010 Eyjafjallajökull eruption,

as revealed by airborne imaging radar". In: *Journal of Geophysical Research: Solid Earth* 117.B7 (cit. on p. 88).

- Mahapatra, P. S., S. Samiei-Esfahany, H. van der Marel, and R. F. Hanssen (2013). "On the use of transponders as coherent radar targets for SAR interferometry". In: *IEEE Transactions on geoscience and remote sensing* 52.3, pp. 1869–1878 (cit. on p. 102).
- Major, J. J. and C. G. Newhall (1989). "Snow and ice perturbation during historical volcanic eruptions and the formation of lahars and floods". In: *Bulletin of volcanology* 52.1, pp. 1–27 (cit. on p. 4).
- Marinkovic, P. and Y. Larsen (2015). "On resolving the local oscillator drift induced phase ramps in ASAR and ERS1/2 interferometric data—the final solution". In: *Proceedings of the 9th international workshop Fringe* (cit. on p. 120).
- Marinkovic, P., G. Ketelaar, F. van Leijen, and R. Hanssen (2007). "InSAR quality control: Analysis of five years of corner reflector time series". In: *Proceedings of Fringe 2007 Workshop (ESA SP-649), Frascati, Italy.* Vol. 26, p. 30 (cit. on p. 102).
- Markoff, A. A. (1912). Wahrscheinlichkeitsrechnung. Leibzig: Teubner (cit. on p. 17).
- Marsh, B. D. (2006). "Dynamics of magmatic systems". In: *Elements* 2.5, pp. 287–292 (cit. on p. 1).
- Martins, J. (2006). Exploração da técnica de Interferometria de Radar às Ilhas do Pico e Faial (cit. on p. 10).
- Martins, J., A. Hooper, and R. Hanssen (2021). "Geothermal reservoir characterization and monitoring through seismic (ambient noise) and geodetic (InSAR) imaging applied on Torfajökull volcano and Reykjanes Peninsula, Iceland." In: *Proceedings World Geothermal Congress* 2021 (cit. on p. 15).
- Martins, J., E. Ruigrok, D. Draganov, A. Hooper, R. Hanssen, R. White, and H. Soosalu (2019). "Imaging Torfajökull's magmatic plumbing system with seismic interferometry and phase velocity surface wave tomography". In: *Journal of Geophysical Research: Solid Earth* 124.3, pp. 2920–2940. ISSN: 2169-9313 (cit. on pp. 15, 65, 69, 118, 126).
- Martins, J., E. Ruigrok, and A. Hooper (2022). *Volcanic harmonic tremors during a non-eruptive event, Torfajokull volcano, Iceland.* Tech. rep. Copernicus Meetings (cit. on pp. 7, 41).
- Martins, J. E. (2018). "New passive seismology network deployed in Los Humeros (Mexico): first results". In: *Cities on Volcanoes 10th meeting* (cit. on p. 118).
- Martins, J. E., C. Weemstra, E. Ruigrok, A. Verdel, P. Jousset, and G. Hersir (2020). "3D S-wave velocity imaging of Reykjanes Peninsula high-enthalpy geothermal fields with ambient-noise tomography". In: *Journal of Volcanology and Geothermal Research* 391, p. 106685 (cit. on pp. 15, 32, 118).
- Martins, J. E. and A. Hooper (2012). "Magma systems beneath Icelandic volcanoes: Exploring Eyjafjallajökull and Torfajökull volcanoes through InSAR time series". In: *NAC 2012: 11th Nederlands aardwetenschappelijk congres, Veldhoven, Netherlands.* 84e05788-0610-45 (cit. on p. 118).
- Massonnet, D. and K. L. Feigl (1998). "Radar interferometry and its application to changes in the Earth's surface". In: *Reviews of geophysics* 36.4, pp. 441–500 (cit. on p. 9).

Masterlark, T., M. Haney, H. Dickinson, T. Fournier, and C. Searcy (2010). "Rheologic and structural controls on the deformation of Okmok volcano, Alaska: FEMs, InSAR, and ambient noise tomography". In: *Journal of Geophysical Research: Solid Earth* (1978–2012) 115.B2 (cit. on p. 8).

- Mavko, G. M. (1980). "Velocity and attenuation in partially molten rocks". In: *Journal of Geophysical Research: Solid Earth* 85.B10, pp. 5173–5189 (cit. on pp. 77, 78).
- Mazzocchi, M., F. Hansstein, and M. Ragona (2010). "The 2010 volcanic ash cloud and its financial impact on the European airline industry". In: *CESifo Forum.* Vol. 11. München: ifo Institut für Wirtschaftsforschung an der Universität München, pp. 92–100 (cit. on p. 4).
- McGarvie, D. W. (1984). "Torfajokull: A volcano dominated by magma mixing". In: *Geology* 12.11, pp. 685–688 (cit. on pp. 31, 129).
- McGarvie, D., R. MacDonald, H. Pinkerton, and R. Smith (1990). "Petrogenetic evolution of the Torfajökull Volcanic Complex, Iceland II. The role of magma mixing". In: *Journal of Petrology* 31.2, pp. 461–481 (cit. on p. 31).
- McNutt, S. R. (2005). "Volcanic seismology". In: *Annual Review of Earth and Planetary Sciences* 33.1, pp. 461–491 (cit. on pp. 6, 7).
- McTigue, D. (1987). "Elastic stress and deformation near a finite spherical magma body: resolution of the point source paradox". In: *Journal of Geophysical Research: Solid Earth* 92.B12, pp. 12931–12940 (cit. on p. 8).
- Minh, D. H. T., R. Hanssen, and F. Rocca (2020). "Radar Interferometry: 20 Years of Development in Time Series Techniques and Future Perspectives". In: *Remote Sensing* 12.9, p. 1364 (cit. on p. 93).
- Mogi, K. (1958). "Relations between Eruptions of Various Volcanoes and the Deformations of the Ground Surfaces around them". In: *Bulletin of the Earthquake Research Institute, University of Tokyo* 36, pp. 99–134 (cit. on pp. 8, 26, 27, 118).
- Moran, S. C. (2003). "Multiple seismogenic processes for high-frequency earthquakes at Katmai National Park, Alaska: evidence from stress tensor inversions of fault-plane solutions". In: *Bulletin of the Seismological Society of America* 93.1, pp. 94–108 (cit. on p. 6).
- Mordret, A., D. Rivet, M. Landès, and N. M. Shapiro (2014). "3-D shear-velocity anisotropic model of Piton de la Fournaise volcano (La Réunion Island) from ambient seismic noise". In: *Journal of Geophysical Research: Solid Earth* (cit. on pp. 8, 57).
- Morishita, Y., T. Kobayashi, and H. Yarai (2016). "Three-dimensional deformation mapping of a dike intrusion event in Sakurajima in 2015 by exploiting the right-and left-looking ALOS-2 InSAR". In: *Geophysical Research Letters* 43.9, pp. 4197–4204 (cit. on p. 9).
- Mørk, M. B. E. (1984). "Magma mixing in the post-glacial Veidivötn fissure eruption, southeast Iceland: a microprobe study of mineral and glass variations". In: *Lithos* 17, pp. 55–75 (cit. on p. 31).
- Moune, S., O. Sigmarsson, P. Schiano, T. Thordarson, and J. Keiding (2012). "Melt inclusion constraints on the magma source of Eyjafjallajökull 2010 flank eruption". In: *Journal of Geophysical Research: Solid Earth* 117.B9 (cit. on p. 116).

Nagaoka, Y., K. Nishida, Y. Aoki, M. Takeo, and T. Ohminato (2012). "Seismic imaging of magma chamber beneath an active volcano". In: *Earth and Planetary Science Letters* 333, pp. 1–8 (cit. on pp. 7, 8, 38).

- Nakagawa, H., M. Murakami, S. Fujiwara, and M. Tobita (2000). "Land subsidence of the northern Kanto plains caused by ground water extraction detected by JERS-1 SAR interferometry". In: *Geoscience and Remote Sensing Symposium, 2000. Proceedings. IGARSS 2000. IEEE 2000 International.* Vol. 5. IEEE, pp. 2233–2235 (cit. on p. 9).
- Nakajima, J. and A. Hasegawa (2003). "Tomographic imaging of seismic velocity structure in and around the Onikobe volcanic area, northeastern Japan: implications for fluid distribution". In: *Journal of Volcanology and Geothermal Research* 127.1-2, pp. 1–18 (cit. on p. 77).
- Nakajima, J., T. Matsuzawa, A. Hasegawa, and D. Zhao (2001a). "Seismic imaging of arc magma and fluids under the central part of northeastern Japan". In: *Tectonophysics* 341.1-4, pp. 1–17 (cit. on p. 77).
- Nakajima, J., T. Matsuzawa, A. Hasegawa, and D. Zhao (2001b). "Three-dimensional structure of Vp, Vs, and Vp/Vs beneath northeastern Japan: Implications for arc magmatism and fluids". In: *Journal of Geophysical Research: Solid Earth* 106.B10, pp. 21843–21857 (cit. on p. 77).
- Nawa, K., N. Suda, Y. Fukao, T. Sato, Y. Aoyama, and K. Shibuya (1998). "Incessant excitation of the Earth's free oscillations". In: *Earth Planets Space* 50.1, pp. 3–8 (cit. on p. 22).
- Neri, M., F. Casu, V. Acocella, G. Solaro, S. Pepe, P. Berardino, E. Sansosti, T. Caltabiano, P. Lundgren, and R. Lanari (2009). "Deformation and eruptions at Mt. Etna (Italy): A lesson from 15 years of observations". In: *Geophysical Research Letters* 36.2 (cit. on p. 9).
- Neuberg, J. (2000). "Characteristics and causes of shallow seismicity in andesite volcanoes". In: *Philosophical Transactions of the Royal Society of London. Series A: Mathematical, Physical and Engineering Sciences* 358.1770, pp. 1533–1546 (cit. on p. 7).
- Newhall, C. G. and R. Punongbayan (1996). *Fire and mud: eruptions and lahars of Mount Pinatubo, Philippines*. Philippine Institute of Volcanology and Seismology Quezon City (cit. on p. 4).
- Newman, G. A., E. Gasperikova, G. M. Hoversten, and P. E. Wannamaker (2008). "Three-dimensional magnetotelluric characterization of the Coso geothermal field". In: *Geothermics* 37.4, pp. 369–399 (cit. on p. 5).
- O'Connell, R. J. and B. Budiansky (1974). "Seismic velocities in dry and saturated cracked solids". In: *Journal of Geophysical Research* 79.35, pp. 5412–5426 (cit. on pp. 77, 78).
- Obermann, A., T. Kraft, E. Larose, and S. Wiemer (2015). "Potential of ambient seismic noise techniques to monitor the St. Gallen geothermal site (Switzerland)". In: *Journal of Geophysical Research: Solid Earth* 120.6, pp. 4301–4316. ISSN: 2169-9356 (cit. on p. 117).
- Obermann, A., M. Lupi, A. Mordret, S. S. Jakobsdóttir, and S. A. Miller (2016). "3D-ambient noise Rayleigh wave tomography of Snæfellsjökull volcano, Iceland". In: *Journal of Volcanology and Geothermal Research* 317, pp. 42–52 (cit. on p. 64).

Ofeigsson, B. G., A. Hooper, F. Sigmundsson, E. Sturkell, and R. Grapenthin (2011). "Deep magma storage at Hekla volcano, Iceland, revealed by InSAR time series analysis". In: *Journal of Geophysical Research: Solid Earth* 116.B5 (cit. on pp. 9, 10, 121).

- Okada, Y. (Aug. 1985). "Surface deformation due to shear and tensile faults in a half-space". In: *BSSA* 75.4, pp. 1135–1154. ISSN: 1943-3573 (cit. on pp. 8, 26, 27, 118).
- Okada, Y. (1992). "Internal deformation due to shear and tensile faults in a half-space". In: *Bulletin of the seismological society of America* 82.2, pp. 1018–1040 (cit. on p. 26).
- Ólafsson, M. and J. Ö. Bjarnason (2000). "Chemistry of fumarole and hot springs in the Torfajökull geothermal area, South Iceland". In: *Proceedings World Geothermal Congress*. Kyushu-Tohoku Japan, pp. 1547–1552 (cit. on p. 32).
- Oliveri del Castillo, A. (1960). "Studio del bradisisma flegreo mediante osservazioni mareografiche". In: *X Meeting of Italian Geophysical Society, Rome*, pp. 18–19 (cit. on p. 8).
- Ómar Friðleifsson, G., W. A. Elders, R. Zierenberg, A. Steafánsson, Ó. Sigurðsson, Þ. Gíslason, T. B. Weisenberger, B. S. Harðarson, and K. G. Mesfin (2017). "ICDP supported coring in IDDP-2 at Reykjanes-the DEEPEGS demonstrator in Iceland-Supercritical conditions reached below 4.6 km depth." In: *EGU General Assembly Conference Abstracts*. Vol. 19, p. 14147 (cit. on p. 5).
- Omori, F. (1913a). "The Usu-san eruption and earthquake and elevation phenomena". In: *Bull. Imp. Earthq. Inv. Com.* 9, pp. 41–76 (cit. on p. 8).
- Omori, F. (1913b). "The Usu-san eruption and the elevation phenomena. II.[Comparison of bench mark heights in the base district before and after the eruption.]" In: *Bull. Imp. Earthquake Comm* 5, pp. 105–107 (cit. on p. 8).
- Oskooi, B., L. B. Pedersen, M. Smirnov, K. Árnason, H. Eysteinsson, A. Manzella, D. W. Group, et al. (2005). "The deep geothermal structure of the Mid-Atlantic Ridge deduced from MT data in SW Iceland". In: *Physics of the Earth and Planetary Interiors* 150.1-3, pp. 183–195 (cit. on p. 5).
- Palmason, G., J. Friedman, R. Williams Jr, J. Jonsson, and K. Saemundsson (1970). "Aerial infrared surveys of Reykjanes and Torfajökull thermal areas, Oceland, with a section on cost of exploration surveys". In: *Geothermics* 2, pp. 399–412. ISSN: 0375-6505 (cit. on p. 32).
- Pálmason, G. and K. Sæmundsson (1974). "Iceland in relation to the Mid-Atlantic Ridge". In: *Annual Review of Earth and Planetary Sciences* 2.1, pp. 25–50 (cit. on p. 32).
- Parascandola, A. (1947). *I fenomeni bradisismici del Serapeo di Pozzuoli*. Stabilmento tipografico G. Genovese (cit. on p. 8).
- Park, C. B., R. D. Miller, and J. Xia (1999). "Multichannel analysis of surface waves". In: *Geophysics* 64.3, pp. 800–808 (cit. on pp. 47, 69).
- Park, C. B., R. D. Miller, and J. Xia (1998). "Imaging dispersion curves of surface waves on multi-channel record". In: *SEG Technical Program Expanded Abstracts* 1998. Society of Exploration Geophysicists, pp. 1377–1380 (cit. on pp. 47, 69).
- Parks, M., F. Sigmundsson, Ó. Sigurðsson, A. Hooper, S. Hreinsdóttir, B. Ófeigsson, and K. Michalczewska (2018). "Deformation due to geothermal exploitation at Reykjanes, Iceland". In: *Journal of Volcanology and Geothermal Research* (cit. on pp. 79, 118).
- Parks, M. M., J. Biggs, P. England, T. A. Mather, P. Nomikou, K. Palamartchouk, X. Papanikolaou, D. Paradissis, B. Parsons, D. M. Pyle, et al. (2012). "Evolution of

Santorini Volcano dominated by episodic and rapid fluxes of melt from depth". In: *Nature Geoscience* 5.10, p. 749 (cit. on p. 10).

- Paul, A., M. Campillo, L. Margerin, E. Larose, and A. Derode (2005). "Empirical synthesis of time-asymmetrical Green functions from the correlation of coda waves". In: *Journal of Geophysical research* 110.B8, B08302 (cit. on p. 11).
- Pedersen, R. and F. Sigmundsson (2004). "InSAR based sill model links spatially offset areas of deformation and seismicity for the 1994 unrest episode at Eyjafjallajökull volcano, Iceland". In: *Geophys. Res. Lett* 31, p. L14610 (cit. on p. 9).
- Pedersen, R. and F. Sigmundsson (2006). "Temporal development of the 1999 intrusive episode in the Eyjafjallajökull volcano, Iceland, derived from InSAR images". In: *Bulletin of volcanology* 68.4, pp. 377–393 (cit. on pp. 30, 89, 90).
- Pedersen, R., S. Jónsson, T. Árnadóttir, F. Sigmundsson, and K. L. Feigl (2003). "Fault slip distribution of two June 2000 MW6. 5 earthquakes in South Iceland estimated from joint inversion of InSAR and GPS measurements". In: *Earth and Planetary Science Letters* 213.3-4, pp. 487–502. ISSN: 0012-821X (cit. on p. 118).
- Peterson, J. (1993). *Observations and modeling of seismic background noise*. US Geological Survey (cit. on p. 41).
- Pinel, V., A. Hooper, S. De la Cruz-Reyna, G. Reyes-Davila, M. Doin, and P. Bascou (2011). "The challenging retrieval of the displacement field from InSAR data for andesitic stratovolcanoes: Case study of Popocatepetl and Colima Volcano, Mexico". In: *Journal of Volcanology and Geothermal Research* 200.1-2, pp. 49–61 (cit. on p. 9).
- Poland, M. P. and E. de Zeeuw-van Dalfsen (2021). "Volcano geodesy: A critical tool for assessing the state of volcanoes and their potential for hazardous eruptive activity". In: *Forecasting and Planning for Volcanic Hazards, Risks, and Disasters.* Elsevier, pp. 75–115 (cit. on p. 8).
- Pritchard, M. E. and M. Simons (2002). "A satellite geodetic survey of large-scale deformation of volcanic centres in the central Andes". In: *Nature* 418.6894, p. 167 (cit. on p. 9).
- Receveur, M., F. Sigmundsson, V. Drouin, and M. Parks (2018). "Ground deformation due to steam cap processes at Reykjanes, SW-Iceland: effects of geothermal exploitation inferred from interferometric analysis of Sentinel-1 images 2015–2017". In: *Geophysical Journal International* 216.3, pp. 2183–2212. ISSN: 0956-540X (cit. on p. 79).
- Reinsch, T., P. Dobson, H. Asanuma, E. Huenges, F. Poletto, and B. Sanjuan (2017). "Utilizing supercritical geothermal systems: a review of past ventures and ongoing research activities". In: *Geothermal Energy* 5.1, p. 16 (cit. on p. 5).
- Rhie, J. and B. Romanowicz (2004). "Excitation of Earth's continuous free oscillations by atmosphere–ocean–seafloor coupling". In: *Nature* 431.7008, pp. 552–556 (cit. on p. 22).
- Richards, M. A., R. A. Duncan, and V. E. Courtillot (1989). "Flood basalts and hot-spot tracks: plume heads and tails". In: *Science* 246.4926, pp. 103–107 (cit. on p. 1).
- Rinehart, J. S. (1980). Geysers and geothermal energy. Vol. 223. Springer (cit. on p. 4).
- Rivalta, E., B. Taisne, A. Bunger, and R. Katz (2015). "A review of mechanical models of dike propagation: Schools of thought, results and future directions". In: *Tectonophysics* 638, pp. 1–42 (cit. on p. 2).

Rivalta, E. and P. Segall (2008). "Magma compressibility and the missing source for some dike intrusions". In: *Geophys. Res. Lett* 35, p. L04306 (cit. on p. 116).

- Robock, A. (2000). "Volcanic eruptions and climate". In: *Reviews of Geophysics* 38.2, pp. 191–219 (cit. on p. 4).
- Rosen, P. A., E. Gurrola, G. F. Sacco, and H. Zebker (2012). "The InSAR scientific computing environment". In: *EUSAR 2012; 9th European Conference on Synthetic Aperture Radar*. VDE, pp. 730–733. ISBN: 3800734044 (cit. on p. 120).
- Rosen, P. A., S. Hensley, G. Peltzer, and M. Simons (2004). "Updated repeat orbit interferometry package released". In: *Eos, Transactions American Geophysical Union* 85.5, pp. 47–47. ISSN: 0096-3941 (cit. on p. 120).
- Rossi, C. and M. Eineder (2015). "High-resolution InSAR building layovers detection and exploitation". In: *IEEE Transactions on Geoscience and Remote Sensing* 53.12, pp. 6457–6468 (cit. on p. 9).
- Rost, S. and C. Thomas (2002). "Array seismology: Methods and applications". In: *Reviews of geophysics* 40.3, p. 1008 (cit. on p. 43).
- Roux, P., K. G. Sabra, P. Gerstoft, W. Kuperman, and M. C. Fehler (2005a). "P-waves from cross-correlation of seismic noise". In: *Geophysical Research Letters* 32.19 (cit. on p. 7).
- Roux, P., K. G. Sabra, P. Gerstoft, W. Kuperman, and M. C. Fehler (2005b). "P-waves from cross-correlation of seismic noise". In: *Geophysical Research Letters* 32.19 (cit. on p. 43).
- Ruigrok, E., X. Campman, and K. Wapenaar (2011). "Extraction of P-wave reflections from microseisms". In: *Comptes Rendus Geoscience* 343.8, pp. 512–525 (cit. on p. 7).
- Ruigrok, E., S. Gibbons, and K. Wapenaar (2017). "Cross-correlation beamforming". In: *Journal of Seismology*, pp. 1–14 (cit. on p. 68).
- Ryder, I., B. Parsons, T. J. Wright, and G. J. Funning (2007). "Post-seismic motion following the 1997 Manyi (Tibet) earthquake: InSAR observations and modelling". In: *Geophysical Journal International* 169.3, pp. 1009–1027 (cit. on p. 9).
- Sabra, K. G., P. Gerstoft, P. Roux, W. Kuperman, and M. C. Fehler (2005a). "Extracting time-domain Green's function estimates from ambient seismic noise". In: *Geophysical Research Letters* 32.3 (cit. on p. 7).
- Sabra, K. G., P. Gerstoft, P. Roux, W. Kuperman, and M. C. Fehler (2005b). "Surface wave tomography from microseisms in Southern California". In: *Geophysical Research Letters* 32.14 (cit. on p. 7).
- Sæmundsson, K. (1979). "Outline of the geology of Iceland." In: *Jokull* 29, pp. 7–28 (cit. on p. 28).
- Saemundsson, K. (1972). "Notes on the geology of the Torfajökull area". In: *Náttúrufraedingurinn* 42.81, p. 144 (cit. on p. 31).
- Sagiya, T., S. Miyazaki, and T. Tada (2000). "Continuous GPS array and present-day crustal deformation of Japan". In: *Pure and applied Geophysics* 157, pp. 2303–2322 (cit. on p. 9).
- Sambridge, M. (1999a). "Geophysical inversion with a neighbourhood algorithm—I. Searching a parameter space". In: *Geophysical Journal International* 138.2, pp. 479–494 (cit. on pp. 57, 74).

Sambridge, M. (1999b). "Geophysical inversion with a neighbourhood algorithm—II. Appraising the ensemble". In: *Geophysical Journal International* 138.3, pp. 727–746 (cit. on pp. 57, 74).

- Samiei-Esfahany, S. (2017). "Exploitation of distributed scatterers in synthetic aperture radar interferometry". PhD thesis. Delft University of Technology (cit. on pp. 20, 25).
- Samiei-Esfahany, S., J. E. Martins, F. van Leijen, and R. F. Hanssen (2016). "Phase estimation for distributed scatterers in InSAR stacks using integer least squares estimation". In: *IEEE Transactions on Geoscience and Remote Sensing* 54.10, pp. 5671–5687 (cit. on p. 121).
- Samsonov, S., J. Beavan, P. J. González, K. Tiampo, and J. Fernández (2011). "Ground deformation in the Taupo Volcanic Zone, New Zealand, observed by ALOS PALSAR interferometry". In: *Geophysical Journal International* 187.1, pp. 147–160 (cit. on p. 9).
- Sánchez, J. J., M. Wyss, and S. R. McNutt (2004). "Temporal-spatial variations of stress at Redoubt volcano, Alaska, inferred from inversion of fault plane solutions". In: *Journal of Volcanology and Geothermal Research* 130.1-2, pp. 1–30 (cit. on p. 6).
- Sánchez-Pastor, P., A. Obermann, M. Schimmel, C. Weemstra, A. Verdel, and P. Jousset (2019). "Short-and long-term variations in the Reykjanes geothermal reservoir from seismic noise interferometry". In: *Geophysical Research Letters*. ISSN: 0094-8276 (cit. on pp. 32, 118).
- Scheiber-Enslin, S. E., P. C. LaFemina, E. Sturkell, A. J. Hooper, and S. J. Webb (2011). "Geodetic investigation of plate spreading along a propagating ridge: the Eastern Volcanic Zone, Iceland". In: *Geophysical Journal International* 187.3, pp. 1175–1194. ISSN: 1365-246X (cit. on pp. 31, 37, 123, 127).
- Schmidt, D. A. and R. Bürgmann (2003). "Time-dependent land uplift and subsidence in the Santa Clara valley, California, from a large interferometric synthetic aperture radar data set". In: *Journal of Geophysical Research: Solid Earth* 108.B9 (cit. on p. 9).
- Schmidt, D. A. (2002). *The Kindematics of Faults in the San Francisco Bay Area Inferred from Geodetic and Seismic Data.* University of California, Berkeley (cit. on p. 120).
- Schmidt, P., r. Lund Bjö, T. Árnadóttir, and H. Schmeling (2012). "Glacial isostatic adjustment constrains dehydration stiffening beneath Iceland". In: *Earth and Planetary Science Letters* 359, pp. 152–161 (cit. on p. 123).
- Schuster, G., J. Yu, J. Sheng, and J. Rickett (2004). "Interferometric/daylight seismic imaging". In: *Geophysical Journal International* 157.2, pp. 838–852 (cit. on p. 7).
- Segall, P. (2010). *Earthquake and volcano deformation*. Princeton University Press. ISBN: 140083385X (cit. on pp. 8, 25, 118).
- Segall, P. and J. L. Davis (1997). "GPS applications for geodynamics and earthquake studies". In: *Annual Review of Earth and Planetary Sciences* 25.1, pp. 301–336 (cit. on p. 9).
- Sella, G. F., T. H. Dixon, and A. Mao (2002). "REVEL: A model for recent plate velocities from space geodesy". In: *Journal of Geophysical Research: Solid Earth (1978–2012)* 107.B4, ETG–11 (cit. on pp. 28, 29).
- Sens-Schönfelder, C., E. Pomponi, and A. Peltier (2014). "Dynamics of Piton de la Fournaise volcano observed by passive image interferometry with multiple references". In: *Journal of Volcanology and Geothermal Research* 276, pp. 32–45 (cit. on p. 8).

Sens-Schönfelder, C. and U. Wegler (2006). "Passive image interferometry and seasonal variations of seismic velocities at Merapi Volcano, Indonesia". In: *Geophysical Research Letters* 33.21 (cit. on p. 8).

- Shapiro, N. M. and M. Campillo (2004). "Emergence of broadband Rayleigh waves from correlations of the ambient seismic noise". In: *Geophysical Research Letters* 31.7 (cit. on p. 7).
- Shapiro, N. M., M. Campillo, L. Stehly, and M. H. Ritzwoller (2005a). "High-resolution surface-wave tomography from ambient seismic noise". In: *Science* 307.5715, pp. 1615–1618 (cit. on pp. 7, 50).
- Shapiro, N. M., M. Campillo, L. Stehly, and M. H. Ritzwoller (2005b). "High-resolution surface-wave tomography from ambient seismic noise". In: *Science* 307.5715, pp. 1615–1618 (cit. on p. 68).
- Shapiro, N. M., M. H. Ritzwoller, P. Molnar, and V. Levin (2004). "Thinning and flow of Tibetan crust constrained by seismic anisotropy". In: *Science* 305.5681, pp. 233–236 (cit. on p. 57).
- Sigmarsson, O., I. Vlastelic, R. Andreasen, I. Bindeman, J.-L. Devidal, S. Moune, J. Keiding, G. Larsen, A. Höskuldsson, and T. Thordarson (2011a). "Remobilization of silicic intrusion by mafic magmas during the 2010 Eyjafjallajökull eruption". In: *Solid Earth* 2.2, pp. 271–281 (cit. on pp. 89, 91).
- Sigmarsson, O., I. Vlastélic, R. Andreasen, I. Bindeman, J.-L. Devidal, S. Moune, J. Keiding, G. Larsen, A. Höskuldsson, and T. Thordarson (2011b). "Remobilization of silicic intrusion by mafic magmas during the 2010 Eyjafjallajökull eruption". In: *Solid Earth* 2.2, pp. 271–281 (cit. on p. 116).
- Sigmundsson, F., S. Hreinsdóttir, A. Hooper, T. Árnadóttir, R. Pedersen, M. Roberts, N. Óskarsson, A. Auriac, J. Decriem, P. Einarsson, et al. (2010). "Intrusion triggering of the 2010 Eyjafjallajökull explosive eruption". In: *Nature* 468.7322, pp. 426–430 (cit. on pp. 9, 30, 88–92, 107, 110, 115).
- Sigmundsson, F. (2016). "New insights into magma plumbing along rift systems from detailed observations of eruptive behavior at Axial volcano". In: *Geophysical Research Letters* 43.24, pp. 12–423 (cit. on p. 2).
- Sigmundsson, F., P. Einarsson, Á. R. Hjartardóttir, V. Drouin, K. Jónsdóttir, T. Arnadottir, H. Geirsson, S. Hreinsdottir, S. Li, and B. G. Ofeigsson (2020). "Geodynamics of Iceland and the signatures of plate spreading". In: *Journal of Volcanology and Geothermal Research* 391, p. 106436 (cit. on pp. 28, 29, 32).
- Sigmundsson, E, M. Parks, H. Geirsson, A. Hooper, V. Drouin, K. S. Vogfjörd, B. G. Ófeigsson, S. H. Greiner, Y. Yang, C. Lanzi, et al. (2024). "Fracturing and tectonic stress drives ultrarapid magma flow into dikes". In: *Science*, eadn2838 (cit. on p. 33).
- Sigmundsson, F., M. Parks, A. Hooper, H. Geirsson, K. S. Vogfjörd, V. Drouin, B. G. Ófeigsson, S. Hreinsdóttir, S. Hjaltadóttir, K. Jónsdóttir, et al. (2022). "Deformation and seismicity decline before the 2021 Fagradalsfjall eruption". In: *Nature* 609.7927, pp. 523–528 (cit. on p. 33).
- Sigmundsson, F., M. Parks, R. Pedersen, K. Jónsdóttir, B. G. Ófeigsson, R. Grapenthin, S. Dumont, P. Einarsson, V. Drouin, E. R. Heimisson, et al. (2018). "Magma movements in volcanic plumbing systems and their associated ground deformation and seismic

patterns". In: *Volcanic and igneous plumbing systems*. Elsevier, pp. 285–322 (cit. on p. 9).

- Sigurdsson, H. (1970). "The petrology and chemistry of the Setberg volcanic region and of the intermediate and acid rocks of Iceland". PhD thesis. Durham University (cit. on p. 31).
- Sigurdsson, H., B. Houghton, S. McNutt, H. Rymer, and J. Stix (2015). *The encyclopedia of volcanoes*. Elsevier (cit. on pp. 2, 3, 6).
- Sigurdsson, H., B. Houghton, H. Rymer, J. Stix, and S. McNutt (1999). *Encyclopedia of volcanoes*. Academic press (cit. on p. 1).
- Simons, M., Y. Fialko, and L. Rivera (2002). "Coseismic deformation from the 1999 M w 7.1 Hector Mine, California, earthquake as inferred from InSAR and GPS observations". In: *Bulletin of the Seismological Society of America* 92.4, pp. 1390–1402 (cit. on p. 118).
- Singh, L. P., C. Van Westen, P. C. Ray, and P. Pasquali (2005). "Accuracy assessment of InSAR derived input maps for landslide susceptibility analysis: a case study from the Swiss Alps". In: *Landslides* 2.3, pp. 221–228 (cit. on p. 9).
- Sinton, J. M. and R. S. Detrick (1992). "Mid-ocean ridge magma chambers". In: *Journal of Geophysical Research: Solid Earth* 97.B1, pp. 197–216 (cit. on p. 3).
- Skolnik, M. (2002). "Role of radar in microwaves". In: *IEEE Transactions on microwave theory and techniques* 50.3, pp. 625–632 (cit. on p. 24).
- Skolnik, M. I. (1980). "Introduction to radar systems". In: New York (cit. on p. 24).
- Snieder, R. (2004). "Extracting the Green's function from the correlation of coda waves: A derivation based on stationary phase". In: *Physical Review E* 69.4, p. 046610 (cit. on p. 60).
- Solaro, G., V. Acocella, S. Pepe, J. Ruch, M. Neri, and E. Sansosti (2010). "Anatomy of an unstable volcano from InSAR: Multiple processes affecting flank instability at Mt. Etna, 1994–2008". In: *Journal of Geophysical Research: Solid Earth* 115.B10 (cit. on p. 9).
- Soosalu, H., R. Lippitsch, and P. Einarsson (2006). "Low-frequency earthquakes at the Torfajökull volcano, south Iceland". In: *Journal of volcanology and geothermal research* 153.3, pp. 187–199 (cit. on pp. 30, 33, 39, 127).
- Soosalu, H. and P. Einarsson (1997). "Seismicity around the Hekla and Torfajökull volcanoes, Iceland, during a volcanically quiet period, 1991–1995". In: *Bulletin of volcanology* 59.1, pp. 36–48 (cit. on pp. 31, 37, 127).
- Soosalu, H. and P. Einarsson (2005). "Seismic characteristics of the Hekla volcano and its surroundings, Iceland". In: *Jökull* 55, pp. 87–106 (cit. on p. 2).
- Soosalu, H. and P. Einarsson (2004). "Seismic constraints on magma chambers at Hekla and Torfajökull volcanoes, Iceland". In: *Bulletin of Volcanology* 66.3, pp. 276–286 (cit. on pp. 31, 37).
- Soosalu, H., P. Einarsson, and B. S. Þorbjarnardóttir (2005). "Seismic activity related to the 2000 eruption of the Hekla volcano, Iceland". In: *Bulletin of volcanology* 68.1, pp. 21–36 (cit. on p. 2).
- Soosalu, H. and R. S. White (2006). "Torfajökull 2005–seismic project". In: *Scientific report, University of Cambridge* (cit. on p. 40).

Sousa, J. and L. Bastos (2013). "Multi-temporal SAR interferometry reveals acceleration of bridge sinking before collapse". In: *Natural Hazards and Earth System Sciences* 13.3, pp. 659–667 (cit. on p. 9).

- Spaans, K., S. Hreinsdóttir, A. Hooper, Ófeigsson, and B. Gunnar (2015). "Crustal movements due to Iceland's shrinking ice caps mimic magma inflow signal at Katla volcano". In: *Scientific reports* 5, p. 10285 (cit. on p. 123).
- Sparks, R., C. Annen, J. Blundy, K. Cashman, A. Rust, and M. Jackson (2019). "Formation and dynamics of magma reservoirs". In: *Philosophical Transactions of the Royal society A* 377.2139, p. 20180019 (cit. on p. 3).
- Spera, F. J. (2000). "Physical properties of magmas". In: *Encyclopedia of volcanoes* (cit. on p. 1).
- Stankiewicz, J., T. Ryberg, C. Haberland, D. Natawidjaja, et al. (2010). "Lake Toba volcano magma chamber imaged by ambient seismic noise tomography". In: *Geophysical Research Letters* 37.17 (cit. on p. 8).
- Stehly, L., M. Campillo, and N. Shapiro (2006). "A study of the seismic noise from its long-range correlation properties". In: *Journal of Geophysical Research* 111.B10, B10306 (cit. on p. 11).
- Stein, S. and M. Wysession (2009). *An introduction to seismology, earthquakes, and earth structure.* John Wiley & Sons (cit. on pp. 21, 22).
- Sturkell, E., F. Sigmundsson, and P. Einarsson (2003). "Recent unrest and magma movements at Eyjafjallajökull and Katla volcanoes, Iceland". In: *J. geophys. Res* 108.2 (cit. on pp. 30, 89, 90).
- Sturkell, E., P. Einarsson, F. Sigmundsson, H. Geirsson, H. Olafsson, R. Pedersen, E. de Zeeuw-van Dalfsen, A. T. Linde, S. I. Sacks, and R. Stefánsson (2006). "Volcano geodesy and magma dynamics in Iceland". In: *Journal of Volcanology and Geothermal Research* 150.1-3, pp. 14–34 (cit. on p. 29).
- Stutzmann, E., F. Ardhuin, M. Schimmel, A. Mangeney, and G. Patau (2012). "Modelling long-term seismic noise in various environments". In: *Geophysical Journal International* 191.2, pp. 707–722 (cit. on pp. 46, 69).
- Sudhaus, H. and J. Sigurjón (2009). "Improved source modelling through combined use of InSAR and GPS under consideration of correlated data errors: application to the June 2000 Kleifarvatn earthquake, Iceland". In: *Geophysical Journal International* 176.2, pp. 389–404 (cit. on p. 9).
- Sudo, Y. and L. Kong (2001). "Three-dimensional seismic velocity structure beneath Aso Volcano, Kyushu, Japan". In: *Bulletin of volcanology* 63.5, pp. 326–344 (cit. on p. 77).
- Takada, Y. and M. Furuya (2010). "Aseismic slip during the 1996 earthquake swarm in and around the Onikobe geothermal area, NE Japan". In: *Earth and Planetary Science Letters* 290.3-4, pp. 302–310. ISSN: 0012-821X (cit. on p. 118).
- Tanimoto, T. and K. Prindle (2007). "Surface wave analysis with beamforming". In: *Earth, Planets, and Space* 59.5, pp. 453–458 (cit. on p. 43).
- Tarasewicz, J., B. Brandsdóttir, R. S. White, M. Hensch, and B. Thorbjarnardóttir (2012a). "Using microearthquakes to track repeated magma intrusions beneath the Eyjafjallajökull stratovolcano, Iceland". In: *Journal of Geophysical Research: Solid Earth* (1978–2012) 117.B9 (cit. on pp. 89, 91).

Tarasewicz, J., R. S. White, A. W. Woods, B. Brandsdóttir, and M. T. Gudmundsson (2012b). "Magma mobilization by downward-propagating decompression of the Eyjafjallajökull volcanic plumbing system". In: *Geophysical Research Letters* 39.19 (cit. on pp. 90, 91, 110, 116, 138, 140).

- Tibaldi, A. (2015). "Structure of volcano plumbing systems: A review of multi-parametric effects". In: *Journal of Volcanology and Geothermal Research* 298, pp. 85–135 (cit. on p. 2).
- Tiggelen, B. A. van (Dec. 2003). "Green Function Retrieval and Time Reversal in a Disordered World". In: *Phys. Rev. Lett.* 91 (24), p. 243904. DOI: 10.1103/PhysRevLett.91. 243904. URL: http://link.aps.org/doi/10.1103/PhysRevLett.91.243904 (cit. on p. 11).
- Tikhonov, A. (1963). "Solution of incorrectly formulated problems and the regularization method". In: *Soviet Math. Dokl.* Vol. 5, pp. 1035–1038 (cit. on pp. 26, 54, 71).
- Toledo, T., P. Jousset, H. Maurer, and C. Krawczyk (2018). "Optimized experimental network design for earthquake location problems: Applications to geothermal and volcanic field seismic networks". In: *Journal of Volcanology and Geothermal Research* (cit. on pp. 32, 79).
- Townsend, M. (2022). "Linking surface deformation to thermal and mechanical evolution of magma reservoirs". In: *Earth and Planetary Science Letters* 577, p. 117272. DOI: 10.1016/j.epsl.2021.117272 (cit. on p. 107).
- Tryggvason, A., S. T. Rögnvaldsson, and Ó. G. Flóvenz (2002). "Three-dimensional imaging of the P-and S-wave velocity structure and earthquake locations beneath Southwest Iceland". In: *Geophysical Journal International* 151.3, pp. 848–866 (cit. on p. 63).
- Tsai, V. C. (2009). "On establishing the accuracy of noise tomography travel-time measurements in a realistic medium". In: *Geophysical Journal International* 178.3, pp. 1555–1564 (cit. on p. 66).
- Tsai, V. C. and M. P. Moschetti (2010). "An explicit relationship between time-domain noise correlation and spatial autocorrelation (SPAC) results". In: *Geophysical Journal International* 182.1, pp. 454–460 (cit. on pp. 7, 38).
- Tuffen, H. (2007). "Models of ice melting and edifice growth at the onset of subglacial basaltic eruptions". In: *Journal of Geophysical Research: Solid Earth (1978–2012)* 112.B3 (cit. on p. 30).
- Ulfarsson, G. F. and E. A. Unger (2011). "Impacts and responses of Icelandic aviation to the 2010 Eyjafjallajökull volcanic eruption: case study". In: *Transportation research record* 2214.1, pp. 144–151 (cit. on p. 87).
- USGS (2006). How many active volcanoes are there on Earth? (https://www.usgs.gov/faqs/how-many-active-volcanoes-are-there-earth) (cit. on p. 1).
- Verdel, A., B. Boullenger, J. E. Martins, A. Obermann, T. Toledo, and P. Jousset (2019). "Ambient noise seismic reflection interferometry at the Los Humeros geothermal field, Mexico". In: *European Geothermal Congress 2019, 11-14 June 2019, The Hague, The Netherlands*, p. 9 (cit. on p. 118).
- Verdel, A., B. Boullenger, J. E. Martins, A. Obermann, T. Toledo, and P. Jousset (2020). "Structural delineation at the Los Humeros geothermal field, Mexico, by P-wave reflection retrieval from noise". In: *EGU General Assembly Conference Abstracts*, p. 7324 (cit. on p. 118).

Verdel, A., H. Wedemeijer, B. Paap, V. Vandeweijer, C. Weemstra, P. Jousset, S. Franke, H. Blanck, K. Águstsson, and G. P. Hersir (2016). "Reykjanes ambient noise reflection interferometry". In: *Proc. European Geothermal Congress, Strasbourg, France* (cit. on pp. 32, 64).

- Villagómez, D. R., D. R. Toomey, E. E. Hooft, and S. C. Solomon (2011). "Crustal structure beneath the Galápagos Archipelago from ambient noise tomography and its implications for plume-lithosphere interactions". In: *Journal of Geophysical Research: Solid Earth* (1978–2012) 116.B4 (cit. on p. 8).
- Villasenor, A., H. Benz, L. Filippi, G. De Luca, R. Scarpa, G. Patanè, and S. Vinciguerra (1998). "Three-dimensional P-wave velocity structure of Mt. Etna, Italy". In: *Geophysical research letters* 25.11, pp. 1975–1978 (cit. on p. 77).
- Villasenor, A., Y. Yang, M. H. Ritzwoller, and J. Gallart (2007). "Ambient noise surface wave tomography of the Iberian Peninsula: Implications for shallow seismic structure". In: *Geophysical Research Letters* 34.11 (cit. on p. 7).
- Wang, X. and Y. Aoki (2019). "Posteruptive thermoelastic deflation of intruded magma in Usu volcano, Japan, 1992–2017". In: *Journal of Geophysical Research: Solid Earth* 124.1, pp. 335–357 (cit. on p. 107).
- Wapenaar, K. (2004). "Retrieving the elastodynamic Green's function of an arbitrary inhomogeneous medium by cross correlation". In: *Physical review letters* 93.25, p. 254301 (cit. on pp. 7, 23, 43, 64).
- Wapenaar, K. and J. Fokkema (2006). "Green's function representations for seismic interferometry". In: *Geophysics* 71.4, SI33–SI46 (cit. on pp. 10, 23, 66).
- Wapenaar, K. and R. Snieder (2007). "From order to disorder to order: a philosophical view on seismic interferometry". In: *SEG Technical Program Expanded Abstracts* 2007. Society of Exploration Geophysicists, pp. 2683–2687 (cit. on p. 7).
- Wathelet, M., D. Jongmans, and M. Ohrnberger (2004). "Surface-wave inversion using a direct search algorithm and its application to ambient vibration measurements". In: *Near surface geophysics* 2.4, pp. 211–221 (cit. on p. 57).
- Wathelet, M. (2008). "An improved neighborhood algorithm: parameter conditions and dynamic scaling". In: *Geophysical Research Letters* 35.9 (cit. on pp. 57, 74).
- Weaver, R. L. and O. I. Lobkis (2004). "Diffuse fields in open systems and the emergence of the Green's function (L)". In: *The Journal of the Acoustical Society of America* 116.5, pp. 2731–2734 (cit. on p. 43).
- Webb, S. and W. Crawford (1999). "Long-period seafloor seismology and deformation under ocean waves". In: *Bulletin of the Seismological Society of America* 89.6, pp. 1535–1542 (cit. on p. 22).
- Weemstra, C., A. Obermann, A. Verdel, B. Paap, H. Blanck, E. Gunason, G. P. Hersir, P. Jousset, and Ó. Sigurdsson (2016). "Time-lapse seismic imaging of the Reykjanes geothermal reservoir". In: *Proc. European Geothermal Congress, Strasbourg, France* (cit. on pp. 32, 65, 118).
- Werner, C., U. Wegmüller, T. Strozzi, and A. Wiesmann (2002). "Processing strategies for phase unwrapping for INSAR applications". In: *Proceedings of the European Conference on Synthetic Aperture Radar (EUSAR 2002)*. Vol. 1, pp. 353–356 (cit. on p. 120).

Wiley, C. A. (1954). "Pulsed Doppler radar methods and apparatus". In: *US. Patent* 3 (cit. on p. 24).

- Woods, A. W. (1995). "The dynamics of explosive volcanic eruptions". In: *Reviews of geophysics* 33.4, pp. 495–530 (cit. on p. 7).
- Wright, T. J., Z. Lu, and C. Wicks (2003). "Source model for the Mw 6.7, 23 October 2002, Nenana Mountain Earthquake (Alaska) from InSAR". In: *Geophysical Research Letters* 30.18 (cit. on p. 9).
- Xia, J., R. D. Miller, and C. B. Park (1999). "Estimation of near-surface shear-wave velocity by inversion of Rayleigh waves". In: *Geophysics* 64.3, pp. 691–700 (cit. on pp. 72, 73).
- Xu, X., D. T. Sandwell, E. Tymofyeyeva, A. González-Ortega, and X. Tong (2017). "Tectonic and anthropogenic deformation at the Cerro Prieto geothermal step-over revealed by Sentinel-1A InSAR". In: *IEEE Transactions on Geoscience and Remote Sensing* 55.9, pp. 5284–5292. ISSN: 0196-2892 (cit. on p. 118).
- Yamasaki, T., T. Kobayashi, T. J. Wright, and Y. Fukahata (2018). "Viscoelastic crustal deformation by magmatic intrusion: a case study in the Kutcharo caldera, eastern Hokkaido, Japan". In: *Journal of Volcanology and Geothermal Research* 349, pp. 128–145 (cit. on p. 9).
- Yang, X.-M., P. M. Davis, and J. H. Dieterich (1988). "Deformation from inflation of a dipping finite prolate spheroid in an elastic half-space as a model for volcanic stressing". In: *Journal of Geophysical Research: Solid Earth* 93.B5, pp. 4249–4257 (cit. on pp. 26, 27, 121).
- Yang, Y.-H., M.-C. Tsai, J.-C. Hu, M. A. Aurelio, M. Hashimoto, J. A. P. Escudero, Z. Su, and Q. Chen (2018). "Coseismic slip deficit of the 2017 Mw 6.5 Ormoc earthquake that occurred along a creeping segment and geothermal field of the Philippine fault". In: *Geophysical Research Letters* 45.6, pp. 2659–2668. ISSN: 0094-8276 (cit. on p. 118).
- Yang, Y., M. H. Ritzwoller, A. L. Levshin, and N. M. Shapiro (2007). "Ambient noise Rayleigh wave tomography across Europe". In: *Geophysical Journal International* 168.1, pp. 259–274 (cit. on p. 7).
- Yao, H., R. D. van Der Hilst, and V. Maarten (2006). "Surface-wave array tomography in SE Tibet from ambient seismic noise and two-station analysis—I. Phase velocity maps". In: *Geophysical Journal International* 166.2, pp. 732–744 (cit. on pp. 7, 11).
- Yokoi, T. and S. Margaryan (2008). "Consistency of the spatial autocorrelation method with seismic interferometry and its consequence". In: *Geophysical Prospecting* 56.3, pp. 435–451 (cit. on pp. 7, 38).
- Yoon, Y. T., M. Eineder, N. Yague-Martinez, and O. Montenbruck (2009). "TerraSAR-X precise trajectory estimation and quality assessment". In: *Geoscience and Remote Sensing, IEEE Transactions on* 47.6, pp. 1859–1868 (cit. on p. 95).
- Yun, S., P. Segall, and H. Zebker (2006). "Constraints on magma chamber geometry at Sierra Negra Volcano, Galapagos Islands, based on InSAR observations". In: *Journal of Volcanology and Geothermal Research* 150.1-3, pp. 232–243 (cit. on pp. 9, 10).
- Zhou, Y., F. Dahlen, and G. Nolet (2004). "Three-dimensional sensitivity kernels for surface wave observables". In: *Geophysical Journal International* 158.1, pp. 142–168 (cit. on p. 72).

A

Supplementary material for chapter 5

This appendix contains supporting information to chapter 5: the single-station GPS time-series, parameters used through the InSAR processing, and additional descriptions on the applied models.

A.1. GPS time-series

Individual station estimated displacements during the Eyjafjallajökull 2010 eruption from the three GPS components of displacement: North (top), East (middle) and Up (bottom).

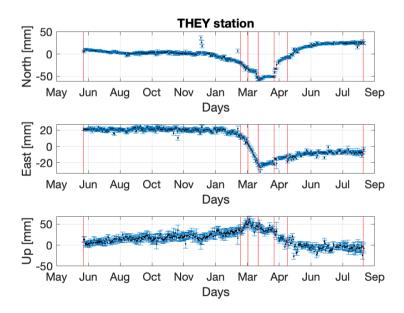


Figure A.1: GPS station THEY with the North (top), East (middle) and Up (bottom) components of displacement with error bars showing 1σ uncertainty. Red lines mark the moments of deformation rate used to model the different magma sources (also identified in Fig. 5.2).

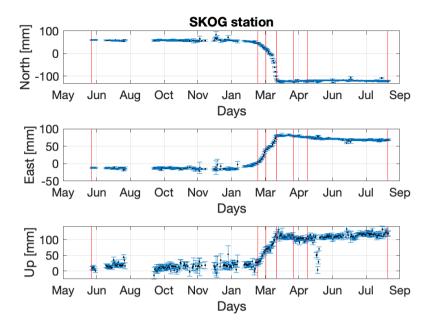


Figure A.2: Same caption as in fig. A.1 for station SKOG.

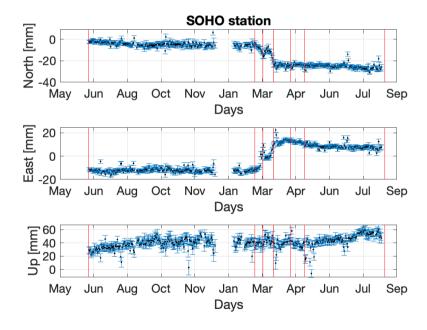


Figure A.3: Same caption as in fig. A.1 for station SOHO.

A.1. GPS time-series 177

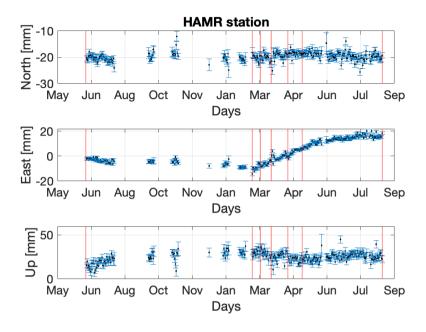


Figure A.4: Same caption as in fig. A.1 for station HAMR.

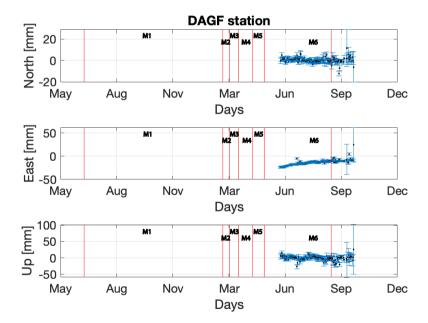


Figure A.5: Same caption as in fig. A.1 for station DAGF.

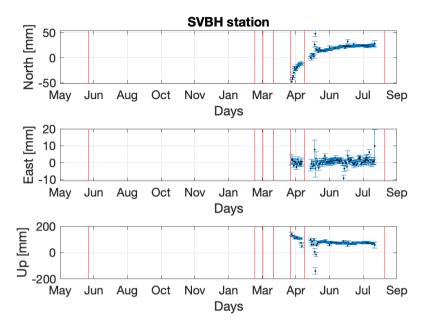


Figure A.6: Same caption as in fig. A.1 for station SVBH.

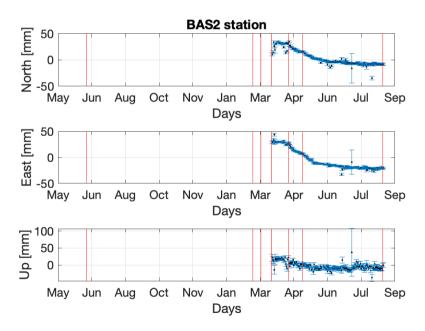


Figure A.7: Same caption as in fig. A.1 for station BAS2.

A.1. GPS time-series 179

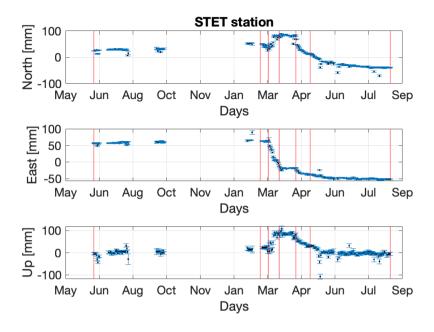


Figure A.8: GPS STE1/2 here renamed as STET. Caption as in fig. A.1.

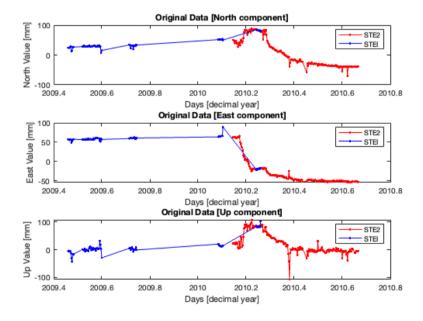


Figure A.9: Original data for SET1/STE1 before the combination display in Fig. A.8

20

%

A.2. Single primary image processing TerraSAR-X over Eyjafjallajökull

Table A.1 shows the parameters used for both interferogram and PSI processing. Two parameters in the table are different from the default parameters. The first is the number of overlapping pixels between patches in both range and azimuth, which are in this case the same as the resolution of TerraSAR-X images similar in both azimuths. The second parameter that is different from the default value (for C-band) is the range and filter grid size, which I chose to be half of the default value to deal with the increased spatial resolution of TerraSAR-X images.

Value Parameter Units **DEM** 25 meter Multilook factor 1 x 1 meter Oversampling no Overlapping pixels between patches in range 50 meter Overlapping pixels between patches in azimuth 50 meter Number of patches 30 Filter grid size 25 meter Dispersion threshold 0.4 Processing method Density

Density random

Table A.1: Fixed processing parameters

Acknowledgements

"I'm astounded whenever I finish something. Astounded and distressed. My perfectionist instinct should inhibit me from finishing; it should inhibit me from even beginning. But I get distracted and start doing something. What I achieve is not the product of an act of my will but of my will's surrender. I begin because I don't have the courage to think; I finish because I don't have the courage to quit. This book is my cowardice."

Bernardo Soares aka Fernando Pessoa.

Rather than copy-pasting a ten-page list of unfinished experiments I wish I had included in this manuscript, I will use Fernando Pessoa's words to characterise my PhD journey. My curiosity and willingness to experiment do not always obey the linear measure of a clock.

I am surely not alone. Every PhD is more than experiments, data, debugging, and publishing — it is a journey shaped by people. I was fortunate to walk this path with mentors, colleagues, friends, and family who guided, supported, and encouraged me and who have shaped my development as a scientist and as an individual. This thesis is the result of four formative years at Delft University of Technology, two stimulating months at the University of Leeds, four intense weeks of fieldwork in Iceland (not counting the touristy detours), one collaborative week in Cambridge, and countless hours squeezed between a full-time job, commuting, and my many other never-ending interests.

The story started even before I moved to Delft. In 2010 I was awarded a scholarship by the Portuguese Science and Technology Foundation (FCT). Although this scheme has since been discontinued, I remain deeply grateful for the opportunity FCT provided. Before applying I contacted Prof. Ramon Hanssen to express my interest in a PhD on InSAR and volcano-related topics at TU Delft. He welcomed me at the Aerospace Engineering faculty, department of Mathematical Geodesy and Positioning to discuss possible directions and spent a day discussing it with Prof. Andy Hooper (now at the University of Leeds). None of the initial proposals ignited me until Ramon suggested I speak with Prof. Kees Wapenaar, a pioneer in seismic interferometry and seismic imaging. Andy and I visited Kees that afternoon, and the project — studying an Icelandic volcano using both InSAR and seismic interferometry — was set. The work of Ramon Hanssen, Andy Hooper, and Kees Wapenaar has since then been a continual source of inspiration. With this settled, at the heart of this journey were my promotors and their patient guidance. Thank you for first offering me this opportunity and then giving me the freedom to pursue the project in my own way, even if a more constrained approach might have been faster. Andy's creativity and patience helped me find new ways forward whenever I felt stuck. Ramon's sharp eye for detail and big-picture thinking constantly challenged me to do better.

Shortly after I began, Kees Wapenaar introduced me to Deyan Draganov, and Deyan in turn introduced me to Elmer Ruigrok, who became my mentors in seismic interferometry. With Deyan I ran numerous forward-modelling experiments that deepened my understanding of wave propagation, I am thankful for all I learnt. Working with Elmer, I learned to translate those insights into real data. Elmer's calmness, clarity in explaining complex concepts, and his willingness to say, "I don't know — shall we figure it out?" reinforced my love of science and rekindled my curiosity when it was overwhelmed by the frustration. I am glad our work on Torfajökull is not finished. I am deeply grateful for how much I learned from you both.

With a topic decided, I needed a volcano. The initial proposal was Askja, but another team was already using that seismic network. An older data set (2005) for Torfajökull was instead made available, and although Askja was attractive for its ongoing surface displacements, Torfajökull 's ice cap, vast caldera, and location near the Mid-Atlantic Ridge extension and a transform zone offered an exceptionally beautiful and scientifically rich (and therefore wonderfully complicated) study area. Shortly before I moved to the Netherlands, Eyjafjallajökull erupted and Andy asked if I would process the excellent TerraSARX images that cover the eruption. I eagerly accepted. That kickstarted my PhD: a full time series processed and my first abstract submitted to AGU within four months of starting. Little I knew at that time that volcanoes are like people: it takes a lifetime to know one, and two volcanoes would take twice the effort.

During my first year, I visited the Department of Earth Sciences at Cambridge University and collaborated with Prof. Bob White and his team. Thank you, Bob, for the warm welcome, for sharing seismic data, and for hosting me so generously. I also appreciated the kindness of your students and your family for making my stay comfortable and enjoyable.

My second year began with two weeks of demanding but rewarding fieldwork in Iceland. I thank Prof. Freysteinn Sigmundsson, Dr. Thora Arnadottir and Dr. Rikke Pedersen for receiving me at the University of Iceland, and Sveinbjörn Steinbórsson for his invaluable fieldwork expertise and for revisiting seismic station locations to check the magnetic deviations we observed. Although I did not use every measurement, revisiting those seismic sites proved crucial to my study. We deployed GNSS stations for short recordings at breathtaking locations; thank you, Pete LaFemina, for selecting those sites, and Andy Hooper, my supervisor, for enabling the experience. Karsten and Mathew, thank you for sharing the fieldwork and the laughs.

The first two years of my PhD were spent at the Faculty of Aerospace Engineering, where I met many kind and brilliant people. I will fondly remember the Atmosphere bar on Friday afternoons and the lively interdisciplinary conversations with João Encarnação, Jan Comans, Prem Prasad, Steven Engelen, and others. I also thank many colleagues from the wind-energy group — Ricardo, Gael, Ben, Giuseppe, Danielle, and others — for the great times we shared, and Prof.Dr.Ġerard van Bussel and Prof.Dr.Ir. Gijs van Kuik for their pleasant conversations and support. During these years I supervised two Design/Synthesis Exercise (DSE) projects. In each project, students collaborated in groups of ten over ten weeks to produce a design in aviation, space, Earth observation, or

a related field. This was an experience I found exceptionally rewarding and an excellent reminder of the celestial mechanics, geodesy, and positioning astronomy courses I loved during my engineering degree.

Having officemates is like sharing a house with roommates, except you are awake much more of the time. In Aerospace I shared an office with two brilliant, warm-hearted women who have become friends and my paranimphs: Pooja Mahapatra and Anneleen Oyen, it was an absolute pleasure to begin this adventure with you, and I am certain there will be more moments to cherish. Thank you for the many late night times leaving the office, pep talks and cups of coffee, contagious laughter, and sometimes beyond honest feedback. After moving to Civil Engineering, I was lucky to share an office with Sylvie Dijkstra-Soudarissanane, Roderik Koenders, Ling Chang, and Jochem Lesparre; I learned so much from each of you, both culturally and technically. I treasure every conversation, coffee break, and tiny moment of cultural exchange - you made long days lighter and work more joyful.

I gratefully acknowledge the administrative and project support of Rebeca Domingo, Lidwien de Jong, Debbie Rietdijk, Marjolein de Niet-de Jager, and File Koot-Stomp. Your help greatly facilitated my work; your kindness and encouraging words meant far more than paperwork ever could. Rebeca, the moment you solved the iguana riddle is unforgettable.

Many informal discussions, collaborations, and friendships – often sparked in the coffee corner – enriched my research. I thank colleagues and fellow PhD students from the Department of Geoscience and Remote Sensing (GRS) and the Mathematical Geodesy and Positioning (MGP) group: Peter Buist, Olga Didova, Siavash Shakeri, Shizhuo Liu, Gertjan van Zwieten, Petar Marinkovic, Taco Broerse, Karsten Spaans, David Bekaert, Piers van der Torren, Ali Mousivand, Gert Mulder, Floris Heuff, Hamid Reza, Marcel Kleinherenbrink, Naresh Soni, Alexandru Lepadatu, Raluca Ianoschi, Saygin Abdikan, Ricardo Reinoso Rondinel, Enayat Hosseini Aria, Reenu Toodesh, Davide Imparato, Ramses Molijn, Yanqing Hou, Elte van Oostveen, Gabrielle Giorgi, Bram te Brake, and visiting researchers such as Zbigniew Perski, Tomokazu Kobayashi, and Thomas Fuhrmann. I also benefited from the expertise and insightful discussions with Dr.ir. Sandra Verhagen, Dr.ir. Hans van der Marel, Dr.ir. Christian Tiberius, Dr. Pavel Ditmar, and others.

A special thanks to my close colleagues and the members of the radar group from whom I learned the many shades of InSAR and radar interpretation. We shared the great and the difficult times, travelled to conferences together, rehearsed presentations late into the evening, enjoyed barbecues, and collected countless other memories that made this journey richer. Freek van Leijen — you are always there; your reliability is unquestionable. Mahmut Arıkan — you made things work: I will never forget when I lost six processing tracks in the cluster (about three months of work) and you stayed until you had tried every possible recovery method to retrieve the data. Pooja Mahapatra, thank you for being there whenever I needed you, for the steady support and the latenight kebab dinners. I still need to figure out how you convinced the whole group to do the CR experiment on that organic farm — but I'm grateful you did. Manuel Delgado Blasco thank you for the burst of joy and being a great listener, for all the fun and support. Miguel Caro Cuenca — little did I know that our short time together at TU Delft would

be rewarded later at TNO; thank you for your calmness every time we worked together. Anneleen Oyen — thank you for all the moments at work and beyond; it is always a pleasure to be with you. Lorenzo Iannini — thank you for always being so uplifting. Sami Samiei Esfahany — you are the true professor: thank you for everything you taught me, for every piece of advice I now recognise I should have followed, and for all the diverse and fantastic times outside work. Prabu Dheenathayalan — you became my friend the moment I met you; I have no words to express my gratitude for your friendship and for listening through the good and bad times.

At the Civil Engineering faculty we formed a PhD committee to organise social and instructive activities so that doctoral candidates would not feel isolated. I met the funniest and brightest colleagues there: Roderik, Rahul, Saskia, and many others (some I sadly lost contact with) — thank you for the camaraderie.

After my scholarship ended, Ramon arranged that I continued at TU Delft for two months. I returned to Iceland as a coach for the GRS master's students and I am grateful to all students and colleagues involved who contributed for such a pleasant time.

Right afterwards, I spent some time at Leeds University. Andy, thank you for arranging my two-month visit to the University of Leeds to help close open ends; I appreciated the academic support and also the kindness of your family — Julia, Sophie, Tom, Ben, and Elena — who made my visit warm and fun. At Leeds, I am grateful to Ekbal Hussain, Pablo Gonzalez, Tim Wright, Anna Hogg, Karsten Spaans, and others for stimulating discussions. At Leeds, David Bekaert and Sarah Lebel welcomed me warmly at their home; we shared nourishing conversations, home-cooked meals, and many restorative moments. I treasure those memories and hope we will make many more in the near future.

Since 2015 I have worked at TNO, where my perspective broadened and I have been translating academic findings and tools into practical solutions that address societal needs. I am thankful to my colleagues, managers, students and collaborators, including those in various EU-funded projects, for enriching my professional development. To avoid the risk of forgetting someone, I will not list names here, but please know that I value each of you deeply.

I would like to express my sincere gratitude to the members of my doctoral committee for their time, careful reading, and constructive feedback. I am especially thankful to my promotors, Prof.Dr.Ir. Ramon F. Hanssen (Delft University of Technology) and Prof.Dr. Andrew J. Hooper (University of Leeds), for their continuous guidance, proofreading and encouragement. I also thank the independent committee members — Prof.Dr. Freysteinn Sigmundsson (University of Iceland), Dr. Michiel J. van der Meulen (TNO – Geological Survey of the Netherlands), Dr. Elske de Zeeuw-van Dalfsen (Royal Netherlands Meteorological Institute / Delft University of Technology), Prof.Dr.Ir. Evert C. Slob (Delft University of Technology) — for their insightful review and recommendations.

I am deeply grateful to my friends outside of work for providing laughter, food, music, and much-needed distraction during my years in Delft and during my visits to Lisbon and Vila Verde. To childhood friends, schoolmates from Geodesy engineering, and those I met in theatre and cinema — you know who you are and the place you have in my heart. Further thanks to Siavash Shakeri and Lorenzo Iannini for their immeasurable support

during the low moments and for the endless fun when we play music together. Laura Hermans and Francesco, thank you for pushing me to go out. Danijela Sijacic, thank you for the fantastic conversations and unwavering support. Alin, Andreas, Dominika, and Slawek — painting my house with you became far more than a task; it was a source of much-needed laughter during a difficult time. Thank you for helping me out. We thank the members of 'Copofonia em Português' for the cherished moments and for always offering wise (and often humorous) advice. Andre van Dam, thank you for the stimulating physical and metaphysical conversations. Tiago and Anneta, thank you for the deep talks when you lived in Utrecht and for our continued exchange I value so much. I thank Pedro, for always being there whenever I needed you — for helping me through practical problems and emotional lows.

I also thank Geneviève, Francis, Sophie, Pedro, Guillaume, Lisa, Charlotte, Margot, Eliete, Théodore, and Léonard for welcoming me so warmly into your family. Sophie and Pedro, thank you for helping to uncover the source of my chronic pain and for correcting a misdiagnosis that lasted fifteen years.

Finally, nothing would have been possible without my family. Minha mae, tens a força de um vulcão, mas és a rocha que nos sustenta a todos, obrigada por todo o teu apoio e por não me teres ajudado a ir à procura do que me faz feliz. Sem o teu apoio e motivação eu não teria conseguido. Meu pai, só tu consegues sentir a minha sensibilidade, obrigada por me mostrares como se luta pela vida, e pela musica que me deste enquanto criança que é o meu refugio em dias mais escuros. Meu mano, obrigada pela tua calma e por sempre tentares arranjar uma solução qualquer que seja o problema. Minha mana, obrigada pelo teu amor, pela tua forma rústica de o mostrares, pelos teus valores, e por me trazeres ao centro senpre que eu me desviava. Zé Pedro - thank you for being you: present, warm, and, yes, my personal winner of 'Most Handsome Man on Earth'. Ni, thank you for reading every book I hand you and for being the only one brave enough to share the stage with that level of handsomeness. Madrinha, obrigada por todo o apoio, pelas longas conversas ao telefone e a visita surpresa a Delft.

François, you are my roots. You allow me to fly and explore while bringing me back to my centre with a smile. Thank you for your help during this long-lasting process, for drying my tears, for helping me grow, for being kindly honest, for the weekends we lost together because of my work, and for handling my physical and metaphysical questions with patience and love. I hope we will have more time for our ongoing experiments.

To everyone named and unnamed here: thank you. This thesis bears the imprint of all our conversations.

Joana Martins, Delft/Vila Verde/Alfama, August 2025.

About the author

Joana E. Martins was born in Oporto, Portugal, on April 15, 1981.

In 1998, Joana Martins enrolled at the University of Porto, Faculty of Sciences, to pursue a degree in Mathematics, where she studied for two years before transferring to the Faculty of Sciences, University of Lisbon, for an additional year.

In mid-2001, she switched to the Geodesy and Surveying Engineering program (now called Geospatial Engineering) at the Faculty of Sciences, University of Lisbon, a five-year program from which she graduated in 2006. As part of her degree, she completed an internship at the National Civil Engineering Laboratory (LNEC), where she researched the use of satellite remote sensing techniques to update cartography and assess land-cover changes.

In 2008, she obtained her Master's degree in Geophysics from the University of Lisbon, with a research project focused on ground deformation using InSAR over the Faial and Pico volcanic islands in the Azores archipelago, Portugal. In parallel with her master's research, she produced a land-cover classification of the Azores archipelago using satellite optical imagery for the Ministry of Agriculture, the Sea, the Environment, and Spatial Planning.

Between 2008 and 2010, she worked as a freelance consultant, collaborating with the Municipality of Lisbon, supporting an IT company outsourced to the telecommunications sector, and teaching remote sensing at a vocational school. In 2010, she was awarded funding from the Portuguese Science and Technology Foundation to pursue a Ph.D. at the Department of Geoscience and Remote Sensing, Delft University of Technology, in the Netherlands.

Since 2015, she has been working at TNO – Geological Survey of the Netherlands, within the Advisory Group of the Ministry of Climate Policy and Green Growth, as a researcher, advisor, and technical lead. Since joining TNO, she has contributed to several European projects, including IMAGE (Integrated Methods for Advanced Geothermal Exploration), GEMex (Geothermal Energy Research Europe-Mexico), GeoERA-HIKE (Hazard and Impact Knowledge for Europe), the validation of the European Ground Motion Service (EGMS), and currently GSEU (Geological Service for Europe).

In 2024, she began a professional course in documentary filmmaking at Kino-Doc Lisboa, reflecting her interest in science communication and her ambition to bring geoscientific topics to broader audiences.

Her current research focuses on the use of Earth observation, remote sensing, seismic data, and data science to address societal challenges. Her main geoscience interests lie in geodesy and geophysics, particularly InSAR, seismic tomography, volcano physics, and surface deformation processes associated with volcanic activity, coastal vulnerability as well as co- and post-mining processes (uplift and subsidence).

